

FREQUENCY AND TEMPERATURE DEPENDENCE  
IN ELECTROMAGNETIC PROPERTIES OF  
MARTIAN ANALOG MINERALS

by

David E. Stillman

A thesis submitted to the Faculty and Board of Trustees of the Colorado School of Mines in partial fulfillment of the requirements for the degree of Doctor of Philosophy (Geophysics).

Golden, Colorado

Date \_\_\_\_\_

Signed: \_\_\_\_\_  
David E. Stillman

Approved: \_\_\_\_\_  
Dr. Gary R. Olhoeft  
Thesis Advisor

Golden, Colorado

Date \_\_\_\_\_

Approved: \_\_\_\_\_  
Dr. Terry K. Young  
Professor and Head  
Department of Geophysics

## ABSTRACT

Over the past decade, much has been learned about the surface of Mars; however, the subsurface of Mars still remains a mystery. Many surfaces on Mars are buried by aeolian deposits or coated with dust and thus hidden from traditional imaging methods. Ground penetrating radar (GPR) has the potential to image beneath these layers to give geological context to drilling targets, locate potential subsurface rover hazards, investigate stratigraphy, and most importantly, image subsurface water. The discovery of Martian groundwater will have significant implications for a manned mission to Mars and could reveal important clues about the possibility of extraterrestrial life. The Martian subsurface appears to be a good radar environment because average subsurface temperatures are below the freezing point of water (down to 1–5 km). However, GPR depth of penetration is extremely dependent on the EM properties of the subsurface which include dielectric permittivity, magnetic permeability, and DC resistivity. Martian soil has a mineralogical composition that is unlike the majority of soils seen on Earth. Furthermore, a magnetic dust layer blankets nearly every surface on the planet. Consequently, attenuation mechanisms such as dielectric and magnetic relaxations losses could cause significant attenuation of radar energy. Dielectric and magnetic relaxations can also be temperature dependent, which is significant since the average temperature on Mars is 213 K with planetary diurnal variations ranging from 154 – 300 K.

In order to understand the effect of EM losses on GPR depth of penetration on Mars, the EM properties of Martian analog samples were measured versus frequency and temperature using an HP8753D vector network analyzer. The measurements were also acquired versus temperature over a range of 180 – 300 K to simulate the Martian environment. Results from these measurements yielded several significant EM relaxations in Martian analog minerals that had never been observed prior to this study.

Grey hematite was found to possess a large temperature dependent dielectric relaxation with a relaxation frequency at 230 and 450 MHz at 213 K in two samples. Magnetite was found to possess a temperature independent magnetic relaxation with a relaxation frequency at 200, 540, and 580 MHz in three samples. Plagioclase feldspar was found to possess a temperature dependent dielectric relaxation over a very broad frequency range in two samples.

Currently, two orbital radars, MARSIS and SHARAD, have been sent to investigate the subsurface of Mars. The designers of MARSIS and SHARAD predicted that their depths of penetration will be 5 km and 1 km, respectively. To demonstrate how these temperature dependent EM losses can impact MARSIS, SHARAD, and future GPR missions to Mars, the maximum GPR depth of penetration (DoP) was determined. Assuming a radar system dynamic range of 50 dB and a Martian average temperature of 213 K, the DoP for MARSIS is 1.6 km for grey hematite, 510 m for magnetite, and 70 m for plagioclase feldspar. Using the same assumptions, the DoP for SHARAD is 55 m for grey hematite, 20 m for magnetite, and 15 m for plagioclase feldspar. The GPR depths of penetration listed above represent the maximum limit because only dielectric and magnetic losses were considered. Other losses (such as geometric spreading, scattering, etc.) will only further reduce the depth of penetration. Results from this study illustrate why it is important to understand the EM properties of Martian soils in the Martian environment when designing a GPR to investigate the subsurface of Mars.

## TABLE OF CONTENTS

ABSTRACT.....	iii
LIST OF FIGURES .....	ix
LIST OF TABLES.....	xii
LIST OF SYMBOLS .....	xiii
ACKNOWLEDGEMENTS.....	xx
CHAPTER 1 INTRODUCTION.....	1
1.1 Introduction.....	1
1.2 Evidence of Water on Mars .....	2
1.3 The Martian EM Environment.....	6
1.4 Previous Measurements of EM Properties.....	10
1.5 Research Objectives.....	13
1.6 MARSIS and SHARAD .....	13
1.7 Overview.....	15
CHAPTER 2 ELECTROMAGNETIC PROPERTIES OF MARTIAN ANALOG MATERIALS.....	16
2.1 EM Theory.....	16
2.1.1 EM Propagation .....	16
2.1.2 EM Reflection and Transmission.....	24
2.1.3 Radar Equation.....	25
2.2 Dielectric Permittivity.....	26
2.2.1 Types of Charge Separation Mechanisms.....	26
2.2.2 Frequency Dependence of Dielectric Permittivity.....	28
2.3 Magnetic Permeability .....	29
2.3.1 Types of Magnetism .....	30
2.3.2 Martian Iron Oxides.....	33
2.3.3 Magnetic Domains.....	38

2.3.4	Grain Size.....	43
2.3.5	Magnetic Hysteresis.....	44
2.3.6	Frequency Dependence of Magnetic Permeability .....	48
2.4	Temperature and Frequency Dependence of Dielectric Permittivity and Magnetic Permeability .....	51
2.5	Mixing Formulas.....	54
CHAPTER 3 MARTIAN ANALOG SAMPLES.....		57
3.1	Observations of Martian Mineralogy.....	57
3.1.1	Martian Meteorites.....	57
3.1.2	Martian Orbiters.....	59
3.1.2.1	Infrared and Visible Spectroscopy .....	59
3.1.2.2	Magnetic Field .....	62
3.1.2.3	Gamma Ray Suite of Instruments .....	64
3.1.3	Martian Landers.....	66
3.1.3.1	Dust.....	67
3.1.3.2	Meridiani Planum.....	72
3.1.3.3	Gusev Crater .....	74
3.1.4	Summary of Martian Observations.....	74
3.2	Limitations of the Methods used to Map Mineralogy on Mars .....	76
3.2.1	Limitations of Infrared and Visible Spectroscopy .....	76
3.2.2	Limitations of the Magnetic Field Measurements .....	79
3.2.3	Limitations of the Gamma Ray Suite of Instruments .....	80
3.2.4	Limitations of the Mössbauer Spectroscopy.....	85
3.2.5	Limitations of Alpha Proton X-ray Spectrometer.....	87
3.2.6	Summary of the Limitations of the Methods used to Map Mineralogy on Mars.....	88
3.3	Sample Selection.....	88
3.4	Sample Preparation .....	89
CHAPTER 4 LABORATORY SETUP AND PROCEDURES .....		90
4.1	Measurement Apparatus, Environment, and Procedure .....	90
4.2	VNA Calibration.....	93
4.3	Theory for Measuring EM Properties in a Coaxial Waveguide .....	94
4.4	Accuracy and Error Analysis.....	100
4.4.1	VNA Measurement Accuracy.....	101
4.4.2	Incoherent and Coherent Sources of Noise.....	110
4.4.3	Improper Apparatus Setup .....	112
4.5	Measurement, Accuracy and Quality Control of Temperature.....	113

CHAPTER 5 EXPERIMENTAL AND MODEL RESULTS .....	122
5.1 Introduction.....	122
5.2 Data Modeling .....	122
5.3 Samples with No Measurable Losses .....	128
5.4 Samples with Dielectric Relaxation Losses.....	130
5.5 Samples with Magnetic Relaxation Losses.....	143
CHAPTER 6 DISCUSSION AND CONCLUSIONS .....	148
6.1 Discussion.....	148
6.2 Grey Hematite.....	148
6.2.1 Temperature Dependent Dielectric Relaxation Mechanism of Grey Hematite .....	149
6.2.2 Implications of the Temperature Dependent Dielectric Relaxation of Grey Hematite for MARSIS, SHARAD, and Future GPR Missions .....	151
6.2.2.1 Thermal Modeling of the Martian Subsurface.....	153
6.2.2.2 Dielectric Permittivity Modeling .....	156
6.2.2.3 Temperature Modeling Results.....	163
6.3 Magnetite .....	164
6.3.1 Temperature Independent Magnetic Relaxation Mechanism of Magnetite.....	166
6.3.2 Implications of the Temperature Independent Magnetic Relaxation of Magnetite for MARSIS, SHARAD, and Future GPR Missions.....	166
6.4 Implications of the EM Losses of Other Measured Samples for MARSIS, SHARAD, and Future GPR Missions .....	168
6.5 Conclusion .....	170
CHAPTER 7 FUTURE WORK.....	172
7.1 Introduction.....	172
7.2 Temperature Range Improvements.....	172
7.3 Additional Martian Analog EM Measurements.....	173
7.4 EM Property Measurement Improvements.....	177
7.5 EM Property Measurements Versus Water/Ice Content.....	176

REFERENCES CITED.....	177
APPENDIX.....	198

## LIST OF FIGURES

1.1. The phase diagram of water.....	5
1.2. Daily surface temperature variations on Mars.....	9
2.1. Cubic inverse spinal structure of magnetite.....	34
2.2. Rhombohedra corundum crystal structure of hematite.....	36
2.3. Magnetic domains.....	39
2.4. How super-exchange, demagnetization, and magnetocrystalline anisotropy energy affect magnetic domains.....	40
2.5. Magnetic domain wall.....	42
2.6. Temperature dependence of magnetic domains.....	43
2.7. Magnetic hysteresis.....	45
2.8. Hysteresis curve of multidomain, singledomain, and superparamagnetic biotite crystals containing magnetite.....	47
2.9. Frequency and temperature dependence of dielectric permittivity.....	53
3.1. Martian magnetic field.....	63
3.2. Near surface distribution of water on Mars.....	66
3.3. MER-A sweep magnet.....	68
3.4. Mars Pathfinder magnets.....	69
3.5. Hematite concretions on Mars.....	73
3.6. Dust covered rocks.....	77

4.1. Apparatus used to measure the EM properties of Martian analogs versus temperature and frequency.....	92
4.2. Electric and magnetic fields in a coaxial waveguide .....	95
4.3. Signal flow chart of the VNA .....	98
4.4. Difference in data and noise envelopes between the maximum manufacturer listed precision and the actual precision .....	104
4.5. Lower limit of conductivity for the VNA measuring system .....	105
4.6. Data and noise envelopes as a function of the real part of the relative dielectric permittivity and the real part of the relative magnetic permeability.....	107
4.7. Data and noise envelopes for a frequency dependent dielectric permittivity and magnetic permeability.....	108
4.8. Data and noise envelopes as a function of sample holder length .....	109
4.9. Standard deviation at each frequency versus number of external stacks.....	111
4.10. Circuit used to find thermistor resistance .....	113
4.11. Resistance vs temperature for thermistors .....	114
4.12. EM properties of air vs frequency and temperature.....	119
4.13. Time constant of relaxation vs temperature.....	121
5.1. Inversion sensitivity analysis .....	125
5.2. The three temperature ranges of the 95.5% confidence interval of the time constant at infinite temperature and the activation energy .....	127
5.3. EM properties of a typical lossless and temperature independent sample.....	129
5.4. Temperature and frequency dependent dielectric relaxation of GHKwMI .....	133
5.5. Arrhenius plot of GHKwMI.....	134

5.6. Temperature and frequency dependent dielectric relaxation of GHSChp .....	136
5.7. Arrhenius plot of GHChp.....	137
5.8. Temperature and frequency dependent dielectric relaxation of JSC1 .....	139
5.9. Temperature and frequency dependent dielectric relaxation of PuNeHIC .....	141
5.10. Arrhenius plot of PuNeHIC .....	142
5.11. Frequency dependent magnetic relaxation of MagRCh.....	145
5.12. Frequency dependent magnetic relaxation of Magn.....	146
5.13. Frequency dependent magnetic relaxation of Yuma .....	147
6.1. Maximum depth of penetration of grey hematite samples.....	152
6.2. Temperature versus depth profile for a diurnal variation at the Viking 1 landing site .....	155
6.3. Temperature versus depth profile for seasonal and diurnal variations for three latitudes on Mars .....	156
6.4. Annual loss difference .....	158
6.5. Diurnal loss difference.....	159
6.6. Dielectric permittivity versus depth for annual variations.....	160
6.7. Dielectric permittivity versus depth for diurnal variations.....	161
6.8. Difference in two-way traveltime in grey hematite .....	162
6.9. Difference in two-way traveltime in grey hematite mixed with Pu'u Nene Horizon C at the Martian equator .....	163
6.10. Maximum depth of penetration for magnetite .....	167
6.11. Maximum depth of penetration for plagioclase feldspar samples .....	169

## LIST OF TABLES

2.1. Various mechanisms for charge separation .....	27
2.2. Various mechanisms for magnetic relaxations .....	50
3.1. The mean particle radius of atmospheric dust at Mars .....	71
4.1. Typical error in temperature .....	117
5.1. EM properties of samples with no measurable losses .....	128
5.2. Cole-Cole and Boltzmann temperature parameters for samples with temperature dependent dielectric relaxations .....	131
5.3. Uncertainties in time constant of relaxation at infinite temperature.....	132
5.4. Cole-Cole parameters for samples with temperature independent magnetic relaxations .....	144
6.1. Diurnal parameter values .....	154
6.2. Diurnal and annual temperature parameter values.....	155

## LIST OF SYMBOLS

Symbol	Terminology	SI unit [Sheriff, 1999]
a	Attenuation of EM energy	dB
A	Ampere	A
a <sub>1</sub>	Output of energy from port 1	dB
a <sub>2</sub>	Output of energy from port 2	dB
<b>B</b>	Magnetic induction	$T = \text{Wb/m}^2 = \text{kg/s}^2\text{A}$
b <sub>1</sub>	Input of energy from port 1	dB
b <sub>2</sub>	Input of energy from port 2	dB
c	Velocity of an EM wave in vacuum ( $2.99 \times 10^8$ )	m/s
c	Shape factor in the BHS equation	unitless
C	Coulomb	As
°C	Centigrade	-273.15 K
<b>D</b>	Displacement currents	$\text{C/m}^2$
d	Bulk Density	$\text{g/cm}^3$
d	data	unitless
dn	Normalized Bulk Density (1.60)	$\text{g/cm}^3$
dB	Decibels	dB
<b>E</b>	Electric field	$\text{V/m} = \text{mkg/s}^3\text{A}$
eV	Electronvolt	$\text{eV} = 1.602 * 10^{-19} \text{ J}$
f	Frequency	$\text{Hz} = 1/\text{s}$
f	Cole-Cole equation	unitless
f <sub>r</sub>	Relaxation frequency	$\text{Hz} = 1/\text{s}$
f <sub>r</sub>	Resonant frequency	$\text{Hz} = 1/\text{s}$
F	Farad	$\text{C/m} = \text{s}^4\text{A}^2/\text{m}^2\text{kg}$

Fe <sup>2+</sup>	Ferrous iron	unitless
Fe <sup>3+</sup>	Ferric iron	unitless
<b>H</b>	Magnetic field	A/m
H	Henry	Wb/A = m <sup>2</sup> kg/s <sup>2</sup> A <sup>2</sup>
H <sub>c</sub>	Coercivity	A/m
Hz	Frequency	Hz = cycles/s
i	$\sqrt{-1}$	unitless
<b>J</b>	Conduction current density	A/m <sup>2</sup>
J	Joule	J=Ws=VA s=kgm <sup>2</sup> /s <sup>2</sup>
J <sub>s</sub>	magnetic saturation normalized by density	Am <sup>2</sup> /kg
M <sub>s</sub>	Saturation magnetization	A/m
k	Boltzmann constant (8.6176 × 10 <sup>-5</sup> )	eV/K
k	Wavenumber	1/m
K	Kelvin	K
K	mode of $\varepsilon_{\infty}^{1/d}$ (1.92)	unitless
L	Sample holder length	m
m	Meter	m
mho	Inverse of electrical resistance	1/Ω
M <sub>r</sub>	Remanent magnetization	A/m
M <sub>s</sub>	Magnetic saturation	A/m
N	Number of data points	unitless
Np	Nepers	Np = 8.686 dB
O <sup>2-</sup>	Oxygen anion	unitless
r <sub>o</sub>	Radius of the outer conductor of the sample holder (0.00700)	m
r <sub>i</sub>	Radius of the inner conductor of the sample holder (0.00305)	m

s	Second	s
S11	Scattering (S) parameter from port 1 to port 1	dB
S12	Scattering (S) parameter from port 1 to port 2	dB
S21	Scattering (S) parameter from port 2 to port 1	dB
S22	Scattering (S) parameter from port 2 to port 2	dB
t	Time	s
T	Tesla	$T = \text{Wb}/\text{m}^2 = \text{kg}/\text{s}^2\text{A}$
$T_C$	Curie temperature	K
$\text{Ti}^{4+}$	Titanium cation	unitless
V	Volt	$V = \text{m}^2\text{kg}/\text{s}^3\text{A}$
V	Velocity	m/s
$V_A$	Output reflected voltage wave	$V = \text{m}^2\text{kg}/\text{s}^3\text{A}$
$V_B$	Output transmitted voltage wave	$V = \text{m}^2\text{kg}/\text{s}^3\text{A}$
$V_{in}$	Input voltage wave	$V = \text{m}^2\text{kg}/\text{s}^3\text{A}$
W	Watt	$W = \text{J}/\text{s} = \text{kgm}^2/\text{s}^2$
Wb	Weber	$\text{Wb} = \text{Vs} = \text{m}^2\text{kg}/\text{s}^2\text{A}$
x	mole% of the titanium in magnetite and maghemite	percent
x	modeled data points	unitless
X	Relative dielectric permittivity or relative magnetic permeability	unitless
$X_\infty$	Infinite or high frequency limit of X	unitless
$X_{DC}$	Static, DC, or low frequency limit of X	unitless
y	mole% of the titanium in hematite	percent
z	Transmission coefficient	dB
Z	Complex impedance	$\Omega$
$Z_0$	Impedance of the cable (50)	$\Omega$
$\square$	Vacancy in the lattice structure	unitless

$\alpha$	Attenuation coefficient	Np/m
$\alpha$	Cole-Cole distribution parameter	unitless
$\beta$	Phase coefficient	radians/m
$\nabla$	Del operator	unitless
$\delta_D$	Dielectric loss tangent	radians
$\delta_C$	Conduction loss tangent	radians
$\delta_E$	Electrical loss tangent	radians
$\delta_M$	Magnetic loss tangent	radians
$\delta_{EM}$	Electromagnetic loss tangent	radians
$\epsilon_0$	Dielectric permittivity of free space ( $8.854 \times 10^{-12}$ )	F/m = $s^4 A^2 / m^3 kg$
$\epsilon_r^*$	Complex relative dielectric permittivity	unitless
$\epsilon_r'$	Real part of the relative dielectric permittivity	unitless
$\epsilon_r''$	Imaginary part of the relative dielectric permittivity	unitless
$\epsilon_{DC}$	Static, DC, or low frequency limit of the real part of the relative dielectric permittivity	unitless
$\epsilon_\infty$	Infinite or high frequency limit of the real part of the relative dielectric permittivity	unitless
$\epsilon_1^*$	Complex relative dielectric permittivity for material 1	unitless
$\epsilon_2^*$	Complex relative dielectric permittivity for material 2	unitless
$\epsilon_m^*$	Complex relative dielectric permittivity predicted for mixture	unitless
$\epsilon_r^{*n}$	Complex relative dielectric permittivity normalized to density	unitless

$\phi^2$	Weighted normalized data misfit	unitless
$\chi$	Magnetic susceptibility	unitless
$\Gamma$	Reflection coefficient	dB
$\lambda$	Wavelength	m
$\mu_o$	Magnetic permeability of free space ( $1.256 \times 10^{-6}$ )	H/m = mkg/s <sup>2</sup> A <sup>2</sup>
$\mu_r^*$	Relative magnetic permeability	unitless
$\mu_r'$	Real part of the relative magnetic permeability	unitless
$\mu_r''$	Imaginary part of the relative magnetic permeability	unitless
$\mu_{DC}$	Static, DC, or low frequency limit of the real part of the relative magnetic permeability	unitless
$\mu_\infty$	Infinite or high frequency limit of the real part of the relative magnetic permeability	unitless
$\pi$	Pi (3.14159)	unitless
$\rho$	Electric charge density	C/m <sup>3</sup>
$\rho$	Resistivity	$\Omega$ m
$\sigma$	Electrical conductivity	1/ $\Omega$ m
$\sigma$	Standard deviation	unitless
$\sigma_{DC}$	Static or DC electrical conductivity	1/ $\Omega$ m
$\tau$	Time constant of relaxation	s
$\tau_\infty$	Time constant of relaxation at infinite temperature	s
$\Omega$	Ohm	$\Omega = V/A = m^2kg/s^3A^2$
$\Omega$	Volume fraction of material 2 in the mixture	%
$\omega$	Angular (radian) frequency	Hz = radians/s
$\xi$	Radar cross section	m <sup>2</sup>

## Prefixes

---

T	Tera	$10^{12}$
G	Giga	$10^9$
M	Mega	$10^6$
k	Kilo	$10^3$
c	Centi	$10^{-2}$
m	Milli	$10^{-3}$
$\mu$	Micro	$10^{-6}$
n	Nano	$10^{-9}$
p	Pico	$10^{-12}$

## Abbreviations

---

EM	Electromagnetic
GPR	Ground Penetrating
MER	Mars Exploration Rovers
MER-A	Mars Exploration Rover – Spirit
MER-B	Mars Exploration Rover – Opportunity
MEX	Mars Express
MGS	Mars Global Surveyor
MO	2001 Mars Odyssey
S	Scattering
SNC	Shergottites, Nakhrites, and Chassigny
TE	transverse electric mode

TEM	transverse electromagnetic mode
TES	Thermal Emission Spectrometer
TM	transverse magnetic mode
THEMIS	Thermal Emission Imaging System
VNA	Vector Network Analyzer

## ACKNOWLEDGEMENTS

This work was sponsored by NASA grant 20119458 NAG5-12754. I would like to thank my advisor Gary Olhoeft for obtaining the funding so that I could explore my passions for geophysics and Mars. I have been in the geophysics department at Mines for the last decade and all of the professors have been great. Specifically, I'd like to thank Mike Batzle, Adel Zhody, Yaoguo Li and Terry Young. I also received a lot of help from outside CSM. Bob Horton and Rich Reynolds of the USGS helped out whenever I had a problem. I also appreciate the help of Steve Sutley of the USGS Denver Federal Center who conducted some of our XRD measurements.

I would also like to thank the graduate, undergrad, and highschool students who assisted with the experiment, programming, and rock crushing including Justin Modroo, Sjoerd de Ridder, Brienne Douthit, Beau Winters, Andy Kass, Ross Wagle, Matt Hergert, Paul Schwering, Jeremy Norman, and Francis Li. A special shout goes out to James Linse who helped rescue files off of my hard drive, install the new hard drive a week before my defense, and who produced the images of me doing GPR on Mars. I would also like to thank the graduate students who helped me in my work including Beth Burton, Erin Wallin, Kate McKinley, Sarah Shearer, Dave Sinex, Barry Kirkendall, Rich Krahenbuhl, Marty Terrell, and Whitney Goodrich.

I could not have accomplished this work without the unwavering support from my wife, parents, and sister. My wife also served as my unofficial advisor and helped transform my writing into something that others could comprehend. Lastly, I would like to thank my parents for encouraging me to follow my passions.

## CHAPTER 1

### INTRODUCTION

#### 1.1 Introduction

Over the past decade, much has been learned about the Martian surface; however, the Martian subsurface still remains a mystery. Many surfaces on Mars are buried by aeolian deposits or coated with dust and thus hidden from traditional imaging methods [Bandfield et al., 2000; Johnson et al., 2002a]. Ground penetrating radar (GPR) has the potential to image beneath these layers. Imaging the Martian subsurface is valuable because it can be used to locate and give geological context to drilling targets, locate potential subsurface rover hazards, investigate stratigraphy, and most importantly, image subsurface water.

“Follow the water” is the guiding principle of NASA’s Mars Exploration Program. It is a top priority because if any extraterrestrial life ever existed or currently exists, it would most likely be found near a source of water. On August 7, 1996, following the announcement that Martian fossils may have been found in a Martian meteorite [McKay et al., 1996], President Clinton spoke about the importance of finding life on Mars, “...it will surely be one of the most stunning insights into our universe that science has ever uncovered. Its implications are as far reaching and awe inspiring as can be imagined.” In 2004, the possibility of active Martian life was suggested as a possible explanation for spatially varying small concentrations (10 parts per billion by volume) of methane gas identified in the Martian atmosphere [Formisano et al., 2005].

The genesis of life on Earth is poorly understood. Nearly all of the evidence for life’s beginning has been destroyed by plate tectonics or erosion. However, it appears that rocks on Mars are billions of years old. If life did take hold on Mars, these rocks

may contain clues regarding the origins of life. Conversely, if life never existed on Mars these rocks may constrain the environmental factors that lead to the beginning of life. Discovering that life once existed or does exist on Mars would prove that the genesis of life occurred at least twice in our solar system. With so many other solar systems in the galaxy, the possibilities for life elsewhere become much greater.

Aside from the potential for extraterrestrial life, the discovery of water also will have significant implications for a manned mission to Mars. Martian water could be used for drinking and breathing, and to extract oxygen and hydrogen for rocket fuel. If an acceptable source of water could be found on Mars, the overall weight of the payload that needs to be transported from Earth would be reduced. This would allow for either additional payload or a smaller and less expensive launch vehicle.

## 1.2 Evidence of Water on Mars

There is substantial evidence that water has been active on the surface of Mars. This evidence includes the following:

- Images from the Mariner 9 and the Viking orbiters revealed giant flood channels [Irwin et al., 2004], extensive valley networks with branching tributaries [Carr, 1996], and dried up lake beds [Williams and Zimbelman, 1994].
- The Viking orbiters found that the northern perennial polar cap was composed of water ice [Kieffer et al., 1976].
- The Viking orbiters also discovered the initial evidence for fluidized ejecta around craters ranging from 5 – 50 km in diameter [Carr et al., 1977]. This is significant since Mars is the only planetary body that has such craters [Barlow et al., 2000]. Fluidized ejecta most likely forms when an impactor strikes a subsurface that is rich in volatiles like water ice [Barlow et al., 2000]. The

mobility of the fluidized ejecta is influenced by crater latitude and altitude and is found to be greatest at high latitudes and low elevations where water ice is most stable [Mougins-Mark, 1979].

- The nakhlites group of Martian meteorites shows evidence of aqueous alterations [Meyer, 2005].
- Mars Global Surveyor found evidence of gullies that are thought to have been formed by water [Malin and Edgett, 2000; Christensen, 2003].
- Mars Global Surveyor and Mars Odyssey found sedimentary evidence that may indicate that water did flow on Mars billions of years ago. Images suggest a distributary, channelized flow that lasted long enough to produce meandering and a delta [Malin and Edgett, 2003, Moore et al., 2003, Bhattacharya, et al., 2005]
- Mars Odyssey found evidence of hydrogen that is believed to be in the form of frozen water at latitudes poleward  $\pm 60^\circ$  and at two mid-latitude locations [Feldman et al., 2004].
- Mars Odyssey observations have also led to the discovery that a layer of water ice exists under the southern perennial CO<sub>2</sub> ice cap [Titus et al., 2003].
- Mars Global Surveyor found the spectral signature of grey hematite, which can form in the presence of water [Christensen et al., 2001]. Opportunity (MER-B) discovered that the spectral signature of grey hematite was caused by grey hematite concretions that were likely precipitated by groundwater [Squyres and Knoll, 2005]. The sedimentary layers that contained the grey hematite concretions contained evidence suggesting that they were formed in an acidic salty playa environment [Squyres and Knoll, 2005].
- Spirit (MER-A) found signs that rocks and soils near Husband Hill have been altered by salty water [Ming et al., 2005].

- Mars Express has mapped hydrated phyllosilicates (clays) mineralogy and hydrated sulfates (salts) on Mars – both require water to form [Bibring et al., 2005].

Presently, liquid water can only exist on about 30% of the Martian surface due to the low pressure (average pressure is 6.1 mbar) [Haberle et al., 2004]. Figure 1.1 shows the phase diagram of water. At the highest Martian pressure of 12.5 mbar [Haberle et al., 2004], liquid water can only exist at temperatures between 273 – 300 K. (Martian temperatures range from 154 K – 300 K.) However, salts dissolved in water can significantly reduce the freezing point of water at all pressures, thus reducing the triple point (the point at the highest pressure where water can exist in three phases) to lower temperatures and pressures. Spirit (MER-A) has found significant evidence of salts [Arvidson et al., 2006]. All of the other landers and Mars Express have also found evidence of salts [Bell III et al., 2000; Squyres and Knoll, 2005; Bibring et al., 2005].

Carr [1986] estimated that 100 – 500 m of a global equivalent layer (GEL) of water was necessary to form the aqueous features found on Mars. It has been suggested that 5 – 50 m of this GEL of water has been broken down by sunlight into hydrogen and oxygen gas, which then escaped into space [Yung et al., 1988; Carr, 1990; Jakosky, 1991; Luhman et al., 1992; Leshin, 2000]. Currently, the largest reservoir of water identified on Mars is the polar residual water ice caps, which would create a GEL of water approximately 30 m deep [Carr, 1986; Smith et al., 1999]. A much smaller water reservoir with a GEL of about  $10^{-5}$  m is found in the current atmosphere of Mars [Jakosky and Farmer, 1982]. These two estimates suggest that a large portion of the Martian water is locked in the subsurface.

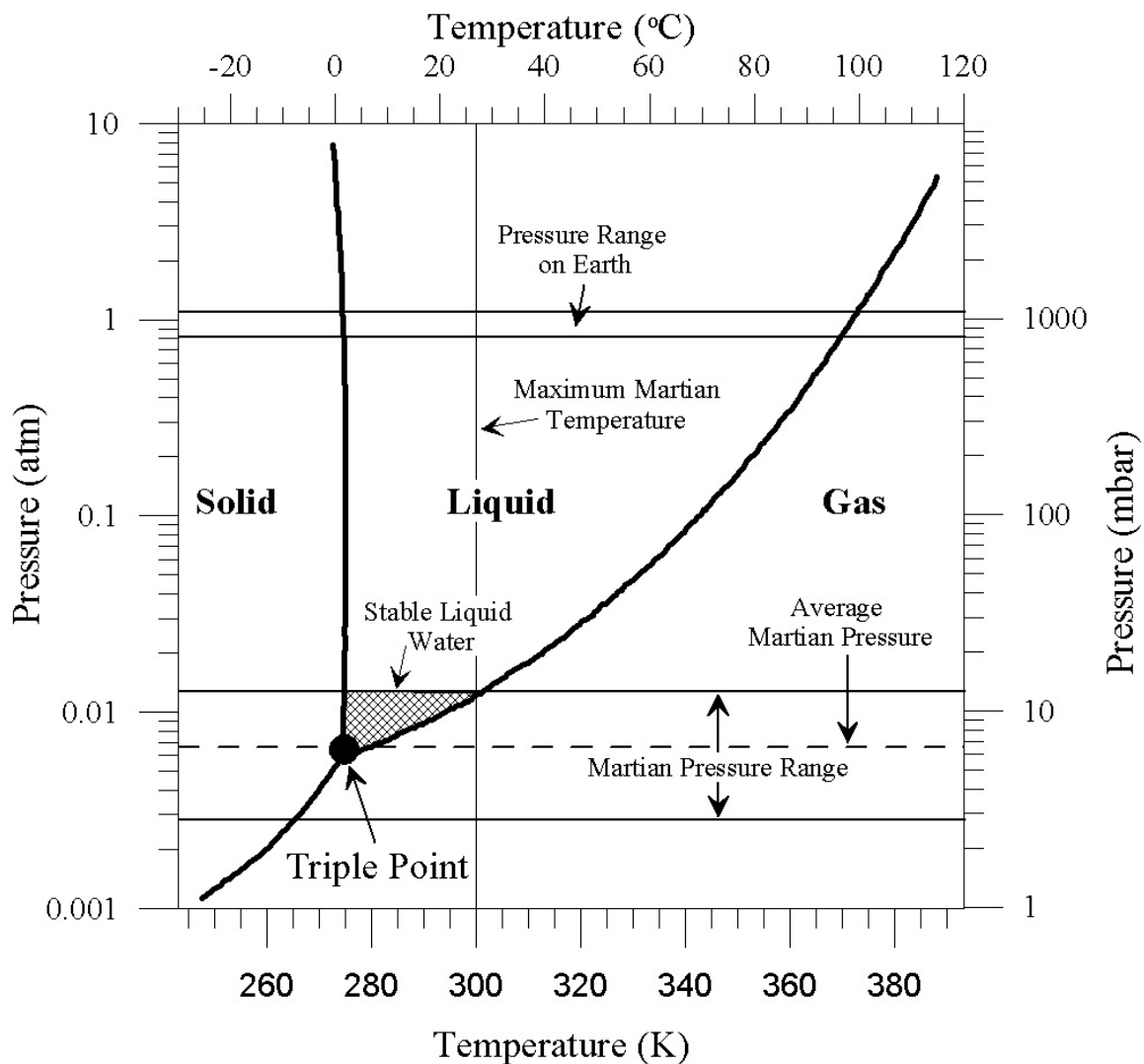


Figure 1.1. This figure shows the phase diagram of water. The Martian pressure range is nearly centered on the triple point. The hatched area shows the range of pressures and temperatures where liquid water is stable on Mars. However, if salts are present in the water, the triple point is significantly lowered in both pressure and temperature. Figure modified from Haberle et al. [2001].

This ground ice was predicted to be within one meter of the Martian surface at latitudes poleward of  $\pm 50^\circ$  and becoming deeper at equatorial latitudes [Mellon and Jakosky, 1993]. Recently, the gamma ray suite of instruments has found evidence of a new water reservoir, ground ice at latitudes poleward of  $\pm 50^\circ$ . While this reservoir can only be measured to about one meter deep, it has a GEL of approximately 14 cm [Feldman et al, 2004]. It is unknown if this ice rich layer extends deep into the subsurface or if it is confined to the top 10s – 100s of meters [Mellon et al., 1997]. If the ground ice does extend deep into the subsurface, it will melt into liquid water as the geothermal gradient increases the temperature with depth [Clifford and Parker, 2001]. The geothermal gradient of Mars has never been measured, but theoretical modeling suggests values ranging from  $0.02 - 0.045 \text{ W/m}^2$  [Fanale, 1976; Toksöz et al., 1978; Stevenson et al., 1983; Schubert and Spohn, 1990; Spohn 1991]. Results from thermal modeling predict that ground water may be present within 1-5 km of the surface at equatorial latitudes, increasing in depth toward the poles [Clifford and Parker, 2001]. The presence of gullies suggests that some liquid water may be very near the Martian surface [Malin and Edgett, 2000] but, due to the cold temperatures on Mars, it is unlikely that large amounts of liquid water are stable in the near ( $<1$  km) subsurface [Clifford and Parker, 2001].

Hydrogen has also been mapped at mid-latitudes and low elevations by the gamma ray suite of instruments. Mellon et al. [1997] and Jakosky et al. [2005] have shown that water ice could be present, but currently unstable, within a meter of the surface. This hydrogen could also be locked up in hydrated minerals such as jarosite, which can contain as much as 10% water in its crystal structure [Rodionov et al., 2005].

### 1.3 The Martian Radar Environment

Before discussing the propagation of radar energy through the Martian subsurface, two GPR targets will be discussed – water ice and liquid water. Water ice is

a difficult GPR target, even if it is within a meter of the Martian surface. At radar frequencies, water ice possesses a dielectric permittivity near or equal to most dry rocks or soils and therefore does not produce a significant contrast that can be identified in GPR data. Even though the ice would increase the dielectric permittivity of the subsurface by filling the pore space, a similar result could also occur due to compaction of the soil.

Unlike water ice, liquid water is an ideal GPR target due to its large relative dielectric permittivity. However, even though there is a large contrast between water's relative dielectric permittivity (about 80) and a dry porous media (about 4), this contrast is decreased since water can only fill the porosity of the media. As depth increases, the porosity will naturally decrease due to increased compaction. Capillary fringes (boundary due to the capillary forces of the pores between the unsaturated and saturated zone that is partially saturated) will produce a gradual change in the contrast of dielectric material properties. Mars may have permafrost or an ice saturated zone above the water table instead of an unsaturated zone. Between the permafrost and water table, a mixture of liquid water and water ice may exist. This would also produce a gradual change in the contrast of dielectric material properties. If the change in contrast is gradual enough, a reflection may not be seen from a high frequency radar signal. As previously stated, liquid water aquifers are predicted to be at least one kilometer deep [Clifford, 2001].

While liquid water is a good GPR reflector, it will significantly attenuate any GPR energy propagating through it. Water causes both dielectric relaxation losses at high frequencies and conduction losses at all frequencies [Olhoeft, 1998]. The interaction of liquid water and mineralogical clay can cause large conductivity and electrochemical losses at all frequencies [Olhoeft, 1998] and high dielectric losses at low frequencies [Lockhart, 1980a, 1980b, Canan, 1999]. (However, finely crushed rock or engineering rock flour, which has a clay designated grain size, does not possess high losses like mineralogical clays.) GPR surveys on Earth can only achieve a depth of penetration greater than a kilometer if there are low concentrations of water. Mars

appears to be a much better radar environment than Earth because the average subsurface temperatures are below the freezing point of water. Without the EM losses caused by liquid water, other loss mechanisms such as magnetic and dielectric relaxations and scattering losses must be considered as the limiting factor for GPR depth of penetration on Mars.

In this thesis, the dielectric and magnetic relaxations of Martian minerals will be examined. Dielectric relaxation losses of Earth soils are typically overwhelmed by losses associated with water and clays. However, the presence of magnetic minerals on Earth has proven to create significant radar losses [Olhoeft and Capron, 1994]. Magnetic relaxations rarely occur on Earth due to the lack of ferromagnetic and ferrimagnetic minerals in Earth soils. Unlike Earth, Mars is known to contain an abundance of ferrimagnetic minerals at its surface [Hargraves et al., 2000]. In fact, every particle of the Martian global windblown dust layer is magnetic at DC (zero) frequency and is believed to be composed of about 2% magnetite [Bertelsen et al., 2004]. Consequently, magnetic and dielectric relaxation losses on Mars may be the dominant loss mechanisms and therefore must be considered when predicting depth of penetration.

Dielectric and magnetic relaxations can also change as a function of temperature [Olhoeft, 1976; Dunlop and Özdemir, 1997]. As shown in Figure 1.2, Mars has a wide range of daily global temperature fluctuations (154 K – 300 K) with an average annual surface temperature ranging from 154 K – 218 K as a function of latitude [Clifford, 2001]. Due to the wide temperature range on Mars, these temperature dependent properties will change as a function of the time of day and have different values than those measured in the typical Earth environment. Consequently, measurements of electromagnetic (EM) properties (dielectric permittivity, magnetic permeability, and DC conductivity) made at terrestrial room temperature ( $\approx 298$  K) will not be representative for Mars.

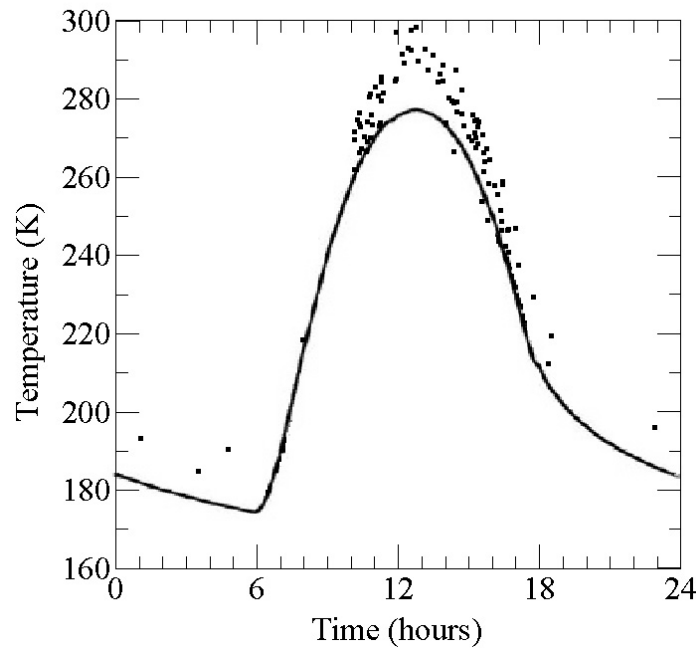


Figure 1.2. Daily surface temperature variations on Mars. The dots are Martian surface temperature as determined by Opportunity over the first 65 Martian days (sols) on Mars [Spanovich et al., 2006]. The solid line is the predicted Martian surface temperature at Opportunity's landing site [Martin et al., 2003].

Pressure can also affect dielectric permittivity and magnetic permeability by altering the crystal structure of the mineral [Böttcher, 1952]. However, pressure changes that affect dielectric permittivity and magnetic permeability in dry samples are usually generated by much higher pressures than those occurring at subsurface depths of a few kilometers. Therefore, all measurements for this study were made at atmospheric Earth pressures  $\approx 1$  bar.

If the subsurface of Mars is favorable to GPR penetration, the ability to image the vertical extent of the groundwater becomes important to estimate its total water volume. The ability of GPR energy to penetrate through a water saturated media strongly depends on the concentrations of salts. The presence of dissolved salts increases the conduction losses at all frequencies. There will also be a dielectric relaxation loss of water at high

frequencies. As discussed in Chapter 3, significant amounts of sulfur, bromide, phosphorus and chloride salts have been found on Mars [Bibring et al., 2005; Squyres and Knoll, 2005; Arvidson et al., 2006]. This leads to the conclusion that the groundwater will most likely possess a high conductivity, which will severely limit any GPR penetration through the aquifer at any radar frequency. Consequently, only reflections from the top of the groundwater may be detected and thus, other methods such as EM induction will be necessary to determine the aquifer's thickness [Grimm, 2002]. In order to uniquely identify subsurface liquid water on Mars a combination of GPR, EM induction, and seismic methods may be necessary [Olhoeft, 2003].

#### 1.4 Previous Measurements of Martian EM Properties

The magnetic properties of Mars at DC frequencies have been studied by making in situ measurements. These measurements have been made by attaching magnets on every Martian lander and by measuring the remanent magnetic field from Martian orbiters. The in situ measurements have found that Martian rocks, soils, and dust contain significantly more magnetic minerals than Earth, and the Martian global dust layer has an average saturation magnetization of 1-4 Am<sup>2</sup>/kg and a density magnetic susceptibility of 9-33×10<sup>-6</sup> m<sup>3</sup>/kg [Morris et al., 2001]. This magnetization is caused by either magnetite or titanomagnetite [Morris et al., 2004; Bertelsen et al., 2004; Goetz et al., 2005; Yen et al., 2005]. Mars also possesses a remanent magnetic field that is 10 times greater than Earth's remanent magnetic field and is most likely caused by thermoremanent magnetization of magnetite or titanomagnetite [Dunlop and Arkani-Hamed, 2005].

Laboratory measurements of the EM properties of Martian analogs at radar frequencies have been made in the past [Olhoeft and Strangway, 1974; Olhoeft and Capron, 1993, 1994; Leuschen, 1999; Heggy et al., 2001, 2003; Heggy and Pommerol, 2005; Williams and Greeley, 2004; Pettinelli et al., 2005]. A brief discussion of these measurements follows.

Olhoeft and Strangway [1974] predicted that the electrical properties of the Martian subsurface would be similar to the Moon, even though the Martian atmosphere contains a small amount of water. This is because small amounts of water absorbed in the soil do not affect dielectric permittivity at high frequencies [McIntosh, 1966]. The water would also typically be in the form of ice, thus reducing its effects further. Other than the water/ice transition, Olhoeft and Strangway [1974] state that temperature had no effect on the electrical properties of the Moon soils and therefore should not have an influence on Mars. However, Olhoeft [1976] later demonstrated that temperature does have an effect on electrical properties of dry soils. Olhoeft and Strangway [1974] make no mention of magnetic properties of the Martian subsurface. However, Olhoeft and Capron [1993, 1994] found that a soil near Yuma, AZ, possessed a magnetic relaxation that was the dominant loss mechanism in the soil. This demonstrates that magnetic losses could be the dominant loss mechanism in the Martian subsurface.

Leuschen [1999] conducted measurements with a vector network analyzer (VNA) and used a slotted line for the sample holder. These measurements were made from 10 MHz to 1 GHz and found that JSC Mars-1 possessed a frequency dependent dielectric permittivity and a frequency dependent magnetic permeability. Slotted line measurements can be more accurate than the waveguide measurements made in this thesis, however they can only be made over a small frequency range. Leuschen's calculation of magnetic permeability is briefly described, but it is most likely incorrect. Numerous measurements of Mars JSC-1 were conducted in this study and a magnetic permeability above one was never recorded for Mars JSC-1. (This is further discussed in Section 5.4.)

Heggy et al. [2001, 2003] and Heggy and Pommerol [2005] have conducted measurements of dielectric permittivity versus frequency for Martian analogs with impedance analyzers. Impedance analyzers cannot measure phase as accurately as the VNA that was used in this thesis, thus VNAs can measure lower losses than impedance

analyzers. Heggy et al. [2001, 2003] and Heggy and Pommerol [2005] did not report any magnetic permeability measurements.

Williams and Greeley [2004] measured the complex dielectric permittivity of JSC Mars-1 and Carbondale red clay from 200 – 1300 MHz at room temperature. Exactly how they measured this is not discussed. They also made microwave transmission measurements on the same samples over a frequency range from 500 – 12,000 MHz. They then assumed no magnetic losses and a magnetic permeability of one to calculate an attenuation rate. Their attenuation rate is slightly larger than the attenuation rates for JSC Mars-1 found in this thesis. (This is further discussed in Section 5.4.)

Pettinelli et al. [2005] conducted measurements of two magnetite samples with an LCR meter from 500 Hz – 1 MHz and time domain reflectometry (TDR) from 1 – 500 MHz. The LCR meter was able to measure both complex dielectric permittivity and complex magnetic permeability because two different sample holders were used to measure each separately. However, these measurements are below the radar frequency range, thus they were used to constrain the low frequency limit of both the dielectric permittivity and magnetic permeability. The TDR measurements are sensitive to the EM velocity of a material. Therefore, TDR measurements cannot uniquely measure complex dielectric permittivity and complex magnetic permeability. However, the TDR measurements showed that the EM velocity did not change from 1 – 500 MHz. Therefore, Pettinelli et al. [2005] concluded that these two magnetite samples did not possess any significant magnetic or dielectric relaxation below 500 MHz. In this thesis, two out of three magnetite samples were found to possess magnetic relaxations at frequencies greater than 500 MHz.

All of these previous measurements were conducted at room temperature ( $\approx 298$  K). The surface temperature on Mars rarely reaches 298 K. Temperature must be accounted for when measuring the EM properties of Martian analogs since EM properties can vary as a function of temperature. Magnetic properties become temperature dependent near and at the Curie, Néel, and Morin temperatures. Research done by Iben

et al. [1996] and Morris et al. [1997] have shown that the electrical properties of some Martian analogs also change as a function of temperature. Iben et al. [1996] observed that both magnetite and red hematite possess a temperature dependent dielectric relaxation centered at 200 and 10 Hz, respectively, at 293 K. Morris et al. [1997] observed that the reflectivity spectrum between 4.62 and 5.45 THz (650 and 550 nm) is temperature dependent in a red hematite powder. These previous studies suggest that powdered red hematite is temperature dependent at very high frequencies in the EM spectrum, while magnetite and red hematite are temperature dependent at very low frequencies in the EM spectrum. Consequently, the EM properties of these minerals could be temperature dependent at radar frequencies.

### 1.5 Research Objective

The primary objective of this research was to evaluate the effect temperature dependent dielectric and magnetic relaxation losses of Martian analogs have on the GPR depth of penetration on Mars. This was done by measuring the complex dielectric permittivity and complex magnetic permeability of Martian analogs as a function of frequency (30 kHz – 3 GHz) and temperature (180 – 300 K). From these measurements, the frequency and temperature dependent attenuation due to EM loss was calculated. By assuming no geometric spreading, scattering, and polarization losses, a maximum depth of penetration versus frequency and temperature for radar was determined.

### 1.6 MARSIS and SHARAD

Currently, two orbital radars have been sent to investigate the subsurface of Mars. MARSIS, onboard the Mars Express orbiter, has been operational since June 2005 and contains four frequency bands centered at 1.8, 3.0, 4.0, and 5.0 MHz each with a bandwidth of 1 MHz [Safaeinili et al., 2001; Picardi et al., 2005]. SHARAD, onboard

Mars Reconnaissance Orbiter, has one band centered at 20 MHz with a bandwidth of 10 MHz and is expected to begin mapping Mars in late 2006 [Seu et al., 2004]. Safaeinili et al. [2001] and Seu et al. [2004] have estimated the depth of penetration for MARSIS and SHARAD at 5 km and 1 km, respectively, assuming an estimated dynamic range of 50 dB in the subsurface. The estimated depth of penetration for both orbital radars was determined assuming very low material property losses, as well as zero subsurface scattering losses. Based on the results of this research, the estimated depth of penetration for both orbiters could be much less depending on the mineral composition of the subsurface. This will be discussed further in Chapter 6.

Currently, MARSIS has proven that it can image through the northern ice cap (northern polar layered deposits) at the 3 MHz and 5 MHz frequency bands to an approximate depth of 1.8 km [Picardi et al., 2005]. This is the first time that the subsurface of Mars has been directly measured and demonstrates the capability of GPR on Mars. However, these polar layered deposits are primarily composed of ice, a very low loss material.

With the exception of the ice rich polar caps, seeing through the Martian subsurface (rock and soil) may be much more difficult than anticipated. However, Picardi et al. [2005] believe they have detected a buried degraded crater on Mars, although their evidence remains circumstantial. In one orbit (1903), the 4 MHz channel detected out of plane reflections that can be modeled as reflections emanating from the buried rim of a 250 km diameter crater. This same orbit also detected a planar reflection with a delay of 29  $\mu$ s from the surface reflection. This reflection has been interpreted as the crater bottom [Picardi et al., 2005]. Assuming this reflection is not out of the plane and a typical real part of the relative dielectric permittivity of 4, the crater bottom would be about 2.2 km deep. In order to see this deep, the subsurface losses must be very low. Therefore, Picardi et al. [2005] have suggested that this crater may be filled with ice and covered with a thin layer of soil. However, in a nearly parallel orbit 50 km offset to the east, the 3 MHz band detected similar out of plane reflections yielding a crater that is 250

km in diameter, but no detection of the crater floor. The 3 MHz channel should see deeper due to its lower frequency, although ionospheric losses can be larger at lower frequencies. Picardi et al. [2005] believe that increased amounts of overburden soil and dust may be attenuating the GPR energy before entering the ice layer. Many other degraded craters similar to this one have been detected by MARSIS. However, MARSIS has been unable to image the base of any of these other degraded craters. Degraded craters or quasi circular depressions have been discovered in the northern plains based on their topographic features [Frey, 1999, 2000, 2001, 2002]. If these new degraded craters are proven to exist, then the basement beneath the northern plains may be as old as the southern highlands [Picardi et al., 2005]. However, none of the MARIS degraded craters match these topographic identified degraded craters. Future MARSIS and SHARAD data, as well as making the raw MARSIS data publicly available, will help to better understand if the degraded craters are real.

### 1.7 Overview

The temperature dependent measurements that are made in this thesis can be used to constrain the EM properties of Mars, thus allowing scientists to better plan future GPR missions to Mars. The measurements will also aid in the modeling and interpretation of the GPR data that will be collected.

The effects of EM properties on GPR, the selection of Martian analogs, the measurement apparatus, modeling of the data, the causes of the relaxation losses, implications for current and future GPR missions, and future work will be discussed in the subsequent chapters of this thesis.

## CHAPTER 2

### ELECTROMAGNETIC PROPERTIES OF MARTIAN ANALOGS

#### 2.1 EM Theory

In this chapter, electromagnetic (EM) theory has been broken into three subsections: EM propagation (Section 2.1.1), EM reflection and transmission (Section 2.1.2), and the radar equation (Section 2.1.3). The EM propagation subsection will mathematically describe how EM material properties affect the attenuation, velocity, wavelength, frequency, and phase of an EM wave. The EM reflection and transmission subsection will mathematically describe how EM material properties affect the amplitude and angle of the reflection and transmission coefficients. The radar equation describes all of the variables that affect EM energy as it transmitted and reflected back to the receiving antenna. This background theory will be used to estimate the maximum depth of GPR penetration due to the EM material properties of the Martian analogs.

##### 2.1.1 EM Propagation

The EM properties of a material affect the way in which EM energy propagates and attenuates through the material. Maxwell's equations (Equation 2.1) along with the constitutive equations (Equation 2.2) describe how electric and magnetic fields interact with matter [Ward and Hohmann, 1988].

$$\begin{aligned}
\nabla \times \mathbf{E} &= -\frac{\partial \mathbf{B}}{\partial t} \\
\nabla \times \mathbf{H} &= \mathbf{J} + \frac{\partial \mathbf{D}}{\partial t} \\
\nabla \cdot \mathbf{D} &= \rho \\
\nabla \cdot \mathbf{B} &= 0
\end{aligned} \tag{2.1}$$

$$\begin{aligned}
\mathbf{J} &= \sigma_{DC} \mathbf{E} \\
\mathbf{D} &= \varepsilon \mathbf{E} \\
\mathbf{B} &= \mu \mathbf{H}
\end{aligned} \tag{2.2}$$

where

$\mathbf{E}$  = electric field (V/m)  
 $\mathbf{J}$  = electric current density (A/m<sup>2</sup>)  
 $\mathbf{D}$  = displacement currents (C/m<sup>2</sup>)  
 $\mathbf{H}$  = magnetic field (A/m)  
 $\mathbf{B}$  = magnetic induction (T)  
 $\rho$  = electric charge density (C/m<sup>3</sup>)  
 $\sigma_{DC}$  = DC conductivity (Siemens/m)  
 $\varepsilon$  = complex dielectric permittivity (F/m)  
 $\mu$  = complex magnetic permeability (H/m)

The constitutive equations (Equation 2.2) are substituted into Maxwell's equations (Equation 2.1) to yield Equations 2.3. These equations show that electric fields are created by the presence of electrical charges and the instantaneous change of magnetic induction versus time, and that magnetic fields are created by the conduction currents and the instantaneous change of the displacement currents versus time [Kaufman, 1983].

$$\begin{aligned}
\nabla \times \mathbf{E} &= -\mu \frac{\partial \mathbf{H}}{\partial t} \\
\nabla \times \mathbf{H} &= \sigma_{\text{DC}} \mathbf{E} + \varepsilon \frac{\partial \mathbf{E}}{\partial t} \\
\nabla \cdot \mathbf{E} &= \frac{\rho}{\varepsilon} \\
\nabla \cdot \mathbf{H} &= 0
\end{aligned} \tag{2.3}$$

Taking the curl of Maxwell's two curl equations (Equation 2.3) with the assumption of no electrical charges ( $\rho = 0$ ) and simplifying the result produces Equation 2.4. These equations are called the Helmholtz time domain equations and represent the way in which the electric and magnetic field diffuse and propagate through a material. The left side of the equations represents how the electric and magnetic fields change spatially in the material. The first term on the right side of the equations represents diffusion and loss due to the movement of the electric and magnetic fields in the media, while the second term on the right represents propagation and storage due to the acceleration of the electric and magnetic fields in the media.

$$\begin{aligned}
\nabla^2 \mathbf{E} &= \mu \sigma_{\text{DC}} \frac{\partial \mathbf{E}}{\partial t} + \mu \varepsilon \frac{\partial^2 \mathbf{E}}{\partial t^2} \\
\nabla^2 \mathbf{H} &= \mu \sigma_{\text{DC}} \frac{\partial \mathbf{H}}{\partial t} + \mu \varepsilon \frac{\partial^2 \mathbf{H}}{\partial t^2}
\end{aligned} \tag{2.4}$$

Assuming that the electric and magnetic fields vary sinusoidally with time as shown in Equation 2.5, Equation 2.4 can be transformed (by substituting in the first and second time derivatives of Equation 2.5) into the frequency domain to yield the Helmholtz frequency domain equations (Equation 2.6). The wavenumber,  $k$ , (Equation 2.7) can be substituted into Equation 2.6 to yield Equation 2.8. The propagation constant,  $\gamma$ , (Equation 2.9) can also be substituted into Equation 2.6 to yield Equation 2.10. Equation 2.11 shows how the wavenumber,  $k$ , and the propagation constant are related. Prior to

1990 when the IEEE standardized the definition of the wavenumber and propagation constant, they were often inconsistently defined.

$$\mathbf{E} = \mathbf{E}e^{i\omega t} \quad (2.5)$$

$$\mathbf{H} = \mathbf{H}e^{i\omega t}$$

$$\nabla^2 \mathbf{E} = (\mu\sigma_{DC}i\omega - \mu\epsilon\omega^2) \mathbf{E} \quad (2.6)$$

$$\nabla^2 \mathbf{H} = (\mu\sigma_{DC}i\omega - \mu\epsilon\omega^2) \mathbf{H}$$

$$k^2 = \omega^2\mu\epsilon - i\omega\mu\sigma_{DC} \quad (2.7)$$

$$\nabla^2 \mathbf{E} = -k^2 \mathbf{E} \quad (2.8)$$

$$\nabla^2 \mathbf{H} = -k^2 \mathbf{H}$$

$$\gamma^2 = i\omega\mu\sigma_{DC} - \omega^2\mu\epsilon \quad (2.9)$$

$$\nabla^2 \mathbf{E} = \gamma^2 \mathbf{E} \quad (2.10)$$

$$\nabla^2 \mathbf{H} = \gamma^2 \mathbf{H}$$

$$\gamma = ik \quad (2.11)$$

where:

$$i = \sqrt{-1}$$

$$\omega = \text{angular frequency (rad/s)}$$

$$k = \text{wavenumber (m}^{-1}\text{)}$$

$$\gamma = \text{propagation constant (m}^{-1}\text{)}$$

The wavenumber,  $k$ , can be broken into its real and imaginary parts as shown in Equation 2.12. The real part of the wavenumber equals the phase parameter,  $\beta$ , while the imaginary part of the wavenumber equals the attenuation parameter,  $\alpha$  [Powers, 1995]. The complex dielectric permittivity and complex magnetic permeability can also be separated into their real and imaginary parts as shown in Equations 2.13 and 2.14, respectively. The real part of the complex dielectric permittivity and complex magnetic permeability represents how much energy can be stored, while the imaginary part

represents how much energy can be lost. (This will be discussed in greater detail in Section 2.2 and 2.3) It is assumed that the conductivity does not vary with frequency and therefore it is referred to as DC conductivity. Since the DC conductivity does not vary as a function of time, it only possesses a real component that represents how much energy can be lost. The speed of light in a vacuum,  $c$ , is defined in Equation 2.15.

$$k^2 = \omega^2 \mu \epsilon - i \omega \mu \sigma_{DC} = (\beta - i\alpha)^2 \quad (2.12)$$

$$\epsilon^* = \epsilon_0 \epsilon_r^* = \epsilon_0 (\epsilon_r' - i\epsilon_r'') \quad (2.13)$$

$$\mu^* = \mu_0 \mu_r^* = \mu_0 (\mu_r' - i\mu_r'') \quad (2.14)$$

$$c = \frac{1}{\sqrt{\epsilon_0 \mu_0}} \quad (2.15)$$

where:

$\beta$  = phase coefficient (radians/m)

$\alpha$  = attenuation coefficient (nepers/m)

$\epsilon^*$  = complex dielectric permittivity

$\epsilon_0$  = dielectric permittivity of vacuum =  $8.8541 \times 10^{-12}$  F/m

$\epsilon_r^*$  = complex relative dielectric permittivity

$\epsilon_r'$  = real part of the relative dielectric permittivity

$\epsilon_r''$  = imaginary part of the relative dielectric permittivity

$\mu^*$  = complex magnetic permeability

$\mu_0$  = magnetic permeability of vacuum =  $4\pi \times 10^{-7}$  H/m

$\mu_r^*$  = complex relative magnetic permeability

$\mu_r'$  = real part of the relative magnetic permeability

$\mu_r''$  = imaginary part of the relative magnetic permeability

$c$  = speed of light in a vacuum ( $2.99792458 \times 10^8$  m/s)

The complex dielectric permittivity (Equation 2.13), complex magnetic permeability (Equation 2.14), and the frequency independent DC conductivity,  $\sigma_{DC}$ , are substituted into the wavenumber (Equation 2.12) to yield Equation 2.16. The complex wavenumber is then broken into its real and imaginary parts to find the attenuation

parameter,  $\alpha$ , (Equation 2.17) and phase parameter,  $\beta$  (Equation 2.18) [Powers, 1995]. For the dry Martian analog samples studied in this research, the DC conductivity was less than  $6.67 \times 10^{-5}$  mho/m and was therefore neglected. However, it will be shown here for completeness.

$$k^2 = \frac{\omega^2}{c^2} \left[ (\mu_r' - i\mu_r'')(\epsilon_r' - i\epsilon_r'') - i(\mu_r' - i\mu_r'') \frac{\sigma_{DC}}{\epsilon_0 \omega} \right] \quad (2.16)$$

$$\alpha = \frac{\omega}{c} \sqrt{\frac{\sqrt{A^2 + B^2} - A}{2}} \quad (2.17)$$

$$\beta = \frac{\omega}{c} \sqrt{\frac{\sqrt{A^2 + B^2} + A}{2}} \quad (2.18)$$

where:

$$A = \mu_r' \epsilon_r' - \mu_r'' \left( \epsilon_r'' + \frac{\sigma}{\omega \epsilon_0} \right)$$

$$B = \mu_r'' \epsilon_r' + \mu_r' \left( \epsilon_r'' + \frac{\sigma}{\omega \epsilon_0} \right)$$

Using Equation 2.19, the attenuation parameter,  $\alpha$ , is converted into an attenuation rate,  $a$ , with units of decibels per meter. The maximum depth of penetration can then be found by dividing the dynamic range of the radar system by twice the attenuation rate as shown in Equation 2.20. This is defined as the maximum depth of penetration because only EM losses have been included. The addition of other loss mechanisms such as scattering and geometrical spreading would further reduce the depth of penetration. Using Equation 2.21, the phase parameter,  $\beta$ , is used to compute the EM velocity,  $V$ , of the sample in meters per second. As the frequency dependence of the phase parameter,  $\beta$ , increases, the dispersion of EM energy increases thus reducing the GPR resolution.

$$a = 8.686\alpha \quad (2.19)$$

$$\text{Maximum Depth of Penetration} = \frac{\text{Dynamic Range}}{2a} \quad (2.20)$$

$$V = \frac{\omega}{\beta} \quad (2.21)$$

$$\lambda = \frac{V}{f} \quad (2.22)$$

As shown in Equation 2.17, the attenuation parameter,  $\alpha$ , varies greatly with frequency. To better illustrate the attenuation caused by the EM properties of the sample, loss tangent graphs will be used in this thesis. The loss tangent,  $\tan \delta$ , quantifies the EM energy lost per cycle. Equation 2.22 describes how the loss tangent is related to the phase angle,  $\theta$ , which is the angle between the stimulus or applied external field and the response field.

$$\tan \delta = \tan\left(\frac{\pi}{2} - \theta\right) = \cot \theta \quad (2.22)$$

Equation 2.23 defines the conduction loss tangent, where the angle between the external electric field,  $\mathbf{E}$ , and the resulting current density,  $\mathbf{J}$ , is the phase angle,  $\theta_{EJ}$ . Since the conductivity of the dry Martian analog samples was less than  $6.67 \times 10^{-5}$  mho/m

(see Section 4.4.1), this term was neglected for each sample because  $\frac{\epsilon_r''}{\epsilon_r'} \gg \frac{\sigma_{DC}}{\omega \epsilon_0 \epsilon'}$ .

$$\tan \delta_{EJ} = \frac{\sigma_{DC}}{\omega \epsilon_0 \epsilon'} = \cot \theta_{EJ} \quad (2.23)$$

Equation 2.24 defines the dielectric loss tangent, where the angle between the external electric field,  $\mathbf{E}$ , and the resulting displacement currents,  $\mathbf{D}$ , is the phase angle,  $\theta_{ED}$ .

$$\tan \delta_{ED} = \frac{\epsilon_r''}{\epsilon_r'} = \cot \theta_{ED} \quad (2.24)$$

Equation 2.25 defines the total electrical loss tangent, which is equivalent to the dielectric loss tangent when neglecting the conduction loss tangent.

$$\tan \delta_{EJD} = \tan \delta_{EJ} + \tan \delta_{ED} = \cot \theta_{EJD} \quad (2.25)$$

Equation 2.26 defines the magnetic loss tangent, where the angle between the external magnetic field,  $\mathbf{H}$ , and resulting magnetic induction,  $\mathbf{B}$ , is the phase angle,  $\theta_{HB}$ .

$$\tan \delta_{HB} = \frac{\mu_r''}{\mu_r'} = \cot \theta_{HB} \quad (2.26)$$

Equation 2.27 defines the total EM loss tangent, where the angle between the external electric field,  $\mathbf{E}$ , and the magnetic field,  $\mathbf{H}$ , is the phase angle,  $\theta_{EH}$ .

$$\tan \delta_{EH} = \tan \left( \frac{\delta_{EJD} + \delta_{HB}}{2} \right) = \cot \theta_{EH} = \frac{\alpha}{\beta} \quad (2.27)$$

The solution of the electric field traveling in a plane wave in the positive  $z$  direction with an electric polarization in the  $x$  direction is given by Equation 2.28 [Balanis, 1989]. Equation 2.29 is the resulting magnetic field that is created by the electric field given in Equation 2.28 [Balanis, 1989].

$$\mathbf{E}(z) = E_o e^{-\alpha z} e^{i(\omega t - \beta z)} \hat{\mathbf{i}} \quad (2.28)$$

$$\mathbf{H}(z) = E_o \frac{\alpha + i\beta}{i\omega\mu} e^{-\alpha z} e^{i(\omega t - \beta z)} \hat{\mathbf{j}} \quad (2.29)$$

where:

$\hat{\mathbf{i}}$  = unit vector in the  $x$  direction

$\hat{\mathbf{j}}$  = unit vector in the  $y$  direction

If the plane wave is traveling through a lossless media, then the attenuation coefficient,  $\alpha$ , is zero. This makes the oscillations of the electric and magnetic field perpendicular and in phase. However, if the plane wave is traveling through a lossy media, then the attenuation coefficient,  $\alpha$ , is greater than zero. A lossy media creates an attenuation envelope, or exponential decay of amplitude versus distance, and the electric and magnetic field become out of phase with an angle equaling the phase angle,  $\theta_{EH}$ . The phase coefficient,  $\beta$ , is most affected by changes in the real part of the dielectric

permittivity and/or magnetic permeability. As the phase coefficient,  $\beta$ , increases, the velocity and wavelength of the EM wave decrease.

### 2.1.2 EM Reflection and Transmission

When EM energy encounters a change in electric and/or magnetic properties, a portion of the EM energy is reflected while the remaining EM energy is transmitted. The direction and amount of EM energy that is reflected and transmitted is dependent upon the EM property contrast. If the roughness of the contrast boundary is smooth, then the direction of the reflected and transmitted energy is given by Snell's law (Equations 2.30 and 2.31).

$$\theta_i = \theta_r \quad (2.30)$$

$$\sin \theta_t = \left( \frac{\mu_1 k_2}{\mu_2 k_1} \right) \sin \theta_i \quad (2.31)$$

where:

$\theta_r$  = angle of reflection

$\theta_i$  = angle of incidence

$\theta_t$  = angle of transmission

The energy of the reflected and transmitted EM energy is given by the Fresnel reflection coefficients in Equations 2.32 and 2.33, respectively. However, if either of the media are lossy, the transmission angle, reflection, and transmission coefficients all become complex. Additional information about reflection and transmission between two lossy media can be found in Powers [1995], Adler et al. [1966], and Balanis [1989].

$$R = \frac{\mu_2 k_1 \cos \theta_i - \mu_1 k_2 \cos \theta_t}{\mu_2 k_1 \cos \theta_i + \mu_1 k_2 \cos \theta_t} \quad (2.32)$$

$$T = \frac{2\mu_2 k_1 \cos \theta_i}{\mu_2 k_1 \cos \theta_i + \mu_1 k_2 \cos \theta_t} \quad (2.33)$$

### 2.1.3 Radar Equation

Detecting reflected EM energy from the subsurface depends on more than just the EM propagation and the transmission and reflection coefficients. Equation 2.34 is the radar equation [Ulaby et al., 1982; Powers, 1995; Burton, 2004]. The parameter values on the right side of the equation determine how much EM power,  $P$ , is detected from the subsurface. Equation 2.35 is used to determine the radar cross section of the scatterer [Powers, 1995; Burton, 2004].

$$P = P_o G_t G_r \left( \frac{1}{4\pi R_t^2} \right) \left( \frac{1}{4\pi R_r^2} \right) \xi \left( \frac{\lambda^2}{4\pi} \right) \quad (2.34)$$

$$\xi = \prod_{j=1}^{n-1} e^{-2\alpha_j r_j} K_j^2 \quad (2.35)$$

where:

$P$  = power received (W),

$P_o$  = initial power (W),

$G_t$  = transmitting antenna gain,

$G_r$  = receiving antenna gain,

$R_t$  = distance from the scatterer to the transmitting antenna (m),

$R_r$  = distance from the scatterer to the receiving antenna (m),

$\xi$  = radar cross section of the scatterer ( $m^2$ ),

$n$  = the number of EM layers from the transmitter to the scatterer and back to the receiver,

$r_j$  = distance the propagating wavefront travels in the  $j^{\text{th}}$  segment,

$\alpha_j$  = attenuation constant (Np/m),

$K_j$  = complex reflection or transmission coefficient,

$\lambda$  = the wavelength of the received energy (m).

Equation 2.34 determines how the initial EM power,  $P_o$ , is attenuated by the subsurface. If the initial EM power is attenuated enough, then the received power will be less than the dynamic range of the radar system and thus it will be undetectable. The transmitter and receiver gain,  $G_t$  and  $G_r$ , are determined by the antenna pattern. The two  $R^{-2}$  terms represent the geometric spreading losses. The radar cross section of the scatterer,  $\xi$ , is a function of three parameters: the amount of attenuation in each layer ( $\alpha_j$ ), the distance the power travels in each layer ( $r_j$ ), and the complex reflection or transmission coefficient of

each layer ( $K_j$ ). The amount of attenuation in each layer ( $\alpha_j$ ) represents the attenuation of EM energy due to conduction, dielectric relaxation, and magnetic relaxation losses. In this study, conduction losses are neglected because the dry magnetic Martian analogs measured all possessed resistivities greater than 15 k $\Omega$ m. The dielectric relaxation and magnetic relaxation losses will be discussed in the following subsections. The last term of the equation represents the aperture of the antenna in the far field (the distance away from the center of the antenna, where the distance traveled by energy radiated from any two points on the antenna will differ by less than one sixteenth of a wavelength) [Ulaby et al., 1982].

## 2.2 Dielectric Permittivity

For a material to possess a real part of the relative dielectric permittivity greater than one, the charges in the material must be able to separate to oppose an external electric field while storing energy. Dielectric permittivity is strongly frequency dependent. Therefore, dielectric relaxations can strongly attenuate GPR energy. This section will address the five types of charge separation mechanisms and frequency dependence.

### 2.2.1 Types of Charge Separation Mechanisms

Dielectric permittivity is a material property that describes how energy is stored through charge separation. It is proportional to the amount of charge and the distance that the charge is moved from an equilibrium position by the application of an external electrical field. Charges of opposite signs move in opposite directions in response to an external field, so that the resultant internal field between the charges opposes the external

field. The charges move until the internal field cancels the external field. Energy is stored in this internal field, and when the external field is removed, the internal field decays as the charges revert back to their original positions. Table 2.1 defines the five different principal mechanisms of charge separation that create a dielectric permittivity in matter greater than that of vacuum [Olhoeft, 1989].

Table 2.1. Various mechanisms for charge separation [Olhoeft, 1989]. The frequency column represents the highest frequency at room temperature that these mechanisms can occur.

Type	Frequency (Hz)	Description
Electronic polarization	$< 10^{24}$	The electron cloud of a nucleus is distorted in response to an external electric field. This mechanism occurs in every material and is density dependent.
Molecular polarization	$< 10^{14}$	Molecules are distorted in response to an external electric field.
Ionic polarization	$< 10^{14}$	Cations and anions are displaced from an equilibrium position in different directions in response to an external electric field.
Orientation polarization	$< 10^{12}$	A polar molecule rotates (without shape distortion) to align its internal electric dipole to oppose an external electric field. This mechanism is responsible for the large dielectric permittivity of water.
Interfacial polarization	$< 10^9$	Charges accumulate at boundaries of the electrical properties at all scales of the material in response to an external electric field. This mechanism occurs in every material.

### 2.2.2 Frequency Dependence of Dielectric Permittivity

Frequency dependence of dielectric permittivity occurs because charge separation does not happen instantaneously. Charges separate with finite velocities, thus if the external field is reversing polarity too quickly the charges cannot move fast enough to keep up. The time it takes for the charges to align from one polarity of the external electric field to the next is twice the time constant of relaxation,  $\tau$ . The relaxation frequency,  $f_r$ , is a function of  $\tau$  and is defined by Equation 2.36.

$$f_r = \frac{1}{2\pi\tau} \quad (2.36)$$

If the frequency of the external field is much less than the relaxation frequency, then the charges have enough time to fully separate before the external field switches polarity. However, if the frequency of the external field is much larger than the relaxation frequency, then the charges do not have enough time to fully separate and no charge separation takes place. If the frequency of the external field is near the relaxation frequency, then the charges are in constant motion and the internal electric field is out of phase with the external electric field. The constant motion of charges results in energy loss, as kinetic energy is converted into thermal energy of the material through momentum transfer (collisions and/or electromagnetic interactions). Consequently, the maximum energy loss occurs at the relaxation frequency because the charges are in constant motion at the maximum separation distance.

Table 2.1 lists the maximum frequency at which the charge separation mechanisms can respond [Olhoeft, 1989]. These mechanisms have different relaxation frequencies because as mass and charge separation distance decrease, the mechanism can react quicker. For example, the charge separation mechanism of interfacial polarization can take place over a very broad frequency range. At frequencies below 1 kHz, charges accumulate at boundaries between electrically distinct geologic layers (i.e. sandstone and

shale). At frequencies below 500 MHz, charges accumulate at boundaries between electrically distinct minerals (i.e. sand and clay) [Canan, 1999].

If two or more charge separation mechanisms take place at the same frequency, then these mechanisms are additive in polarization. As the frequency is increased, fewer charge separation mechanisms can occur. Therefore, the dielectric permittivity of a material will decrease with increasing frequency, eventually equaling that of vacuum.

### 2.3 Magnetic Permeability

This section will address different types of magnetism with an emphasis on the magnetic properties of the three most common Martian iron oxides (magnetite, maghemite, and hematite). Magnetic domains will be introduced, as well as grain size effects, and hysteresis. Lastly, frequency dependence of magnetic permeability will be discussed. Eddy current loss mechanisms are ignored because the dry magnetic Martian analogs measured in this study all possessed resistivities greater than 15 kΩm.

In Section 2.1, the magnetic permeability was defined using the constitutive equations (Equation 2.2) as the ratio of the magnetic induction to the magnetic field. Physically, the relative complex magnetic permeability of a material is defined by the strength of the material's internal magnetic field or magnetization,  $\mathbf{M}$ , in the presence of an external magnetic field,  $\mathbf{H}$ . As shown in Equation 2.37, the strength of the internal magnetic field is a function of the magnetic susceptibility,  $\chi^*$ , (unitless in the SI system).

$$\mathbf{B} = \mu_0 \mu_r^* \mathbf{H} = \mu_0 (\mathbf{H} + \mathbf{M}) = \mu_0 (1 + \chi^*) \mathbf{H} \quad (2.37)$$

In the literature, magnetic susceptibility is stated in various units in the SI system (volume susceptibility ( $\text{m}^{-3}$ ), mass susceptibility ( $\text{kg}^{-1}$ ), and density susceptibility ( $\text{m}^3/\text{kg}$ )) and in the CGS-EMU system. Before converting to magnetic permeability, the magnetic susceptibility must be in the SI system and unitless.

### 2.3.1 Types of Magnetism

The magnetic properties of Mars are believed to be the result of iron oxides [Madison et al., 2005]. For the purpose of this research, the subsequent discussion of magnetic properties will be limited to iron oxides. Goethite, an iron oxyhydroxide was measured in this study, but did not possess any magnetic properties at radar frequencies and therefore iron oxyhydroxides will not be discussed. Iron sulfates were not measured in this study, but may be important on Mars. The iron cations that make up the iron oxides are  $\text{Fe}^{2+}$  (ferrous) and  $\text{Fe}^{3+}$  (ferric) [Cornell and Schwertmann, 2003]. These cations bond with oxygen ( $\text{O}^{2-}$ ) anions to form a molecule of the iron oxide. Molecules are then arranged in a specific crystal structure depending on the mineral type.

In iron oxides, the magnetic properties are created by the angular momentum of electrons [Dunlop and Özdemir, 1997]. Each electron possesses orbital and spin angular momentum. Orbital angular momentum is created by the electron as it orbits the nucleus thereby creating a current because it is a moving charged particle. This current creates an orbital magnetic dipole moment. The spin of the electron itself creates an internal angular momentum, which then creates a spin magnetic dipole moment. The origin of electron spin is poorly understood [Tomonaga and Oka, 1998]. However, each electron possesses a spin that is either up or down. This creates a spin magnetic dipole moment that is either positive or negative. The paired electrons of a material are unimportant because the Pauli exclusion principle states that electrons occupying the same suborbital must have opposite spins. This results in the spin magnetic dipole moments of paired electrons canceling each other out.

The electron configuration of the two iron cations that form the iron oxides are  $\text{Fe}^{2+}$  ( $[\text{Ar}^{18}]3d^64s^0$ ) and  $\text{Fe}^{3+}$  ( $[\text{Ar}^{18}]3d^54s^0$ ) [Dunlop and Özdemir, 1997]. The d orbital shell contains five sub-shells, each consisting of two paired electrons. However, both iron cations do not possess enough electrons to fill the d orbital shell. Hund's first rule states that the vector sum of electron spins must be maximized when filling an orbital shell [Dekker, 1957]. Therefore, the sub-shells are filled with one electron of the same

spin. Once all the sub-shells are half filled, the remaining d orbital electrons with opposite spins will fill the sub-shells. This gives  $\text{Fe}^{2+}$  four unpaired electrons, while  $\text{Fe}^{3+}$  has five in its 3d shell. Therefore,  $\text{Fe}^{3+}$  is slightly more magnetic than  $\text{Fe}^{2+}$  because it possesses one more unpaired electron. The effects of the orbital magnetic dipole moment are dominated by the spin magnetic dipole moment in iron oxides [Dunlop and Özdemir, 1997]. This is because the orbital magnetic dipole moment cannot move as freely due to a strong electrostatic field in the crystal structure [Dunlop and Özdemir, 1997].

Iron oxides do not consist of just iron cations, but also iron cations that are bonded to oxygen anions. Therefore, the magnetic properties of iron oxides are dominated by their crystal structure, more specifically the way the bonds between the iron cations and the oxygen anions allow the iron's unpaired electron spins to align. When two iron cations ( $\text{Fe}^{2+}$  and  $\text{Fe}^{3+}$ ) bond with oxygen anions  $\text{O}^{2-}$  ( $1s^2 2s^2 2p^6$ ), they share a pair of 2p electrons with opposite spins. One of the oxygen electrons is exchanged with a 3d electron from an iron cation, while the other 2p electron is exchanged similarly with another iron cation. Since the 2p electrons possessed opposite spins, the bonded iron cations must also possess opposite spins. This creates two magnetic sublattices, A and B, that have opposite magnetic moments. If these sublattices are equal in magnitude, the material is antiferromagnetic. If these sublattices are not equal in magnitude, the material is ferrimagnetic. The energy that keeps these magnetic sublattices antiparallel is called the super-exchange energy [Cornell and Schwertmann, 2003]. This energy depends strongly on the bond angle and is also affected by the bond length. Oxygen bond angles of  $180^\circ$  give the maximum super-exchange energy because this is where the probability of p electrons interacting with the iron cations is largest due to the dumbbell shape of the p orbital [Morrish, 1965]. Likewise, super-exchange energy is minimized when bond angles are  $90^\circ$  because this is where the probability of p electrons interacting with the iron cations is smallest. Bond length affects the super-exchange energy much less than the bond angle because as bond length increases, the

probability of p electrons interacting with iron cations decreases more slowly than it does as a function of angle [Morrish, 1965].

Temperature in the crystal structure can significantly affect the magnetic properties. While super-exchange energy works to keep the magnetic sublattices aligned, temperature acts to randomize the magnetic moments of individual electrons. Eventually, the temperature randomizing effects become greater than the super-exchange energy and the magnetic sublattices become uncoupled. The temperature at which this occurs is defined as the Curie temperature for ferrimagnetic materials and the Néel temperature for antiferromagnetic materials. Above this temperature, there is a very slight alignment of electron spins with an external magnetic field. This weak form of magnetism is called paramagnetism. Below the Curie or Néel temperature, the electron spins of the crystal can remain aligned without the influence of an external magnetic field. This is referred to as magnetic remanence, or spontaneous magnetization. Magnetic remanence can occur in a number of different ways, the most common natural process being thermoremanent magnetization. This process occurs during the cooling of a magnetic mineral below its Curie or Néel temperature in the presence of an external magnetic field [Dunlop and Özdemir, 1997]. Another type of magnetization is chemical remanent magnetization, which results from the formation of a new magnetic mineral in the presence of a magnetic field [Dunlop and Özdemir, 1997].

Impurities in the crystal structure can also significantly affect the magnetic properties. Titanium is a common impurity in iron oxides that significantly reduces the Curie temperature [Hunt et al., 1995]. Similar to oxygen, titanium ( $\text{Ti}^{4+}$ ) does not have any unpaired electrons and therefore is not a magnetic element. However, titanium replaces an iron cation which reduces the super-exchange energy and affects the magnetic properties. Magnetite and maghemite become less magnetic as the titanium concentration increases, while hematite becomes more magnetic [Hunt et al., 1995]. This will be discussed further in the sections below.

### 2.3.2 Martian Iron Oxides

The crystal structure of magnetite ( $\text{Fe}_3\text{O}_4$ ) is a cubic inverse spinel structure [Cornell and Schwertmann, 2003] (Figure 2.1(a) and 2.1(b)) that possesses the largest saturation magnetization of any iron oxide at  $92 \text{ Am}^2/\text{kg}$  [Hunt et al., 1995]. Saturation magnetization is a magnetic property that describes the maximum magnitude of magnetization in the presence of a large external magnetic field. To emphasize the inverse spinel structure, magnetite can be described as  $\text{Fe}^{3+}[\text{Fe}^{2+}\text{Fe}^{3+}]\text{O}_4^{2-}$ . The  $\text{Fe}^{2+}$  and  $\text{Fe}^{3+}$  in brackets occupy the center of an oxygen octahedral, or B sublattice. The  $\text{Fe}^{3+}$  outside the brackets occupies the center of an oxygen tetrahedral, or A sublattice [Cornell and Schwertmann, 2003]. When an external magnetic field is present below the Curie temperature, the B sublattice aligns parallel to the direction of the external field, while the A sublattice aligns antiparallel. Figure 2.1(c) shows the bond with the strongest superexchange energy, where the bond angle between the A and B sublattices is  $125.25^\circ$ . The B sublattice contains one mole of  $\text{Fe}^{2+}$  and one mole of  $\text{Fe}^{3+}$ , while the A sublattice only contains one mole of  $\text{Fe}^{3+}$ . This gives the B sublattice a larger magnetization by a factor of about two, which makes magnetite ferrimagnetic below the Curie temperature [Dunlop and Özdemir, 1997]. Since the A and B sublattice contain the same amount of  $\text{Fe}^{3+}$  and their magnetizations are in opposite directions, they cancel each other out. This gives magnetite a saturation magnetization aligned with the external magnetic field with a magnitude approximately equal to  $\text{Fe}^{2+}$  [Dunlop and Özdemir, 1997].

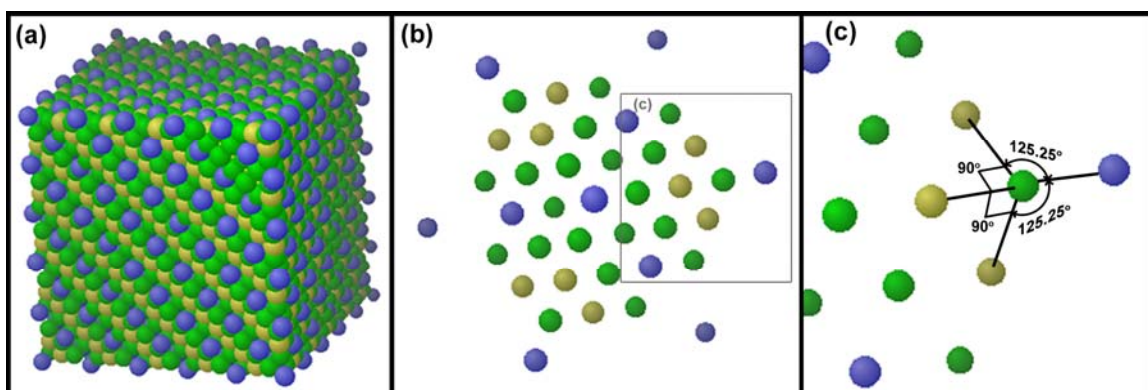


Figure 2.1. This figure shows the cubic inverse spinel crystal structure of magnetite  $\text{Fe}^{3+}[\text{Fe}^{2+}\text{Fe}^{3+}]\text{O}_4^{2-}$ , where the A sublattice (both  $\text{Fe}^{2+}$  and  $\text{Fe}^{3+}$ ) is shown in yellow, the B sublattice (only  $\text{Fe}^{3+}$ ) is shown in blue, and  $\text{O}^{2-}$  is shown in green [Chan, 2005]. Part (a) emphasizes the cubic crystal structure by displaying  $5 \times 5 \times 5$  unit cells. Part (b) shows the unit cell of magnetite along the  $\bar{1} \bar{1} \bar{1}$  axis. Part (c) shows the bond angles along the  $100$  axis. These bond angles control the super-exchange energy of the two magnetic sublattices.

Titanium ( $\text{Ti}^{4+}$ ) is a common impurity in magnetite and can significantly reduce its Curie temperature and saturation magnetization by reducing the super-exchange energy [Hunt et al, 1995]. The mineral is renamed titanomagnetite when titanium impurities are present.  $\text{Ti}^{4+}$  can only replace  $\text{Fe}^{3+}$  in titanomagnetite. Due to charge conservation, another  $\text{Fe}^{3+}$  must be converted into  $\text{Fe}^{2+}$  when this occurs [Dunlop and Özdemir, 1997]. The formula of a titanomagnetite is  $\text{Fe}_{(2-2x)}^{3+}\text{Fe}_{(1+x)}^{2+}\text{Ti}_x^{4+}\text{O}_4^{2-}$  where  $x$  is the mole% of the titanium impurity [Dunlop and Özdemir, 1997]. Equations 2.38 and 2.39 are used to find the Curie temperature ( $T_K$ ) in Kelvin and saturation magnetization ( $J_S$ ) in  $\text{Am}^2/\text{kg}$ , respectively, versus titanium mole% for a titanomagnetite [Hunt et al, 1995]. On Earth, mid-oceanic ridge basalt contains titanomagnetite with a titanium impurity of approximately 60 mole% [Dunlop and Arkani-Hamed, 2005], yielding a Curie temperature that is 440 K ( $167^\circ\text{C}$ ). In order for titanomagnetites to have a Curie

temperature that varies as a function of year or day on Mars, the titanium mole% must range from 77 to 92.

$$T_K = 848 - 552.7x - 213x^2 \quad (2.38)$$

$$J_S = 92(1 - 1.23x) \quad (2.39)$$

Maghemite ( $\gamma\text{Fe}_2\text{O}_3$ ) is similar to magnetite in that it is a ferrimagnetic mineral with an inverse spinel structure [Cornell and Schwertmann, 2003] that possesses a large saturation magnetization at  $80 \text{ Am}^2/\text{kg}$  [Hunt et al., 1995]. To emphasize its inverse spinel structure, maghemite can also be written as  $\text{Fe}^{3+}[\text{Fe}_{5/3}^{3+}\square_{1/3}]\text{O}_4^{2-}$ , where octahedral sites, or the B sublattice, are inside the brackets, where  $\square$  indicates an iron vacancy in the B site, and where the  $\text{Fe}^{3+}$  outside the brackets occupies the tetrahedral sites, or the A sublattice [Dunlop and Özdemir, 1997]. Even though maghemite has the same crystal structure as magnetite, it possesses a weaker saturation magnetization because it contains iron vacancies in its strongest B sublattice.

Maghemite is renamed titanomaghemite when titanium impurities are present. Titanomaghemite has the following formula,  $\text{Fe}_{(3-x)(8/(9+x))}^{3+}\text{Ti}_{x(8/(9+x))}^{4+}\square_{3(1-(8/(9+x)))}\text{O}_4^{2-}$ , where  $x$  is the mole% of the titanium impurity [Dunlop and Özdemir, 1997]. As the quantity of titanium in a titanomaghemite increases, its saturation magnetization decreases along with its Curie temperature [Dunlop and Özdemir, 1997]. The Curie temperature of maghemite is about 850 K [Dunlop and Özdemir, 1997]. This temperature is difficult to measure since titanomaghemite and maghemite will oxidize to hematite in air before reaching their Curie temperature [Dunlop and Özdemir, 1997].

Hematite ( $\alpha\text{Fe}_2\text{O}_3$ ) consists of a rhombohedra corundum crystal structure [Cornell and Schwertmann, 2003] as shown in Figure 2.2(a) that possesses a small (0.5% of magnetite) saturation magnetization of  $0.4 \text{ Am}^2/\text{kg}$  [Hunt et al., 1995]. In the corundum crystal structure, the cations and anions are arranged hexagonally and stacked in alternating basal planes as shown in Figure 2.2(b) and (c). Unlike an anion hexagon,

each cation hexagon contains two vacancies. The super-exchange energy creates two sublattices (A and B) that correspond to the alternating cation hexagons as shown in Figure 2.2(c) [Dunlop and Özdemir, 1997]. Both magnetic sublattices contain equal amounts of  $\text{Fe}^{3+}$  [Cornell and Schwertmann, 2003]. Below the Néel temperature (953 K), the magnetizations of the sublattices still align antiparallel to the external magnetic field, but each sublattice's magnetization is canted by an angle of  $0.2^\circ$  perpendicular to the external magnetic field [Dunlop and Özdemir, 1997]. This gives hematite its canted antiferromagnetic (parasitic ferromagnetic) properties [Cornell and Schwertmann, 2003; Dunlop and Özdemir, 1997]. However, below  $\approx 260$  K, the magnetizations of the sublattices no longer are canted and align perfectly antiparallel to the external magnetic field. This is called the Morin temperature and is defined as the temperature where hematite will transition from having canted antiferromagnetic properties to antiferromagnetic properties [Dunlop and Özdemir, 1997].

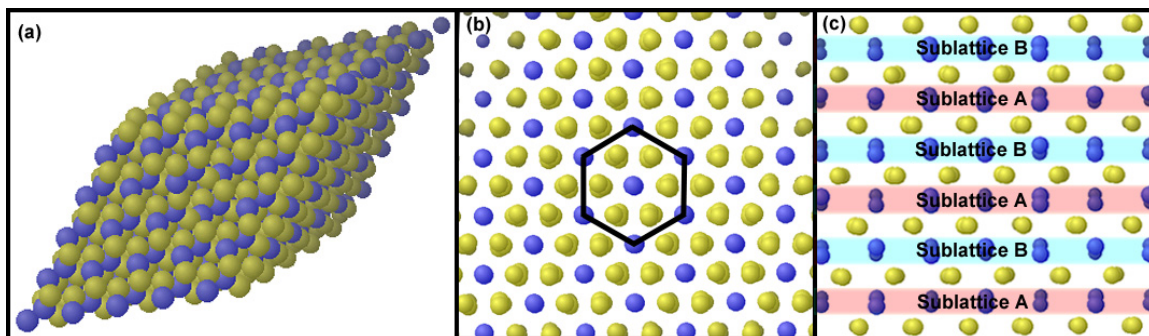


Figure 2.2. This figure shows the rhombohedra corundum crystal structure of hematite ( $\alpha\text{Fe}_2^{3+}\text{O}_3^{2-}$ ), with  $\text{Fe}^{3+}$  shown in blue and the  $\text{O}^{2-}$  shown in yellow [Chan, 2005]. Part (a) emphasizes the rhombohedra crystal structure. Part (b) shows the basal plane of the crystal structure. In this view, the iron cation hexagons are stacked on each other. Each hexagon actually contains two vacancies, which are not evident because of the stacking of multiple hexagons. Part (c) shows a section view of part (b). This view displays the vertical stacking of the cation hexagons and the two magnetic sublattices.

Titanium ( $\text{Ti}^{4+}$ ) is also a common impurity in hematite [Dunlop and Özdemir, 1997]. The mineral is renamed titanohematite or hemoilmenite when titanium impurities are present. Similar to magnetite, when  $\text{Ti}^{4+}$  replaces a  $\text{Fe}^{3+}$ , another  $\text{Fe}^{3+}$  must convert into a  $\text{Fe}^{2+}$  to maintain charge balance. Titanohematite is described as  $\text{Ti}_y^{4+}\text{Fe}_y^{2+}\text{Fe}_{2-2y}^{3+}\text{Fe}_2^{3+}\text{O}_3^{2-}$ , where  $y$  is the mole% of titanium [Dunlop and Özdemir, 1997]. Unlike magnetite or maghemite, titanium can greatly increase hematite's saturation magnetization. For titanium concentrations of less than 45 mole%, the saturation magnetization of titanohematite does not significantly change because titanium randomly replaces iron [Hunt et al., 1995]. However, when the titanium concentration exceeds 45 mole%, the replacement of iron becomes partially ordered, and the saturation magnetization greatly increases from 0.4 to 33  $\text{Am}^2/\text{kg}$  as titanohematite becomes ferrimagnetic [Hunt et al., 1995]. This occurs because the titanium will fill every other hexagon, while  $\text{Fe}^{+2}$  will fill those hexagons in between [Dunlop and Özdemir, 1997]. The titanium hexagons are not magnetic, but the  $\text{Fe}^{+2}$  hexagons are magnetic. This creates an imbalance between the two magnetic sublattices that makes the material ferrimagnetic. However, the presence of titanium also greatly reduces the Néel/Curie and Morin temperatures [Hunt et al, 1995]. The Néel/Curie temperature of titanohematite is significantly lower than pure hematite and is given by Equation 2.40 in Kelvin [Hunt et al, 1995]. In order for titanohematites to have a Curie temperature that varies as a function of year or day on Mars, the titanium mole%,  $y$ , must range from 74 to 90.

$$T_K = 953(1 - 0.928y) \quad (2.40)$$

The Morin temperature is also reduced with decreasing grain size and vanishes when grain sizes are less than  $0.01 \mu\text{m}$  [Dunlop and Özdemir, 1997]. As will be discussed in Section 3.1.3 and Table 3.1, the mean grain size of the atmospheric dust varies from  $2.44 - 5 \mu\text{m}$ . The grain size of the homogenous dust layer is most likely larger due to the settling of the larger heavier grains.

### 2.3.3 Magnetic Domains

Iron oxides not only contain magnetic sublattices where the magnetic moments are ordered, but they also possess magnetic ordering at a macroscopic scale called magnetic domains (Figure 2.3). Magnetic domains occur because the orientations of magnetic moments are influenced by other forms of energy including super-exchange energy, demagnetization energy, and magnetocrystalline anisotropy energy. If super-exchange energy was the only energy affecting the orientation of the magnetic moments, then the mineral would have all of its magnetic domains oriented in the same direction as shown in Figure 2.4a. At small distances, magnetic moments align themselves parallel due to the super-exchange energy. These parallel magnetic moments create an internal magnetic field. As more parallel magnetic moments are added, the internal magnetic field increases in size. Since magnetic field lines must close, internal magnetic fields are created that are no longer parallel to the original magnetic moments. The demagnetization energy, or magnetostatic energy, arises because magnetic moments try to align themselves parallel to the internal magnetic field. Therefore, magnetic moments remain parallel to the magnetic moments around them, until the demagnetization energy overwhelms the super-exchange energy and the magnetic moments align with the internal magnetic field as shown in Figure 2.4(b). Consequently, demagnetization energy dominates over super-exchange energy at large distances and acts to reduce any spontaneous magnetization [Dunlop and Özdemir, 1997].

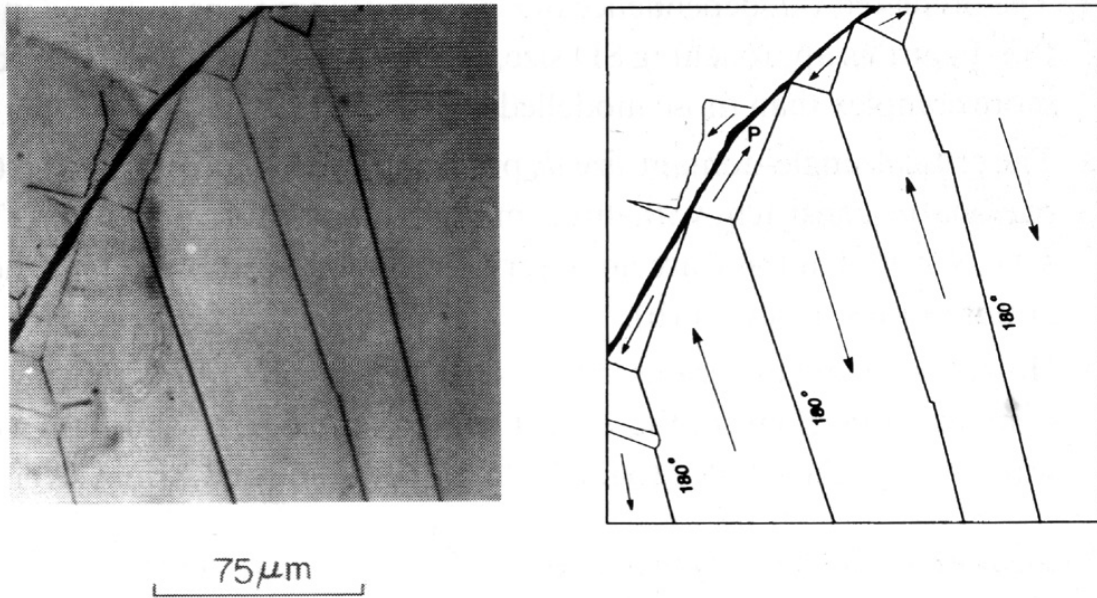
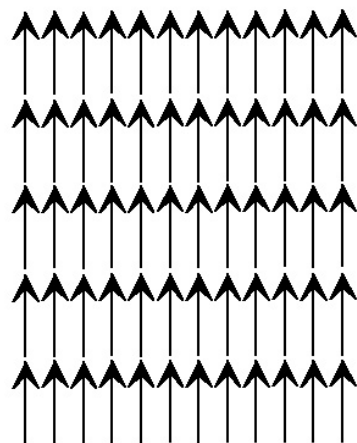
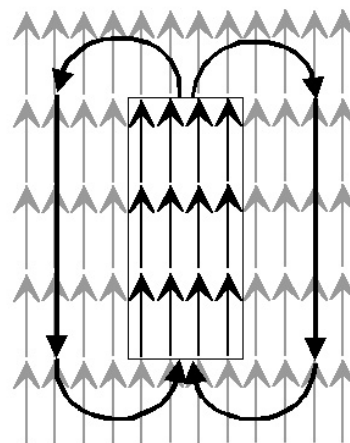


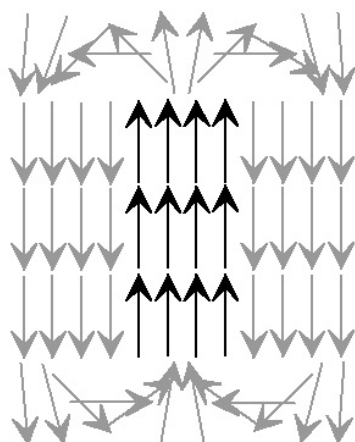
Figure 2.3. (Left) Observations of magnetic domains in a magnetite crystal, where the thick black line represents a crack in the crystal and the thin black lines represent magnetic domain walls [Dunlop and Özdemir, 1997]. This image was created by polishing the surface of a magnetite crystal and then adding a colloidal suspension of ultra-fine magnetite particles. These particles collect at the domain walls and can be imaged with a scanning electron microscope [Dunlop and Özdemir, 1997]. (Right) A schematic describing the direction of the magnetic domains seen on the left side of the figure [Dunlop and Özdemir, 1997].



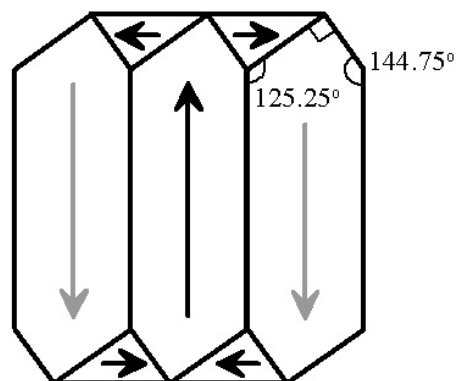
**(a)** Super-exchange energy



**(b)** Demagnetization field produced by central magnetic moments



**(c)** Demagnetization and super-exchange energy



**(d)** Magnetocrystalline anisotropy, demagnetization and super-exchange energy

Figure 2.4. This figure shows how super-exchange, demagnetization, and magnetocrystalline anisotropy energy combine to create magnetic domains in magnetite. Part (a) shows the magnetic moments of the magnetite crystal if super-exchange energy was the only energy present. Part (b) shows the demagnetization field created by the magnetic moments in the center of the magnetite crystal. Part (c) shows the magnetite crystal if super-exchange and demagnetization energy were the only energies present. Part (d) depicts true magnetite magnetic domains. Figure modified from Dunlop and Özdemir [1997].

If only super-exchange and demagnetizing energy affected the orientation of magnetic domains, they would appear like Figure 2.4(c). However, magnetocrystalline anisotropy energy also affects the alignment of magnetic moments. This energy is created by the anisotropy of the electrostatic crystalline field. This field creates easy axes in which the orbital magnetic dipole moments can contribute to the total magnetization of the mineral. Likewise, hard axes are created where the orbital magnetic dipole moments cannot contribute to the total magnetization of the mineral. Magnetocrystalline anisotropy energy is reduced when the magnetic moments are aligned with the easy axes of the crystal. Therefore, magnetic domains typically only occur in distinct directions that coincide with the direction of easy axes.

Overall, magnetic domains are created to reduce the super-exchange, magnetocrystalline anisotropy, and demagnetization energy in ferromagnetic, ferrimagnetic, and antiferromagnetic minerals as shown in Figure 2.4(d) [Dunlop and Özdemir, 1997]. These magnetic domains are on the order of 0.50-1000  $\mu\text{m}$  in width [Dunlop and Özdemir, 1997]. Inside a magnetic domain, the net magnetic moments of the two sublattices are all aligned in the same direction along an easy axis [Dunlop and Özdemir, 1997]. This creates a saturation magnetization in the same direction in the magnetic domain, as shown in Figure 2.3 or 2.4(d) [Dunlop and Özdemir, 1997]. In a mineral that has no magnetic remanence, multiple magnetic domains are equally distributed and cancel out each of the saturation magnetizations produced by the individual magnetic domains [Dunlop and Özdemir, 1997].

Magnetic domain walls, or Bloch walls, occur at the boundary between two magnetic domains with differing magnetization directions (Figure 2.5) [Dunlop and Özdemir, 1997]. Within these walls, the net magnetic moments of the magnetic sublattices rotate from the magnetic moment direction of one magnetic domain to the magnetic moment direction of the neighboring magnetic domain [Dunlop and Özdemir, 1997]. The width of the walls varies depending on the super-exchange energy. Super-exchange energy favors a broad wall compared to magnetocrystalline anisotropy energy,

which favors a narrow wall [Dunlop and Özdemir, 1997]. Since magnetic domains and walls are formed to reduce the super-exchange, magnetocrystalline anisotropy, and demagnetization energy, they can change as a function of temperature if any of these forms of energy change as a function of temperature (Figure 2.6) [Dunlop and Özdemir, 1997].

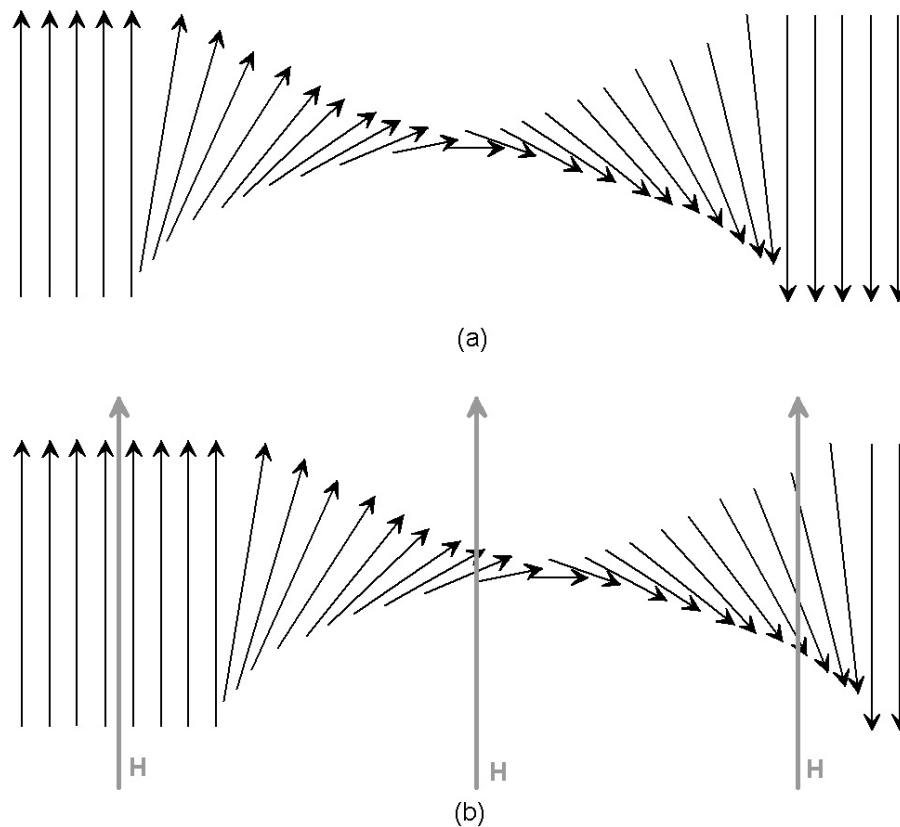


Figure 2.5. (a) Example of the rotation of magnetic moments across a magnetic domain wall. (b) Example of magnetic domain wall displacement in the presence of an external magnetic field,  $H$ . Note that the magnetic domain shown on the left is larger since it is oriented along the same direction as the external magnetic field. Figure modified from Dunlop and Özdemir [1997].

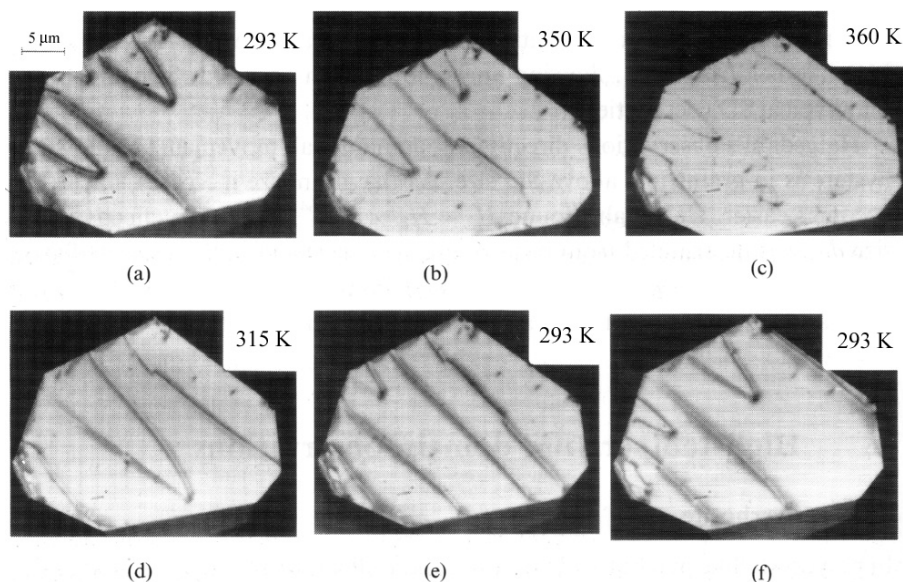


Figure 2.6. Temperature dependence of magnetic domains in a 30  $\mu\text{m}$  magnetite crystal during a heating and cooling cycle [Dunlop and Özdemir, 1997]. (a) Shows the original domain structure at 293 K (20° C). (b) Shows the domain structure at 350 K (77° C). (c) Shows the domain structure at 360 K (87° C). (d) Shows the domain structure at 315 K (42° C). (e) Shows the domain structure after one complete heating and cooling cycle 293 K (20° C). (f) Shows the domain structure after a second complete heating and cooling cycle 293 K (20° C).

#### 2.3.4 Grain Size

As grain size decreases, the number of magnetic domains also decreases. Below the critical grain size, the singledomain (SD) structure (only one magnetic domain per grain) has a lower energy than the multidomain (MD) structure because the demagnetization energy has been reduced. The critical grain size varies depending on its shape and on the mineral's saturation magnetization. Minerals that are more elongated have a larger critical grain size due to the magnetocrystalline anisotropy energy. The critical grain size also decreases as the saturation magnetization increases. This results in the critical grain size of similar shaped particles of hematite (15  $\mu\text{m}$ ) being two orders of magnitude larger than magnetite (0.06  $\mu\text{m}$ ) [Dunlop and Özdemir, 1997]. Since

saturation magnetization is temperature dependent near the Curie temperature, the critical grain size decreases with increasing temperature near the Curie temperature.

SD particles usually have a magnetization direction that is parallel to the easy axes of the crystal. An energy barrier keeps all of the magnetic moments of the electron spins aligned parallel to the easy axes of the crystal. However, as the volume of the grain size is reduced, this energy barrier decreases. The barrier can become so low that the SD particles are no longer stable and the thermal energy of the electrons can cause the magnetization energy to reorient to another easy axis every second to minute depending on the temperature and grain size. This phenomenon is referred to as superparamagnetism [Dunlop and Özdemir, 1997]. Superparamagnetism does not significantly vary with different types of iron oxides since the magnetocrystalline anisotropy energy is similar in all. Superparamagnetism typically occurs in grain sizes less than  $0.03 \mu\text{m}$  [Dunlop and Özdemir, 1997].

### 2.3.5 Magnetic Hysteresis

When an external magnetic field is applied to a magnetic mineral, it becomes magnetized in the direction of the external magnetic field. The initial susceptibility is defined as the increase in magnetization divided by the small external magnetic field that produced this increase and is shown as point A in Figure 2.7. As the external magnetic field increases, the susceptibility (slope of the line) changes. This is depicted as point B in Figure 2.7. In this region, the mineral is being nonlinearly magnetized; this will cause it to maintain a positive magnetic remanence when the external field is removed. If the external magnetic field is increased so that every magnetic domain is aligned with the external magnetic field, then any further increase in the external magnetic field will yield no further change in the magnetization strength. This is shown as point C in Figure 2.7. This point is referred to as the saturation magnetization ( $M_s$ ). If the external magnetic

field is removed after the sample reaches saturation magnetization, it will be magnetized to a value defined as the saturation remanence ( $M_r$ ). This is shown as point D in Figure 2.7. To reduce the saturation remanence to yield a magnetization of zero, an external magnetic field in the reverse direction must be applied. This is depicted as point E in Figure 2.7 and is defined as the coercivity. If the external magnetic field is increased in the reverse direction, all of the magnetic domains will align with the external magnetic field. This is shown as point F in Figure 2.7. Point F possesses the same saturation magnetization as point C, but in the opposite direction. If the external magnetic field is then reduced to zero (point G) and then increased to saturation (point C), the magnetization creates a loop defined as the hysteresis loop (CDEFGC) [Morrish, 1965].

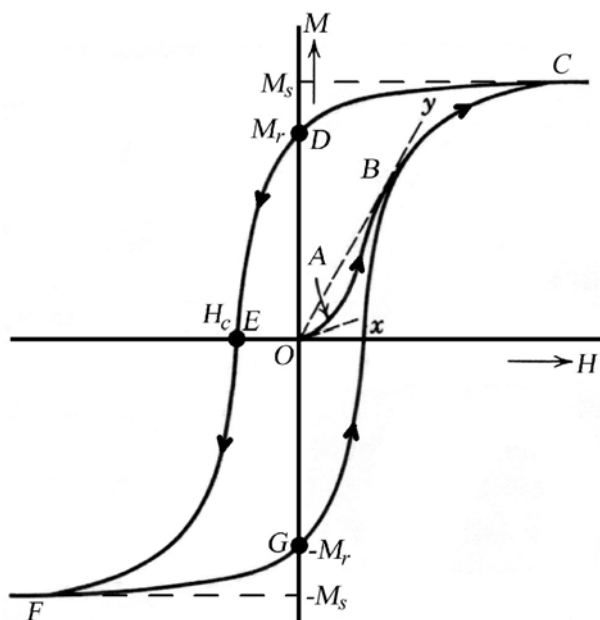


Figure 2.7. This figure depicts magnetic hysteresis. Point A indicates the initial susceptibility, which is shown as the slope of line x. Point B shows the susceptibility becoming nonlinear and reaching its maximum value, which is shown as the slope of line y. At point C, the mineral has reached its saturation magnetization ( $M_s$ ). Point D, shows the saturation remanence ( $M_r$ ) when the external field is removed. Point E shows the coercivity ( $H_c$ ), which is the external magnetic field required to reduce the saturation remanence back to zero. Figure modified from Morrish [1965].

The hysteresis curve is dependent on mineral type, temperature, impurities, and grain size as shown in Figure 2.8. A multidomain (MD) magnetic mineral can respond to an external magnetic field by shifting its domain walls, nucleation of new domains, and rotating the direction of the domain magnetization [Dunlop and Özdemir, 1997]. Domain wall displacement is the lowest energy mechanism and is responsible for the initial susceptibility (Figure 2.7 point A). The magnetic domain walls displace, as shown in Figure 2.5(b), to enlarge the magnetic domains that are nearest to the alignment of the external magnetic field. Consequently, the magnetic domains that are not aligned with the external magnetic field are shrunk [Dunlop and Özdemir, 1997]. It takes more energy to shift the magnetic domain walls when they are near imperfections in the magnetic structure. In the presence of large external magnetic fields, the domain walls can shift around these imperfections. However, when the field is removed, the domain walls do not have enough energy to shift back around these imperfections. This nonlinear process leads to magnetic remanence and coercivity.

The nucleation of new domains takes more energy than linear domain wall displacement. The nucleation process works by creating a new domain usually near an imperfection in the crystal that has reduced the magnetocrystalline anisotropy energy or near sharp corners where demagnetization energy is high. Once these new domains are created, it takes a large external magnetic field to remove the domain since they were nucleated in areas where domain wall displacement requires a lot of energy. Therefore, this process also increases magnetic remanence and coercivity in the mineral.

Domain rotation requires the most energy and only occurs with external magnetic fields near saturation magnetization in MD minerals. In this situation, the magnetic domain walls have already displaced as much as they can and no additional magnetic domains can nucleate. The only way to keep the internal magnetization proportional to the external magnetic field is to rotate the direction of the magnetic domains so that they align perfectly with the external magnetic field. This process requires more energy because the rotation must overcome the magnetocrystalline anisotropy energy. As the

external field is increased, all of the domains will align. At this point, the external magnetic field has produced one large domain in the same magnetic direction. If the magnetic field increased further, the magnetization cannot increase. This is the saturation magnetization which is shown as point C in Figure 2.7.

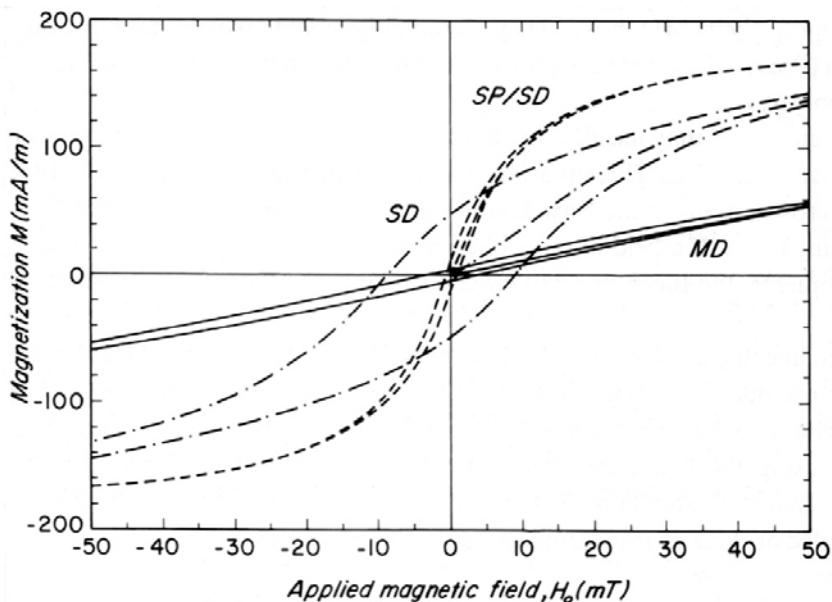


Figure 2.8. This figure shows the hysteresis curve of multidomain (MD), singledomain (SD), and superparamagnetic (SP) biotite crystals containing magnetite [Dunlop and Özdemir, 1997]. This shows that SP materials have the largest magnetic susceptibility and that SD materials contain the largest remanence,  $M_r$ .

Singledomain (SD) magnetic minerals can only be magnetized by domain rotation. Therefore, only large magnetic fields can magnetize SD minerals since magnetic domain rotation requires a lot of energy. Therefore, SD minerals are referred to as magnetically “hard” as opposed to MD minerals which are magnetically “soft”. However, this is not always the case, because the more spherical a SD grain is, the softer it becomes. SD grains can actually be softer than MD grains because domain wall displacement is limited by the demagnetization energy [Dunlop and Özdemir, 1997].

Since domain rotation is a nonlinear process, the SD grains will magnetize to their nearest easy axis once the external magnetic field is removed. This gives SD grains the largest magnetic remnance and coercivity of any grain size, as seen in Figure 2.10.

Like SD minerals, superparamagnetic (SP) minerals can only be magnetized by domain rotation. In SP minerals, domain rotation is no longer a high energy process and no longer nonlinear since domain sizes are so small. This gives SP minerals initial susceptibilities that are two orders of magnitude larger than SD or MD minerals, as shown in Figure 2.10 [Dunlop and Özdemir, 1997]. SP minerals possess very little magnetic remanence, as shown in Figure 2.10, since the domains can reorient magnetization due to thermal energy.

### 2.3.6 Frequency Dependence of Magnetic Permeability

The previous discussion about magnetic properties was limited to the magnetic properties in a constant, or DC, magnetic field. This section will concentrate on the behavior of magnetic properties at radar frequencies. Typical radar magnetic field intensities are very low, thus the magnetic properties are assumed to behave linearly and in a non-hysteretic manner.

The relative magnetic permeability is a measure of the number of magnetic moments that are realigned parallel to an external magnetic field. These magnetic moments store energy and represent the real part of the relative magnetic permeability. When the external magnetic field is removed, these magnetic moments will realign to their original locations, which converts stored energy into thermal energy through momentum transfer (collisions and/or electromagnetic interactions). Frequency dependence of magnetic permeability occurs when the magnetic moments can no longer realign parallel to the external magnetic field before the field switches direction. This can occur on a number of different scales that are described below and summarized in Table 2.2.

The highest frequency at which the spin magnetic dipole moments can stay aligned with an external magnetic field is near 10 GHz [Morrish, 1965]. Consequently, magnetic materials have a magnetic permeability of free space at frequencies greater than 10 GHz. This temperature independent magnetic relaxation mechanism is known as spin-spin and is a measure of how quickly an electron can align its spin magnetic dipole moment with an external magnetic field [Morrish, 1965]. Orbital magnetic dipole moments are also frequency dependent. This temperature dependent magnetic relaxation is known as spin-lattice and occurs at lower frequencies than the spin-spin relaxations [Morrish, 1965].

Frequency dependent magnetic permeability can occur in MD grains by magnetic wall displacement. In this case, the magnetic domains that are aligned in the same direction as the external magnetic field will expand while the magnetic domains not aligned with the magnetic field will shrink. This causes the magnetic domain walls to move when an external magnetic field is present. However, magnetic domain walls move with a finite velocity. Therefore, frequency dependence will occur when the magnetic domain walls cannot move fast enough to fully displace before the external magnetic field switches direction.

SD grains cannot change their magnetization by increasing the size of domains aligned with the external magnetic field. SD grains must either rotate the magnetization of the domain (domain rotation) or rotate the entire grain to align their magnetic domain (detrital rotation) with the external magnetic field. The magnetization mechanism the SD grain follows depends on which one takes the least amount of energy. As discussed in Section 2.2.5, domain rotation can be a high energy mechanism due to the shape and the large magnetocrystalline anisotropy energy of iron oxides. Therefore, detrital rotation typically occurs in rod-like shaped grains and domain rotation typically occurs in round grains. Detrital rotation can only occur at radar frequencies when the grain size is small because the entire grain must rotate to align the SD with the external magnetic field. If

the grains are too big, they cannot keep up with the external magnetic field. Therefore, at radar frequencies, this process can only occur in the smallest SD or SP minerals.

SP domains are defined by their ability to flip directions along the easy axes of the mineral. However, these changes generally occur over a time period of seconds to minutes. At radar frequencies, the external magnetic field is alternating over a time period of nanoseconds. Therefore, these spontaneous polarization changes are of no effect at radar frequencies.

Table 2.2. Various mechanisms for magnetic relaxations.

Type of Mechanism	Type of Magnetism	Description
Spin-Spin	All	The ability of the spin magnetic dipole moment to align with an external magnetic field.
Spin-Lattice	All	The ability of the orbital magnetic dipole moment to align with an external magnetic field.
Domain Wall Displacement	Ferro-, Ferri-	The ability of the domain wall to move to enlarge the domains that are aligned with an external magnetic field.
Domain Rotation	Ferro-, Ferri-	The ability of the domain to rotate the magnetization of the domain to become aligned with an external magnetic field.
Detrital Rotation	Ferro-, Ferri-	The ability of the domain to rotate the orientation of the grain to become aligned with an external magnetic field.

## 2.4 Frequency and Temperature Dependence of Dielectric Permittivity and Magnetic Permeability

Relative dielectric permittivity and relative magnetic permeability are each defined as a complex number with the real part representing the amount of stored energy, and the imaginary part representing the amount of energy converted to thermal energy. Relative dielectric permittivity and relative magnetic permeability become frequency dependent when the polarization mechanism or magnetization mechanism can no longer move fast enough to completely polarize or magnetize before the external field switches polarity. To model the frequency dependence of Martian analog samples, the data were inverted (this is discussed in detail in Section 5.2) to determine the best-fit Cole-Cole parameters, Equation 2.41 [Cole and Cole, 1941].

$$X_r^* = X_r' - iX_r'' = X_\infty + \frac{X_{DC} - X_\infty}{1 + (i\omega\tau)^\alpha} \quad (2.41)$$

where:

$X_r^*$  = relative dielectric permittivity or relative magnetic permeability

$X_\infty$  = high frequency limit of X

$X_{DC}$  = low frequency limit of X

$\omega$  = angular frequency (radians/second)

$\tau$  = time constant of relaxation (second)

$\alpha$  = Cole-Cole distribution parameter

The time constant of relaxation represents the period of the relaxation frequency where the maximum loss occurs. The Cole-Cole equation assumes a log-normal distribution of the time constants of relaxation,  $\tau$ . The log-normal distribution is described by the Cole-Cole distribution parameter,  $\alpha$ , and the mode of the distribution is the time constant of relaxation [Cole and Cole, 1941]. If the Cole-Cole distribution parameter,  $\alpha$ , is unity, then there is a single time constant of relaxation and the Cole-Cole equation is reduced to the Debye equation [Debye, 1929]. Typically, the distribution parameter is only equal to one in gases because they are perfectly homogeneous. Any

heterogeneity in the crystal structure or grain size will cause a soil sample to have a distribution parameter less than one.

Kauzmann [1942] demonstrated that the generalized Boltzmann temperature dependence could be used to predict how the time constant of relaxation,  $\tau$ , changes as a function of temperature, Equation 2.42. The generalized Boltzmann temperature dependence is typically used to predict the probability of a chemical reaction to occur, where the activation energy,  $E$ , is an energy barrier that the reaction must overcome to take place. In this situation, the activation energy,  $E$ , represents an energy barrier that must be overcome for the polarization or magnetization mechanisms to occur. As temperature increases, the polarization or magnetization mechanisms can move faster thereby shifting the time constant of relaxation to a smaller period. An Arrhenius plot (natural log of the time constant of relaxation versus the inverse product of temperature and the Boltzmann constant) was used to display this change (See Figure 2.9). In an Arrhenius plot, the activation energy is determined by the slope and the y-axis crossing represents the natural log of  $\tau_{\infty}$ , as shown in Equation 2.43.

$$\tau = \tau_{\infty} e^{E/kT} \quad (2.42)$$

$$\ln \tau = E \frac{1}{kT} + \ln \tau_{\infty} \quad (2.43)$$

where:

$\tau_{\infty}$  = time constant of relaxation at infinite temperature (sec)

$E$  = activation energy (eV)

$k$  = Boltzmann's constant =  $8.6176 \times 10^{-5}$  eV/K

$T$  = temperature (K)

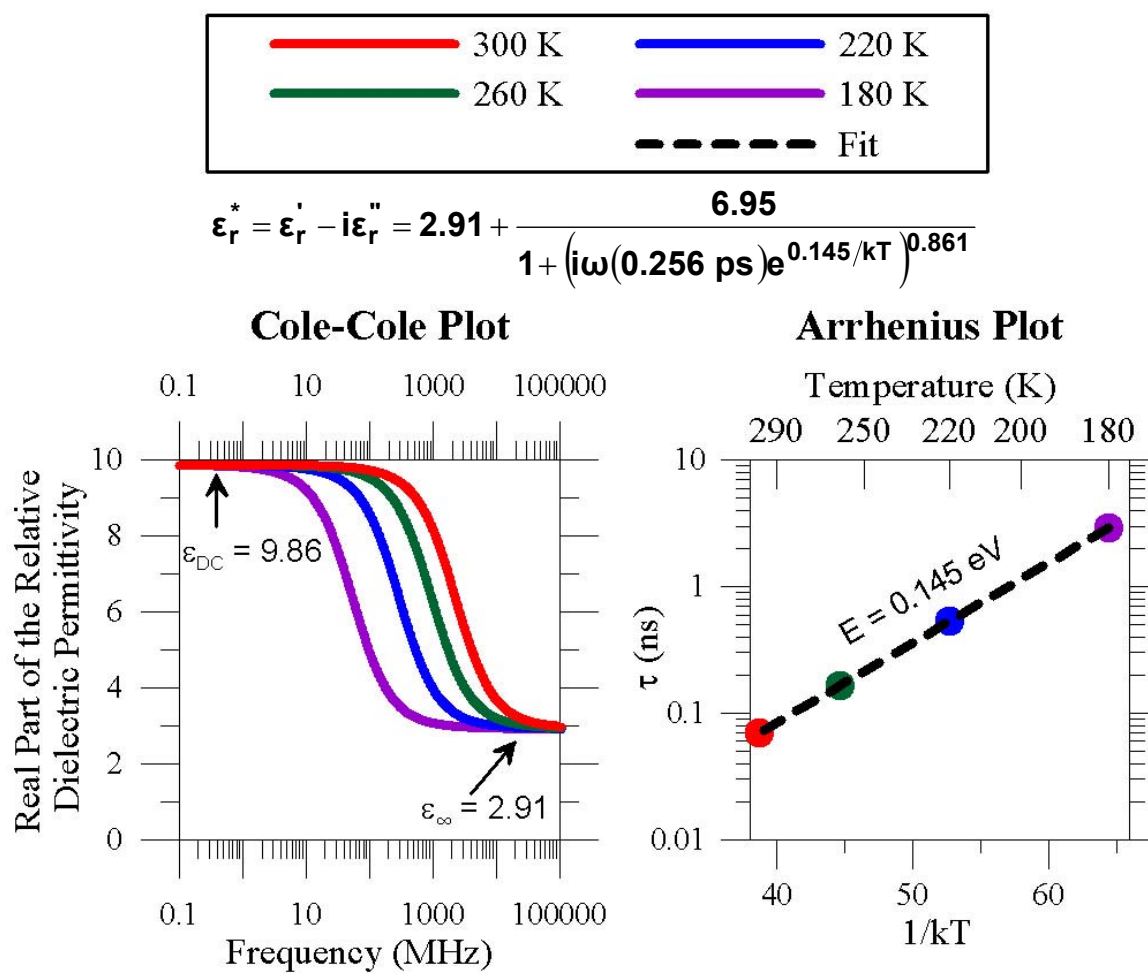


Figure 2.9. This figure shows the frequency and temperature dependence of the dielectric permittivity of grey hematite [Stillman and Olhoeft, 2005]. The left graph shows the real part of the dielectric permittivity versus log frequency while the right graph shows the log  $\tau$  versus the inverse of the product of the Boltzmann constant and the temperature to make an Arrhenius plot.

The Néel model (Equation 2.44) is used to model the time constant of relaxation for magnetic permeability where the activation energy is a function of particle volume, saturation magnetization, and coercivity [Dunlop and Özdemir, 1997].

$$\tau = \frac{\tau_0}{2} e^{\frac{\mu_0 v M_s H_c}{2kT}} \quad (2.44)$$

$\tau_0 \approx 10^{-9}$  s = atomic reorganization time or interval between successive thermal excitations

$v$  = magnetic grain volume ( $\text{m}^3$ )

$H_c$  = coercivity (A/m)

$M_s$  = saturation remnance (A/m)

$k$  = Boltzmann's constant (J/K)

To model both the temperature and frequency dependence of a sample, the generalized Boltzmann temperature dependence can be inserted into the Cole-Cole Equation (2.45) as shown in Figure 2.9. This equation can then be used to model the EM properties of the material at any temperature and frequency. With this information, the GPR depth of penetration can be calculated using Equation 2.20.

$$X_r^* = X_r' - iX_r'' = X_\infty + \frac{X_{DC} - X_\infty}{1 + (i\omega\tau_\infty e^{E/kT})^\alpha} \quad (2.45)$$

## 2.5 Mixing Formulas

In this research, most of the Martian analog samples measured were pure mineralogical samples. To simulate mixing of these minerals that might be found on Mars, the Bruggeman, Hanai, Sen (BHS) mixing equation was used to calculate the resulting complex relative dielectric permittivity of the combination, Equation 2.46 [Sen et al., 1981]. This formula assumes that both materials contribute equally to the mixture's total complex dielectric permittivity [Sihvola, 1999] and that the two materials do not interact.

$$\frac{\varepsilon_1^* - \varepsilon_m^*}{\varepsilon_1^* - \varepsilon_2^*} \left( \frac{\varepsilon_2^*}{\varepsilon_m^*} \right)^c = \Omega \quad (2.46)$$

where:

$\varepsilon_1^*$  = complex relative dielectric permittivity for material 1

$\varepsilon_2^*$  = complex relative dielectric permittivity for material 2

$\varepsilon_m^*$  = complex relative dielectric permittivity predicted for mixture

$\Omega$  = volume fraction of material 2 in the mixture

$c$  = shape factor (1/3 for spherical grains) assumed to be 1/3 in all cases.

Another important factor when comparing lab values to field values is the density of the soil. Since the dielectric permittivity and magnetic permeability vary as a function of density, they were normalized to a bulk density of 1.60 g/cm<sup>3</sup>. The high frequency limit dielectric permittivity, or electronic polarization, can be found using a Lichtenecker power law mixing formula, Equation 2.47 [Olhoeft and Strangway, 1975; Olhoeft, 1985]. To normalize the dielectric permittivity, Equation 2.48 was used. This equation only normalizes the electronic polarization mechanism for density.

$$\varepsilon_\infty = (K)^d = (1.92)^d \quad (2.47)$$

$$\varepsilon_r^{*n} = \varepsilon_r^* (1.92)^{d_n - d} \quad (2.48)$$

where:

$\varepsilon_\infty$  = high frequency limit of the real part of the relative dielectric permittivity

$K$  = mode of  $\varepsilon_\infty^{1/d} = 1.92 \pm 0.17$ . This was determined through measurements of 114 lunar samples, 261 pure minerals, and 367 rocks [Olhoeft, 1985]

$\varepsilon_r^{*n}$  = corrected complex relative dielectric permittivity

$d$  = bulk density (g/cm<sup>3</sup>)

$d_n$  = normalized bulk density of 1.60 g/cm<sup>3</sup>

$\varepsilon_r^*$  = uncorrected complex relative dielectric permittivity

Density corrections for magnetic permeability are more difficult than density corrections for dielectric permittivity because magnetic particles interact with each other.

The most commonly used magnetic permeability mixing law was empirically derived and is shown in Equation 2.49 [Strangway, 1967]. Equation 2.50 is the same as Equation 2.49, only the density ratio,  $d_n/d$ , has been substituted for the volume,  $V$ . The volume, or density ratio, cannot be greater than one, thus the magnetic permeability cannot be density corrected if the measured density is less than the normalized density. This problem occurred with only one sample, HEM. Therefore, this sample could not have its magnetic permeability corrected for density.

$$\mu_r^* = \frac{\mu_r^{*M} - 1}{2V - \mu_r^{*M}V + \mu_r^{*M} - 1} V^2 + 1 \quad (2.49)$$

$$\mu_r^{*n} = \frac{\mu_r^{*M} - 1}{2\frac{d_n}{d} - \mu_r^{*M}\frac{d_n}{d} + \mu_r^{*M} - 1} \left(\frac{d_n}{d}\right)^2 + 1 \quad (2.50)$$

where:

$\mu_r^n$  = corrected real part of the relative magnetic permeability

$\mu_r$  = uncorrected real part of the relative magnetic permeability

$\mu_r^M$  = real part of the relative magnetic permeability at a volume of 100% or density that equals  $d$ .

$d$  = bulk density ( $\text{g/cm}^3$ )

$d_n$  = normalized bulk density of  $1.60 \text{ g/cm}^3$

## CHAPTER 3

### MARTIAN ANALOG SAMPLES

#### 3.1 Observations of Martian Mineralogy

Our understanding of the mineralogical composition of Mars comes from laboratory measurements of Martian meteorites and observations made by robotic Martian orbiters and landers. Martian meteorites provide extremely detailed mineralogical data, but limited geologic context since their location of origin on Mars is unknown. Information about the global distribution of Martian mineralogy primarily comes from infrared and visible spectroscopic data gathered by three orbiters: Mars Global Surveyor (MGS), 2001 Mars Odyssey (MO), and Mars Express (MEX). More detailed mineralogical data of the surface have been acquired by the five landers/rovers: Viking 1, Viking 2, Mars Pathfinder, and two Mars Exploration Rovers (MER) – Spirit (MER-A) and Opportunity (MER-B). The observations of the Martian meteorites, orbiters, and landers listed above will be described in more detail in the sections which follow.

##### 3.1.1 Martian Meteorites

As of 2006, there are only 35 Martian samples available on Earth. All of the samples are meteorites. (See Meyer [2005] for a review of Martian meteorites.) Before these meteorites were believed to originate from Mars, they were named the SNC meteorites because they can be broken into three mineralogical groups: the shergottites, nakhlites, and chassigny. These meteorites are believed to be from Mars, and not asteroids or any other planetary body, for two main reasons. First, the meteorites are

relatively young [Papanastassiou and Wasserburg, 1974; Meyer, 2005]. All but one of the SNC meteorites are less than 1.3 billion years old, as compared to meteorites from asteroids which are at least 4.5 billion years old [Meyer, 2005]. Second, the composition of the gases trapped within the shock melted glass of the SNCs perfectly (within experimental error) matches the current Martian atmosphere [Bogard and Johnson, 1982; Leshin et al., 1996; Meyer, 2005]. The Martian atmosphere was captured in gas pockets trapped in the melted glass of the rock as it was ejected off the planet. The Martian meteorites are thought to have been ejected off Mars during 5-8 different impact events and/or volcanic eruptions over the last 20 million years [Eugster et al., 2002; Meyer, 2005]. All of the Martian meteorites are primarily volcanic, but they do contain some subtle and important differences.

The shergottites are the largest group of Martian meteorites with 24 total samples. They resemble the spectroscopic Mars type 1 unit that will be discussed in Section 3.1.2. This group has been classified into three mineralogical subgroups: basaltic, lherzolithic, and olivine-phyric [Meyer, 2005]. The ten basaltic shergottites contain pyroxene and plagioclase with small amounts of phosphates, sulfides, and titanomagnetite [Meyer, 2005]. The six lherzolithic shergottites contain mostly olivine, pyroxenes, and plagioclase with minor amounts of chromite, phosphates and sulfides [Meyer, 2005]. The olivine and chromite are poikilitically enclosed in large orthopyroxene crystals [Meyer, 2005]. The eight olivine-phyric shergottites are similar to basaltic shergottites with the addition of xenocrystals that resemble the lherzolithic shergottites [Meyer, 2005].

The second largest group of Martian meteorites is the nakhlites with seven total samples. The nakhlites are clinopyroxenites that consist primarily of pyroxene and olivine with minor amounts of plagioclase and titanomagnetite [Meyer, 2005]. The nakhlites show evidence of aqueous alterations due to trace concentrations of secondary minerals including clays, carbonates, salts, and sulfides [Meyer, 2005].

With only two samples, the chassignies are the smallest group of Martian meteorites. The chassignies are dunite cumulates, composed almost entirely of olivine

[Meyer, 2005]. These samples are totally unaltered and therefore were formed from an unfractionated magma.

Only one of the 34 meteorite samples, ALH84001, does not fit into the SNC meteorite classification. This Martian meteorite is by far the oldest at 4.5 billion years. It is classified as an orthopyroxenite, which is composed almost entirely of pyroxene with minor amounts of carbonates and magnetite [Meyer, 2005]. ALH84001 is the subject of much debate since some scientists believe that the meteorite's small ( $< 10$  nm) magnetite crystals are Martian fossils produced by magnetotactic bacteria [McKay et al., 1996; Tomas-Keprta et al., 2002].

### 3.1.2 Martian Orbiters

The scientific instruments on Mars Global Surveyor (MGS), 2001 Mars Odyssey (MO), and Mars Express (MEX) have made discoveries about the global distribution of minerals on Mars. Each of these instruments and their observations will be discussed in the subsections below.

#### 3.1.2.1 Infrared and Visible Spectroscopy

The Thermal Emission Spectrometer (TES) onboard MGS has been mapping Mars since 1997 with 143 spectral bands over a wavelength range of 5.5 - 60  $\mu\text{m}$  and a spatial resolution of 3 km [Christensen et al., 1992]. Utilizing its superior spectral resolution, TES has found that much of the Martian surface can be described by three spectroscopic units: Martian dust, type 1, and type 2 [Bandfield et al., 2000]. The Martian dust is spectroscopically homogeneous globally [Christensen et al., 1998]. This is due to the global dust storms that frequent Mars every couple of years [Goetz et al., 2005]. (Martian dust mineralogy is best characterized by the landers and is therefore discussed in Section 3.1.3.) Mars surface type 1 is confined to the older southern highlands and has a mineralogical composition that resembles basalt [Bandfield et al.,

2000, Wyatt and McSween, Jr., 2002]. Mars surface type 2 is confined to the younger northern plains and has a mineralogical composition that resembles andesite [Bandfield et al., 2000] or weathered basalt [Wyatt and McSween, Jr., 2002].

In localized areas on Mars, TES has discovered grey hematite [Christensen et al., 2001] and high concentrations of olivine [Hoefen and Clark, 2003]. Grey hematite was discovered in three areas on Mars and was believed to be associated with layered, sedimentary units [Christensen et al., 2001]. Since grey hematite can form in the presence of water on Earth [Cornell and Schwertmann, 2003] and is believed to be found in areas of layered sedimentary units on Mars, NASA sent Opportunity (MER-B) to a grey hematite rich area in hopes of finding evidence of water. Opportunity did find grey hematite and evidence of water; this is discussed further in Section 3.1.3. TES also observed olivine in small outcrops distributed globally over the Martian surface between  $\pm 60^\circ$  latitude [Hoefen and Clark, 2003]. Concentrations of about 30% olivine were found in the Nili Fossae region [Hoefen and Clark, 2003]. It is believed that this region has been at the Martian surface for at least 3.6 billion years due to the amount of cratering [Hiesinger and Head, 2002]. This is significant because olivine will alter into secondary minerals in the presence of a warm wet environment.

The Thermal Emission Imaging System (THEMIS) onboard 2001 Mars Odyssey (MO) has been mapping Mars since late 2001 with 5 visual bands and 10 infrared bands with a spatial resolution of 18 m to 100 m, respectively [Christensen et al., 2004]. Utilizing its superior spatial resolution, THEMIS has been able to more accurately map areas of grey hematite [Christensen et al., 2005a] and olivine [Hamilton et al., 2005] than TES. It has also identified several different types of igneous rocks (basalt, dacite, and granite) on Mars [Christensen et al., 2005b]. This evidence suggests that Martian magmas have undergone crystallization fractionation [Bandfield et al., 2004]. This process occurs when igneous rocks are partially reheated or when magma is partially cooled, so that only minerals with a low melting point (as defined by the Bowen's reaction series) compose the new fractionated magma.

The OMEGA spectrometer onboard Mars Express (MEX) has been mapping Mars since 2004 with 352 spectral bands ranging from 0.35 – 5.1  $\mu\text{m}$  with a spatial resolution of 0.3 – 5 km [Martin, 2003; Bibring et al., 2005]. Early results from OMEGA have confirmed the TES observations of three major spectroscopic units (dust, type 1, and type 2). However, utilizing its near infrared channels, OMEGA can map at a higher spatial resolution than TES, which has revealed much more mineralogical diversity [Bibring et al., 2005].

There are several key observations about this mineralogical diversity and its relevance to water on Mars. Olivines and pyroxenes have been mapped in areas of ancient lava flows in the southern highlands [Bibring et al., 2005]. More recent lava flows in the northern plains do not contain any olivine or pyroxene and appear to be altered [Bibring et al., 2005]. However, no alteration minerals (clays) have been mapped at these locations [Bibring et al., 2005]. Nevertheless, olivine mineralogy has been found in large (>20 km in diameter) craters in the northern plains [Bibring et al., 2005]. Hydrated sediments have not been found in the material ejected from the crater or inside the crater itself, which suggests an unaltered crust at depth [Bibring et al., 2005]. If an ocean existed in the northern plains, hydrated minerals would have been deposited in the sediments above this unaltered volcanic layer [Bibring et al., 2005]. OMEGA has mapped hydrated phyllosilicates (clays) mineralogy on Mars, but they are restricted to the older southern highlands [Bibring et al., 2005]. Hydrated sulfates (salts) have been detected in three regions of Mars: Valles Marineris, Terra Meridiani, and near the northern polar cap [Bibring et al., 2005]. Both the phyllosilicates and sulfates require water to form [Bibring et al., 2005].

In a  $\text{CO}_2$  atmosphere, carbonates would have likely formed on Mars if large bodies of standing water had existed. The identification of carbonates on Mars has been controversial. Their presence would represent an important sink for thicker  $\text{CO}_2$  in the Martian atmosphere of the past, prove that water existed on the surface, and potentially lead to evidence of Martian life [Bandfield et al., 2003]. Trace concentrations (<1%) of

carbonates have been found in Martian meteorites [Meyer, 2005] and small concentrations (2-5%) of carbonates have been spectroscopically identified by TES in the Martian dust layer [Bandfield et al., 2003]. However, only the 6.5  $\mu\text{m}$  absorption band was used by Bandfield et al. [2003] to identify this small concentration of carbonates. The absorption at this wavelength is just above the noise level of TES, therefore the evidence has been deemed inconclusive by Kirkland et al. [2003] because of the non-detection of the carbonate absorption bands at 11.2  $\mu\text{m}$  and 33  $\mu\text{m}$  which contain a larger signal to noise ratio. OMEGA has not observed carbonates on Mars as of early 2006 [Bibring et al., 2005].

#### 3.1.2.2 Martian Magnetic Field

While spectroscopic data have yielded information about the global distribution of the surface mineralogy of Mars, the magnetic field observations of MGS reveal information about the global distribution of subsurface magnetic mineralogy [Connerney et al., 2005]. Magnetic field data from MGS show that the field is strongest in the older southern highlands while the younger northern plains contain a much weaker magnetic field [Connerney et al., 2005]. (See Figure 3.1.) The magnetic field is absent in the volcanic provinces of Tharsis and Elysium and the major impact crater basins of Hellas and Argyre [Connerney et al., 2005]. These observations have resulted in the theory that Mars possessed an internally driven global magnetic field for about 500 Myr after accretion [Dunlop and Arkani-Hamed, 2005]. This ancient global magnetic field was recorded in thermoremanent magnetization and/or the less likely chemical remanent magnetization of the magnetic minerals of the Martian crust [Dunlop and Arkani-Hamed, 2005]. (Thermoremanent magnetization and chemical remanent magnetization were discussed in Section 2.3.1.) The crustal remanent field in the southern highlands is 10 times greater than the remanent fields found on Earth [Dunlop and Arkani-Hamed, 2005]. The weak magnetic anomalies of the northern plains suggest a recent upper crust formed after the internally driven global magnetic field turned off, underlain by a deeper

magnetic crust [Connerney et al., 2005]. The volcanic provinces of Tharsis and Elysium are not magnetized because they formed after the global internal magnetic field shut off [Acuña et al., 1999, 2001]. The impact crater basins of Hellas and Argyre have been thermally and shock demagnetized [Arkani-Hamed, 2005]. Smaller impacts (crater diameters of  $\approx 50$  km) can demagnetize the upper 10-20 km of the crust, while larger impacts (crater diameters of  $\approx 200$  km) can demagnetize the entire crust beneath the impact [Arkani-Hamed, 2005].

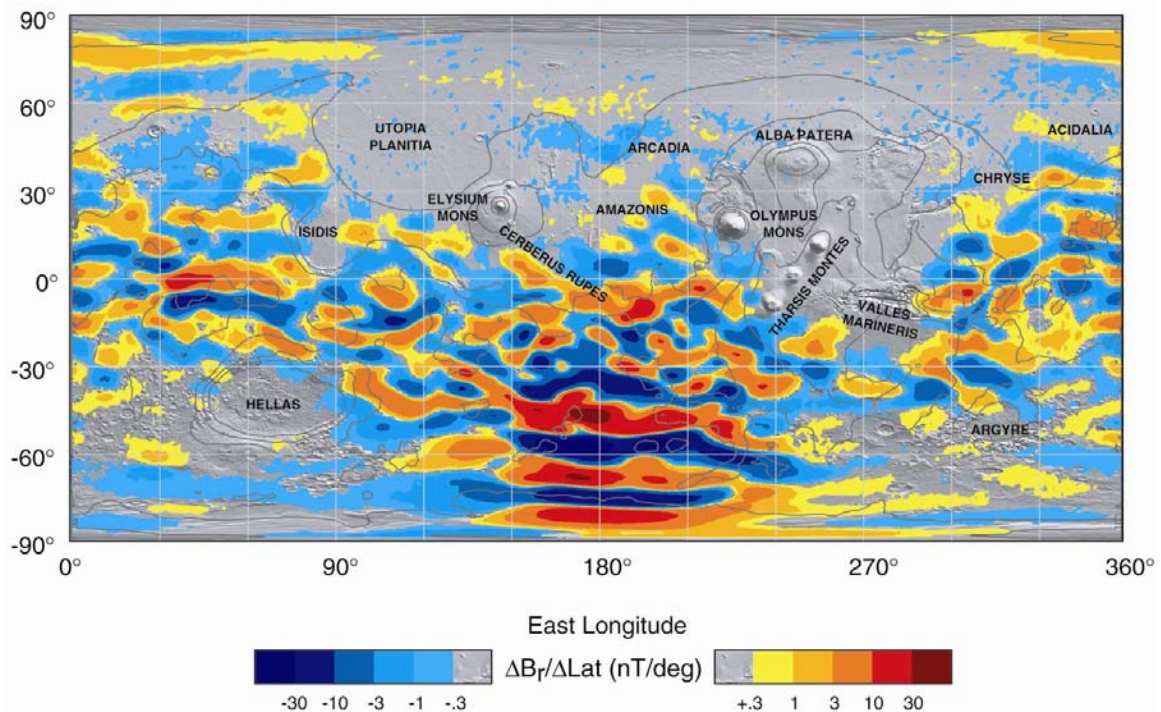


Figure 3.1. Radial Martian magnetic field at an altitude of  $\approx 400$  km with two Martian years of data overlaid on a shaded topography map [Connerney et al., 2005]. Notice the lack of magnetization at the volcanic provinces of Tharsis and Elysium and at the large impact basins of Hellas and Argyre.

The depth limit of the remanent magnetization depends on the thermal properties of the crust and the Curie temperature of the magnetic mineral [Dunlop and Arkani-Hamed, 2005]. The grain size of the remanent magnetization is limited by viscous demagnetization in which the self-demagnetization field of the magnetic mineral demagnetizes the mineral. The self-demagnetization field is large in multidomain (MD) magnetite and pyrrhotite, but small in MD and singledomain (SD) hematite, SD magnetite, and SD pyrrhotite at temperatures  $\approx 100$  K below their Curie temperatures [Dunlop and Arkani-Hamed, 2005]. Therefore, the most likely magnetic minerals causing the remanent magnetization, in order of likelihood based on the mineralogical findings of landers and orbiters, are SD magnetite (0.2-0.4 volume% with a layer thickness of 40-50 km), SD pyrrhotite (1-2 volume% with a layer thickness of 15-20 km), and MD and/or SD hematite (1.5-3 volume% with a layer thickness of 50-60 km) [Dunlop and Arkani-Hamed, 2005].

### 3.1.2.3 Gamma Ray Suite of Instruments

The gamma ray spectrometer, neutron spectrometer, and high energy neutron detector instruments have been mapping Mars since late 2001 onboard the 2001 Mars Odyssey (MO) spacecraft. The goal of this suite of instruments is to detect the hydrogen concentration to a depth of one meter with a spatial resolution of 600 km [Feldman et al., 2004] and measure the elemental composition of the surface to a depth of a few tens of centimeters with a spatial resolution of 300 km [Boynton et al., 1992]. Hydrogen on Mars could be in the form of water ice or hydrated minerals [Jakosky et al., 2005]. However, it is assumed this hydrogen is in the form of water ice because locations with high hydrogen concentrations correspond to locations where water ice could have been stable when the obliquity of Mars was much larger [Jakosky et al., 2005]. Figure 3.2 shows the global distribution of frozen water if hydrogen is in the form of water ice as measured by the neutron spectrometer.

Data from the neutron spectrometer has been used to estimate the water ice concentrations of 70-80% by volume at latitudes south of  $-60^{\circ}$ , which is significantly greater than the porosity of the material [Prettyman et al., 2004]. Similarly, data from the high energy neutron detector estimated water ice concentrations greater than 50% near the poles [Mitrofanov et al., 2004]. The formation of the ice rich layer is uncertain at this time because the ice concentration is greater than the likely soil porosity [Prettyman et al., 2004]. Therefore, the ice could not have formed solely by water vapor diffusing into the subsurface [Prettyman et al., 2004]. Mid-latitude hydrogen concentrations are between 2-3% at some locations and 10-16% at other locations [Mitrofanov et al., 2004]. There seems to be a very limited number of surfaces on Mars that are in between these two hydrogen concentrations [Mitrofanov et al., 2004]. The low hydrogen concentration locations have been normalized to 2-3% by mass because that is the amount of hydrogen that was found at the Viking 1, Viking 2, and Pathfinder landing sites [Mitrofanov et al., 2004; Feldman et al., 2004]. These areas of low hydrogen concentration are believed to be caused by hydrated minerals. The areas of high hydrogen concentration have been proposed as water ice [Jakosky et al., 2005] and/or hydrated minerals [Basilevsky et al., 2003; Mitrofanov et al., 2004].

The gamma ray instrument has also detected variations in the elemental composition (Cl, Fe, K, Si, and Th) of the top few tens of centimeters of the Martian surface [Boynton et al., 2003]. This indicates that the homogenous global dust layer could be relatively thin in depth and soils that are representative of the local geology are located just beneath the dust layer. Of the elements mapped by the gamma ray spectrometer, only iron has variations that match topography and/or spectral units. The northern lowlands and spectral type 2 have an iron concentration of about 18%, while the southern highlands and spectral type 1 have an iron concentration of about 12% [Taylor et al., 2006].

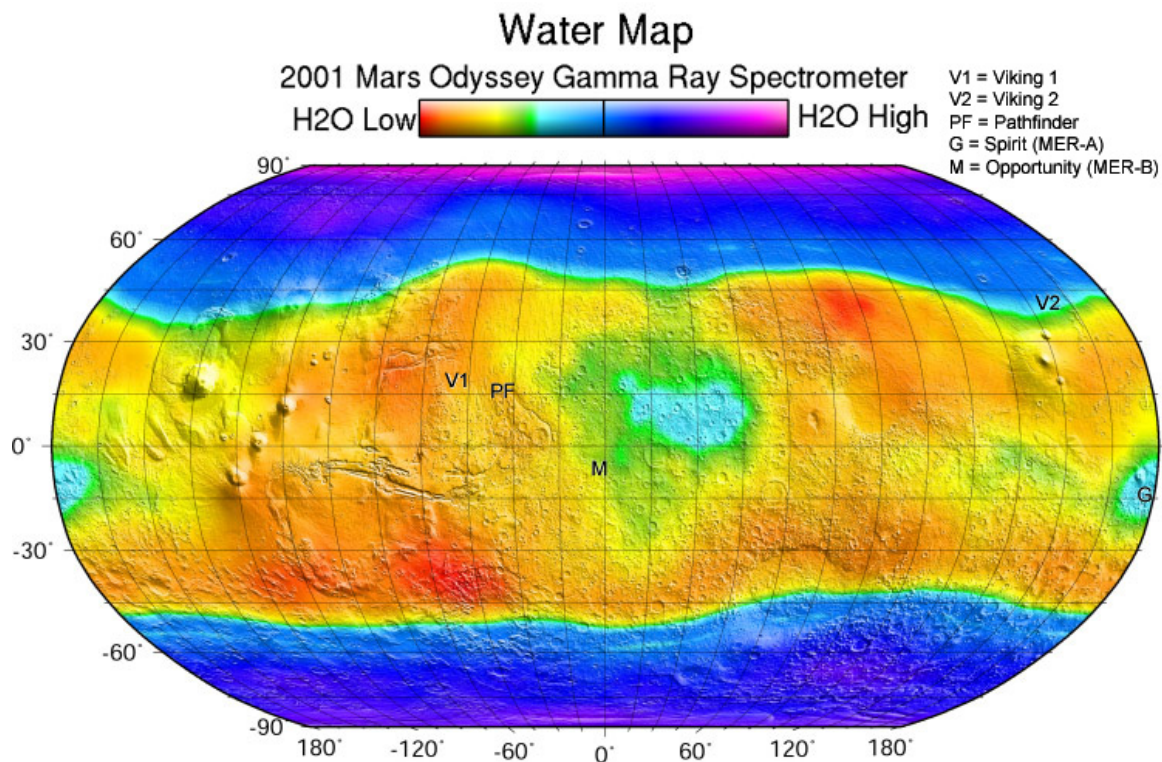


Figure 3.2. A map of the water distribution on Mars assuming all hydrogen is in the form of water ice (Image Credit: NASA/JPL/UA). The five lander locations are also shown. Notice that the presence of water is predicted in the top meter at the Meridiani Planum and Gusev Crater. While no water has been found at these locations, hydrated minerals have been found (discussed in Section 3.1.3). However, the possibility of water cannot be ruled out since the rovers have no way of “seeing” into the subsurface.

### 3.1.3 Martian Landers

Martian landers have made numerous discoveries about the mineralogy of the Martian dust, rocks, and soils found at Meridiani Planum and Gusev Crater. These discoveries and their implications will be discussed in the subsections below.

### 3.1.3.1 Dust

While much has been learned about the global mineralogy of Mars from orbiters, landers have provided detailed information about the global dust layer and mineralogical data from their landing sites. The landers have confirmed a homogeneous dust layer blanketing the Martian surface [Goetz et al., 2005]. Results from Viking 1 and Viking 2 [Hargraves, 1979], Pathfinder [Hviid et al., 1997, 1998; Madsen et al., 1999; Hargraves et al., 2000; Morris et al., 2001], and Mars Exploration Rovers (MER-A and MER-B) [Morris et al., 2004; Bertelsen et al., 2004; Madsen et al., 2003, 2005; Goetz et al., 2005; Yen et al., 2005] have shown that every particle of the global Martian dust layer is magnetic ( $>0.5 \times 10^{-6} \text{ m}^3/\text{kg}$ ) at DC (zero) frequency. (See Figure 3.3.) The magnetic properties of the dust are estimated to have an average saturation magnetization of 1-4  $\text{Am}^2/\text{kg}$  and a density magnetic susceptibility of  $9\text{-}33 \times 10^{-6} \text{ m}^3/\text{kg}$  [Morris et al., 2001]. The capture (magnetic field of 0.46 T) and filter (magnetic field of 0.2 T) magnets experiment on both MER landers has found that the dust does vary in magnetic properties, with darker colored dust (magnetite rich) being more magnetic than lighter colored dust [Madsen et al., 2003; Bertelsen et al., 2004]. The average saturation magnetization of the dust is too weak for pure magnetite or maghemite, and too strong for pure hematite. (See Figure 3.4.) Mössbauer spectroscopy on MER confirmed that the mineral causing these magnetic properties is magnetite, which has a concentration of about 2% by weight in the dust [Morris et al., 2004; Bertelsen et al., 2004; Goetz et al., 2005; Yen et al., 2005]. The amount of oxidation of the magnetite is unknown, as is the titanium content. The alpha proton X-ray spectrometer onboard Mars Pathfinder and both MER landers and a similar X-ray fluorescence spectrometer on both Viking landers, have determined that the homogenous dust layer has an elemental composition of 18% iron, 0.8% titanium, and 640 ppm of nickel by weight [Bell III et al., 2000; Gellert et al., 2004; Rieder et al., 2004]. The titanium in the dust could be in the form of titanomagnetite and/or titanohematite, but this is unknown. If titanomagnetite does exist

in the dust, then its concentration would be greater than 2%. The nickel in the dust is believed to originate from remnants of chondritic meteorite impacts [Yen et al., 2005].

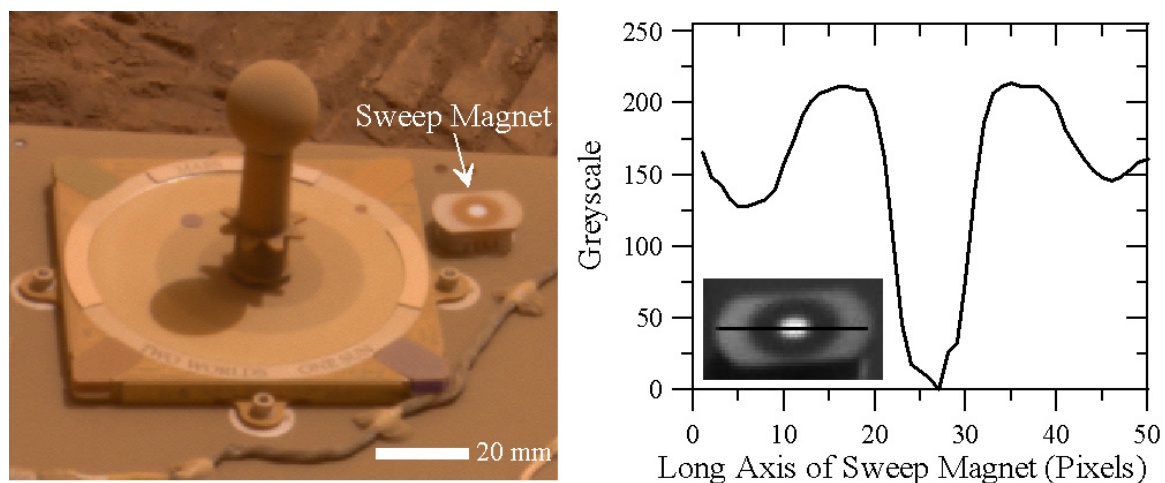


Figure 3.3. (Left) This image (PIA07303 [LaVoie, 2006]) shows the panoramic camera calibration target and sweep magnet on Spirit (MER-A) on sol 357 (Jan. 3, 2005). Dust coats the entire surface of Spirit except at the bulls eye of the sweep magnet. In order for dust to coat the surface at the bulls eye, it must pass through a magnetic field. Any dust with a magnetic susceptibility of at least  $0.5 \times 10^{-6} \text{ m}^3/\text{kg}$  will be attracted to the ring around the bulls eye [Madsen et al., 2003]. (Right) This graph shows the greyscale pixel value (255 = black and 0 = white) across the long axis of the sweep magnet at a wavelength of 436 nm (2p158057470esfa269p2839r1c1.img [Arvidson and Slavney, 2006]). The inset image on the graph displays the long axis where the pixels were selected. The bulls eye of the sweep magnet is the cleanest/brightest part of the picture. The ring around the bulls eye of the sweep magnet has a greyscale value of about 210, while the center of the bulls eye is nearly 0. The edges of the aluminum plate have greyscale value ranges of about 150. This experiment proves that all Martian dust is magnetic.

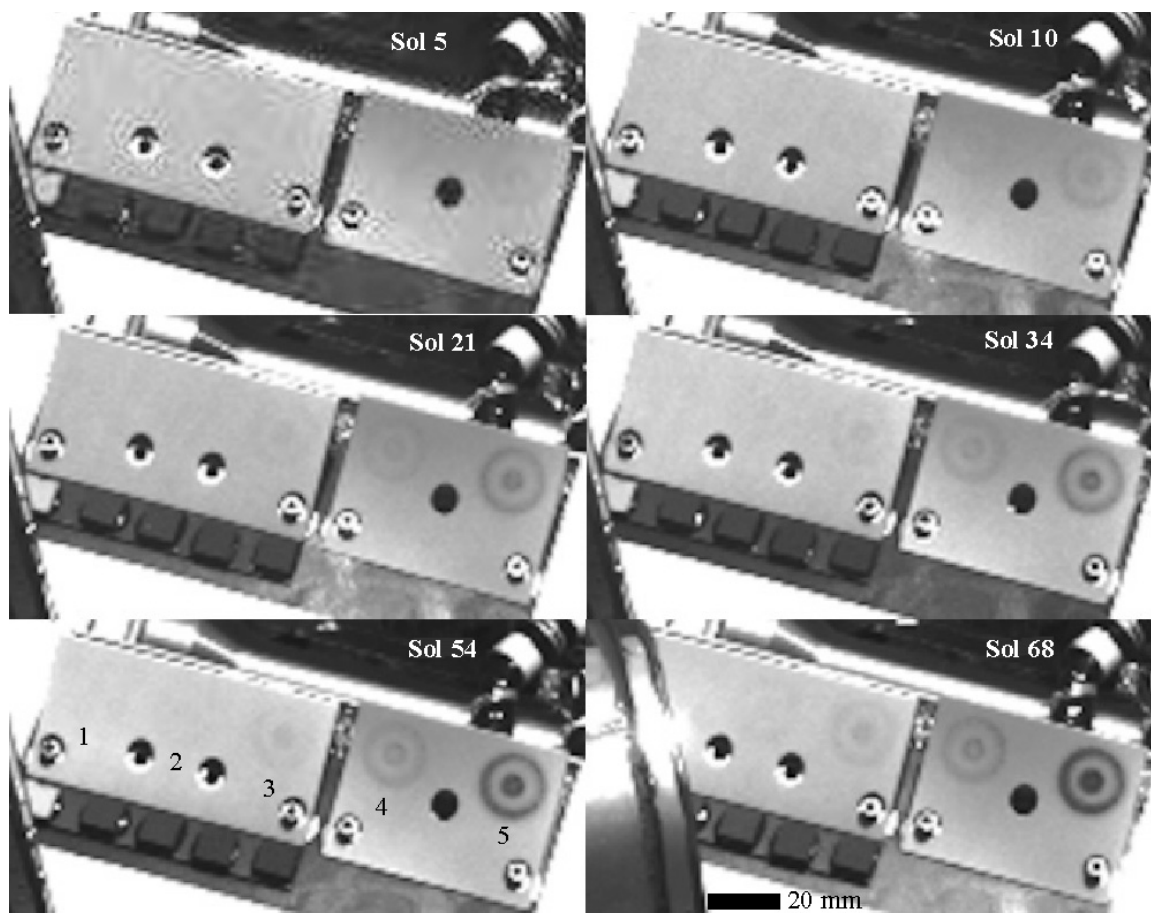


Figure 3.4. This image, taken at a wavelength of 440 nm, is a time lapse of the magnetic properties experiment on Mars Pathfinder [Hviid et al., 1997]. The experiment consisted of five magnets (labeled in the sol 54 image) varying in magnetic field strength from 11, 23, 49, 70, 280 mT with the weakest magnet (#1) on the left and strongest magnet (#5) on the right [Hviid et al., 1997]. (The magnets are labeled in the Sol 54 image.) Note that only the four strongest magnets gathered dust. If the dust was composed of pure magnetite or maghemite, then it would have collected on all of the magnets. If the dust was composed of pure hematite, then the dust would have only collected on the strongest magnet. This dust possesses an average saturation magnetization of 1-4 Am<sup>2</sup>/kg, which is in between a pure magnetite or maghemite and a pure hematite [Morris et al., 2001]. The MERs found that the magnetic dust is composed of  $\approx 2\%$  magnetite [Morris et al., 2004; Bertelsen et al., 2004; Goetz et al., 2005; Yen et al., 2005].

The grain size (diameter) of the global homogenous dust layer can be estimated by observing the light scattering of dust in the atmosphere [Pollack and Cuzzi, 1980]. Table 3.1 shows the mean particle radius of atmospheric dust as determined by the Mariner 9 orbiter, Viking 1 lander and orbiter, Viking 2 lander and orbiter, Phobos orbiter, Mars Pathfinder lander, Mars Global Surveyor (MGS) orbiter during normal Mars conditions and during the 2001 global dust storm, Spirit (MER-A) rover, and Opportunity (MER-B) rover. These measurements show that there is a large distribution of dust particle sizes in the atmosphere. This distribution is difficult to constrain, but has been estimated to have a particle radius variance of  $0.80 \mu\text{m}$  [Tomasko et al., 1997; Clancy et al., 1995]. In addition, the particle distribution is not Gaussian, but skewed to lower particle radii thus yielding a mode particle radius near  $0.20 \mu\text{m}$  [Clancy et al., 1995]. The mean particle radius of the atmospheric dust increased during the 2001 global dust storm because larger heavier grains were lifted into the atmosphere by high winds.

Several experiments, including the wheel abrasion experiment on Pathfinder's rover, have confirmed that the grain size (diameter) of the homogenous surface dust layer is less than  $20\text{-}40 \mu\text{m}$  [Ferguson et al., 1999]. The grain size of the dust layer was found to be less than the maximum resolution of the microscopic imager,  $30 \mu\text{m}$  per pixel, on both MER landers [Herkenhoff et al., 2003]. Lastly, the texture of soils compacted by the MER Mössbauer spectrometer and the MER airbags suggests the presence of very fine grains in the dust layer [Arvidson et al., 2004].

Both MER Mössbauer instruments detected the presence of olivine and nanophase iron oxide in the global dust layer [Klingelhöfer et al., 2004; Morris et al., 2004]. The presence of olivine in the dust layer indicates that liquid water did not play a dominant role in its formation [Goetz et al., 2005]. The nanophase iron oxide may be superparamagnetic (defined in Chapter 2) and is most likely a nanophase hematite, which can be formed in the presence of water and by physical erosion [Klingelhöfer et al., 2004; Morris et al., 2004].

The formation of the global magnetic homogenous dust layer is complex [Goetz et al., 2005]. The dust is believed to consist of a primary unaltered group, a secondary hydrated group, and nickel remnants from chondritic meteorites [Goetz et al., 2005]. The unaltered primary group consists of olivine, pyroxene, and magnetite (possibly titanomagnetite) that was physically eroded from basaltic rock [Goetz et al., 2005]. The secondary hydrated group consists of red nanophase hematite that may have been formed by water [Goetz et al., 2005]. This nanophase hematite gives the dust its red color and could be superparamagnetic [Goetz et al., 2005]. The primary and secondary group and the nickel are believed to have formed separately and then bonded together by electrostatic forces [Goetz et al., 2005].

Table 3.1. The mean particle radius of atmospheric dust as determined by the Mars orbiter and landers.

Spacecraft	Mean Particle Radius ( $\mu\text{m}$ )	Authors
Mariner 9	1.80	Clancy et al., 1995
Viking 1 (lander)	$1.52 \pm 0.30$	Pollack et al., 1995
Viking 2 (lander)	$1.85 \pm 0.30$	Pollack et al., 1995
Viking 1 (orbiter)	1.80	Clancy et al., 1995
Viking 2 (orbiter)	1.80	Clancy et al., 1995
Phobos	1.80	Clancy et al., 1995
Pathfinder	$1.60 \pm 0.15$	Tomasko et al., 1997
Pathfinder	$1.71 + 0.29 / - 0.26$	Markiewicz et al., 1999
MGS (normal)	$1.50 \pm 0.10$	Clancy et al., 2003
MGS (storm)	$2.15 \pm 0.35$	Clancy et al., 2003
Spirit	$1.47 \pm 0.21$	Lemmon et al., 2004
Opportunity	$1.52 \pm 0.18$	Lemmon et al., 2004

### 3.1.3.2 Meridiani Planum

Grey hematite that was believed to be formed in the presence of water was discovered in Meridiani Planum by TES [Christensen et al., 2001]. Therefore, NASA sent Opportunity (MER-B) to investigate. Opportunity's Mössbauer instrument determined that the spectral grey hematite signal at Meridiani Planum was caused by grey hematite concretions, as seen in Figure 3.5 [Klingelhöfer et al., 2004]. Opportunity has imaged thousands of these ubiquitous concretions. The rock abrasion tool on Opportunity has cut through many of the concretions and confirmed that they are composed entirely of grey hematite [Squyres and Knoll, 2005]. Although size statistics have not been performed, the spherical concretions range in size from a few mm up to 1 cm [Calvin et al., 2004]. The distribution of the concretions that are embedded in the bedrock is overdispersed (i.e. more uniform than random), and not along bedding planes as would be the cause for lapilli or impact spherules [Calvin et al., 2004; Squyres and Knoll, 2005]. Some of the concretions have formed so closely together that they are now connected. The concretions do not deform the bedding planes of the bedrock, but rather have formed by scavenging or dissolving surrounding material as they form [Calvin et al., 2004; Squyres and Knoll, 2005]. Opportunity's (MER-B) Mössbauer instrument also detected jarosite (a sulfur hydroxide that can contain up to 10% water by weight in its crystal structure) in the bedrock at Meridiani Planum [Rodionov et al., 2005]. Jarosite can only form in acidic conditions [Klingelhöfer et al., 2004].

The bedrock at Meridiani Planum in which the grey hematite concretions and jarosite was found is sandstone that is composed of a mixture of altered siliciclastics and sulfate salts. The sandstone was most likely formed by chemical weathering of olivine basalt in sulfuric acid aqueous solution, which formed the jarosite, followed by the evaporation of this aqueous solution, which left behind the sulfate salts. This process most likely occurred in a playa lake. These grains were then reworked by wind to form sand dunes and sand sheets, which were then cemented and buried. Finally, an iron rich groundwater filled the pore spaces of the rock and precipitated the hematite concretions

[Squyres and Knoll, 2005]. Much of the sandstones at Meridiani Planum have eroded away leaving a lag deposit that is heavily concentrated in grey hematite concretions primarily because they are heavier and have not blown away. The lag deposit is also rich in olivine and magnetite, which are not seen in the sandstone. The origin of the olivine and magnetite in the lag deposit is most likely from the global homogenous dust layer.

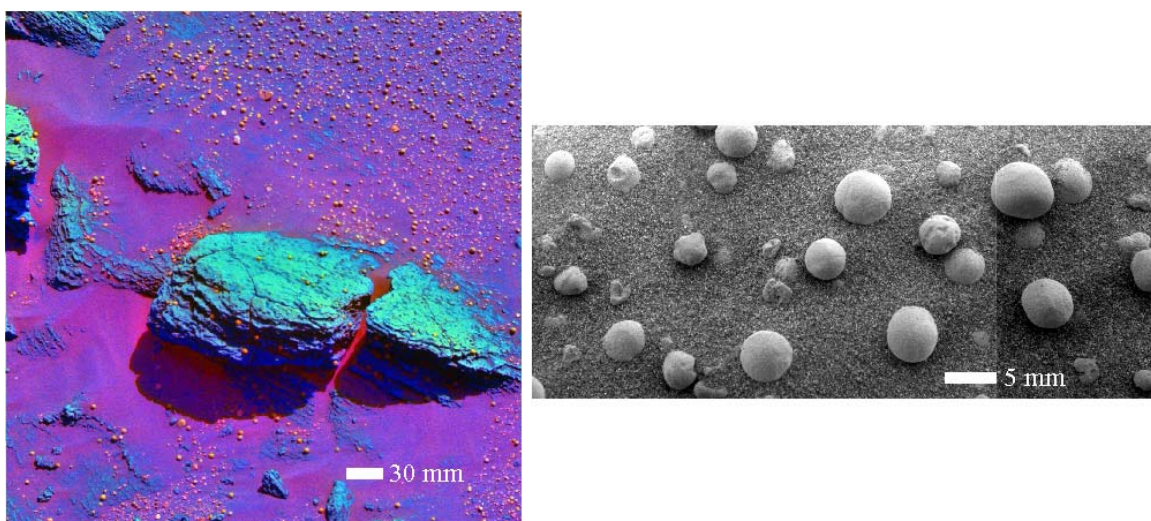


Figure 3.5. (Left) This is a false color image of Stone Mountain rock taken by the panoramic camera onboard Opportunity (MER-B) (PIA05236 Image Credit: NASA/JPL/Cornell/USGS [LaVoie, 2006]). In this image, the hematite concretions are shown in orange. (Right) This greyscale image was taken of the hematite concretions in the soil deposit above Stone Mountain by Opportunity's (MER-B) microscopic imager (PIA05273 Image Credit: NASA/JPL/Cornell/USGS [LaVoie, 2006]).

### 3.1.3.3 Gusev Crater

Spirit (MER-A) landed in Gusev crater in hopes of finding evidence of vast lacustrine deposits. However to date, no lacustrine deposits have been found. These deposits are now thought to be buried by an olivine rich basaltic lava flow. Evidence of water alteration was found when Spirit arrived at the west spur of Husband Hill. In this area, Spirit's Mössbauer detected an abundance of goethite (an iron oxyhydroxide) in Clovis rock and a smaller abundance in four other rocks in the vicinity of Clovis rock. Goethite can only be formed by water alteration [Ming et al., 2005]. Rocks and soils in this area have an anomalously high concentration of sulfur, bromide, phosphorus and chloride and are soft (factor of 10-20) in comparison to the unaltered basaltic rocks found on the plains of Gusev crater [Ming et al., 2005]. The rocks and soils near Husband Hill are volcanoclastic and/or impact ejecta deposits that have been altered by an aqueous acid-sulfate condition [Arvidson et al., 2006a]. However, the mechanism of aqueous alteration remains unclear [Ming et al., 2005].

### 3.1.4 Summary of Martian Observations

Overall, Mars is an iron rich, magnetic, impact cratered, volcanic planet which has not had much of its surface minerals altered by water. The Martian subsurface contains a significant remanent magnetization that is most likely caused by singledomain titanomagnetite [Dunlop and Arkani-Hamed, 2005]. At large scales (>1 km), Mars can be divided into three spectroscopic units consisting of dust, type 1 basalt (older southern highlands), and type 2 weathered basalt or andesitic layer (younger northern plains) [Bandfield et al., 2000; Wyatt and McSween, Jr., 2002]. The global magnetic dust layer is remarkably homogenous due to global dust storms [Goetz et al., 2005]. This dust layer is believed to have formed by electrostatic forces that bound together a primary unaltered group (olivine, pyroxene, and magnetite), a secondary hydrated group (red nanophase hematite), and nickel remnants from chondritic meteorites [Goetz et al., 2005]. The

atmospheric dust has a mean particle radius of  $\approx 1.7 \mu\text{m}$  during normal conditions on Mars. However, during the 2001 dust storm the mean particle radius of the atmospheric dust increased to  $\approx 2.1 \mu\text{m}$ . Other experiments have confirmed that the grain size (diameter) of the homogenous surface layer is less than 20-40  $\mu\text{m}$ . The depth of the surface dust layer is believed to be thin since dust devils and rovers leave tracks with a different albedo than dust that has not been disturbed [Arvidson et al., 2006a].

Below the kilometer scale, Mars reveals a greater diversity of minerals [Bibring et al., 2005]. Water is believed to have formed or altered existing Martian minerals to form grey hematite concretions [Squyres and Knoll, 2005], jarosite [Klingelhöfer et al., 2004], goethite [Ming et al., 2005], sulfate salts [Bibring et al., 2005], clays [Bibring et al., 2005], and carbonates in the Martian meteorites [Meyer, 2005]. As discussed in Chapter 1, there is also substantial visual evidence of water on Mars: giant flood channels [Irwin et al., 2004], extensive valley networks with branching tributaries [Carr, 1996], dry lake beds [Williams and Zimbelman, 1994], and gullies [Malin and Edgett, 2000; Christensen, 2003]. There is also evidence that water ice currently exists at both polar caps [Kieffer et al., 1976; Titus et al., 2003] and within a meter of the surface on Mars at certain mid-latitude locations and ubiquitous locations at latitudes poleward of  $\pm 60^\circ$  [Feldman et al., 2004; Prettyman et al., 2004].

There is mineralogical evidence that liquid water has never existed for long periods of time on the Martian surface. This evidence includes the following: no significant concentration of carbonates have ever been mapped on the Martian surface [Bibring et al., 2005], water altered minerals are localized [Bibring et al., 2005], olivine has been found globally in the rocks [Hoefen and Clark, 2003] and dust [Goetz et al., 2005], and the nakhlites meteorites show only trace concentrations of aqueous alteration minerals while the other Martian meteorites show no evidence of water [Meyer, 2005]. Consequently, water seems to have only been stable for short periods of time on the

Martian surface, and the planet may have been cold and dry for a long period since that time [Hoefen and Clark, 2003].

### 3.2. Limitations of the Methods Used to Map Mineralogy on Mars

While many important discoveries about Martian mineralogy have been made, it is important to understand the limitations of the observations made and the assumptions made when interpreting the data. The limitations of infrared and visible spectroscopy, Mössbauer spectroscopy, magnetic field measurements, gamma ray spectroscopy, neutron spectroscopy, the high energy neutron detector, alpha proton spectroscopy, and the X-ray spectroscopy measurements will be discussed.

#### 3.2.1 Limitations of Infrared and Visible Spectroscopic Observations

Infrared and visible spectroscopy used by TES, THEMIS, and OMEGA both suffer from similar problems. First, the Martian atmosphere absorbs part of the light spectrum. For example, the TES instrument has a wavelength range of 5.5 – 60  $\mu\text{m}$ , but the Martian atmosphere, including atmospheric dust, absorbs nearly all of the energy from 12 – 20  $\mu\text{m}$ . Therefore, any mineral containing absorption bands from 12 – 20  $\mu\text{m}$  cannot be resolved by infrared spectroscopic instruments. Second, dust coats nearly all of the surfaces on Mars. (See Figure 3.6.) At infrared frequencies, dust coatings as thin as 10 - 20  $\mu\text{m}$  can significantly reduce any spectral contrast from the surface [Johnson et al., 2002a]. Consequently, as spectral contrast decreases, mineral identification becomes more difficult. When the dust coating becomes thicker than 50  $\mu\text{m}$ , the spectral contrast from the surface can be completely reduced at infrared frequencies [Johnson et al., 2002a]. Due to its smaller wavelength, the visible spectrum is more sensitive to dust coatings than the infrared spectrum.

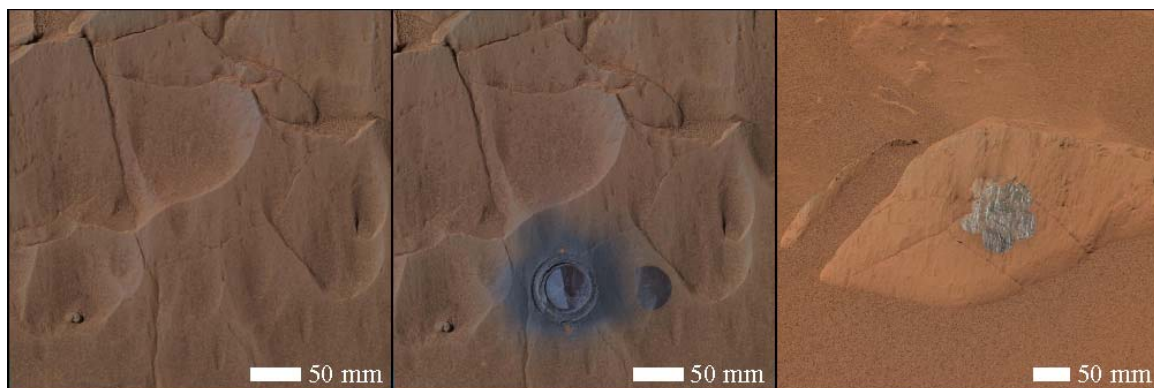


Figure 3.6. These images were taken by Spirit's panoramic camera and are shown at approximate true color. (Left) This image (PIA05682 Image Credit: NASA/JPL/ Cornell [LaVoie, 2006]) is a close-up of a basaltic rock called Mazatzal. (Center) After a brushing (right hole) and a grinding (left hole) in Mazatzal rock, its true color was revealed after removing  $\approx 1$  mm of dust (PIA05684 Image Credit: NASA/JPL/Cornell [LaVoie, 2006; Arvidson et al., 2004]). (Right) This image (PIA05074 Image Credit: NASA/JPL/Cornell [LaVoie, 2006]) was taken after brushing a daisy pattern on a rock called Route 66. This daisy pattern allows for an infrared spectrometer (Mini-TES) on Spirit to get an accurate spectrum of the rock. The composition of Mazatzal and Route 66 could not be determined before brushing. However after brushing the dust off, they were shown to have slightly different compositions.

Another notable limitation for infrared and visible spectroscopy is that shock effects from impact events can alter the spectra of minerals [Johnson et al., 2002b]. By experimentally shocking anorthosite and pyroxenite, Johnson et al. [2002b] found that small and large absorption bands are significantly reduced and can disappear altogether as the pressure of the shock is increased. They also found that bands can shift in wavelength as the pressure of the shock is increased [Johnson et al., 2002b]. As stated previously, the Martian dust contains 640 ppm of nickel, which scientists believe came from chondrite meteorite remnants. This, along with visual evidence of impact craters, indicates that many Martian minerals have been shocked by impacts.

Lastly, the spectra from TES, THEMIS, and OMEGA can contain multiple minerals in each pixel. Spectral linear mixing models have been created to identify the

mineral types and portions that fit each spectrum [Ramsey and Christensen, 1998]. These models match mineral types through a library of laboratory spectra. The matches can be ambiguous because many minerals are spectroscopically similar. This leads to ambiguity in the mineralogical interpretation as is demonstrated by both weathered basalt and andesite matching Mars surface type 2 [Wyatt and McSween, Jr., 2002]. Consequently, the models are only as good as their libraries. Most laboratory spectra are generated from smooth polished samples at certain grain sizes at room temperature ( $\approx 298$  K). The spectrum of a mineral can change based on surface roughness and grain size [Kirkland et al., 2003]. These effects can be large enough to effectively hide large exposed areas of the mineral and can also shift the wavelength of the absorption bands to lower wavelengths [Kirkland et al., 2003]. As discussed in Chapter 1, the surface of Mars rarely reaches 298 K and mineral spectra can be temperature dependent [Morris et al., 1997]. The libraries are also limited to minerals found on Earth and the available Moon samples. Since the Moon possesses minerals that had never been discovered on Earth, it is likely that Mars also possesses undiscovered minerals.

The limitations of infrared and visible spectroscopy including Martian atmospheric absorption, dust coating, shock alteration of minerals, surface roughness dependence, grain size dependence, temperature dependence, and undiscovered Martian minerals all increase the ambiguity in the interpretation of the Martian surface spectra. This also leads to the conclusion that certain minerals may exist on Mars even though they have never been detected [Kirkland et al., 2003]. For example, Martian carbonates may possess rough surfaces or be covered in dust and therefore be spectroscopically stealthy. An example of this stealth is exhibited by the deposit known as “White Rock”, a proposed lacustrine deposit [Williams and Zimbelman, 1994] that contains no mineralogical spectral signature [Ruff et al., 2001].

### 3.2.2 Limitations of the Magnetic Field Measurements

The three component magnetometer onboard Mars Global Surveyor takes measurements of the Martian magnetic field. The latest released magnetic map of Mars is based on measurements that were acquired over two Martian years (one Martian year equals 687 Earth days) at an altitude of 370-438 km [Connerney et al., 2005]. Due to the high altitude, these data do not provide detailed information about the shallow subsurface and are only sensitive to regional areas of magnetization. In addition, at this altitude the magnetic field is a combination of the internal Martian remnant magnetic field and the external magnetic field created by the solar wind interaction with the Martian magnetosphere [Connerney et al., 2005]. The remnant magnetic field can be as great as 220 nT and does not have a diurnal fluctuation. The external magnetic field can be as large as 100 nT on the day side of the planet and as small as 10 nT on the night side [Connerney et al., 2005].

The external magnetic field is not random and is greatest near the subsolar point (the point on Mars which is closest to the Sun) [Connerney et al., 2005]. On the day side of Mars, the variations in the external magnetic field contain a spatial frequency content that is similar to the spatial frequency content of the remnant magnetic field of Mars [Connerney et al., 2005]. Consequently, the external magnetic field data cannot be removed and any magnetic field data acquired on the day side cannot be used [Connerney et al., 2005]. On the night side of Mars, the external magnetic field is much smaller because it is protected from the solar wind. Magnetic field data acquired on the night side can be used because the external magnetic field is not as strong, and its spatial frequency content is lower than the spatial frequency content of the remnant magnetic field. Consequently, the external magnetic field data can be filtered out by removing the low frequency content of the magnetic field data [Connerney et al., 2005]. While this filtering is necessary, it can also remove deep trends in the internal magnetic field of Mars. Acquiring additional night side data helps to more efficiently remove the effects of the external magnetic field without removing true variations in the internal magnetic

field. Therefore, the Martian magnetic field maps made with two Martian years of data reveal many more features than the Martian magnetic field maps made with only 0.73 Martian years of data [Connerney et al., 2001; 2005].

In the modeling of the Martian remnant magnetic field, it was assumed that only magnetic minerals from Earth could be producing the remnant magnetic field on Mars. Also, the initial strength of the Martian dipole field was assumed to be equal to that of Earth's. However, Bode's law of magnetism states that the dipole magnetic field of every planet in the solar system is directly related to its angular momentum [Merrill et al., 1996]. Mars is known to have less angular momentum than Earth, therefore the Martian magnetic dipole field should be less. Furthermore, a stronger external magnetic field will create a larger remnant magnetization. Thus, the concentration of Martian magnetic minerals predicted by Dunlop and Arkani-Hamed [2005] needs to be adjusted upward to account for the smaller remnant magnetization on Mars.

### 3.2.3 Limitations of the Gamma Ray Suite of Instruments

Before the limitations of the gamma ray spectrometer, neutron spectrometer, and the high energy neutron detector can be discussed, an explanation of how these instruments work is necessary. This suite of instruments onboard the Mars Odyssey (MO) spacecraft are used to detect the concentration of hydrogen in the top meter of the Martian subsurface and the elemental concentration of the top few tens of centimeters of the Martian subsurface. The gamma ray spectrometer records the number of gamma rays versus energy from 0.2 – 10 MeV [Evans et al., 2002] to find the elemental composition of the top few tens of centimeters with a spatial resolution of 300 km [Boynton et al., 1992]. The elemental composition data, specifically Fe, Ti, and Cl, are needed to interpret data from the neutron spectrometer and the high energy neutron detector.

The neutron spectrometer is used to determine the amount of neutron leakage from the near surface of Mars in three different energy ranges: thermal (<0.4 eV),

epithermal (0.4 eV – 0.7 MeV), and fast (0.7 – 1.6 MeV) neutrons [Feldman et al., 2004]. The high energy neutron detector is similar to the neutron spectrometer in that it measures the amount of neutron leakage at energies of 0.4 – 1000 eV, 0.4 eV – 100 keV, and 10 eV – 1 MeV [Mitrofanov et al., 2002]. It can also measure high energy neutron flux versus energy at 16 logarithmic channels from 0.85 – 15 MeV [Mitrofanov et al., 2002]. Data from these instruments are then used to determine the concentration of hydrogen in the top meter of the subsurface with a spatial resolution of 600 km. As discussed in Section 3.1.2, this suite of instruments (gamma ray spectrometer, neutron spectrometer, and the high energy neutron detector) has detected significant quantities of hydrogen on Mars, even though the data are still preliminary [Boynton et al., 2002].

The MO passive suite of instruments is designed to measure the amount and energy of gamma rays and neutrons that leak from the Martian surface. When a radioactive element decays, it emits gamma rays with energies that are unique to that element [Boynton et al., 1992]. Some gamma rays and all thermal, epithermal, and fast neutrons are created when various elements of the Martian surface interact with galactic cosmic rays (protons and alpha particles) [Feldman et al., 2004]. As galactic cosmic rays interact with the subsurface of Mars, they create neutrons with energies from 0.1 – 20 MeV [Boynton et al., 1992]. The energies and number of neutrons are independent of the composition of the subsurface. However, the manner in which the neutrons are scattered and absorbed is highly dependent on the subsurface composition [Boynton et al., 1992]. The probability of a neutron scattering off a nucleus is not dependent upon its composition, but the resulting energy of the neutron is dependent upon its composition [Boynton et al., 1992]. This occurs because as the mass of the nucleus decreases, more energy can be transferred from the neutron to the nucleus by nucleus recoil [Boynton et al., 1992]. This energy loss, or moderation, is greatest in hydrogen since it is the lightest element and is responsible for the formation of thermal neutrons from epithermal and fast neutrons [Boynton et al., 1992]. Thermal neutrons can also be absorbed by nuclei such as hydrogen, iron, titanium, and chlorine [Feldman et al., 2004]. These absorptions lead to

an excited state that causes a gamma ray to be emitted as the nucleus returns to a deexcited state. The energy of the gamma ray is unique to the element [Mitrofanov et al., 2003].

A portion of the neutrons and gamma rays leaks out of the subsurface and is detected by the suite of instruments. Gamma rays and fast neutrons that originated from as deep as a few tens of centimeters can leak out, while epithermal and thermal neutrons can leak out from two to three times deeper, or approximately one meter [Boynton et al., 2002]. A concentration of hydrogen will produce a gamma ray emission with an energy of 2.223 MeV along with a reduction in fast and epithermal neutrons.

The gamma ray spectrometer is somewhat limited because quality gamma ray spectra cannot be gathered by a single pass over Mars. Instead, quality spectra must be generated by averaging multiple spectra taken over approximately the same Martian subsurface location. The amount of spectral stacking that is required depends upon the signal strength, which varies spatially and as a function of the element concentration. In the polar orbit of Mars Odyssey, there is a lower spectra data density near the equator in comparison to the poles. To account for this problem, the data are binned at larger spatial resolutions until the statistics of the spectra improve enough for meaningful interpretation. As more orbits are completed, the data can then be grouped into smaller and smaller bins. Currently, these bins average 5° latitude by 5° longitude [Taylor et al., 2006], whereas in 2003 they were 10° latitude by 10° longitude [Boynton et al., 2003].

Another limitation that affects the entire suite of instruments is CO<sub>2</sub> frost that covers the surface near the poles ( $\pm 50^\circ$ ) during the winter [Mitrofanov et al., 2004]. This CO<sub>2</sub> frost layer reduces the depth at which the neutrons and gamma rays can leak out [Feldman et al., 2003]. Therefore, seasonal effects must be taken into account near the poles.

The abundance of hydrogen in the top meter can be calculated from the neutron spectrometer and the high energy neutron detector data if the soil's elemental composition (specifically Fe, Ti, and Cl) is known [Prettyman et al., 2004].

Unfortunately, the results from the gamma ray spectrometer do not provide a high enough resolution. Even if the elemental composition could be determined from the gamma ray spectrometer, it would only be sensitive to the top few tens of centimeters, while the neutrons leak from as deep as a meter [Feldman et al., 2004]. Assumptions are necessary to deal with this depth discrepancy. Since the elemental composition from the gamma ray spectrometer is not available, the elemental composition of the dust layer measured at the Pathfinder landing site is used to interpret the epithermal and fast neutron data [Feldman et al., 2004]. The thermal neutron data can not be interpreted because slight variations in Fe, Ti, and Cl, which can also absorb thermal neutrons, can lead to large errors in the hydrogen concentration [Feldman et al., 2004]. The epithermal and fast neutrons can be interpreted because they are not as sensitive to slight variations in Fe, Ti, and Cl [Feldman et al., 2004]. While the dust layer has been found to be homogenous, the thickness of the dust layer is unknown. Spirit (MER-A) dug a trench about 30 centimeters deep (by spinning its wheels), in the soil near Husband Hill and found a very different composition than the global dust layer [Arvidson et al., 2006a]. Martian dust devils leave albedo streaks along their paths as they remove the bright thin homogenous dust layer and usually reveal a darker soil underneath [Edgett and Malin, 2000]. In addition, preliminary data from the gamma ray spectrometer also show variations in many element concentrations [Taylor et al., 2006, Boynton et al., 2003]. In conclusion, the assumption that the elemental composition of the top meter of soil is equal to the homogeneous dust layer is most likely violated in many places on Mars.

Another limitation of the neutron spectrometer and the high energy neutron detector is that the spatial resolution of the instruments is immense at 600 km (the area of Olympus Mons – the largest volcano in the solar system) [Feldman et al., 2004]. Therefore, spatial mixing of the observations must be accounted for [Prettyman et al., 2004]. If water did exist in a Martian “oasis”, the data from this localized water source would be severely reduced. This could lead to a false interpretation of low water content

over a large area instead of the true interpretation of large water content over a small area.

The assumption that hydrogen is in the form of water and not hydrated minerals is untested, and is one of the major goals of the 2007 Phoenix mission [Arvidson et al., 2006b]. While scientists [Mellon and Jakosky, 1993; Mellon et al., 1997; Jakosky et al., 2005] have proposed mechanisms to explain water in these hydrogen rich areas, observations from the MER missions have discovered hydrated minerals in hydrogen rich mid-latitude regions. In addition, Mars Express has detected hydrated sulfates (salts) in three regions of Mars: Valles Marineris, Sinus Meridiani, and near the northern polar cap [Bibring et al., 2005]. With the exception of Valles Marineris, these areas are mapped as hydrogen rich areas by the neutron spectrometer. It should be noted that the non-detection of hydrogen in Valles Marineris may be a result of the limited 600 km resolution.

The limitations and interpretations of the gamma ray spectrometer, neutron spectrometer, and the high energy neutron detector are summarized below:

- To date, the gamma ray spectrometer has not collected enough data, so spatial stacking is necessary to determine the elemental composition of Mars. Therefore, measurements used to determine the elemental composition of Mars have a much larger spatial resolution than 300 km (resolution of the gamma ray spectrometer).
- The elemental composition of the top meter of soil is necessary to interpret the hydrogen concentration by measuring the flux of thermal, epithermal, and fast neutrons. Since the gamma ray spectrometer data are not at a high enough resolution to accurately determine the elemental composition, the elemental composition of the homogenous dust layer is used to interpret the neutron spectrometer data [Feldman et al, 2004]. This assumption is most likely violated in many places on Mars. Since thermal neutrons are

very sensitive to the elemental composition of Fe, Ti, and Cl, they cannot be used to estimate the hydrogen concentration.

- The spatial resolution of the neutron data is immense at 600 km (the area of Olympus Mons) [Feldman et al., 2004]. Therefore, spatial mixing of the observations must be accounted for [Prettyman et al., 2004]. This could hide local sources that have a high concentration of hydrogen.
- The interpretation that most, if not all, of the hydrogen in the top meter of the subsurface is in the form of water has not been proven by landers. While mechanisms have been proposed to explain water in these hydrogen rich areas, observations from the MER missions and Mars Express have discovered hydrated minerals in the hydrogen rich mid-latitude regions. One of the goals of the 2007 Phoenix mission is to determine if the hydrogen concentrations near the Martian poles is indeed caused by water ice.

### 3.2.4 Limitations of the Mössbauer Spectroscopy

The MER Mössbauer spectroscopy instrument works by using a  $^{57}\text{Co}$  radioactive source to emit gamma rays with a precise energy of 14.4 keV [Wdowiak et al., 2003]. As the gamma rays are directed into a sample (rock or soil) over an area of  $1.5\text{ cm}^2$ , they are either absorbed into the sample or a resonance interaction occurs between the gamma ray and a  $^{57}\text{Fe}$  nucleus (an isotope of iron with a natural abundance of 2.14% on Earth) [Wdowiak et al., 2003]. This resonance interaction raises the  $^{57}\text{Fe}$  nucleus to an excited state for 98 ns when it then deexcites by emitting a gamma ray in any direction of exactly the same energy [Wdowiak et al., 2003]. The resonance interaction between the gamma ray and a  $^{57}\text{Fe}$  nucleus can change as a function of the  $^{57}\text{Fe}$  nucleus valence state, molecular structure due to the internal electric and magnetic fields produced by the crystal structure, and external magnetic fields [Wdowiak et al., 2003]. To account for

this change, the energy of the 14.4 keV gamma ray must be slightly increased or decreased [Wdowiak et al., 2003]. In order to produce this slight increase or decrease in energy, the  $^{57}\text{Co}$  source is moved ( $\pm 10$  mm/s) in relation to the sample so that Doppler shifting can produce a range of energies [Wdowiak et al., 2003].

In order for the Mössbauer instrument to acquire a detailed Mössbauer spectrum on Mars, the measurement time is 6 – 12 hours at the beginning of the mission [Klingelhöfer et al., 2003]. The 14.4 keV gamma ray source,  $^{57}\text{Co}$ , has a half-life of only 270 days [Wdowiak et al., 2003]. As the MERs approach 810 days (Spirit April 14th, 2006; Opportunity May 5th, 2006) on Mars, the initial 150 mCi source of  $^{57}\text{Co}$  [Klingelhöfer et al., 2003] will decay to 37.5 mCi, which in turn will require longer measurement times.

As discussed in Chapter 2, temperature, impurities, and grain size can all strongly affect the internal magnetic fields of a mineral. Therefore, Mössbauer spectroscopy is also dependent on temperature, impurities, and grain size. Daily temperature extremes on Mars are much greater than on Earth. Thus the temperature on Mars varies much more rapidly than on Earth. Since the temperature dependent spectra measurement times are so long and the temperature variations so rapid, the temperature is recorded as the measurements are made [Klingelhöfer et al., 2003].

Like infrared and visible spectroscopy, the Mössbauer spectrum can contain more than one iron mineralogy in its  $1.5\text{ cm}^2$  field of view. Therefore, an algorithm is used to find the Mössbauer parameters from the raw data [Wdowiak et al., 2003]. These Mössbauer parameters are characteristic of mineralogy and are only known for certain Earth minerals at specific grain sizes and specific temperatures [Wdowiak et al., 2003]. However, when a mixture of iron mineralogies is present it can be difficult to uniquely determine the mineralogy of the mixture [Dyar et al., 2006]. Mars may also possess iron minerals that do not exist on Earth. Furthermore, if the minerals measured on Mars are temperature dependent, their temperature dependent Mössbauer spectrum will be “blurred” over the temperature varying measurement. Although temperature is recorded

as the measurement is made, the spectrum cannot be fragmented into quality spectra as a function of temperature. Therefore, temperature dependent statistical models need to be determined to more accurately interpret the data. Unfortunately, temperature dependent laboratory studies are lacking [Dyar et al., 2006; Wdowiak et al., 2003].

Nearly all of the Mössbauer laboratory measurements on Earth are made with a transmission geometry, which utilizes a thin section of the sample and places the gamma ray source on one side of the sample and the detector on the other side. Transmission geometry is used in the lab because it greatly reduces the measurement time. On Mars, measurements are made with a backscatter geometry. This method places both the source and detector on the same side of the sample since creating thin sections is not practical. The problem with this method is that very few Mössbauer spectra have been acquired in the lab utilizing the backscatter geometry and those that have been acquired do not produce an inverse result of transmission geometry [Wdowiak et al., 2003]. Consequently, more backscatter spectroscopy must be completed as well as theoretical modeling to reduce uncertainty in the interpretation of Mössbauer spectroscopy data from Mars [Wdowiak et al., 2003].

In conclusion, the Mössbauer spectroscopy instrument was flown to Mars to identify iron mineralogies. Although the instrument has many limitations, it did identify the mineralogy of the grey hematite concretions and the magnetic dust layer. However, it is important to recall these limitations when a mineral is identified using only Mössbauer spectroscopy (i.e. jarosite and goethite).

### 3.2.5 Limitations of Alpha Proton X-ray Spectrometer

By using an alpha proton X-ray spectrometer onboard Mars Pathfinder and both MER and a similar X-ray fluorescence spectrometer on both Viking landers, the elemental compositions of the Martian homogeneous dust layer, soils, and rocks were estimated. Attempts to constrain the mineralogy of these targets by using normative

calculations have been made, but have not yielded any acceptable solutions [Bell et al., 2000]. Therefore, these findings were not discussed in Section 3.1.3.

### 3.2.6 Summary of the Limitations of the Methods Used to Map Mineralogy on Mars

In summary, any remote sensing method used to determine Martian mineralogy suffers from ambiguity. Even so, these measurements can be used to constrain the geologic, hydrologic, and even biologic events in Martian history. Assumptions based on the non-detection of certain minerals can only be made if the limitations allow for it. When discoveries are made, the limitations of these discoveries should be determined and then examined during future missions for validation. A good example is the discovery of grey hematite in Meridiani Planum by TES, which was then later confirmed by Opportunity (MER-B).

### 3.3 Sample Selection

The collective information gathered from Martian meteorites, orbiters, and landers was used to determine which minerals were used as Martian analogs for this research. In particular, the minerals present in the global homogenous magnetic dust layer were selected since any GPR survey would be required to see through this layer. Minerals that had been found on Mars, or were thought to be on Mars, were measured if they had the potential to possess high dielectric or magnetic losses. The study examined many magnetic iron rich minerals and hydrated iron minerals such as goethite and jarosite before they were even discovered on Mars.

A total of 57 Martian analog soil samples were gathered from around the world for this study. These samples were selected based on their similarity to Martian dust and mineral properties including visible and infrared spectra, saturation magnetization, X-ray diffraction (XRD), chemical composition, and mineralogy. Johnson Space Center

distributes Mars JSC-1, Martian soil simulant mined from Pu'u Nene cinder cone, Hawaii [Allen et al., 1997]. JSC-1 was selected as the best Martian analog on Earth due to its similar spectral and magnetic properties to Martian soil [Allen et al., 1997, 1998, 1998b, 1999]. However, JSC-1 is not a perfect Martian analog because it lacks hematite, contains particles that are nonmagnetic, and contains too much magnetite [Hargraves et al., 1999]. Consequently, other Martian analog samples were gathered for this study. Natural magnetic soils were collected from Hawaii. Samples of hematite, grey hematite, maghemite, magnetite, jarosite, and olivine were gathered from Michigan, Utah, Colorado, Russia, and Peru. All measured samples were characterized by XRD. A detailed sample list can be found in Appendix A and XRD results are provided in Appendix B.

#### 3.4 Sample Preparation

A number of samples could not be collected in a soil form. In these cases, rock specimens were crushed into a soil using a nonmetallic mortar and pestle. Each sample was then vacuum dried before it was measured. Vacuum drying is necessary for two reasons: soils on the surface of Mars are extremely dry [Head et al., 2003] and the presence of water can significantly change the dielectric frequency dependence and the DC conductivity of the sample [Olhoeft, 1985].

## CHAPTER 4

### EXPERIMENTAL SETUP AND PROCEDURES

#### 4.1. Measurement Apparatus, Environment, and Procedure

Network analyzers have been used to acquire high frequency electromagnetic (EM) measurements since the 1960's. For this study, an HP 8753D vector network analyzer (VNA) was used and controlled by a computer with custom software (see DVD). Two phase matched cables were attached to two ports on the VNA. The cables are both 0.61 m long, have an impedance of  $50\Omega$ , and have a 7 mm diameter connector (APC-7). Each cable was attached to a 7 mm/14 mm adapter that has a 7 mm diameter connector (APC-7) (on one end and a 14 mm diameter connector (GR-900) on the other end. The 14 mm adapter connectors were then attached to either end of a 14 mm diameter coaxial waveguide, which served as the sample holder. The coaxial waveguide sample holder contains two conductors; the outer conductor has an inner diameter of 14 mm, while the inner conductor has an outer diameter of 6.1 mm. The impedance of an empty coaxial waveguide sample holder is determined by the diameters of its two conductors. The sample holders used in this experiment possessed an impedance of  $50\Omega$  [Adams, 1969]. Three sample holder lengths of 3 cm, 5 cm, and 10 cm were utilized for this research. Once the sample holder is connected, a waveguide is created from VNA port 1 to VNA port 2. The 7 mm cables must be phase matched because the VNA measures minute phase changes. Therefore, the electrical length from VNA port 1 to the port 1 side of the sample holder must be exactly the same length as VNA port 2 to the port 2 side of the sample holder.

To acquire measurements as a function of temperature, the sample holder was placed in an insulated So-Low Ultra-Low freezer (model #C85-5). The temperature was varied from 180 – 300 K with VNA measurements made at intervals of 5 – 20 K.

Computer fans were used to provide circulation, which maintained a uniform temperature inside the freezer. The lowest measurement temperature was obtained by increasing the amount of insulation inside the freezer, using an air-conditioner to maintain a cool room temperature outside the freezer, and turning off all circulating fans in the freezer to minimize heat contribution. Three YSI 44006 epoxy-encapsulated thermistors were placed inside the freezer: one at the bottom of the freezer, one on the outside of the sample holder, and one inside a duplicate sample holder that was packed with the same material and placed next to the actual test sample holder. A VNA measurement was taken once the temperature inside the duplicate sample holder remained within  $\pm 0.1$  K of the target temperature for approximately 15 minutes. Since the temperature inside the actual test sample holder could not be measured, the temperature of the measurement was determined by averaging the temperature measurements of the duplicate sample holder for 15 minutes prior to the measurement and for 4 minutes during the measurement. The measurement apparatus described above is depicted in Figure 4.1.

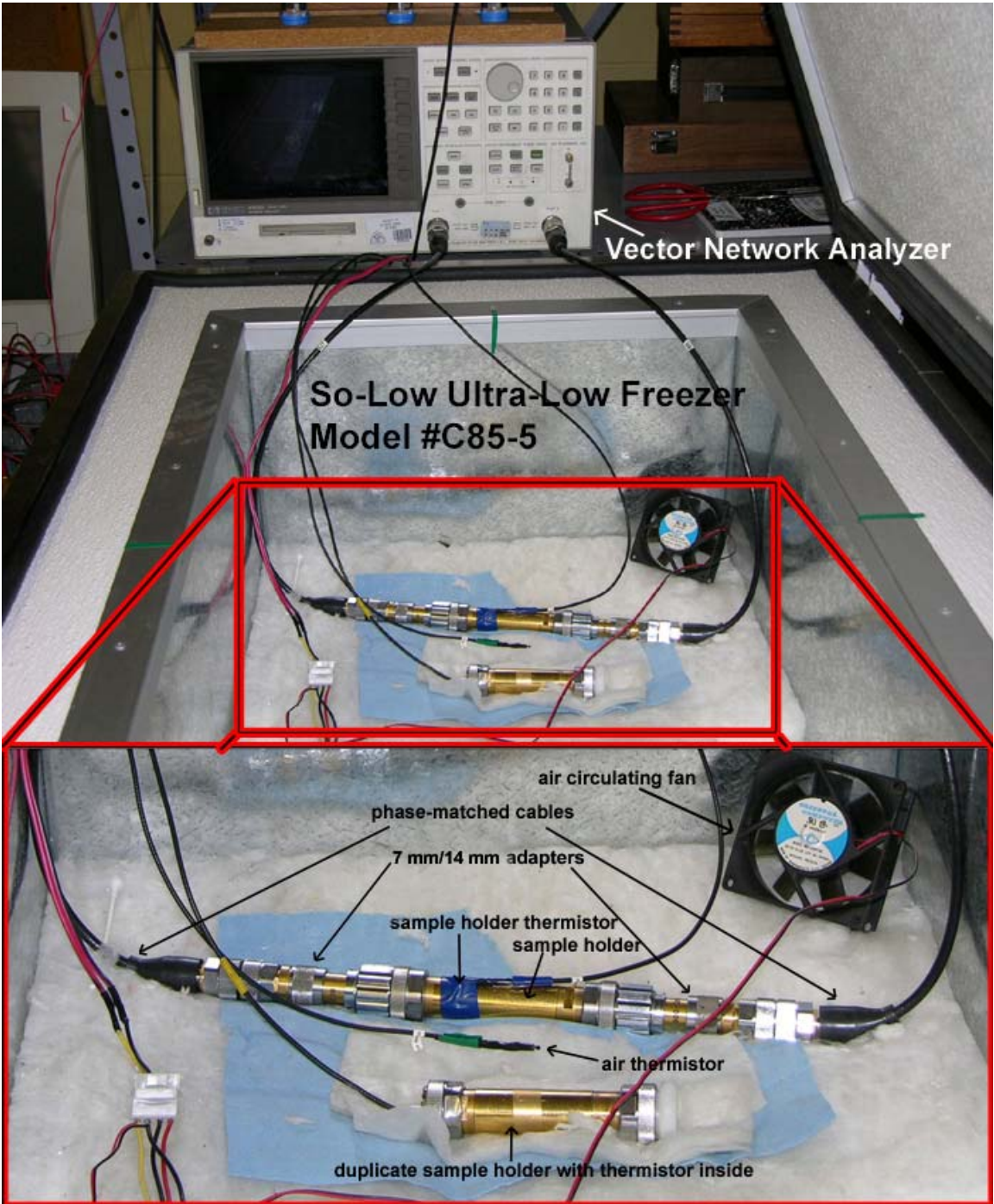


Figure 4.1. Experimental apparatus used to measure the EM properties of Martian analogs versus temperature and frequency.

#### 4.2. VNA Calibration

Prior to measuring a sample, the VNA and associated cable connections had to be calibrated. The phase matched cables along with the 7 mm/14 mm adapters act to extend the VNA ports to the sample holder. In order to solve for the complex dielectric permittivity and complex magnetic permeability, the electrical length from the sample holder to the VNA port must be known. The 12 term two port calibration, which is described below, was used to determine the electrical length, dynamic range of the system, and crosstalk or leakage between the ports. This calibration was performed each time a new sample was measured. The calibration was found to be stable for at least a week if the cable was not moved, and the room temperature remained constant ( $\pm 1$  K).

The four connection points (two 7 mm phase matched cables to the 7 mm/14 mm adapters, and two 7 mm/14 mm adapters to the sample holder) were all tested using an open, short, and load as test standards. The open has infinite impedance, the short has an impedance of zero, and the load has the same impedance as the cables. Therefore, the impedance of the test reflectors should yield a reflection coefficient of one for the open, negative one for the short, and zero for the load. The open and short were used to find the range of the system because they represent the largest positive and negative amplitudes, respectively. The load was used to find the lowest measurable amplitude. Together these tests (open, short, and load) yield the dynamic range of the system. The open and short were also used to determine the electrical length from the VNA port to the sample holder.

One load-load calibration test was performed to calibrate the crosstalk or leakage between the VNA ports. In this calibration, both 7 mm loads are connected to the two cables at the same time. The VNA puts energy into port 1 and measures the response in port 2, and vice versa. There should be no energy received in the measuring port because this port is not physically connected to the port where the energy is being input. If any energy is received in the measuring port, it is due to crosstalk or leakage of the other port.

Two through calibration tests were performed to determine the electrical length from VNA port 1 to VNA port 2. The first through calibration is performed by connecting the two phase matched cables to each other. The second through calibration is performed by connecting all of the measurement components together, as shown in Figure 4.1. The impedance contrast of both through measurements should be zero, yielding a reflection coefficient of zero. Likewise, the transmission coefficient should equal one if there are no impedance contrasts and no attenuation losses along the path. Impedance contrast can result from loose connections or scattering due to scratches on the sample holder. Attenuation losses are the result of the very low resistivity of the cables, adapters, and sample holder.

#### 4.3 Theory for Measuring EM Properties in a Coaxial Waveguide

When a sample is placed inside the coaxial waveguide sample holder, the complex impedance of the sample holder changes as a function of the sample's complex relative dielectric permittivity, DC conductivity, and complex relative magnetic permeability [Adams, 1969; Nicolson and Ross, 1970; Weir, 1974; Baker-Jarvis et al., 1993]. To measure the EM properties of the sample, the VNA transmits a voltage wave down the inner conductor of the coaxial waveguide. Since the outer conductor is grounded, the voltage wave creates a changing electric field, which in turn produces a changing magnetic field. This process is depicted in Figure 4.2.

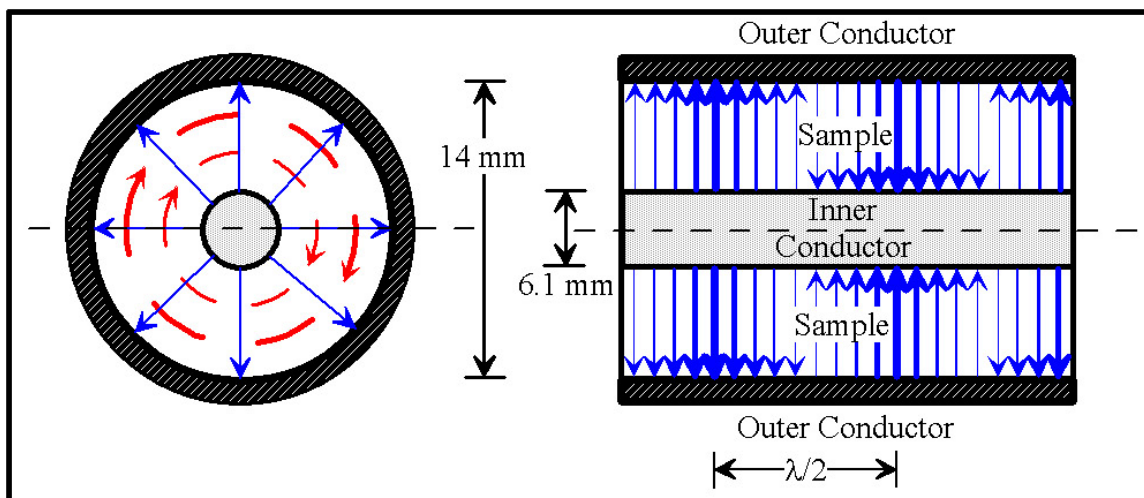


Figure 4.2. Electric (blue) and magnetic (red) field distribution for the TEM in a 14 mm coaxial waveguide, or sample holder. The electric field is created by the difference in voltage between the inner conductor and outer conductor (always grounded). Since the voltage difference changes as a function of time, so too does the electric field. Consequently, a magnetic field is produced perpendicular to the changing electric field. The diagram on the left shows the cross section of the sample holder and depicts the direction of the electric and magnetic fields when the voltage wave is at its maximum value. At its minimum value, the direction of the electric and magnetic fields would be reversed. The diagram on the right shows the lengthwise cross-section of the sample holder and depicts the direction of the electric field as the voltage wave propagates through the sample holder. The magnitude and direction of the electric field is displayed by the thickness and direction of the arrow. The magnetic field is not shown because it is going into and out of the page. Figure modified from Adams [1969].

The electric and magnetic fields travel in a transverse electromagnetic mode (TEM). Higher order modes such as transverse electric mode (TE) and transverse magnetic mode (TM) can occur at higher frequencies. The wavelength where TEM mode waves convert into TE and TM is known as the cutoff wavelength,  $\lambda_c$ , and is given by Equation 4.1, assuming low loss materials [Adams, 1969]. If the relative dielectric permittivity and relative magnetic permeability are equal to one, then the cutoff frequency,  $f_c$ , occurs at 24.2 GHz and does not decrease into the VNA frequency range

until the product of the relative dielectric permittivity and relative magnetic permeability is greater than 65. Even when the TE and TM modes occur at the high frequency range of the VNA, sample holder resonance occurs at much lower frequencies. The first resonant frequency of the sample holder establishes the high frequency limit of the usable data. Therefore, any affects from TE and TM waves can be ignored. At the connection points between the sample holder and the 7 mm/14 mm adapters, the TEM wave encounters a boundary in complex impedance which is determined by Equation 4.2 [Adams, 1969].

$$\lambda_c = \pi(r_o - r_i) \sqrt{\epsilon_r \mu_r} \quad (4.1)$$

$$Z = 138 \sqrt{\frac{\mu_r^*}{\epsilon_r^*}} \log \frac{r_o}{r_i} \quad (4.2)$$

where:  $\lambda_c$  = cutoff wavelength

$r_o$  = inner radius of the outer conductor of the sample holder (0.00700 m)

$r_i$  = outer radius of the inner conductor of the sample holder (0.00305 m)

$Z$  = complex impedance of the sample

If relative complex dielectric permittivity and relative complex magnetic permeability are equal to one, then the complex impedance of the sample holder is the same as the impedance of the adapters (50Ω). In this case, an impedance boundary will not be encountered at the interface of the adapter and the sample holder. If the complex dielectric permittivity and complex magnetic permeability are not equal to one and are complex, then the reflection and transmission coefficients of the impedance boundary are complex, as shown in Equations 4.3 and 4.4. The amplitude and phase of the transmitted and reflected TEM waves will be a function of the EM properties of the sample.

$$\Gamma = \frac{Z - Z_o}{Z + Z_o} = \frac{\sqrt{\mu^* / \epsilon^*} - 1}{\sqrt{\mu^* / \epsilon^*} + 1} \quad (4.3)$$

$$z = e^{-i\omega L \sqrt{\mu^* \epsilon^*} / c} \quad (4.4)$$

where:  $\Gamma$  = reflection coefficient (energy reflected from the adaptor/sample holder boundary)

$Z_0$  = impedance of the cable and adaptor ( $50\Omega$ )

$z$  = transmission coefficient (energy transmitted from the cable to the sample holder)

$L$  = length of the sample holder (m)

$\omega$  = angular frequency (rad/s)

$c$  = speed of light in vacuum ( $2.99792458 \times 10^8$  m/s)

To determine the EM properties of the sample, the VNA measures the input and output energy from both ports and then determines the real and imaginary parts of the four scattering parameters, or S parameters, versus frequency. The first subscript of the S parameter describes the port where the signal was measured, while the second subscript describes the port where the signal originated [Adams, 1969].  $S_{11}$  and  $S_{22}$ , are duplicate measurements, as are  $S_{12}$  and  $S_{21}$ , and thus used for quality control. If these S parameter pairs are different, there is either a loose connection or the sample was packed so that it is electromagnetically heterogeneous. Figure 4.3(a) and Equations 4.5 and 4.6 demonstrate how the VNA computes the S parameters.

$$b_1 = S_{12}a_2 + S_{11}a_1 \quad (4.5)$$

$$b_2 = S_{21}a_1 + S_{22}a_2 \quad (4.6)$$

where:  $S_{11}$  = S parameter from VNA port 1 to VNA port 1

$S_{22}$  = S parameter from VNA port 2 to VNA port 2

$S_{12}$  = S parameter from VNA port 2 to VNA port 1

$S_{21}$  = S parameter from VNA port 1 to VNA port 2

$a_1$  = output energy from VNA port 1

$a_2$  = output energy from VNA port 2

$b_1$  = input energy from VNA port 1

$b_2$  = input energy from VNA port 2

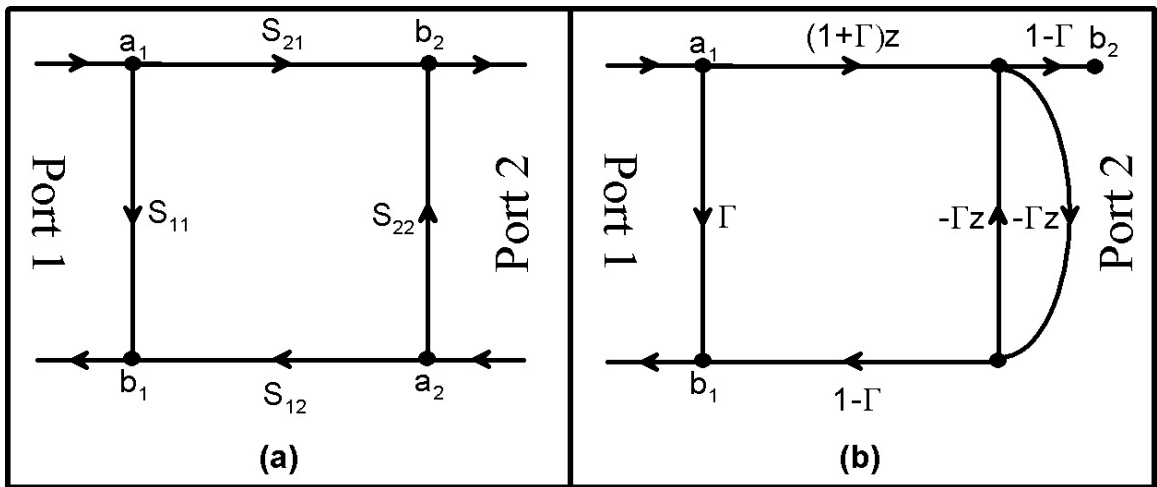


Figure 4.3. Signal flow charts of the VNA. Box (a) shows the signal flow chart used to find the S parameters [Adams, 1969]. Box (b) shows the signal flow chart used to find the S parameters as a function of the reflection ( $\Gamma$ ) and transmission ( $z$ ) coefficients [Nicolson and Ross, 1979].

Once the VNA outputs the S parameters to the computer, the software then computes the complex dielectric permittivity and complex magnetic permeability using Equations 4.7-4.15. Before any calculations can be made, the phase of the  $S_{21}$  and  $S_{12}$  parameters must be corrected. The S parameters are output by the VNA assuming a sample holder length of 0 cm. The phase differences caused by the finite sample holder length are corrected for using Equation 4.7.

$$S_{21}^{\text{cor}} = S_{21} e^{-i \frac{\omega L}{c}} \quad (4.7)$$

Figure 4.3(b) and Equations 4.8 and 4.9 describe the S parameters as a function of the reflection and transmission coefficients [Nicolson and Ross, 1979, Agilent, 2000].

where:  $S_{21}^{\text{cor}}$  = corrected S parameter from port 1 to port 2

$$S_{11} = \frac{b_1}{a_1} = \frac{\Gamma(1-z^2)}{1-\Gamma^2 z^2} \quad (4.8)$$

$$S_{21}^{\text{cor}} = \frac{b_2}{a_1} = \frac{z(1-\Gamma^2)}{1-\Gamma^2 z^2} \quad (4.9)$$

Equations 4.8 and 4.9 can be rearranged to produce Equations 4.10 and 4.11, which describe the reflection and transmission coefficients in terms of the S parameters. Equations 4.2 and 4.3 can be rearranged to produce Equations 4.12 and 4.13. The complex relative magnetic permeability (Equation 4.14) and the complex relative dielectric permittivity (Equation 4.15) can then be found. Overall, the software outputs two data sets (from measuring the sample holder in both directions), each including the real part of the relative dielectric permittivity, the electrical loss tangent, the real part of the complex relative magnetic permeability, and the magnetic loss tangent versus frequency (30 kHz – 3 GHz).

$$\Gamma = \frac{S_{11}^2 - S_{21}^{\text{cor}2} + 1}{2S_{21}^{\text{cor}}} \pm \sqrt{\left(\frac{S_{11}^2 - S_{21}^{\text{cor}2} + 1}{2S_{21}^{\text{cor}}}\right)^2 - 1} \quad (4.10)$$

$$z = \frac{S_{21}^{\text{cor}} + S_{11} - \Gamma}{1 - (S_{21}^{\text{cor}} + S_{11})\Gamma} \quad (4.11)$$

$$\frac{\mu_r^*}{\varepsilon_r^*} = \left(\frac{1+\Gamma}{1-\Gamma}\right)^2 = c_1 \quad (4.12)$$

$$\mu_r^* \varepsilon_r^* = -\left(\left(\frac{c}{\omega L}\right) \ln\left(\frac{1}{z}\right)\right)^2 = c_2 \quad (4.13)$$

$$\mu_r^* = \sqrt{c_1 c_2} \quad (4.14)$$

$$\varepsilon_r^* = \sqrt{\frac{c_2}{c_1}} \quad (4.15)$$

There is a problem with the solution shown above. In Equation 4.13, the natural log of the inverse of z is not unique and possesses an infinite number of roots [Baker-Jarvis et al., 1993]. This occurs because the imaginary part of the natural log answer equals the phase angle of the complex root. Since angles are not unique, the correct root

can be found by not allowing the angle to “wrap”, or only allowing it to vary from  $\pi$  to  $-\pi$  radians.

Another problem with the solution is that it is very sensitive to noise at sample holder resonance. Sample holder resonance occurs when the EM wave approaches half wavelength multiples of the sample holder length as shown in Equation 4.16. Resonant frequencies can be identified in the data at high frequencies where the real part of the relative dielectric permittivity, real part of the relative magnetic permeability, electrical loss tangent, and magnetic loss tangent all have a spike. Since the resonant frequency is a function of wavelength, it is dependent on the EM properties of the sample. Unfortunately, these resonant frequencies are a function of both complex magnetic permeability and complex dielectric permittivity, so assumptions must be made in order to solve for either parameter at resonant frequency. Resonant frequencies observed in the data for this study are actually stronger and broader than the modeled responses predict, though it is uncertain why.

$$f_r = \frac{\sqrt{2}c}{\frac{2L}{n} \sqrt{\sqrt{(\mu_r' \varepsilon_r' - \varepsilon_r'' \mu_r'')^2 + (\mu_r'' \varepsilon_r' + \mu_r' \varepsilon_r'')^2} + \varepsilon_r' \mu_r' - \varepsilon_r'' \mu_r''}} \quad (4.16)$$

where  $f_r$  = frequency of the  $n$ 's resonant frequency

$n$  = number of harmonic 1, 2, 3, ...

$\varepsilon_r'$  = real part of the relative dielectric permittivity

$\varepsilon_r''$  = imaginary part of the relative dielectric permittivity

$\mu_r'$  = real part of the relative magnetic permeability

$\mu_r''$  = imaginary part of the relative magnetic permeability

#### 4.4. Error and Accuracy Analysis

Although the experimental apparatus was calibrated, the measurements were still not perfect. The collected data were also affected by the finite precision of the VNA,

coherent and incoherent noise sources, and loose connections along the apparatus setup. Each of these issues will be discussed in the sections below.

#### 4.4.1. VNA Measurement Accuracy

One of the most significant limitations of the experiment apparatus was the finite precision of the VNA. This was primarily caused by the  $0.01^\circ$  phase accuracy of the HP8753D [Hewlett-Packard, 1994]. When the wavelength of the EM energy is significantly greater than the length of the sample holder, only minute changes ( $<0.01^\circ$ ) in phase are observed. Consequently, the VNA cannot accurately measure the EM properties of a sample at low frequencies. (For the Martian analog samples measured in this thesis with a 10 cm sample holder, this typically occurred near 1 MHz.) The precision of the phase accuracy and amplitude accuracy can also be expressed as the precision of the S parameters, which were found after calibrating with a stack of 16. The manufacturer listed precision for the  $S_{11}$  and  $S_{22}$  parameters is  $\pm 0.001$  dB at frequencies less than 1.3 GHz and  $\pm 0.005$  dB at frequencies greater than 1.3 GHz. Likewise, the manufacturer listed precision for the  $S_{21}$  and  $S_{12}$  parameters is  $\pm 0.008$  dB at less than 1.3 GHz and  $\pm 0.009$  dB at greater than 1.3 GHz [Hewlett-Packard, 1994].

To display the effect of precision on the measurements, a data envelope and measurable lower loss limit were modeled for each VNA measurement shown in this thesis. The data envelope defines the boundaries where all of the data should reside unless sources of noise are present. The maximum part of the measurable lower loss limit represents the noise floor of the system, thus only data above the measurable lower loss limit were used for modeling. In this thesis, the data envelope will always be shown in a diagonally crosshatched pattern on graphs displaying the real part of the relative dielectric permittivity and magnetic permeability and on loss tangent graphs that possess

loss tangents that are above the measurable lower loss limit. Likewise, the measurable lower loss limit will be plotted on each loss tangent graph in a crosshatched pattern.

The data envelope was created by finding the electric and magnetic Cole-Cole models. The Cole-Cole models were transformed into S parameters. The VNA precision was added and subtracted to each of the S parameters for a total of 16 combinations. The revised S parameters were then transformed into the real part of the relative dielectric permittivity, electrical loss tangent, real part of the relative magnetic permeability, and magnetic loss tangent. The maximum and minimum S parameter values for each of the 16 combinations at each frequency were then used to produce the data envelope.

The measurable lower loss limit was determined using a similar process as the data envelope. First, the electric and magnetic Cole-Cole models were found. Then the Cole-Cole models were transformed into S parameters assuming that the electrical and magnetic loss tangents equaled zero. Next, the maximum VNA precision was added and subtracted to each of the simulated S parameters for a total of 16 different combinations. The S parameter combinations were then transformed into electrical and magnetic loss tangents. The measurable lower loss limit is defined as the maximum loss tangent for each of the 16 combinations at each frequency. The electrical and magnetic loss tangents also possessed some error due to EM energy scattering off the minute imperfections of the sample holder's inner conductor and also due to resonance. This is shown in the data in Figure 4.4 where the slope of the loss tangent increases before reaching the first resonant frequency at 1.5 GHz. The error was due to scattering because the slope of the loss tangent is proportional to the fourth power of the frequency. (Scattering is the only mechanism that could produce such a positive slope.) To account for this error, scattering was added to both the electric and magnetic measurable lower loss limit to ensure that any temperature independent high frequency loss tangent curves were considered noise.

In Figure 4.4, the manufacturer listed VNA precision was used to generate a predicted data envelope and a measurable lower loss limit for a set of real data for an

empty (air-filled) 10 cm sample holder measured at room temperature at a stack of eight. Since the real data do not approach the boundaries of the predicted data envelope and the measurable lower loss limit, the actual noise in the measurement was less than the predicted noise given by the manufacturer, Hewlett-Packard [1994]. The actual measurement precision was found by adjusting the data envelope and measurable lower loss limit to better match the variations observed in the data set. This led to a factor of four increase in the actual precision. Consequently, the precision of the  $S_{11}$  and  $S_{22}$  parameters varied by  $\pm 0.00025$  dB at less than 1.3 GHz and  $\pm 0.00125$  dB at greater than 1.3 GHz. The precision of the  $S_{21}$  and  $S_{12}$  parameters varied by  $\pm 0.002$  dB at less than 1.3 GHz and  $\pm 0.00225$  dB at greater than 1.3 GHz. These precisions were used to generate the data envelopes used in this thesis. Furthermore, the loss tangent graphs in Figure 4.4 should have equaled zero because air contains no losses. However, the data did contain electrical and magnetic loss tangents. Since the data were confined to the measurable lower loss limit, the nonzero loss tangent data were due solely to the limited accuracy of the experimental apparatus. The limited VNA accuracy also restricted the lower limit of the DC conductivity ( $6.67 \times 10^{-5}$  mho/m) or DC resistivity (15 k $\Omega$ m) as shown in Figure 4.5.

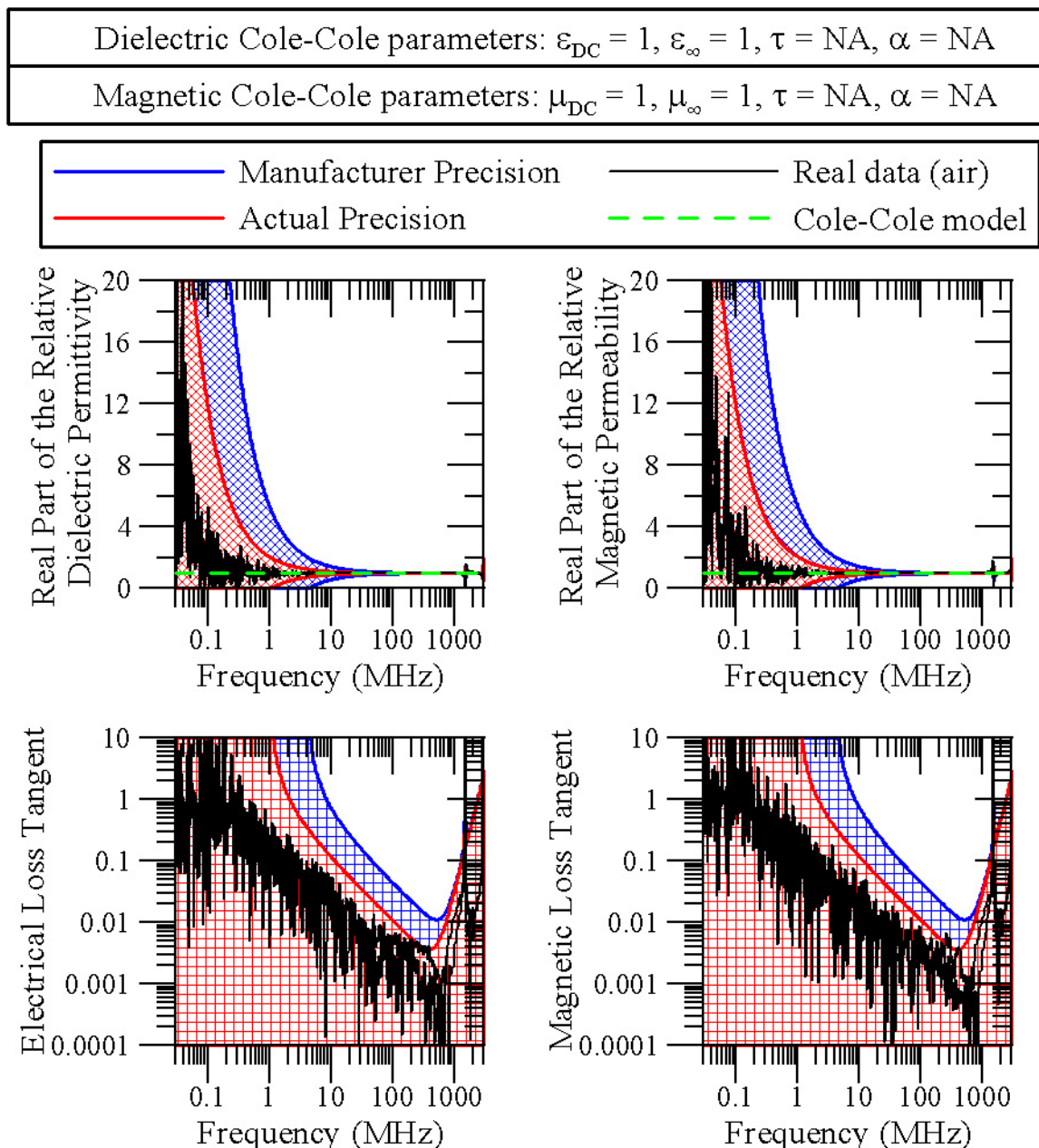


Figure 4.4. This figure shows real data from an empty 10 cm sample holder measured at room temperature at a stack of eight, along with the data envelopes and the measurable lower loss limits. The blue envelopes assume the manufacturer listed precision while the red envelopes depict the actual precision. In this figure and thesis, the data envelopes are diagonally crosshatched and the noise envelopes are crosshatched.

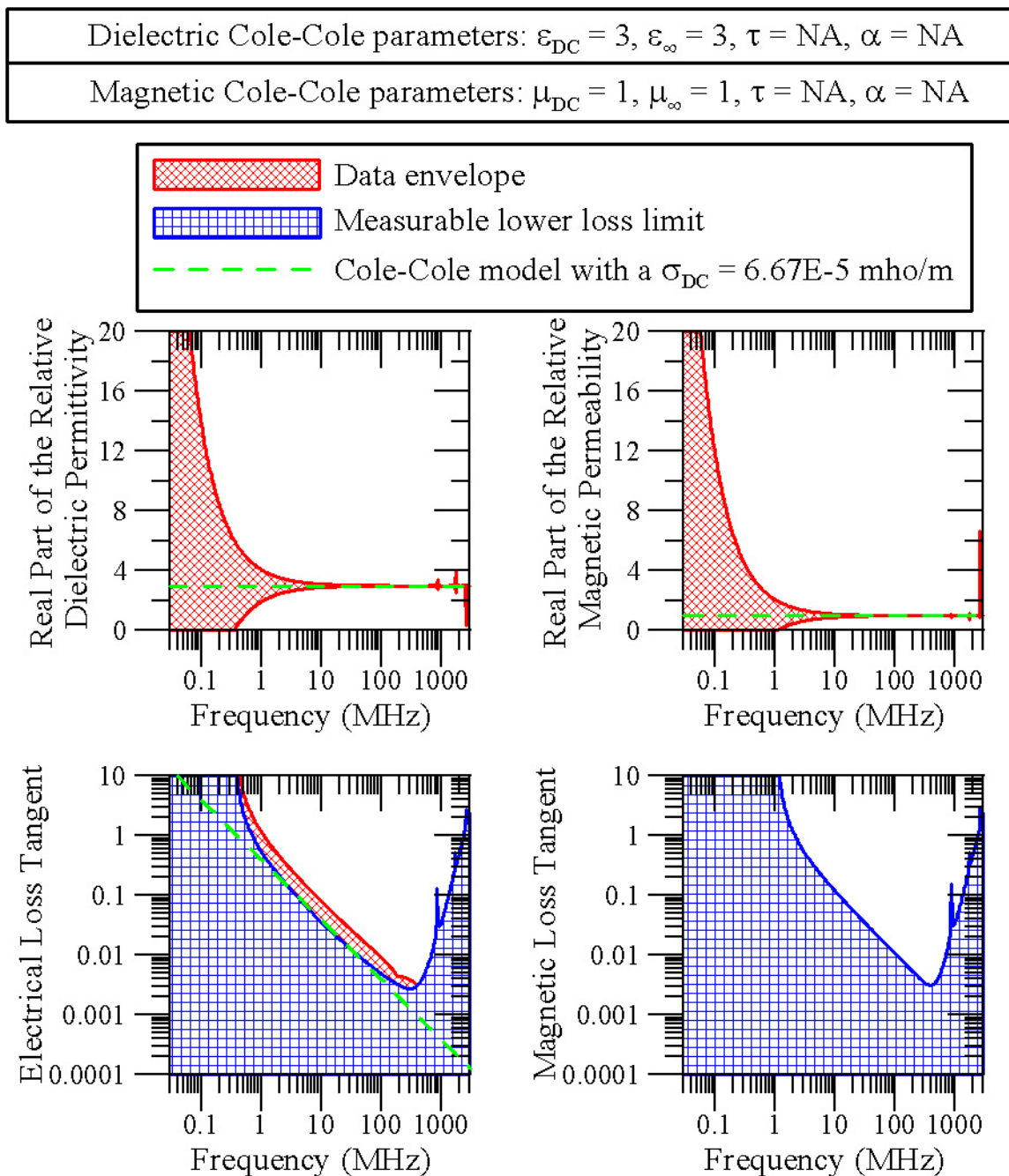


Figure 4.5. This figure shows the theoretical lower limit of DC conductivity ( $6.67 \times 10^{-5}$  mho/m) or DC resistivity (15 k $\Omega$ m) measured in a 10 cm sample holder assuming the actual VNA accuracy error.

Many VNA plots will be shown in this thesis. Each plot contains four graphs. The top left graph displays the real part of the relative dielectric permittivity versus frequency, where the ordinate is linear and the abscissa is logarithmic. The bottom left graph displays the electrical loss tangent versus frequency where both the ordinate and abscissa are logarithmic. The top right graph displays the real part of the relative magnetic permeability versus frequency, where the ordinate is linear and the abscissa is logarithmic. The bottom right graph displays the magnetic loss tangent where both the ordinate and abscissa are logarithmic. Each loss tangent graph has a measurable lower loss limit in a crosshatched pattern. All graphs have a data envelope in a diagonal crosshatched pattern for the electric and magnetic Cole-Cole model that best fit the data. The data envelope is only shown on the loss tangent graphs if it is greater than the measurable lower loss limit.

As the errors in precision decrease, the data envelope contracts to the correct value at lower frequencies and the measurable lower loss limit decreases (Figure 4.4). Figures 4.6, 4.7, and 4.8 show that the data envelope and the measurable lower loss limit change as a function of the real part of the relative dielectric permittivity and the real part of the relative magnetic permeability, frequency dependent complex dielectric permittivity and frequency dependent magnetic permeability, and sample holder length, respectively.

Increasing the real part of the relative dielectric permittivity and the real part of the relative magnetic permeability does not significantly change the data envelope, but it does shift the measurable lower loss limit lower as shown in Figure 4.6. The measurable lower loss limit is lowered because the electrical loss tangent is proportional to the inverse of the real part of the relative dielectric permittivity, while the magnetic loss tangent is proportional to the inverse of the real part of the relative magnetic permeability. The data envelope is relatively unchanged because at low frequencies, only

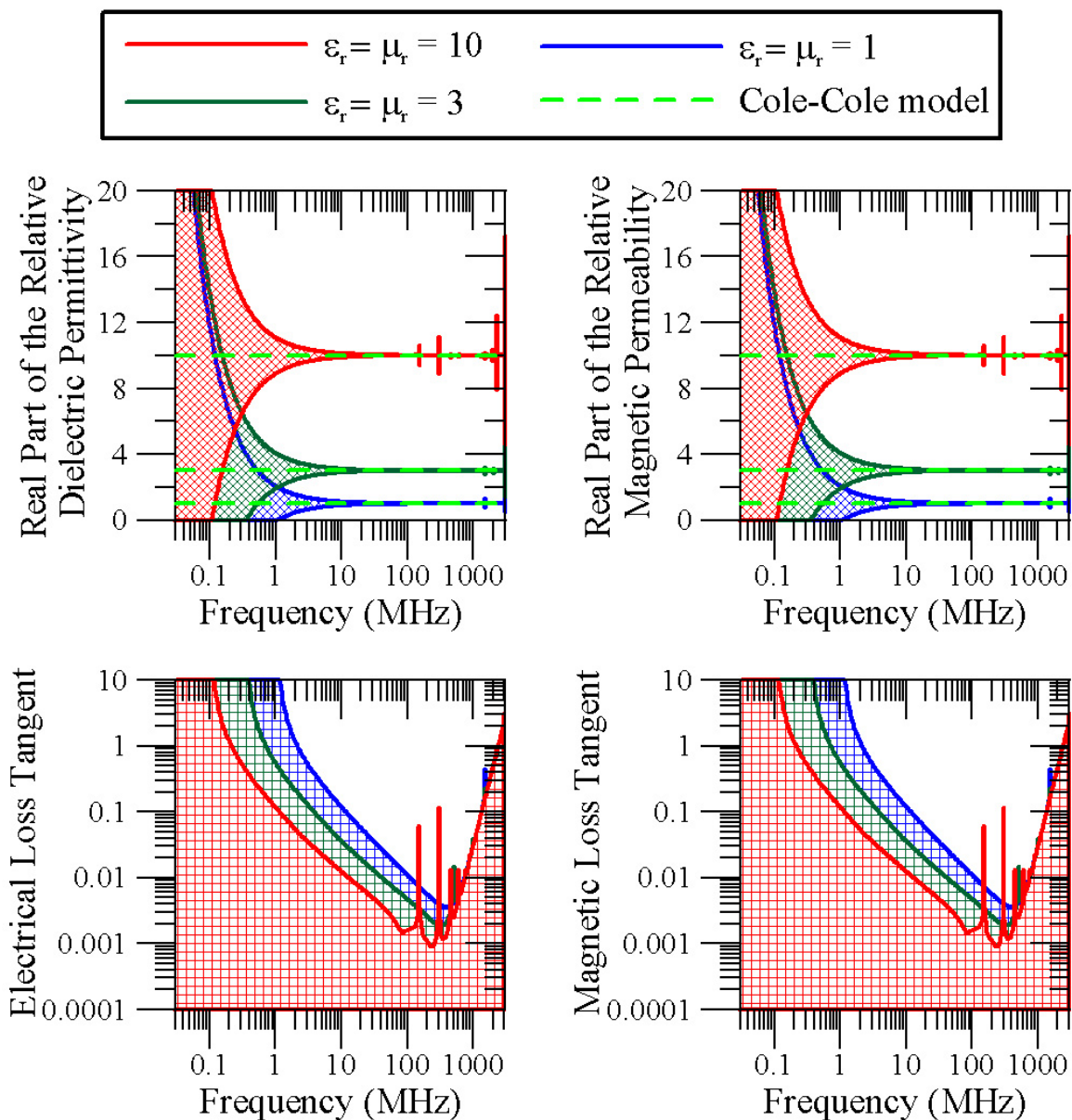


Figure 4.6. This figure shows how the data envelopes (diagonal crosshatched pattern in top graphs) and measurable lower loss limit (crosshatched pattern in bottom graphs) vary as a function of the frequency independent real part of the relative dielectric permittivity and frequency independent real part of the relative magnetic permeability. As relative dielectric permittivity and relative magnetic permeability increase, the data envelopes do not significantly change. However, the measurable lower loss limit decreases and the resonant frequencies decrease.

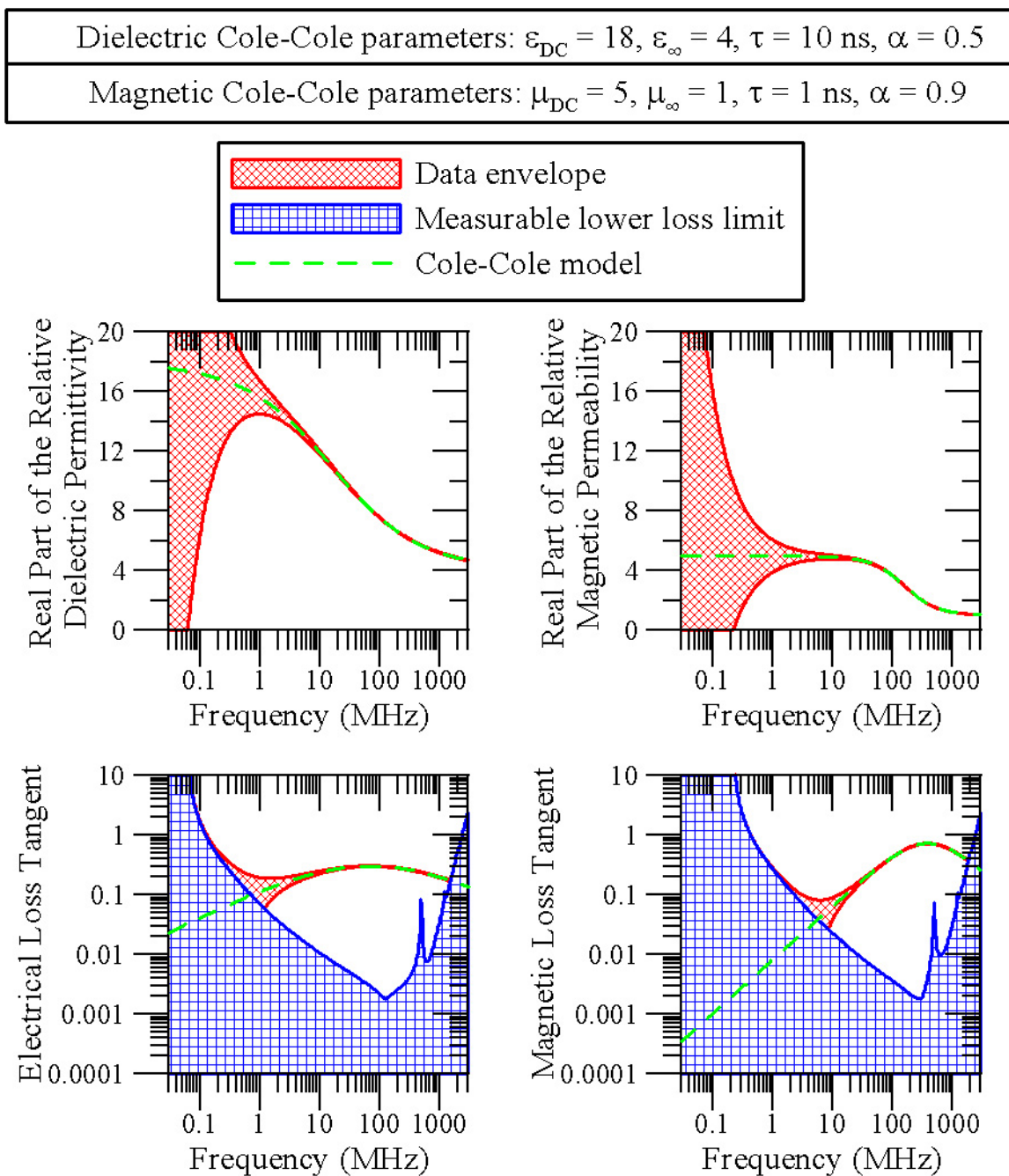


Figure 4.7. This figure shows the theoretical data envelopes for a material with frequency dependent dielectric permittivity and magnetic permeability measured in a 10 cm sample holder assuming the actual VNA accuracy error.

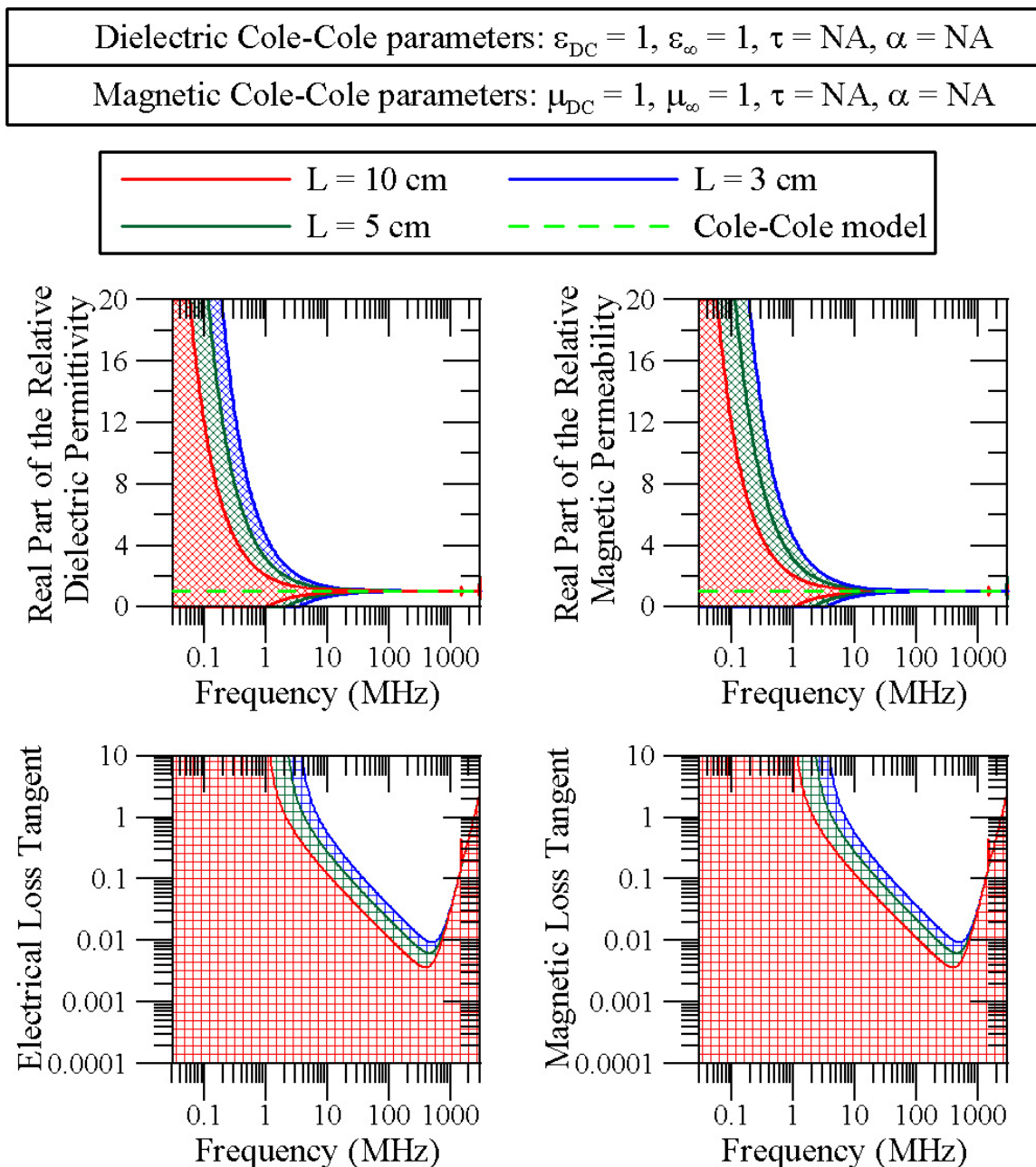


Figure 4.8. This figure shows the data envelopes (top graphs) and measurable lower loss limit (bottom graphs) as a function of sample holder lengths of 3, 5, and 10 cm assuming the measured precision.

the EM energy inside the sample holder has a smaller wavelength than the EM energy inside the cables. This difference in wavelength does not significantly enhance the data envelope. However, as the real part of the relative dielectric permittivity and the real part of the relative magnetic permeability increase, resonance occurs at lower frequencies.

If the sample possessed frequency dependence, then the loss tangent graphs contain both a data envelope and a measurable lower loss limit as shown in Figure 4.7. However, if the relaxation was too small or at a frequency where the measurable lower loss limit was large, the data envelope may have been hidden by the larger measurable lower loss limit.

As the sample holder length decreases, the data envelope and measurable lower loss limit become larger at each frequency as shown in Figure 4.8. This occurs because as the sample holder length decreases, the EM energy at each frequency travels through less of the sample. Therefore, the purpose for using the smallest sample holder (3 cm) is to increase the frequency at which the first resonant frequency occurs, so that the high frequency limit of the usable measurements is greater.

#### 4.4.2 Incoherent and Coherent Sources of Noise

Both incoherent and coherent sources of noise can exist that corrupt the data. The difference between these two types of noise is that incoherent noise decreases as more data are stacked while coherent noise increases as more data are stacked. Therefore, these two types of noise must be addressed separately.

To test for incoherent and coherent noise, VNA measurements were repeatedly made with a stack of one. These measurements were then combined with varying stacks and a standard deviation for each measured frequency was calculated and plotted in Figure 4.9. This figure shows that the various stacks essentially possess the same standard deviation versus frequency. The large increase in the 1024 stack may be due to drifting room temperature during the 19.3 hour measurement time. Since the standard deviation does not improve or degrade with the amount of stacking, the majority of the

error causing the standard deviation is most likely due to the limited accuracy of the VNA. Therefore, the incoherent noise levels of the measurements are extremely low. Only one form of coherent noise, sample holder resonance, was found to affect the measurements. This was discussed at the end of Section 4.3.

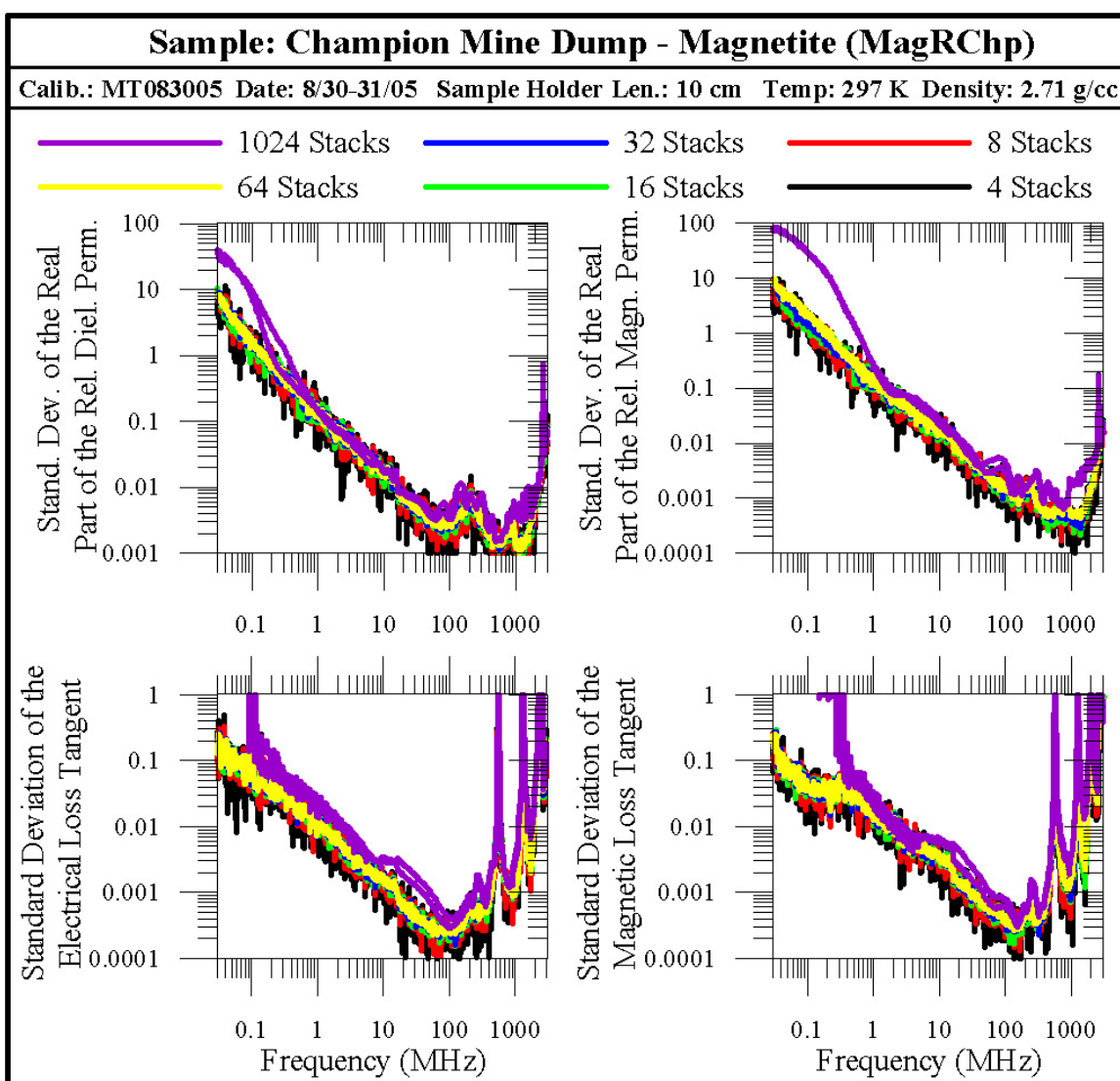


Figure 4.9. Standard deviation at each frequency versus number of external stacks.

#### 4.4.3. Improper Apparatus Setup

The last form of measurement error is due to improper apparatus setup. These types of errors typically obliterate data at all frequencies, although small apparatus errors can mimic real data. Common apparatus errors include loose connections between the cables, adapters, and sample holder, heterogeneous packing of the sample, and contaminating the inside of the inner conductor of the sample holder and/or any connectors with the sample. Loose connections between the cables, adapters, and sample holder will usually produce data that is all noise because it creates a large impedance contrast. However, if there is just a small connection problem, the  $S_{11}$  and  $S_{21}$  solution and the  $S_{22}$  and  $S_{12}$  solution will be offset at all frequencies. Heterogeneity in the packing of a sample holder can lead to internal scattering in the sample holder and/or different reflection coefficients,  $\Gamma$ , at both ends of the sample holder. This causes the  $S_{11}$  and  $S_{12}$  solution and the  $S_{22}$  and  $S_{21}$  solution to diverge at high frequencies as the internal impedance boundary causes more scattering.

The most difficult coherent noise source to identify is when the sample is inside or on the ends of the sample holder's inner conductor. This can lead to a false frequency and temperature dependent dielectric permittivity or magnetic permeability measurement. To ensure that temperature and frequency dependence is not produced by noise, the sample holder must be disconnected from the waveguide. The inner conductor and the 14 mm part of the 7 mm/14 mm adapter are then cleaned with the sample still packed inside. After cleaning, the sample holder is reattached to the waveguide and remeasured. If the temperature and frequency dependence has not changed, it is most likely being produced by the sample itself. Another way to prevent false frequency and temperature dependent measurements is to unpack the sample, clean the sample holder, repack the same sample, and remeasure. All temperature and frequency dependent relaxations reported in this thesis have been verified using both of these methods.

#### 4.5. Measurement, Accuracy, and Quality Control of Temperature

The circuit shown in Figure 4.10 was used to measure the resistance of the thermistors, while accounting for input impedance of the voltmeters and joule heating of the thermistors. Input impedance problems occur when the thermistor resistance approaches the internal resistance of the voltmeter. This causes the voltmeter to have an increased influence on the circuit as more current travels through the voltmeter instead of the circuit. The voltmeters used for this research were Fluke 77 Series II Multimeters, which were found to possess an input impedance of  $R_V = 11 \text{ M}\Omega$  when measuring to three decimal points. The resistance of the thermistors varied from  $8.2 \text{ k}\Omega$  near  $303 \text{ K}$  and  $10 \text{ M}\Omega$  near  $180 \text{ K}$  as shown in Figure 4.11.

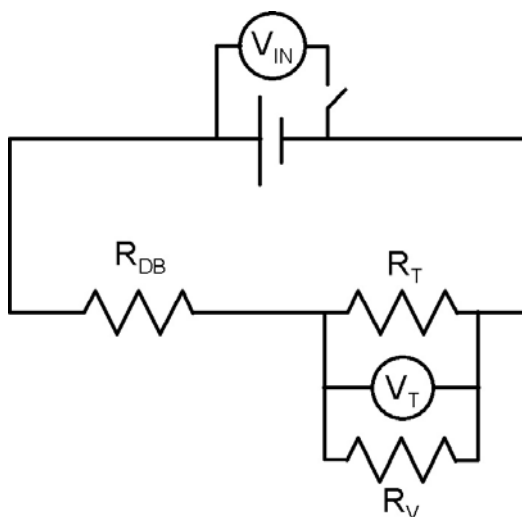


Figure 4.10. Circuit used to find the resistance of the thermistor where:  $V_{IN}$  is the measured total voltage,  $V_T$  is the measured voltage across the thermistor,  $R_{DB}$  is the known resistance of the decade resistor,  $R_T$  is the resistance of the thermistor, and  $R_V$  is the resistance of the voltmeter. Decade resistances and power source voltages into the circuit can be found on the DVD.

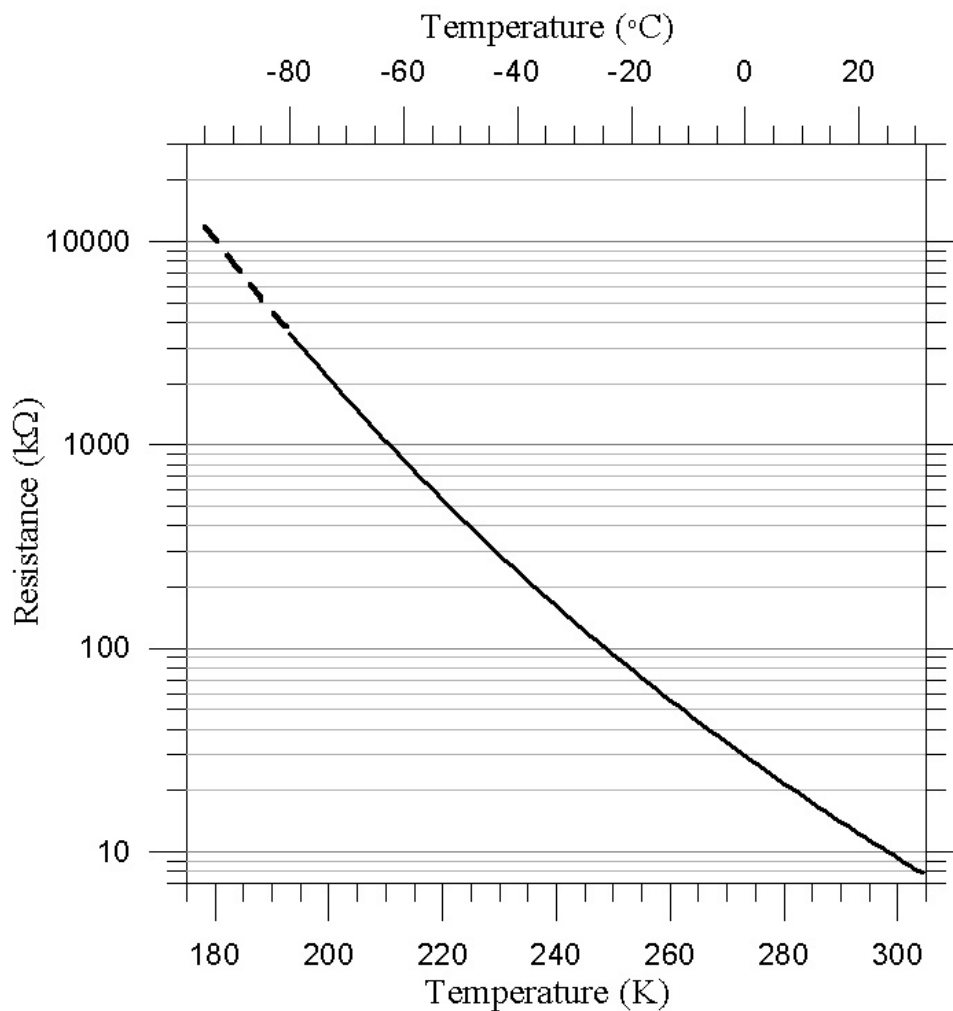


Figure 4.11. Resistance versus temperature for the YSI 44006 epoxy-encapsulated thermistors. The curve is accurate to 0.2 K. The dashed portion of the curve is extrapolated from the lower temperature resistances.

Since the thermistor resistance approaches the input impedance of the voltmeter, the input impedance of the voltmeter was compensated for when calculating the thermistor resistance,  $R_T$ . Another complication was that in order to determine the resistance of the thermistor, current must flow through it. This current flow then causes joule heating as the thermistor converts voltage to heat. The YSI 44006 epoxy-

encapsulated thermistors have a dissipation constant,  $D$ , of 0.001 W/K in still air [YSI, 2006]. In short, it takes 1 mW of power to increase the thermistor temperature by 1 K. Joule heating cannot be avoided, therefore the power was limited by decreasing the current so that the thermistor could only be heated by a maximum temperature of 0.2 K,  $\Delta T$ . The power of the joule heating,  $P$ , is found using Equation 4.17. The power can then be used in Equation 4.18 to find the maximum allowable current to maintain the temperature accuracy,  $\Delta T$ .

$$\Delta T = \frac{P}{D} \quad (4.17)$$

$$P = I^2 R_T \quad (4.18)$$

As shown in Figure 4.10, the total voltage put into the circuit,  $V_{IN}$ , and the voltage across the thermistor,  $V_T$ , was measured. The resistance of the QuadTech decade resistor (model #1433-26),  $R_{DB}$ , and the internal resistance of the voltmeter,  $R_V$ , were already known. (The decade resistor is a resistor in which any resistance from 10 – 9,999,990  $\Omega$  can be dialed in at intervals of 10  $\Omega$  and with an accuracy of 0.01%.) The thermistor resistance was found using Equation 4.19. The input impedance of the voltmeter that is measuring total voltage,  $V_{IN}$ , is not included because the total voltage does not vary with time or electrical load. To ensure the total voltage,  $V_{IN}$ , did not vary, the total voltage was measured at least twice during each EM property measurement at each temperature.

$$R_T = \frac{\frac{V_T}{V_{IN} - V_T} * R_{DB} * R_V}{R_V - \frac{V_T}{V_{IN} - V_T} * R_{DB}} \quad (4.19)$$

If the temperature is above 193 K, the thermistor resistance can be converted into temperature by interpolating manufacturer resistances versus Celsius temperatures using the spreadsheet ThermR.xls, which can be found on the attached DVD, or by downloading the manufactures spreadsheets R\_vs\_t.xls and ST&H\_EQ.xls at the YSI website. The temperature accuracy of the thermistors is  $\pm 0.2$  K down to 193 K.

However, the So-Low Ultra-Low freezer's lower temperature limit was found to be about 180 K at the bottom of the freezer. Consequently, at temperatures less than 193 K, thermistor resistances were extrapolated using the spreadsheet ThermR.xls, which can be found on the attached DVD.

The total accuracy of the thermistors versus temperature is shown in the last column of Table 4.1. The total accuracy is the sum of the maximum joule heating and the accuracy of the thermistors. The maximum joule heating was calculated using Equation 4.20 with the parameter values that were typically used to find the temperature of the thermistor (see DecadeR.xls on the attached DVD). The dissipation constant of still air, 0.001 W/K, was used. Even though fans were circulating the air inside the freezer, the thermistor that was used to find the actual temperature of the sample was inside the duplicate sample holder.

$$\Delta T = \frac{I_T^2 * R_T}{D} = \frac{\left( \frac{V_{IN}}{\frac{R_V R_T}{R_V + R_T} + R_{DB}} \right)^2 * R_T}{D} \quad (4.20)$$

---

Table 4.1. (next page) This table shows the typical error in temperature (total accuracy column) for the temperature range used in this research (178.15 K – 303.15 K or -95°C – 30°C). At temperatures above 260 K, the total voltage was varied to increase measurement accuracy. Below 260 K, the total voltage was held constant at 6.2 volts so that three decimal points could be read on the voltmeters. The thermistor accuracy decreases at temperatures greater than 193 K due to extrapolation errors. The upper limit of the total accuracy is found by adding joule heating to the upper limit of the thermistor accuracy. The lower limit of the total accuracy equals the lower limit of the thermistor accuracy because the value in the joule heating column is the maximum joule heating value. The table shows the typical error in temperature because the total voltage guidelines and decade resistor settings were not always followed. For the recommended voltage and decade resistor settings, see DecadeR.xls on the attached DVD. To see what values were actually used for each measurement, see the digital logbook which can be found on the attached DVD.

Temperature (K)	Joule Heating (K)	Therm. Accuracy (K)	Total Accuracy (K)
178.15	0.00	$\pm 0.25$	$\pm 0.25$
183.15	0.00	$\pm 0.23$	$\pm 0.23$
188.15	0.00	$\pm 0.21$	$\pm 0.21$
193.15	0.00	$\pm 0.20$	$\pm 0.20$
198.15	0.00	$\pm 0.20$	$\pm 0.20$
203.15	0.01	$\pm 0.20$	-0.20, +0.21
208.15	0.01	$\pm 0.20$	-0.20, +0.21
213.15	0.01	$\pm 0.20$	-0.20, +0.21
218.15	0.01	$\pm 0.20$	-0.20, +0.21
223.15	0.02	$\pm 0.20$	-0.20, +0.22
228.15	0.03	$\pm 0.20$	-0.20, +0.23
233.15	0.04	$\pm 0.20$	-0.20, +0.24
238.15	0.05	$\pm 0.20$	-0.20, +0.25
243.15	0.07	$\pm 0.20$	-0.20, +0.27
248.15	0.09	$\pm 0.20$	-0.20, +0.29
253.15	0.11	$\pm 0.20$	-0.20, +0.31
258.15	0.15	$\pm 0.20$	-0.20, +0.35
263.15	0.19	$\pm 0.20$	-0.20, +0.39
268.15	0.17	$\pm 0.20$	-0.20, +0.37
273.15	0.14	$\pm 0.20$	-0.20, +0.34
278.15	0.17	$\pm 0.20$	-0.20, +0.37
283.15	0.12	$\pm 0.20$	-0.20, +0.32
288.15	0.15	$\pm 0.20$	-0.20, +0.35
293.15	0.18	$\pm 0.20$	-0.20, +0.38
298.15	0.10	$\pm 0.20$	-0.20, +0.30
303.15	0.12	$\pm 0.20$	-0.20, +0.32

In order to test the suitability of conducting measurements inside the freezer, a quality control experiment was conducted using an air sample (empty sample holder). The results of the quality control test confirmed that accurate data could be acquired inside the freezer at the temperatures used in this study. (See Figure 4.12.) During the quality control test, a VNA measurement was made every 10 K from 298 K to 193 K. Air possesses a frequency independent dielectric permittivity and magnetic permeability equal to one and no measurable electric or magnetic loss tangent. A slight change (20%) was seen in the real part of the relative dielectric permittivity and magnetic permeability in the quality control test. This change was due to thermal contraction of the cables caused by the temperature decrease, and was not corrected for because it was easily recognizable. The cable thermal contraction causes errors in the measurements because the electrical lengths of the cables change as a function of temperature. Since each cable has a different length inside the freezer, one cable will most likely contract more than the other. Thus, the cables will have different electrical lengths as temperature decreases. Smaller sample holder lengths are much more affected by the thermal contraction of the cables than larger sample holder lengths because the change in the length of the cables is a larger percentage of the total waveguide length. Therefore, it strongly affects the measurement of phase. A 3 cm sample holder yields a maximum error of 80%; a 10 cm sample holder's maximum error is 20%.

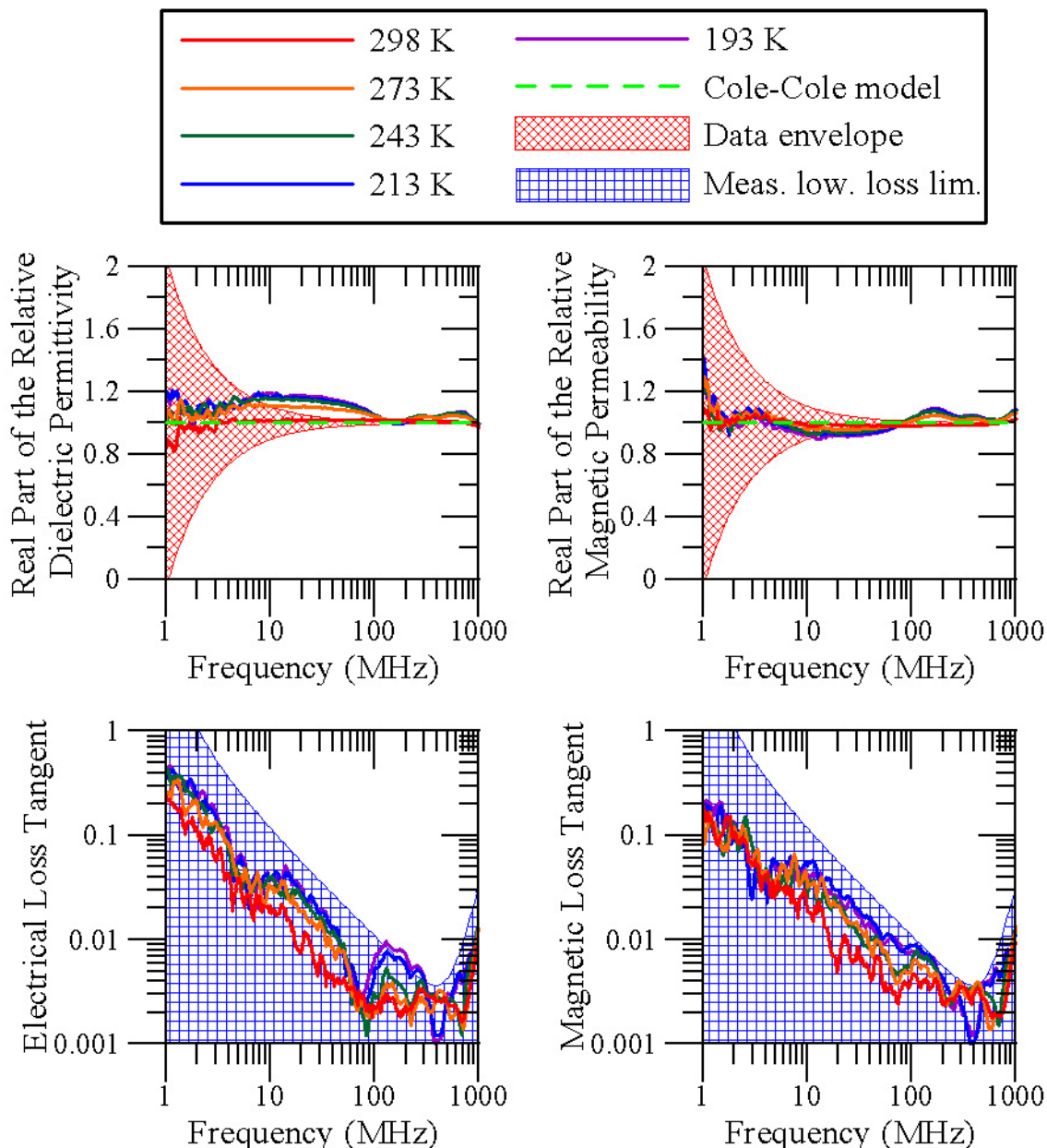


Figure 4.12. The EM properties of air versus frequency and temperature were measured as a quality control test of the apparatus. Air should possess a frequency independent  $\mu_r = \epsilon_r = 1$  and a loss tangent of zero. Five temperature measurements were made using a 10 cm sample holder. The data envelope and measurable lower loss limit are plotted assuming the measured precision (discussed in Section 4.4.1). The top two graphs contain data that are outside of the data envelope – these points are created by the contraction of the cable as temperature is decreased.

As shown in Figure 4.12, the thermal contraction of the cables can be recognized in the real part of the relative dielectric permittivity graph by a higher value at low frequencies that trends down to the original value and then slightly increases at high frequencies. The thermal contraction of the cables can be recognized in the real part of the magnetic permeability graph by a lower value at low frequencies that trends toward the original value and then trends toward a higher value at high frequencies. The electrical and magnetic loss tangents do not measurably change due to thermal contraction. This is because both of the imaginary and real parts are changing in the same manner. Each time the temperature is lowered, these discrepancies in the graphs become larger as the cables continue to contract. The resulting change in the real part of the relative dielectric permittivity and the real part of the magnetic permeability caused by the thermal contraction of the cable is reduced as the impedance of the sample holder increases. This occurs because greater impedance contrasts create reflections and transmissions that have larger phase differences.

Since the temperature reading of the duplicate sample holder was used to deduce the temperature reading of the measuring sample holder, a quality control test was conducted using grey hematite to determine the accuracy of this method. Grey hematite (GHKwMI sample) was used because it possesses a temperature dependent dielectric permittivity relaxation (discussed further in Chapter 5). For this test, ten VNA measurements were made using grey hematite at a temperature of  $203.15 \pm 0.20$  K. The time constant of relaxation was then found and plotted versus temperature as seen in Figure 4.13. This figure shows that the uncertainty of the temperature measurement is greater than the difference in temperature between the duplicate sample holder and the measurement sample holder. Consequently, the method of using the temperature reading in the duplicate sample holder was deemed acceptable.

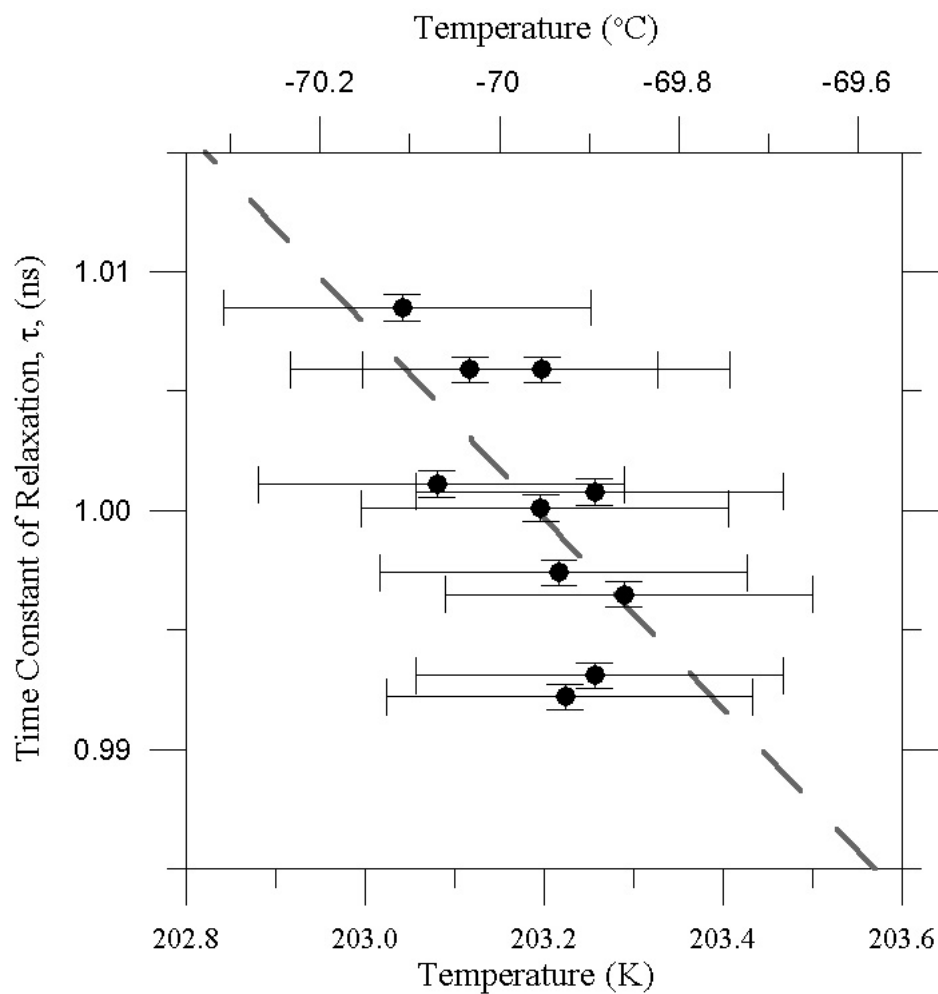


Figure 4.13. This figure displays 10 measurements of the time constant of relaxation versus temperature. The dashed line is the predicted time constant of relaxation versus temperature found using the generalized Boltzmann temperature equation to fit the grey hematite (sample GHKwMI) data over a temperature range of 300 – 180 K (further discussed in Chapter 5). The temperature error bars represent the error in thermistor accuracy as shown in Table 4.1. Since the dashed line passes through the error bars of the data, no additional uncertainty is generated by measuring the temperature in a duplicate sample holder.

## CHAPTER 5

### EXPERIMENTAL AND MODEL RESULTS

#### 5.1. Introduction

Both dielectric and magnetic relaxations were observed in some of the measured Martian analog samples. In order to understand the nature of the relaxations, the data were modeled using inversion. In this chapter, the Martian analogs are grouped into three categories for discussion: samples with no measurable losses, samples with dielectric relaxation losses, and samples with magnetic relaxation losses. Samples with no measurable losses are favorable for GPR exploration. Consequently, the GPR depth of penetration will be limited by losses such as scattering and geometric spreading and not EM relaxation losses or electrical conduction losses. Samples with EM relaxation losses are not favorable for GPR exploration. Therefore, the GPR depth of penetration will likely be limited by the EM relaxation loss mechanism. Only limited amounts of data are presented in this chapter. All of the data collected can be viewed on the attached DVD.

#### 5.2. Data Modeling

If a Martian analog sample possessed temperature and/or frequency dependent EM properties, the data were inverted to find the Cole-Cole parameters at each measured temperature. Prior to inverting the data, any coherent noise, errors due to cable contraction, and resonance were removed. A program was developed using MATLAB®'s optimization toolbox (version 2.2) inversion to determine the best fit value and confidence intervals for each of the four Cole-Cole parameters ( $\epsilon_{DC}$ ,  $\epsilon_{\infty}$ ,  $\tau$ ,  $\alpha$ ). Similar data had been inverted before using a Levenberg-Marquardt routine [Canan,

1999]. The Levenberg-Marquardt [Levenberg, 1944, and Marquardt, 1963] inversion is used by the MATLAB® optimization toolbox to determine the global minimum of a weighted normalized data misfit, Equation 5.1, of the Cole-Cole equation.

$$\phi^2 = \frac{1}{N} \sum_{i=1}^N \left( \frac{d_i - f(x_i; \epsilon_{DC}, \epsilon_{\infty}, \tau, \alpha)}{\sigma_i} \right)^2 \quad (5.1)$$

where:  $\phi^2$  = weighted normalized data misfit

d = data

f = modeled data using the Cole-Cole equation (Equation 2.40)

x = modeled data points

N = number of data points

$\sigma$  = standard deviation

In order to calculate the data misfit using Equation 5.1, the standard deviation must be determined for each frequency data point. This is done so that frequency data points with large standard deviations will affect the misfit less than data with low standard deviation. For a typical data set the standard deviation remains the same for each measurement. However, this must be done because the standard deviation varies over three orders of magnitude in this data as a function of frequency.

At the beginning of this study, the standard deviation of the data was found by calculating the standard deviation of the nearest ten frequency data points. Later in the study, the standard deviation for each frequency was determined by making multiple measurements with a stack of one. The individual VNA measurements were then combined to calculate the average value and standard deviation at each frequency data point. This process was performed at both room temperature and the coldest temperature ( $\approx 180$  K) since these were the only two stable temperatures. It was shown in Section 4.5.2 that the standard deviation does not vary as a function of the number of stacks. Therefore, the standard deviations from the warmest and coldest temperatures were interpolated at each temperature in between to determine the standard deviation at each

frequency. This second method for determining the standard deviation was an improvement over the first method and should be used for future work.

An inversion with no bounds on any of the Cole-Cole parameters was first applied to the data collected at the temperature which contained the largest portion of the relaxation with the least amount of cable contraction. This was done because as the relaxation shifts with temperature, it often shifts outside the frequency range of useable data. This initial inversion set the bounds for the Cole-Cole parameters, with the exception of the time constant of relaxation ( $\tau$ ). Since the time constant of relaxation was the only Cole-Cole parameter expected to change as a function of temperature, the remaining temperature data sets were only inverted for  $\tau$  with the other Cole-Cole parameters fixed.

Once the global minimum of the weighted normalized data misfit,  $\phi^2$ , was found, two adjusted data sets were created by adding and subtracting two standard deviations from the original averaged data set. The adjusted  $\phi^2$  values were found for each of the adjusted data sets using the previous best fit model. The Cole-Cole model parameters were then varied individually in a sensitivity analysis to match the adjusted  $\phi^2$ . This gave the 95.5% confidence intervals for each Cole-Cole parameter. (See Figure 5.1.)

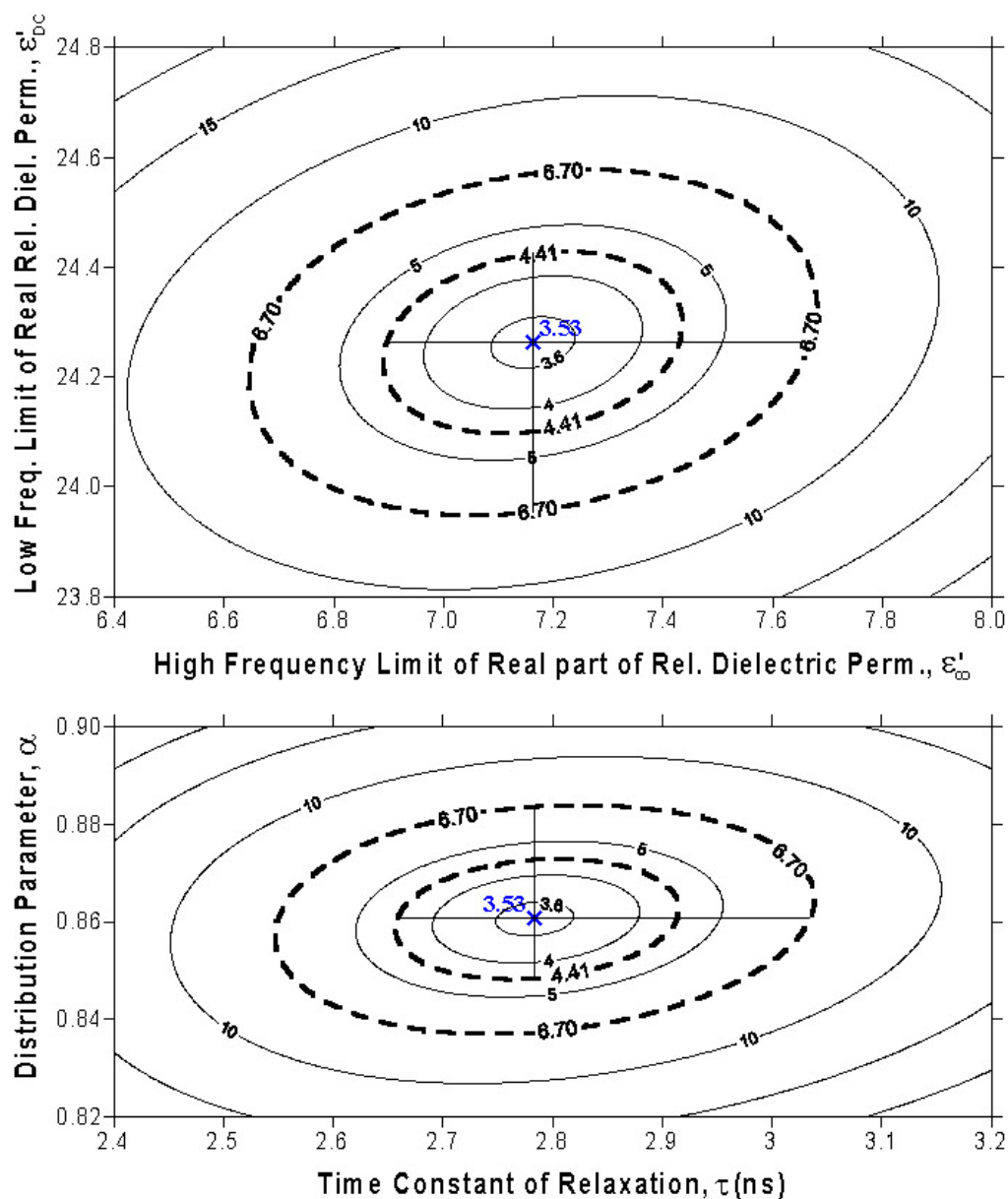


Figure 5.1. This figure shows a sensitivity analysis of the Cole-Cole parameters for the grey hematite sample, GHKwMI, at the coldest temperature (180.9 K). Both graphs contour the weighted normalized data misfit,  $\phi^2$ , as a function of the graph parameters with the global minimum of 3.53, a plus two standard deviation value of 4.41, and a minus two standard deviation value of 6.70. The 95.5% confidence intervals for each parameter were then found by keeping all other parameters constant and shifting the value to the appropriate  $\phi^2$  contour line.

Once the time constant of relaxation ( $\tau$ ) for each temperature measurement was determined, the generalized Boltzmann temperature dependence (Equation 2.41) was used to find the activation energy,  $E$ , and time constant at infinite temperature,  $\tau_{\infty}$ . Next, the time constant of relaxation and the temperature were both varied within their 95.5% confidence intervals to produce a range of activation energies and associated time constants at infinite temperature. The activation energy and the time constant at infinite temperature were found to possess three different 95.5% confidence interval ranges. These ranges are associated with a range of temperatures. The three temperature ranges found included: high temperature values that were extrapolated, median temperature values that were interpolated, and low temperature values that were extrapolated. (See Figure 5.2.)

Once the electric and magnetic Cole-Cole and generalized Boltzmann parameters for the sample were found, they were substituted into the modified Cole-Cole equation, Equation 2.44. This equation describes how complex dielectric permittivity and complex magnetic permeability vary as a function of frequency and temperature. To calculate the maximum GPR depth of penetration, the complex dielectric permittivity, and complex magnetic permeability can be inserted into Equation 2.20. The GPR depth of penetration will be discussed in Chapter 6.

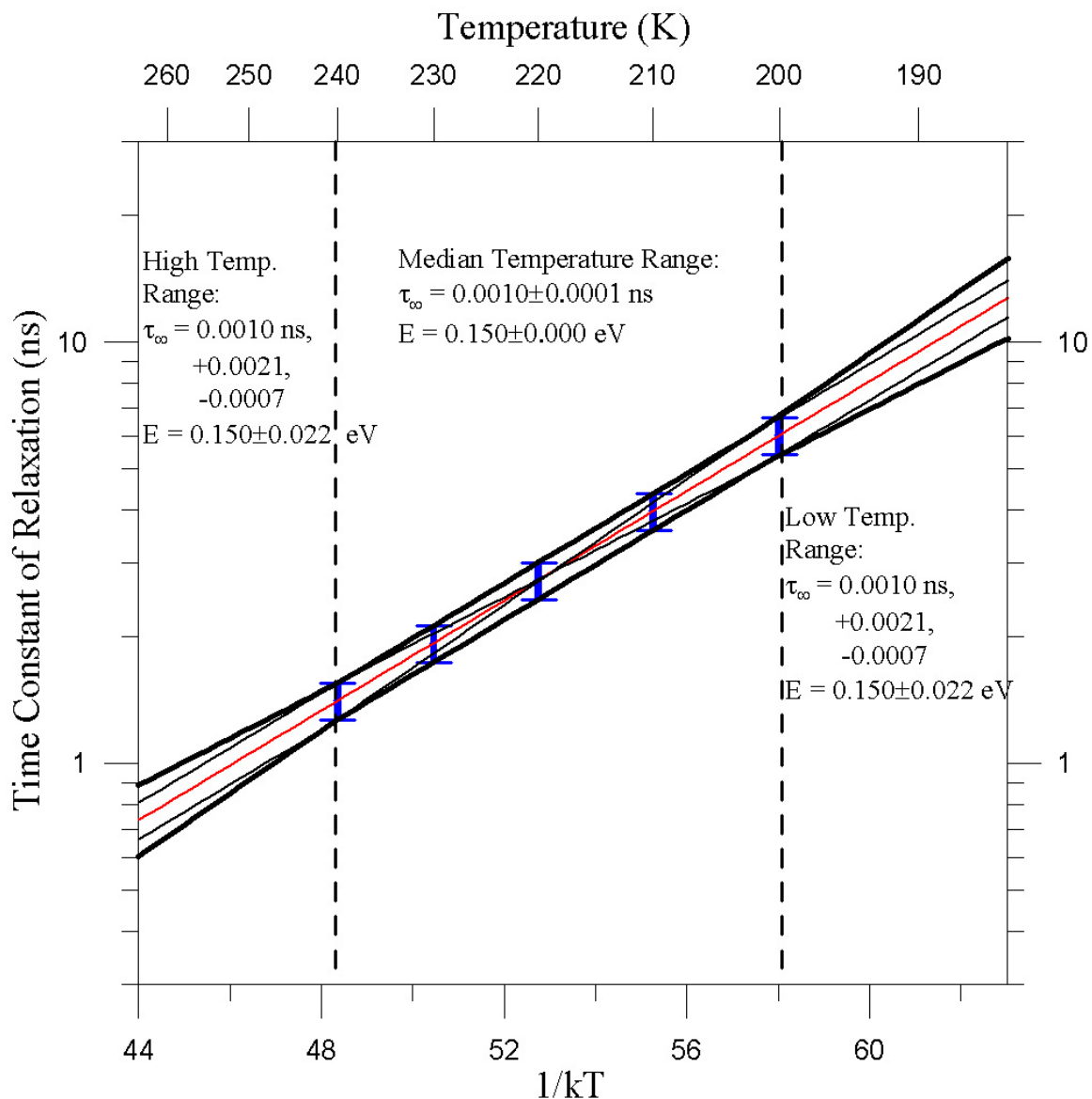


Figure 5.2. This figure graphically demonstrates the how the 95.5% confidence interval of the time constant at infinite temperature,  $\tau_{\infty}$ , and the activation energy,  $E$ , change in three temperatures ranges. The blue lines depict the error bars of the data. The red line is the model that fits the data points the best. The light black lines show four fits of data that has been adjusted within its 95.5% confidence intervals. The dark black lines show the maximum and minimum model error.

### 5.3. Samples with No Measurable EM Losses

Five of the measured samples possess no measurable EM losses. (This does not mean that these samples do not possess any losses, since they may possess losses that are less than the measurement limits of the apparatus.) Table 5.1 lists the real part of the relative dielectric permittivity, real part of the relative magnetic permeability, and the DC resistivity for these samples. Since they do not possess any measurable losses, they are also frequency independent and therefore they do not possess any measurable imaginary parts. Figure 5.3 shows a representative sample with no measurable EM losses from this group of data. Data from the remaining samples can be found on the DVD.

Table 5.1. EM properties for samples possessing no measurable EM losses. The first row shows the modeled results of the measured data. In the second row, the modeled data was corrected for density using a Lichtenecker power law mixing formula, Equation 2.47.

Sample	Density (g/cc)	Real Part of the Relative Dielectric Permittivity, $\epsilon_r$	DC Resistivity, $\sigma_{DC}$ (k $\Omega$ m)	Real Part of the Relative Magnetic Permeability, $\mu_r$
Sand (Sand)	1.47	$2.57 \pm 0.01$	>15	$1.00 \pm 0.02$
	1.60	$2.80 \pm 0.01$	>15	$1.00 \pm 0.02$
Jarosite (Jaro)	1.39	$3.07 \pm 0.02$	>15	$1.00 \pm 0.02$
	1.60	$3.52 \pm 0.02$	>15	$1.00 \pm 0.02$
Ferric Oxide (FeOxd)	0.68	$1.70 \pm 0.02$	>15	$1.00 \pm 0.02$
	1.60	$3.10 \pm 0.04$	>15	$1.00 \pm 0.02$
Green Sand Beach (GSBHI)	2.00	$3.61 \pm 0.03$	>15	$1.00 \pm 0.02$
	1.60	$2.78 \pm 0.04$	>15	$1.00 \pm 0.02$
Hematite (Hem)	1.14	$2.41 \pm 0.02$	>15	$1.28 \pm 0.02$
	1.60	$3.25 \pm 0.03$	>15	

Sample: Jarosite (Jaro)	Length = 10 cm	Density = 1.39 g/cc
Cal: MT041504	Date: 4/15/04	Stack: 16

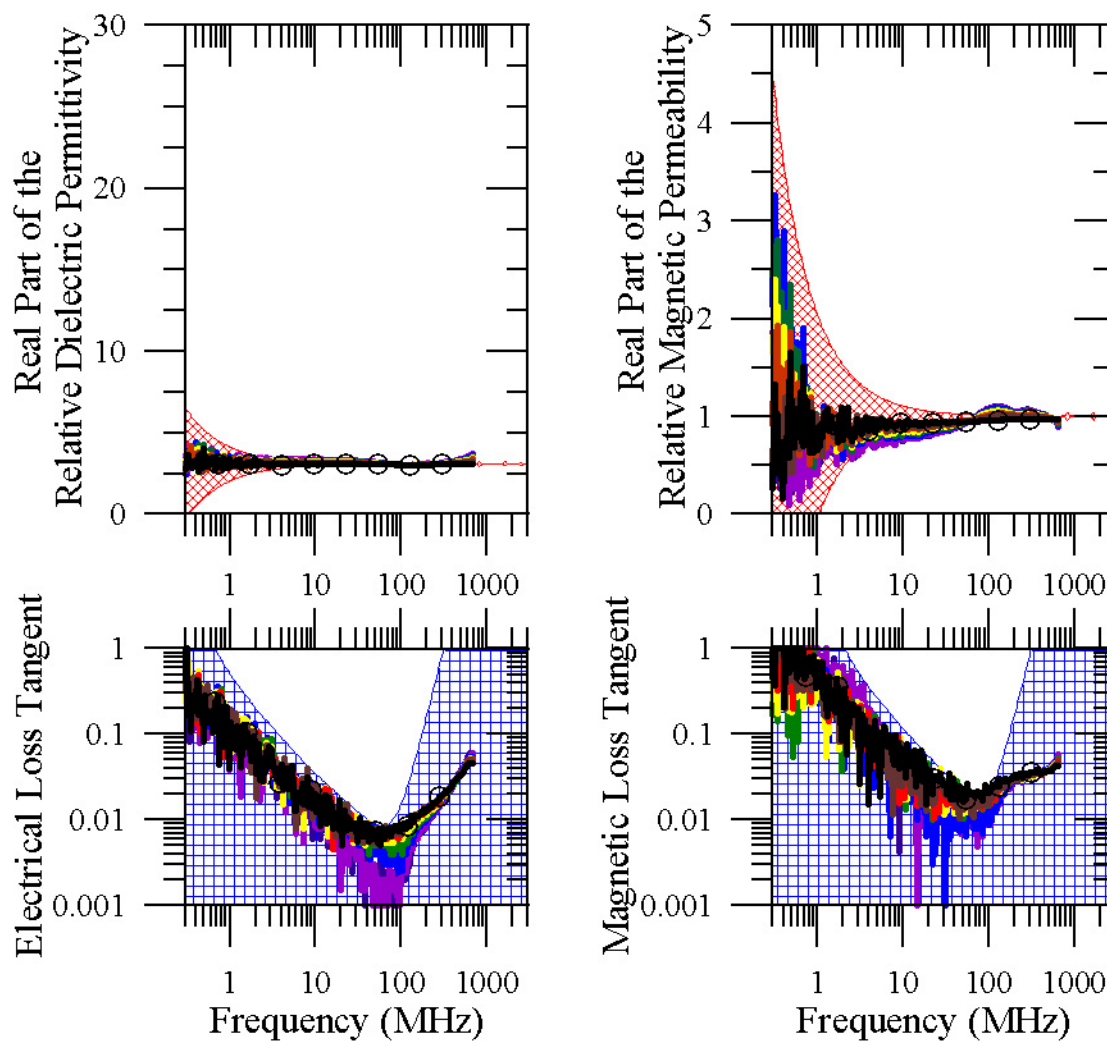


Figure 5.3. This figure shows the EM properties of a typical sample that contains no measurable EM losses. These samples possess no measurable frequency or temperature dependence. Therefore, the loss tangents are constrained to the measurable lower loss limit.

#### 5.4. Samples with Dielectric Relaxation Losses

Four of the measured samples possess temperature dependent dielectric relaxation losses. Their Cole-Cole and Boltzmann parameters are listed in Table 5.2. Four of these samples (GHKwMI, GHSChp, JSC-1 and PuNeHIC) will be discussed in detail below. The data from all of the samples with dielectric relaxation losses are provided on the DVD.

Figure 5.4 shows the temperature dependent dielectric relaxation of sample GHKwMI. This sample possesses the largest dielectric or magnetic loss of any sample measured in this study. The sample was crushed from a rock that originated from the Keweenaw Peninsula in Michigan and consists primarily of grey hematite (see XRD results in Appendix A). The high frequency limit of the relative dielectric permittivity could not be constrained until the temperature dropped below 182 K. At temperatures less than 182 K, the frequency of relaxation is less than the resonant frequency, therefore the peak of the dielectric relaxation in the loss tangent can be measured. This peak is proportional to the difference between the high and the low frequency limits of the relative dielectric permittivity. Figure 5.5 shows the Arrhenius plot for this sample. The plot shows that the dielectric relaxation shifted out of the accurate frequency range at temperatures greater than 227 K. Therefore, only temperatures in the range of 181 – 227 K were used to determine the Boltzmann parameters.

Table 5.2. Cole-Cole and Boltzmann temperature parameters for samples with temperature dependent dielectric relaxations and frequency independent magnetic permeability. Uncertainties in the time constant of relaxation at infinite temperature,  $\tau_\infty$  (ns), and activation energy, E (eV), are given in Table 5.3. The first row shows the modeled results of the measured data. In the second row, the modeled data was corrected for density using a Lichtenecker power law mixing formula, Equation 2.42.

Sample	Density (g/cc)	$\epsilon_{DC}$	$\epsilon_\infty$	$\tau_\infty$ (ns)	E (eV)	$\alpha$	$\sigma_{DC}$ (k $\Omega$ m)	$\mu_r$
Grey Hematite, Keweenaw Pen. (GHKwMI)	3.11	27.24 ( $\pm 0.21$ )	6.61 ( $\pm 0.18$ )	$2.811 \times 10^{-4}$	0.1434	0.843 ( $\pm 0.010$ )	>15	1.00 $\pm$ 0.02
	1.60	10.17 ( $\pm 0.08$ )	2.47 ( $\pm 0.07$ )	$2.811 \times 10^{-4}$	0.1434	0.843 ( $\pm 0.010$ )	>15	1.00 $\pm$ 0.02
Grey Hematite, Champion Mine Soil (GHSchp)	2.40	17.0 ( $\pm 0.7$ )	4.9 (+3.5,-3.9)	$2.33 \times 10^{-4}$	0.134	0.55 (+0.14,-0.08)	>15	1.22 $\pm$ 0.03
	1.60	10.1 ( $\pm 0.4$ )	2.9 (+2.0,-1.7)	$2.33 \times 10^{-4}$	0.134	0.55 (+0.14,-0.08)	>15	
Pu'u Nene Horizon C (PuNeHIC)	1.59	8.4 (+0.6,-0.5)	2.84	0.0863	0.111	0.291 ( $\pm 0.016$ )	>15	1.00 $\pm$ 0.02
	1.60	8.4 (+0.6,-0.5)	2.84	0.0863	0.111	0.291 ( $\pm 0.016$ )	>15	1.00 $\pm$ 0.02
JSC Mars-1 (JSC1)	0.90	3.4 ( $\pm 1.0$ )	1.80	$9.3 \times 10^{-5}$	0.175	0.13 (+0.01,-0.05)	>15	1.00 $\pm$ 0.02
	1.60	5.3 ( $\pm 1.0$ )	2.84	$9.3 \times 10^{-5}$	0.175	0.13 (+0.01,-0.05)	>15	1.00 $\pm$ 0.02

Table 5.3. Uncertainties in the time constant of relaxation at infinite temperature,  $\tau_{\infty}$  (ns), and activation energy, E (eV), for selected samples with dielectric permittivity relaxations.

Sample	Temperature Range	$\tau_{\infty}$	E
Grey Hematite, Keweenaw Pen. (GHKwMI)	>227 K	$2.811 (+0.393, -0.353) \times 10^{-4}$	0.1434 ( $\pm 0.023$ )
	181 - 227 K	$2.811 (+0.154, -0.159) \times 10^{-4}$	0.1434 ( $\pm 0.007$ )
	<181 K	$2.811 (+0.353, -0.393) \times 10^{-4}$	0.1434 ( $\pm 0.023$ )
Grey Hematite, Champion Mine Soil (GHSChp)	>213 K	$2.33 (+1.23, -0.96) \times 10^{-4}$	0.134 (+0.009, -0.007)
	184 - 213 K	$2.33 (+0.46, -0.64) \times 10^{-4}$	0.134 (+0.005, -0.003)
	<184 K	$2.33 (+0.96, -1.23) \times 10^{-4}$	0.134 (+0.007, -0.009)
Pu'u Nene Horizon C (PuNeHIC)	303 - 180 K	0.0863 (+0.0028, -0.0008)	0.111 ( $\pm 0.005$ )
JSC Mars-1 (JSC1)	303 - 180 K	$9.3 (+14.8, -5.9) \times 10^{-5}$	0.175 ( $\pm 0.021$ )

Sample: <b>Grey Hem., Kew. P. MI (GHKwMI)</b>	Length = 10 cm	Density = 3.11 g/cc
Cal: MT090305	Date: 9/3-12/05	Stack: 8
 T = 227.64 K	 T = 208.35 K	 T = 188.08 K
 T = 223.71 K	 T = 203.42 K	 T = 183.14 K
 T = 218.22 K	 T = 198.21 K	 T = 181.24 K
 T = 213.49 K	 T = 193.18 K	 Data Env.
 Measurable Lower Loss Limit		

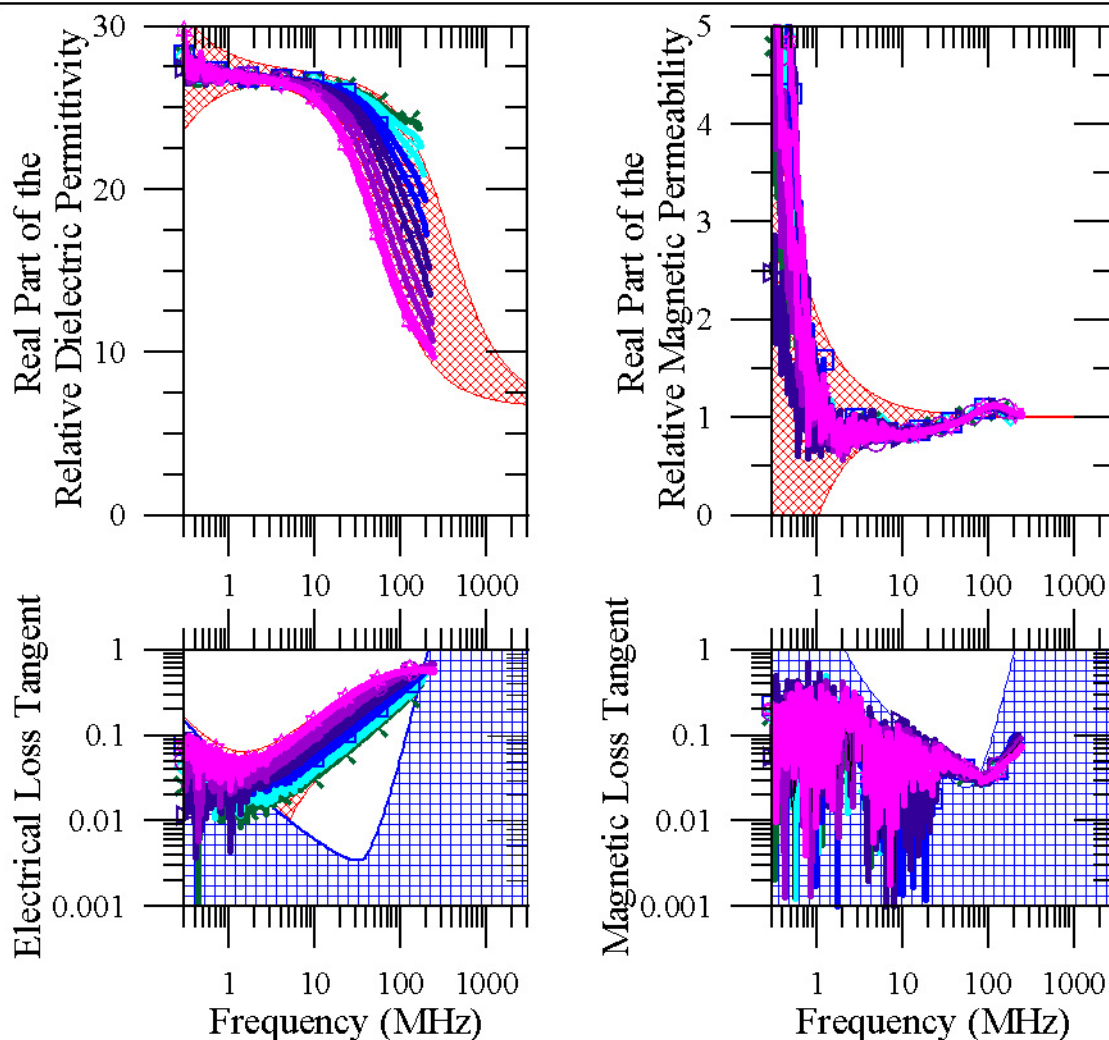


Figure 5.4. This figure shows the temperature dependent dielectric relaxation from 181 – 227 K for sample GHKwMI from the Keweenaw Peninsula in Michigan. The complete data set, temperature uncertainties, additional measurements using the same sample holder length, and other sample holder lengths are provided on the DVD.

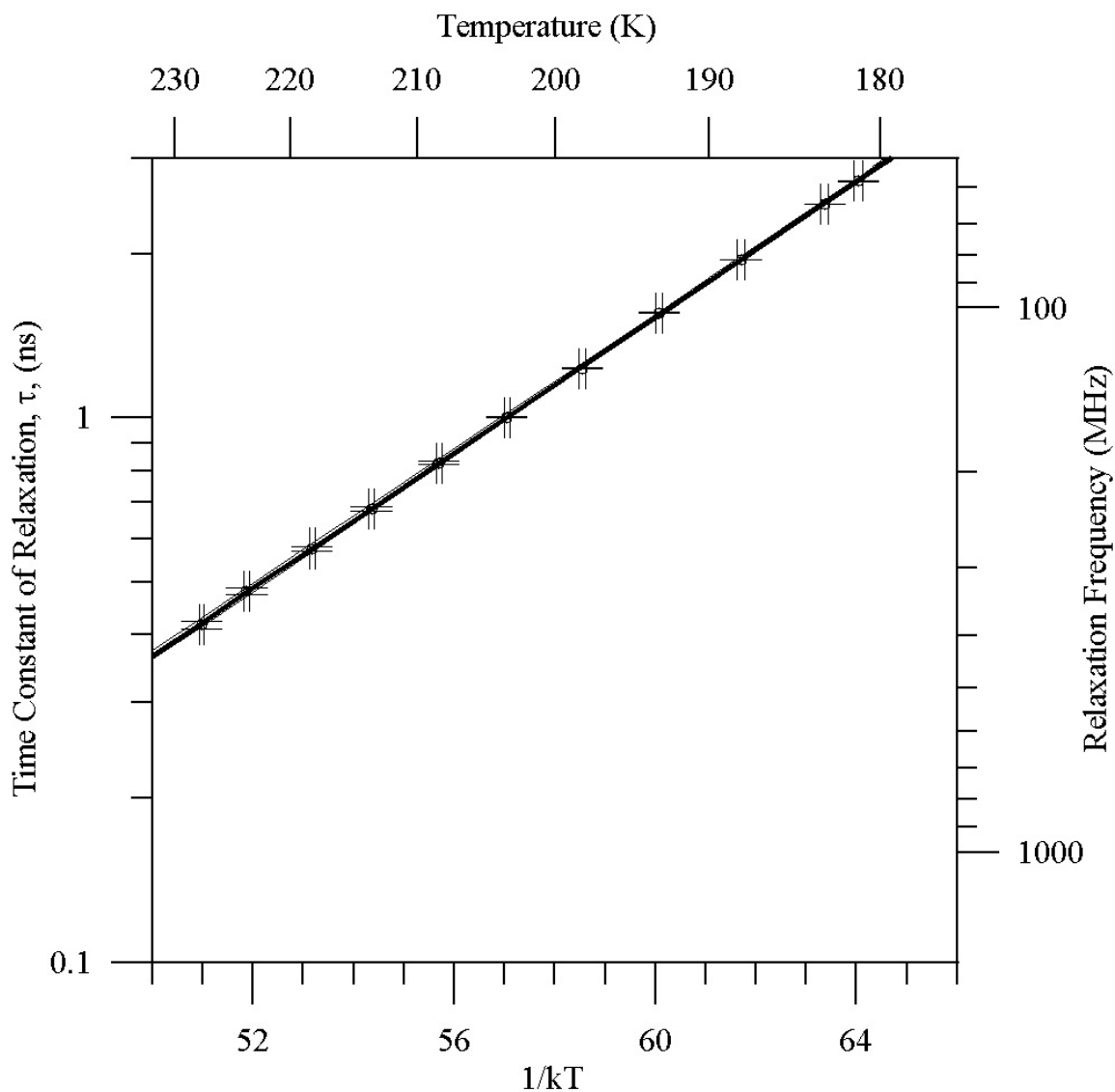


Figure 5.5. This figure shows an Arrhenius plot of the grey hematite sample from the Keweenaw Peninsula (GHKwMI). The dark black line is the best fit line of data points with a temperature range from 181 – 227 K (black data points). The two light black lines are the boundaries of the minimum and maximum best fit. Only data from the coldest temperature measurements are shown since the relaxation shifted outside the range of usable data as the temperature increased. The error bars show the 95.5% confidence intervals of the time constant of relaxation (vertical) and temperature (horizontal).

Figure 5.6 shows the temperature dependent dielectric relaxation of sample GHSChp. This sample was collected in soil form from the Champion Mine dump in Michigan. The major mineralogical components are grey hematite ( $\approx 65\%$  of the sample) and magnetite ( $\approx 10\%$  of the sample). (For detailed mineralogy see the XRD results in Appendix A.) The large temperature dependent dielectric loss is most likely caused by the grey hematite component. Unfortunately, even at the coldest temperature of  $\approx 183$  K, the relaxation frequency is greater than the resonant frequency. Because of this, the high frequency limit of the relative dielectric permittivity is poorly constrained. Figure 5.7 shows the Arrhenius plot for this sample. The plot shows that the dielectric relaxation could not be accurately modeled at temperatures greater than 214 K. Therefore, only temperatures in the range of 183 – 214 K were used to find the Boltzmann parameters.

GHSChp has a relative magnetic permeability greater than one. This is caused by its magnetite component. Magnetite has a temperature independent magnetic relaxation near 177 – 884 MHz. (Discussed in Section 5.5.) Although this sample was measured in a 3 cm sample holder to obtain higher frequencies, the magnetic relaxation could not be detected. The first resonant frequency occurs near 400 MHz with the 3 cm sample holder. This is much lower in frequency than the other magnetite samples because this sample possesses a much larger dielectric permittivity due to its grey hematite component. Therefore, even though no magnetic relaxation is seen, this sample could possess a magnetic relaxation at frequencies greater than 400 MHz. As discussed in Section 5.5, two of the three samples containing magnetite did possess magnetic relaxations at frequencies greater than 400 MHz

Sample: <b>Grey Hem., Ch. Mine Soil (GHSChp)</b>		Length = 10 cm	Density = 2.40 g/cc
Cal: MT071205		Date: 7/12/05	Stack: 8
○	T = 301.84 K	—	T = 253.07 K
—	T = 293.46 K	—	T = 243.25 K
—	T = 283.09 K	—	T = 233.04 K
—	T = 273.03 K	—	T = 223.23 K
—	T = 263.14 K	—	T = 213.33 K
			▨ Data Envel.
			▩ Meas. L.L.L.

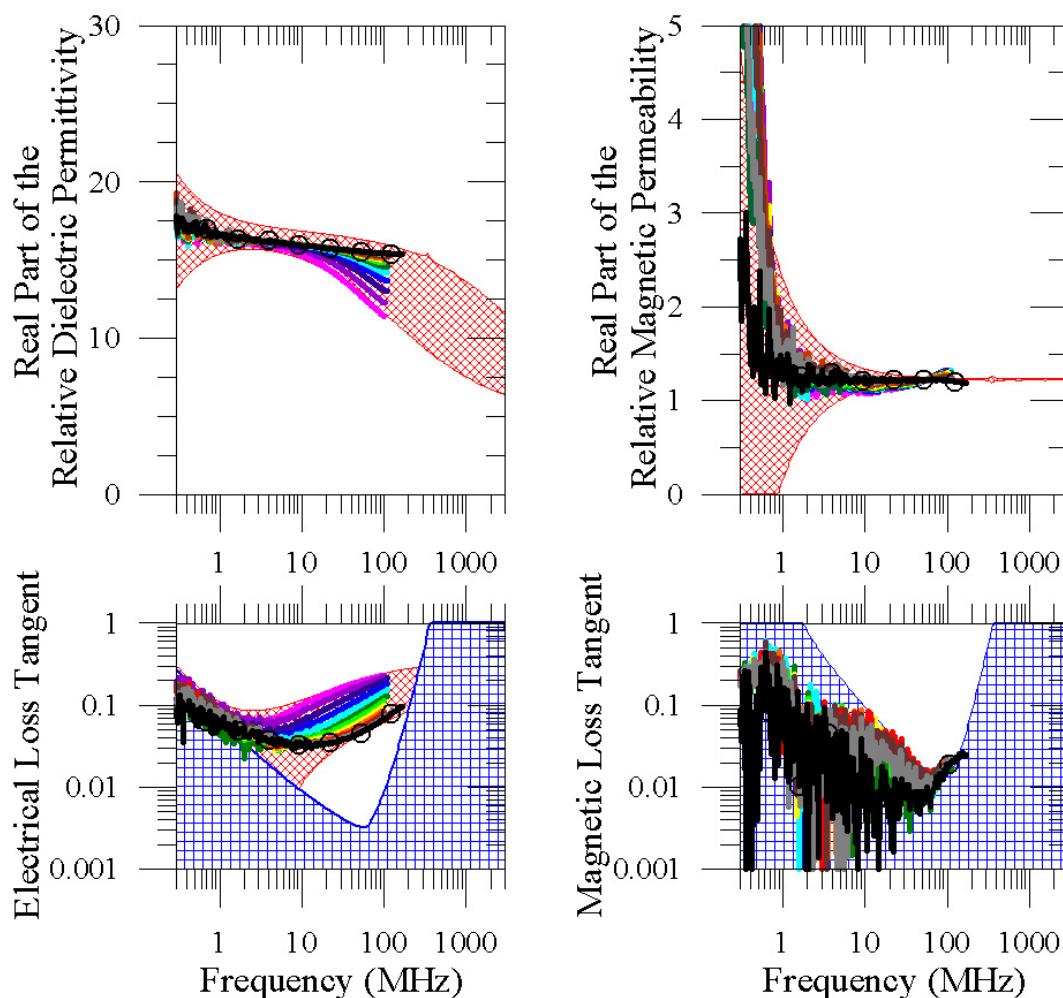


Figure 5.6. This figure shows the temperature dependent dielectric relaxation of the GHSChp sample (grey hematite soil from the Champion Mine dump in Michigan). Temperature uncertainties and additional measurements using the same sample holder length and other sample holder lengths are provided on the DVD.

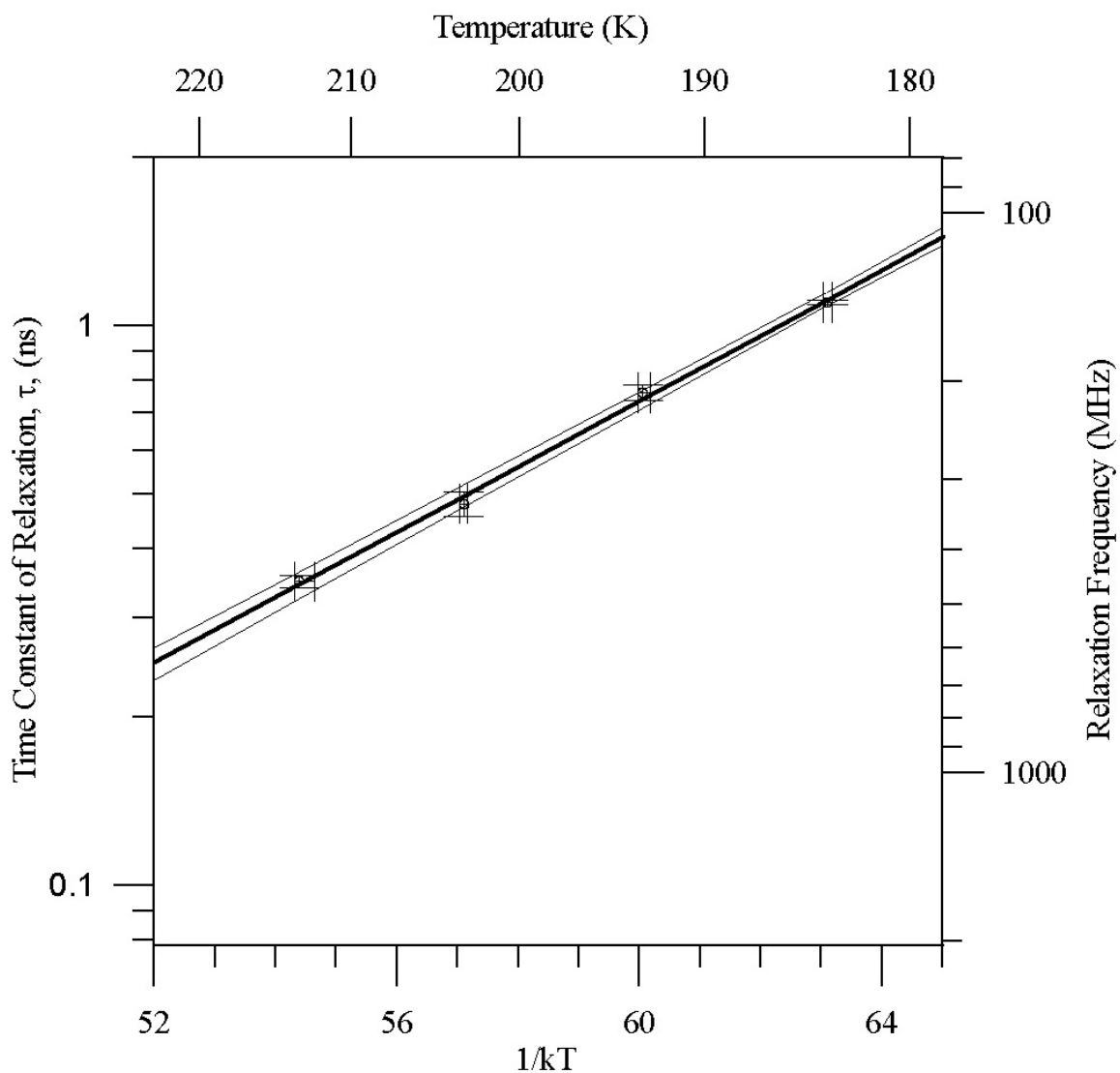


Figure 5.7. This figure shows an Arrhenius plot of the grey hematite from the Champion Mine dump (GHSChp). The dark black line is the best fit line of data points with a temperature range from 184 – 213 K (black data points). The two light black lines are the boundaries of the minimum and maximum best fit. Only data from the coldest temperature measurements are shown since the relaxation shifted outside the range of usable data as the temperature increased. The error bars show the 95.5% confidence intervals of the time constant of relaxation (vertical) and temperature (horizontal).

JSC Mars-1 possesses a small broad dielectric loss that is just above the measurable lower loss limit of the apparatus. (See Figure 5.8.) This sample is distributed by Johnson Space Center as the Earth soil that best represents a soil or regolith simulant of Mars. It is composed primarily of plagioclase feldspar and minor amounts of magnetite, hematite, olivine, pyroxene, and/or glass [Allen, 1997]. Approximately, 25% of the sample is highly magnetic at DC frequency [Allen, 1997]. Two previous studies have examined the EM properties of JSC Mars-1 at radar frequencies [Leuschen, 1999; Williams and Greeley, 2004].

Leuschen [1999] measured the complex dielectric permittivity and complex magnetic permeability of JSC Mars-1 at terrestrial room temperature with a vector network analyzer (VNA), used a slotted line for the sample holder over a frequency range from 10 – 1000 MHz. Williams and Greeley [2004] measured the complex dielectric permittivity of JSC Mars-1 from 200 – 1300 MHz at room temperature. (Details of the measurement procedure were not discussed.) They calculated an attenuation rate from these measurements, assuming no magnetic losses and a magnetic permeability of one. These previous measurements and the measurements acquired in this thesis are shown in Figure 5.8. It appears that both Leuschen [1999] and Williams and Greeley [2004] measured a JSC Mars-1 sample that was slightly more dense than the sample measured in this research, as their real part of the relative dielectric permittivity are slightly greater than those measured in this study. However, neither of the previous studies report sample density.

The electrical loss tangents of the two previous and the ones reported in this thesis are all different. Leuschen's [1999] are believed to be incorrect because he used a Debye model, which assumes a single relaxation, to fit his data. (The Cole-Cole model reduces into the Debye model when the Cole-Cole distribution parameter,  $\alpha$ , is equal to one.) It is unclear why Williams and Greeley [2004] measured such a large loss tangent. It is also unclear why Leuschen's [1999] complex magnetic permeability measurements are so different from the measurements made in this thesis.

Sample: JSC Mars-1 (JSC1)	Length = 10 cm	Density = 0.91 g/cc
Cal: MT093005	Date: 9/30-10/2/05	Stack: 1024
—○— T = 297.3 K	—☆— T = 181.7 K	▨ Data Envel.
	▨ Measurable Lower Loss Limit	
— T = 298 K [Leuschen, 1999]	— T = 298 K [Williams and Greeley, 2004]	

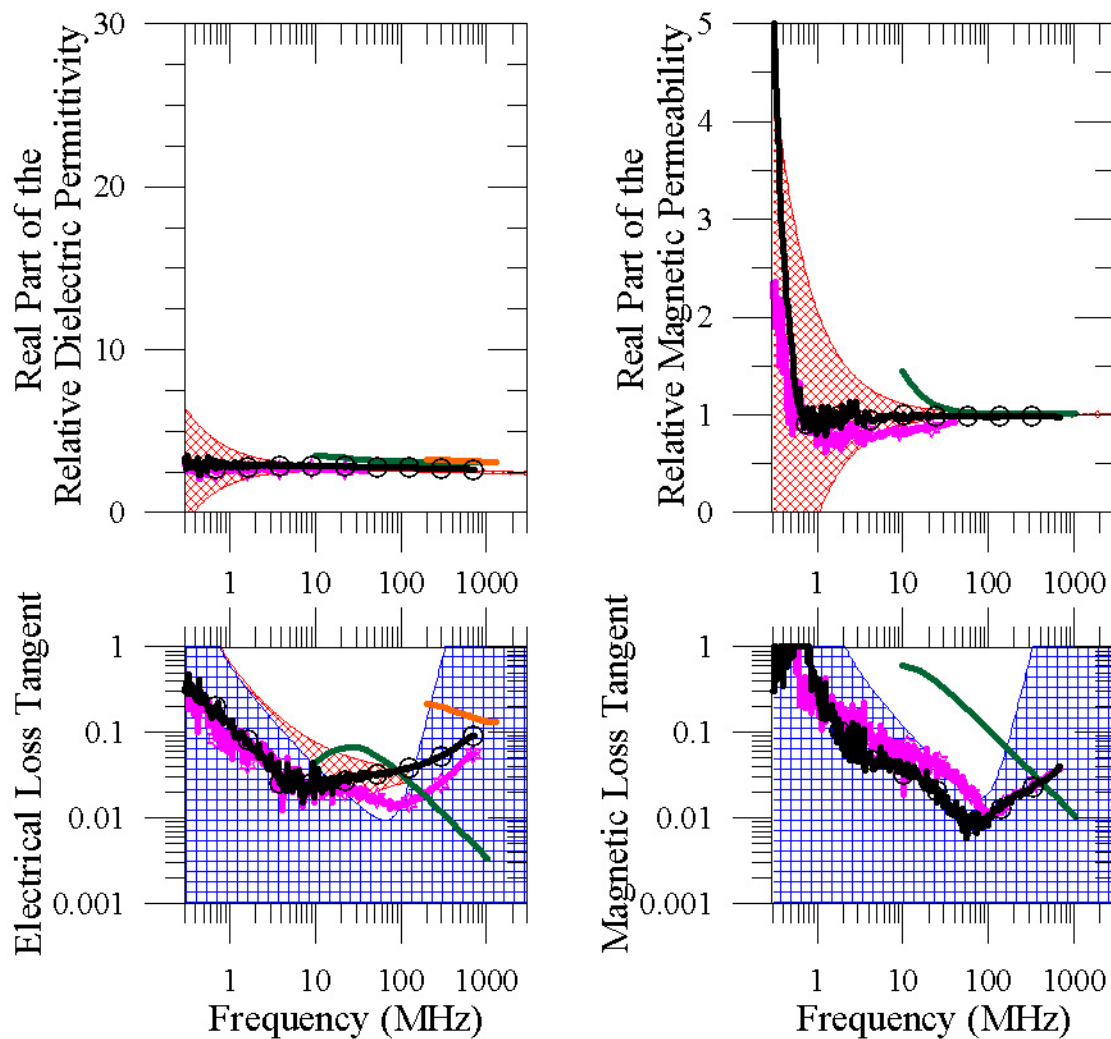


Figure 5.8. This figure shows the broad temperature dependent dielectric relaxation of the JSC Mars-1 sample (JSC1) along with measurements made by Leuschen [1999] and Williams and Greeley [2004]. The complete data set, temperature uncertainties, additional measurements using the same sample holder length, and other sample holder lengths are provided on the DVD.

The Cole-Cole and the generalized Boltzmann temperature model of JSC Mars-1 was very difficult to constrain because both the low frequency and high frequency limit of the real part of the dielectric permittivity could not be measured and the electrical loss tangent was just above the measurable lower loss limit. Consequently, the high frequency limit was assumed to have a real part of the relative dielectric permittivity of 1.80, which is the density controlled electronic polarization value as determined by a Lichtenecker power law mixing formula, Equation 2.47. While the models are poorly constrained, it is important to note that these models produce complex dielectric permittivity values that mimic the data from 1 – 1000 MHz over a temperature range from 298 – 180 K.

Figure 5.9 shows the temperature dependent dielectric relaxation of sample PuNeHIC. This sample was collected at the cinder cone Pu'u Nene, which is located in the saddle between Mauna Loa and Mauna Kea in Hawaii. More specifically, this sample was collected from the plagioclase feldspar layer beneath the oxidized tephra layer where NASA collected its JSC Mars-1. (For detailed mineralogy see the XRD results on the DVD.) As shown in Figure 5.8, this sample possesses a broad dielectric permittivity loss that is similar but stronger than JSC Mars-1. The relaxation was difficult to model since neither the low nor high frequency limit could be measured. Consequently, the high frequency limit was assumed to have a real part of the relative dielectric permittivity of 2.84, which is the density controlled electronic polarization value as determined by a Lichtenecker power law mixing formula, Equation 2.47. Figure 5.10 shows the Arrhenius plot for this sample.

Sample: <b>Pu'u Nene Hor. C, HI (PuNeHIC)</b>	Length = 10 cm	Density = 1.59 g/cc
Cal: MT012805	Date: 12/28/05	Stack: 8
○ T = 300.54 K	— T = 243.69 K	— T = 200.75 K
○ T = 296.75 K	— T = 223.73 K	☆ T = 180.48 K
— T = 264.18 K	— T = 213.05 K	▨ Data Envel.
▨ Measurable Lower Loss Limit		

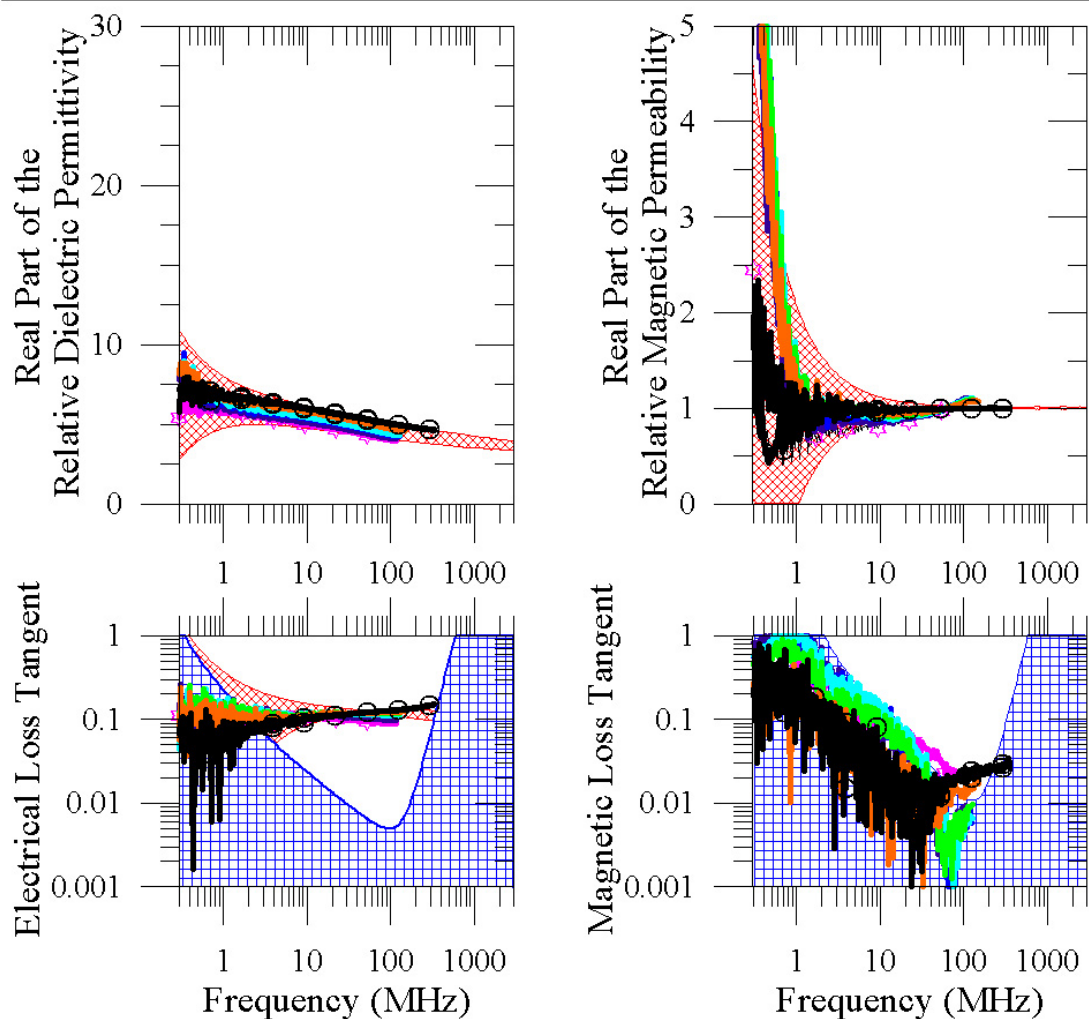


Figure 5.9. This figure shows the broad temperature dependent dielectric relaxation of PuNeHIC sample (Pu'u Nene horizon C). Temperature uncertainties, additional measurements using the same sample holder length and other sample holder lengths are provided on the DVD.

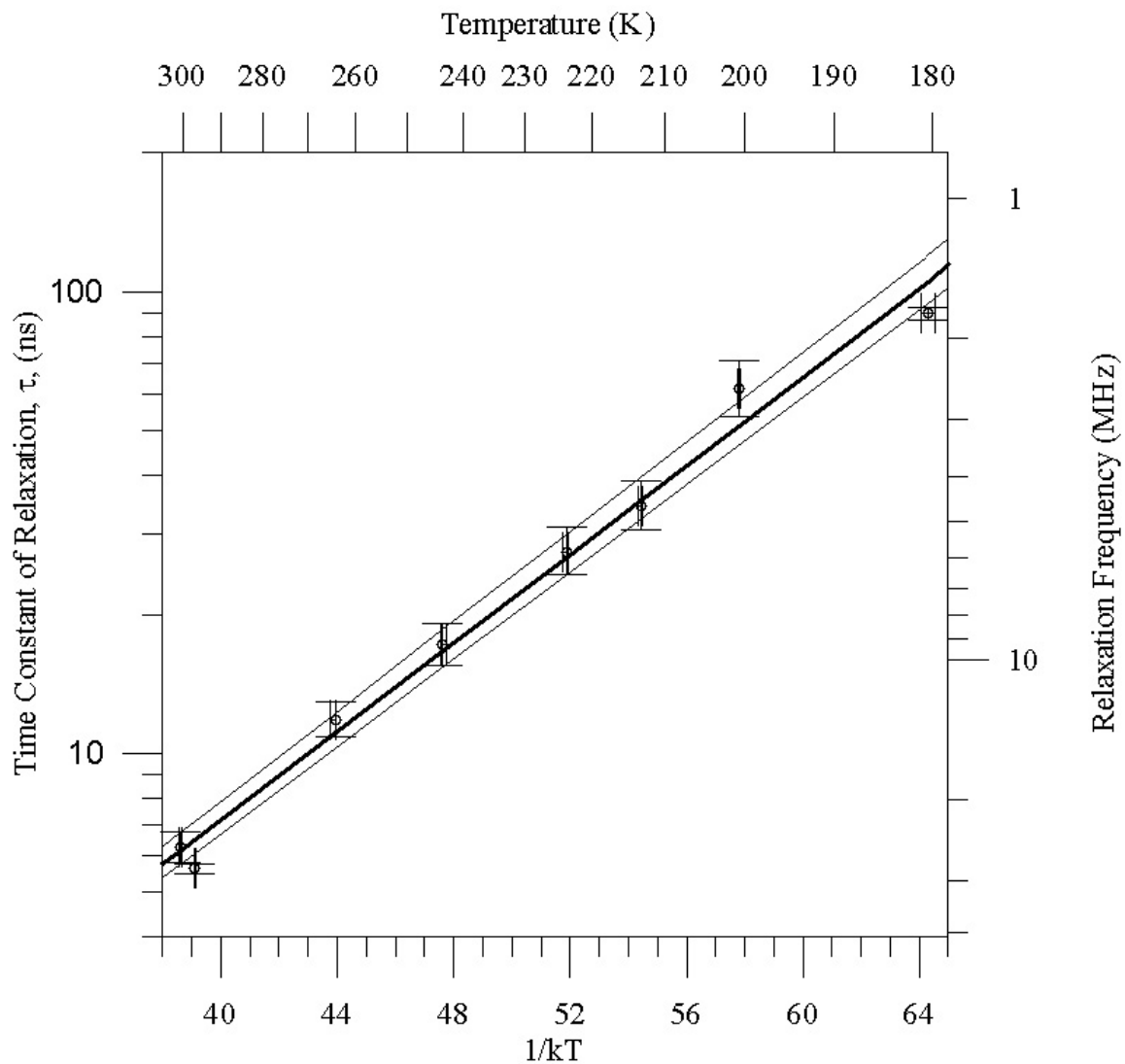


Figure 5.10. This figure shows an Arrhenius plot of Pu'u Nene horizon C (PuNeHIC). The dark black line is the best fit line of all the data points. The two light black lines are the boundaries of the minimum and maximum best fit. This data is provided on the DVD.

### 5.5. Samples with Magnetic Relaxation Losses

Three of the Mars analog samples possess temperature independent magnetic relaxation losses. Table 5.4 lists the inverted Cole-Cole parameters for these samples. Magnetite is believed to be causing the magnetic relaxations in all of these samples. Unfortunately, the magnetic relaxations all have poorly constrained high frequency limits, as the relaxation frequency is greater than the resonant frequency. The magnetic relaxations possess narrow distribution of time constants of relaxation (high  $\alpha$ ). This means that there are few variations in the mechanism that cause the magnetic relaxation.

Figure 5.11 shows the temperature independent magnetic permeability of sample MagRCh. This sample was collected in rock form from the Champion Mine dump in Michigan. The sample consists of about 73% magnetite (see XRD results on the DVD). Figure 5.12 shows the temperature independent magnetic permeability of sample Magn. This sample was collected from Peru by Universal Minerals and consists primarily of magnetite (see XRD results on the DVD). Figure 5.13 shows the temperature independent magnetic permeability of the Yuma sample, as well as the Cole-Cole model that Olhoeft and Capron [1993, 1994] found. This sample was collected from a dry stream bed near Yuma, Arizona, and was found to possess a magnetic relaxation by Olhoeft and Capron [1993, 1994]. Olhoeft and Capron's [1993, 1994] model fits the data very well. The sample consists of nonmagnetic white grains and highly magnetic black grains of magnetite (see XRD results on the DVD). The discrepancies in the model fit are most likely because the sample was measured with more magnetic black grains of magnetite in this thesis.

Table 5.4. Cole-Cole parameters for samples with temperature independent magnetic relaxations and frequency independent dielectric permittivity. The first row shows the modeled results of the measured data. In the second row, the modeled data was corrected for density using a Lichteneker power law mixing formula for the dielectric permittivity, Equation 2.47, and using Equation 2.49 for the magnetic permeability.

Sample	Density (g/cc)	$\epsilon_r'$	$\mu_{DC}$	$\mu_\infty$	$\tau$ (ns)	$\alpha$	$\sigma_{DC}$ (k $\Omega$ m)
Magnetite Champion Mine (MagChR)	2.56 1.60	10.61 ( $\pm 0.11$ ) 5.67 ( $\pm 0.06$ )	4.89 (+0.05,-0.12) 1.73 (+0.02,-0.04)	1.66 (+0.23,-0.17) 1.29 (+0.18,-0.13)	0.80 (+0.01,-0.07) 0.80 (+0.01,-0.07)	0.76 (+0.04,-0.05) 0.76 (+0.04,-0.05)	>15 >15
Magnetite (Magn)	1.88 1.60	6.92 ( $\pm 0.10$ ) 5.76 ( $\pm 0.08$ )	2.35 (+0.02,-0.01) 1.93 (+0.02,-0.01)	1.93 (+0.18,-0.25) 1.68 (+0.16,-0.22)	0.28 (+0.13,-0.07) 0.28 (+0.13,-0.07)	1.00 1.00	>15 >15
Yuma (Yuma)	2.23 1.60	6.82 ( $\pm 0.10$ ) 4.52 ( $\pm 0.07$ )	1.73 (+0.01,-0.03) 1.41 (+0.01,-0.02)	1.24 ( $\pm 0.24$ ) 1.16 ( $\pm 0.22$ )	0.30 (+0.2,-0.12) 0.30 (+0.2,-0.12)	0.75 (+0.1,-0.02) 0.75 (+0.1,-0.02)	>15 >15

Sample: Magnetite Rock, Champion Mine, MI (MagRCh)	Length = 3 cm	Density = 2.56 g/cc
Cal: MT090205	Date: 9/2/05	Stack: 1024

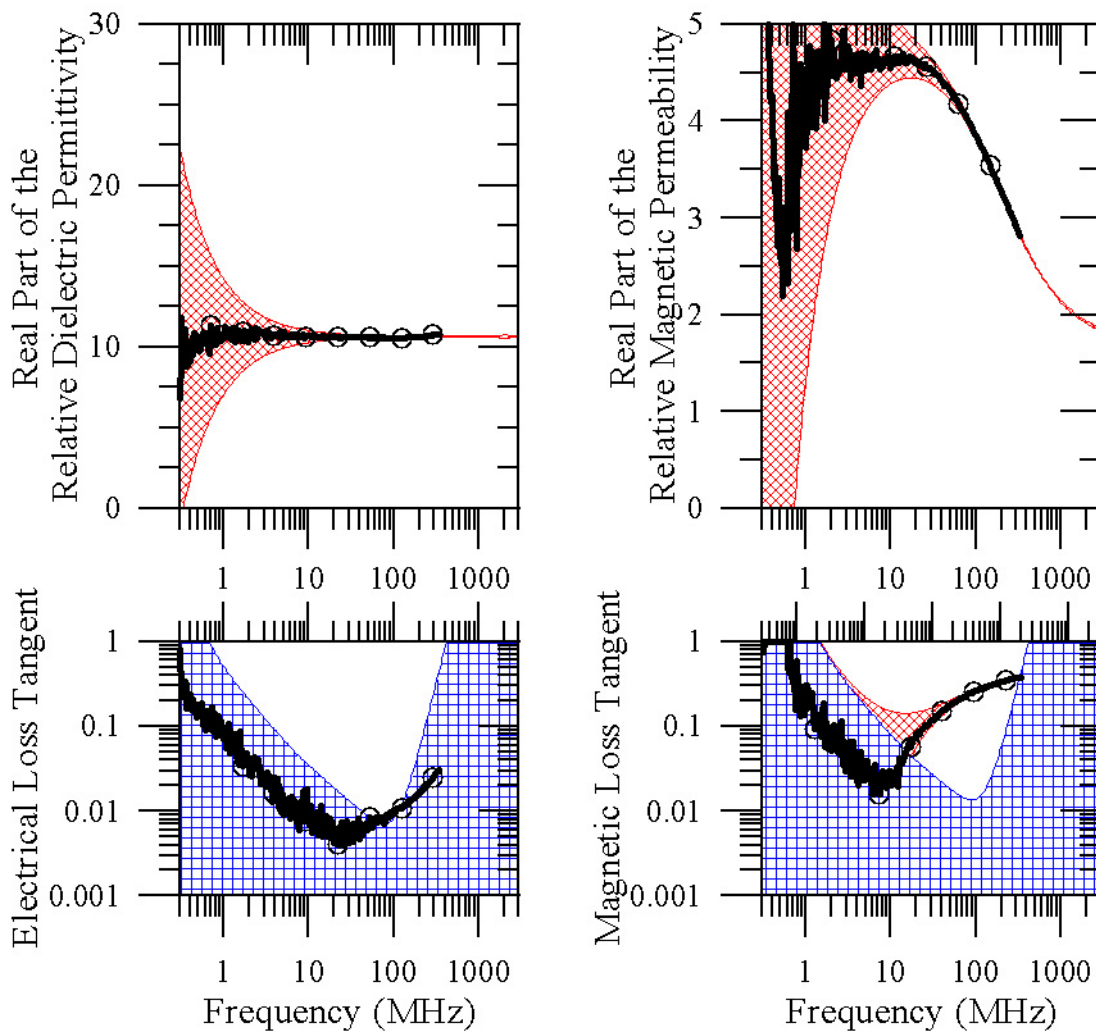


Figure 5.11. This figure shows the magnetic relaxation of the MagRCh sample (magnetite rich rock collected at the Champion mine dump). The complete data set versus temperature, as well as additional measurements using the same sample holder length, and other sample holder lengths are provided on the DVD.

Sample: <b>Magnetite (Magn)</b>	Length = 3 cm	Density = 1.88 g/cc
Cal: MT022506	Date: 2/27/06	Stack: 1024

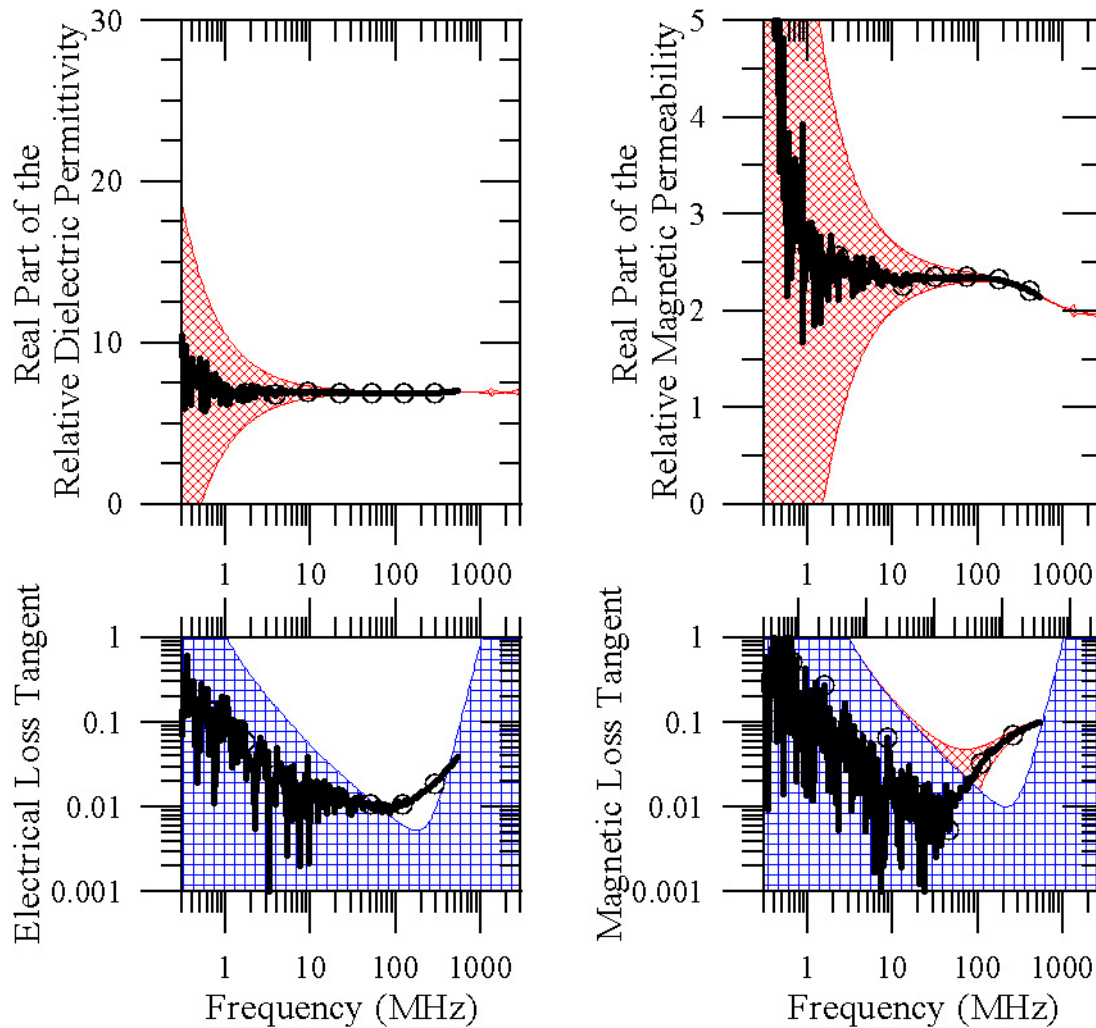


Figure 5.12. This figure shows the magnetic relaxation of the Magn sample (magnetite from Peru). The complete data set versus temperature, as well as additional measurements using the same sample holder length, and other sample holder lengths are provided on the DVD.

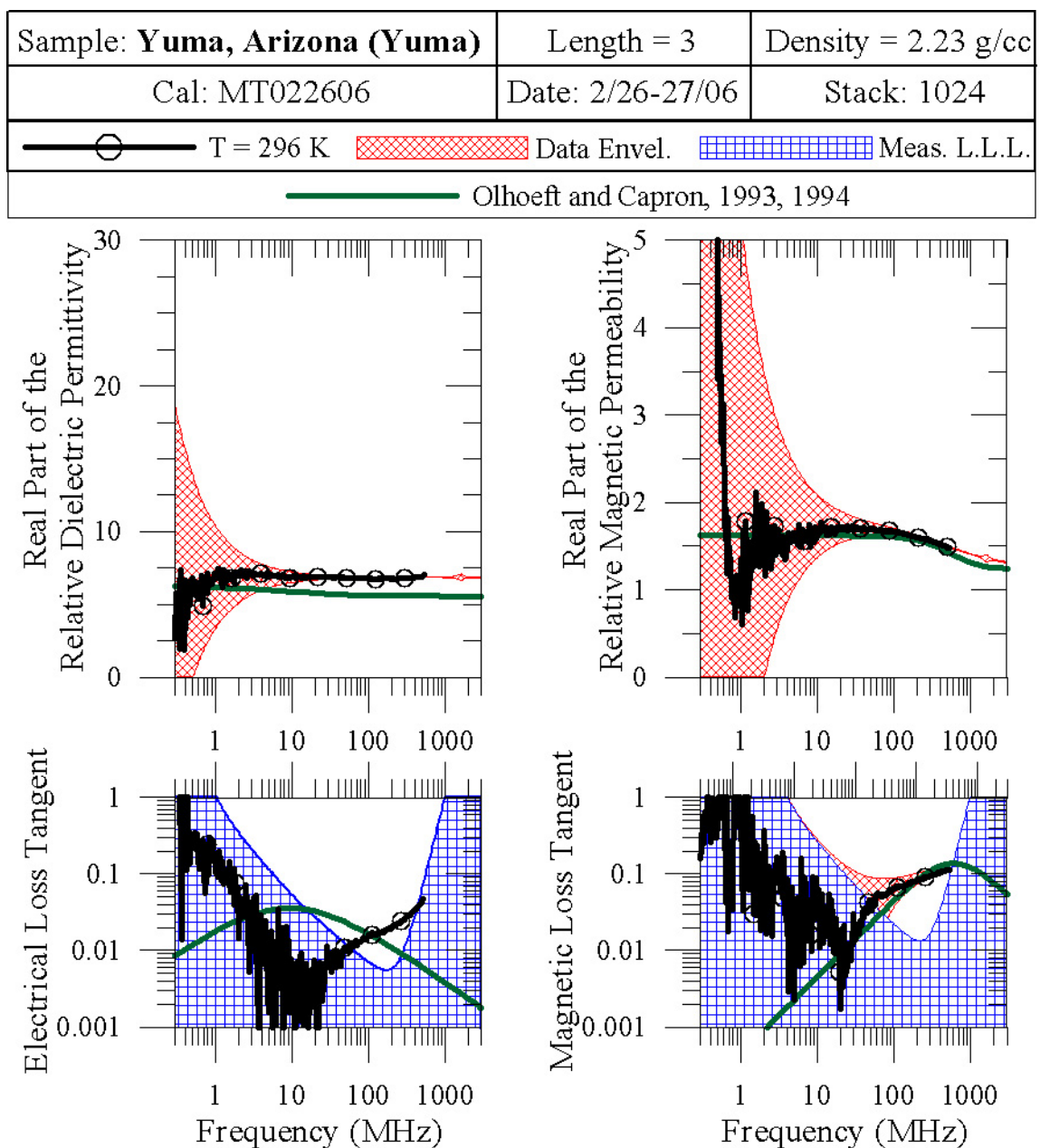


Figure 5.13. This figure shows the magnetic relaxation of the Yuma sample (magnetite rich soil sample from Yuma, AZ) along with measurements made by Olhoeft and Capron [1993, 1994]. The complete data set versus temperature, as well as additional measurements using the same sample holder length, and other sample holder lengths are provided on the DVD.

## CHAPTER 6

### DISCUSSION AND CONCLUSIONS

#### 6.1 Introduction

The dielectric and magnetic relaxations presented in Chapter 5 can all be attributed to unique polarization and magnetization mechanisms, respectively. The mechanisms, along with the implications of EM relaxations on current and future Mars GPR missions, will be discussed in this chapter.

#### 6.2 Grey Hematite

Christensen et al., [2001] spectroscopically identified grey hematite on Mars in three different locations. Since grey hematite can form in the presence of water, NASA sent Opportunity (MER-B) to explore one of these areas, Meridiani Planum. Opportunity determined that the spectroscopic grey hematite signal at Meridiani Planum was caused by grey hematite concretions that are believed to have precipitated from an iron rich groundwater [Squyres and Knoll, 2005].

Two grey hematite samples (GHKwMI and GHSChp) were selected as Martian analogs and their EM properties were measured. Both samples were found to possess a temperature dependent dielectric relaxation and a temperature and frequency independent magnetic permeability of one. The GHKwMI sample is composed largely of grey hematite and it possesses a dielectric relaxation centered at 1.42 GHz at room temperature (298 K) and 230 MHz at the average Martian temperature (213 K). Its activation energy was determined to be 0.1434 ( $\pm 0.0023$ ) eV. The GHSChp sample is composed of 65% grey hematite and 10% magnetite. It possesses a dielectric relaxation centered at 2.52 GHz at terrestrial room temperature (298 K) and 450 MHz at the average

Martian temperature (213 K). Its activation energy was determined to be 0.134 (+0.009, - 0.007) eV. Previous studies had identified dielectric relaxations in red hematite, but a temperature dependent dielectric relaxation had never been observed in grey hematite prior to this study. The following sections will explain the cause of the temperature dependent dielectric relaxation in grey hematite and the implications of this loss mechanism for current and future Martian GPR missions.

### 6.2.1 Temperature Dependent Dielectric Relaxation Mechanism of Grey Hematite

As discussed in Section 2.2.1, there are five potential polarization mechanisms that could cause a dielectric relaxation in grey hematite. Interfacial polarization is not likely because the relaxation is large and centered at a frequency of 2.52 GHz at terrestrial room temperature. (The difference between the low frequency limit and the high frequency limit of the real part of the relative dielectric permittivity is 20.63.) Large interfacial polarization relaxations do occur at frequencies less than 300 MHz at terrestrial room temperature [Canan et al., 1999]. These relaxations are typically caused by the electrical double layer (water adsorbed to the grains). Interfacial polarization relaxations can occur in the GHz frequency range, but they are generally much smaller in magnitude.

Ionic and orientation polarization are not a possibility since the sample was dry and contained no surface charges. Electronic polarization did occur in the grey hematite sample. However, this mechanism is always frequency independent at radar frequencies. (The value of the electronic polarization is equal to the high frequency limit of the relative dielectric permittivity,  $\epsilon_{\infty}$ , minus one.) This leaves molecular polarization as the most likely mechanism that caused the grey hematite dielectric relaxation.

The molecular polarization mechanism in grey hematite is caused by its rhombohedra corundum crystal structure. This crystal structure creates parallel planes of cation and anions as shown in Figure 2.2c. The application of an external electric field

causes the hematite crystal to distort by shifting the planes of cations and anions in opposite directions. This shift creates charge separation. As the temperature is decreased, the cations and anions possess less energy and can no longer polarize as quickly. The activation energy describes how quickly this shift occurs with temperature and represents the energy barrier that the charges must overcome in order to become polarized. The grey hematite samples, GHKwMI and GHSChp, have activation energies of 0.1434 ( $\pm 0.0023$ ) eV and 0.134 (+0.009, -0.007) eV, respectively.

Previous EM measurements of red hematite determined that it does not possess a molecular polarization mechanism at radar frequencies (1 – 1000 MHz). Red hematite has the same chemical formula and the same unit cell crystal structure as grey hematite. The difference between the two is that red hematite is composed of randomly oriented unit cell crystals, while grey hematite is composed of densely packed and aligned unit cell crystals that are bonded together to form a coarse grained crystal. This change in crystal packing strongly affects the relaxation frequency of the molecular polarization mechanism. Iben et al., [1996] found that red hematite has a temperature dependent dielectric relaxation centered at 20 kHz at 303 K.

It is no surprise that hematite possesses temperature dependent EM properties. Iben et al. [1996] observed that red hematite possesses a temperature dependent dielectric relaxation centered at 10 Hz at 293 K. Morris et al. [1997] found that the visible and infrared spectrum of red hematite varies between 300 K and 140 K. Hematite possesses a Morin temperature of approximately 263 K, where its magnetic properties change from being canted antiferromagnetic to perfectly antiferromagnetic (as discussed in Section 2.3.1). However, as previously mentioned, this is the first time that a temperature dependent dielectric relaxation has been observed in grey hematite.

### 6.2.2 Implications of the Temperature Dependent Dielectric Relaxation of Grey Hematite for MARSIS, SHARAD, and Future GPR Missions

Figure 6.1 shows the maximum GPR depth of penetration of the two grey hematite samples at their measured densities. The 160 K curve for GHKwMI becomes less frequency dependent because the relaxation frequency of grey hematite at this temperature is 17 MHz. The range in depth of penetration at MARSIS and SHARAD frequencies varies by one and one-half orders of magnitude for GHKwMI. With such large variations, the temperature dependent dielectric relaxation of grey hematite could be used to map areas of grey hematite or remotely measure the temperature profile of a grey hematite soil. However, the Martian subsurface would never experience the temperature extremes shown in Figure 6.1. Therefore, thermal modeling and soil models that account for density variations versus depth and concentration of grey hematite were used to better describe how temperature may affect GPR loss and velocity.

#### 6.2.2.1 Thermal Modeling of the Martian Subsurface

The Viking thermal model was used to constrain the Martian surface temperatures [Kieffer, 1977; Jakosky, 1981]. Using this data, two sinusoids were determined, one to match the period of a Martian day (sol) and the other to match the period of a Martian year (669 sols). Equation 6.1 (diurnal variations) and Equation 6.2 (diurnal and annual variations, hereafter referred to as annual variations) were then used to model the temperature in the subsurface as a function of depth,  $z$ , and time,  $t$ , for a complete annual cycle [Carslaw and Jaeger, 1954]. The maximum and minimum subsurface temperatures were determined as a function of depth to determine the hot and cold soil temperature envelopes at latitudes of 35°N, 0°, and 35°S.

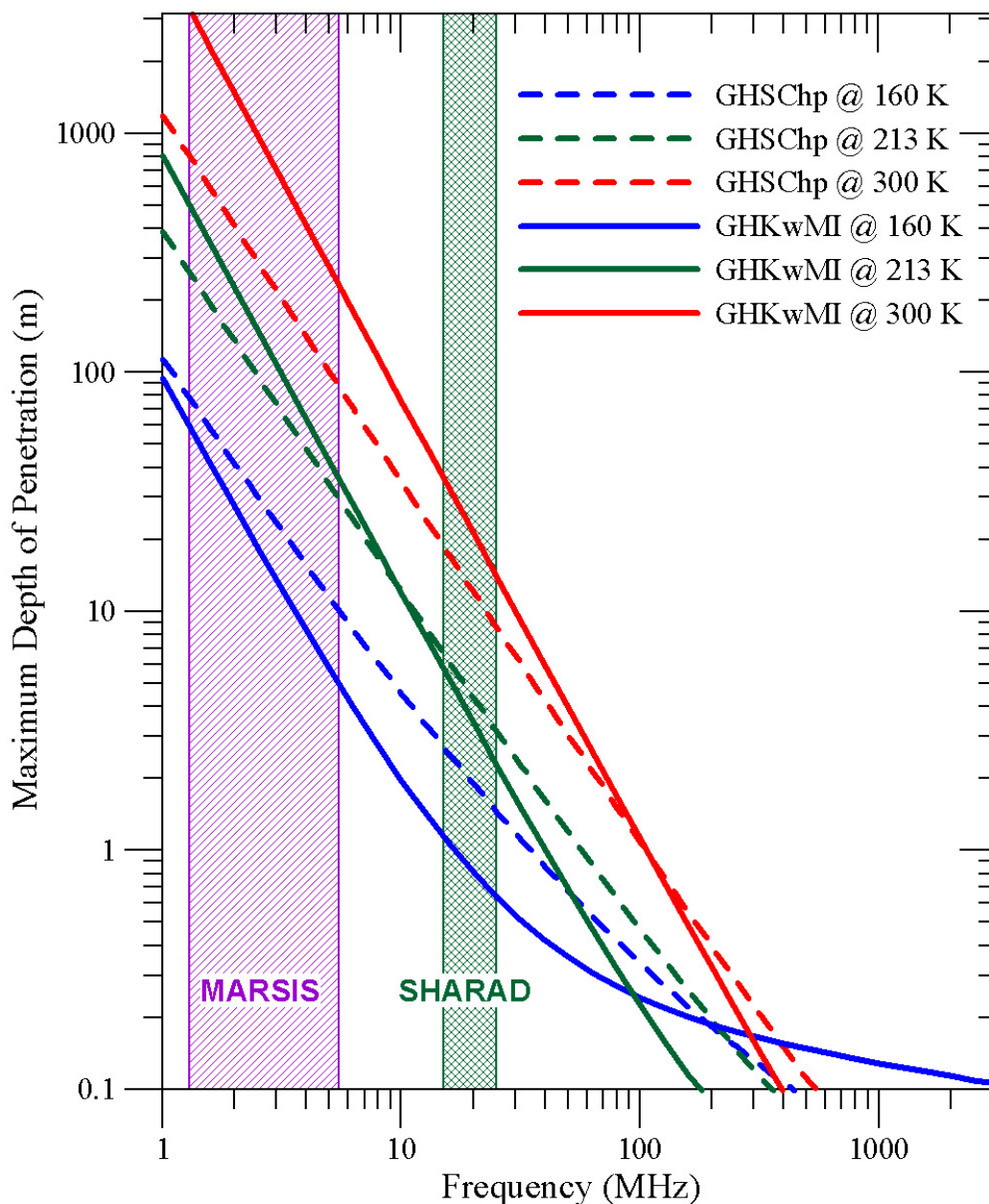


Figure 6.1. Maximum depth of penetration of the two measured grey hematite samples. The three temperature curves assume 100% grey hematite at a density of 3.11 g/cc and 2.40 g/cc for GHKwMI and GHSChp, respectively. The MARSIS and SHARAD radar systems were assumed to have a dynamic range of 50 dB. A perfect reflector at the maximum depth of penetration and no other losses other than the dielectric loss of grey hematite were assumed.

$$T(z,t) = T_o + T_d e^{\sqrt{n_d \rho c / 2k} z} \sin\left(\omega t - \sqrt{n_d \rho c / 2k} z\right) \quad (6.1)$$

$$T(z,t) = T_o + T_a e^{\sqrt{n_a \rho c / 2k} z} \sin\left(\omega t - \sqrt{n_a \rho c / 2k} z\right) + T_d e^{\sqrt{n_d \rho c / 2k} z} \sin\left(\omega t - \sqrt{n_d \rho c / 2k} z\right) \quad (6.2)$$

where (units are given in parenthesis, while values or tables of values are given in square brackets):

T = temperature as a function of depth and time (K) [Fig 7]

T<sub>o</sub> = average temperature (K) [Table 6.1 and 6.2]

T<sub>a</sub> = half of total annual variation (K) [Table 6.1]

T<sub>d</sub> = half of total diurnal variation (K) [Table 6.1 and 6.2]

n<sub>a</sub> = number of cycles during the annual cycle [1]

n<sub>d</sub> = number of cycles during the diurnal cycle [669]

ρ = density (g/cc) [Equation 6.3]

ω = frequency of the annual cycle (Hz) [1.0576 × 10<sup>-7</sup>]

c = specific heat capacity (Jkg<sup>-1</sup>K<sup>-1</sup>) [0.1]

k = surface thermal conductivity (Wm<sup>-1</sup>K<sup>-1</sup>) [800]

Since little is known about the density profile of the Martian subsurface, a density profile was assumed based on Apollo 15 lunar cores, Equation 6.3 [Mitchell et al., 1972].

$$z = -0.01 + 3.23 \times 10^{-4} \times e^{0.00429\rho} + 1.9 \times 10^{-41} \times e^{0.0602\rho} \quad (6.3)$$

The three temperature parameters (T<sub>o</sub>, T<sub>a</sub>, T<sub>d</sub>) in Equations 6.1 and 6.2 are latitude dependent. The values for these parameters were found using the Viking thermal model [Jakosky, 1981]. Equations 6.1 and 6.2 assume that Martian surface temperatures vary as a sinusoid, but in reality, and in the Viking thermal model, they do not. To accommodate this assumption, the T<sub>a</sub> and T<sub>d</sub> parameters were separated into minimum and maximum values. (See Tables 6.1 and 6.2.) When calculating the cold temperature envelope, T<sub>a</sub><sup>min</sup> and T<sub>d</sub><sup>min</sup> values were used. Conversely, T<sub>a</sub><sup>max</sup> and T<sub>d</sub><sup>max</sup> were used to calculate the hot temperature envelope. This method produced diurnal variation temperature envelopes that closely matched Kieffer's 1977 temperature envelopes using the Viking thermal model as shown in Figure 6.2. Figure 6.3 depicts the two calculated envelopes at three different latitudes: latitude 0° has the largest known concentration of grey hematite at the

Martian surface, latitude  $35^{\circ}\text{N}$  has geologic evidence of an ancient ocean basin, and latitude  $35^{\circ}\text{S}$  is the location where the temperature varies the most over an annual cycle.

Table 6.1. Diurnal parameter values used in Equation 6.1.  $T_o^{\max}$  occurs during the summer while  $T_o^{\min}$  occurs during the winter. All temperatures are in Kelvin.

Latitude	$T_{\text{ave}}$	$T_{\text{a}}^{\min}$	$T_{\text{a}}^{\max}$	$T_{\text{d}}^{\min}$	$T_{\text{d}}^{\max}$
$35^{\circ}\text{N}$	207	22	12	24	51
$0^{\circ}$	215	9	9	36	63
$35^{\circ}\text{S}$	204	32	31	20	58

Table 6.2. Diurnal and annual temperature parameter values used in Equation 6.2. All temperatures are in Kelvin.

Latitude	Data Set	$T_{\text{d}}^{\min}$	$T_{\text{ave}}$	$T_{\text{d}}^{\max}$
$35^{\circ}\text{N}$	$T_o^{\max}$	39	219	48
	$T_o^{\min}$	24	185	48
$0^{\circ}$	$T_o^{\max}$	43	224	63
	$T_o^{\min}$	35	206	50
$35^{\circ}\text{S}$	$T_o^{\max}$	47	235	58
	$T_o^{\min}$	20	172	36

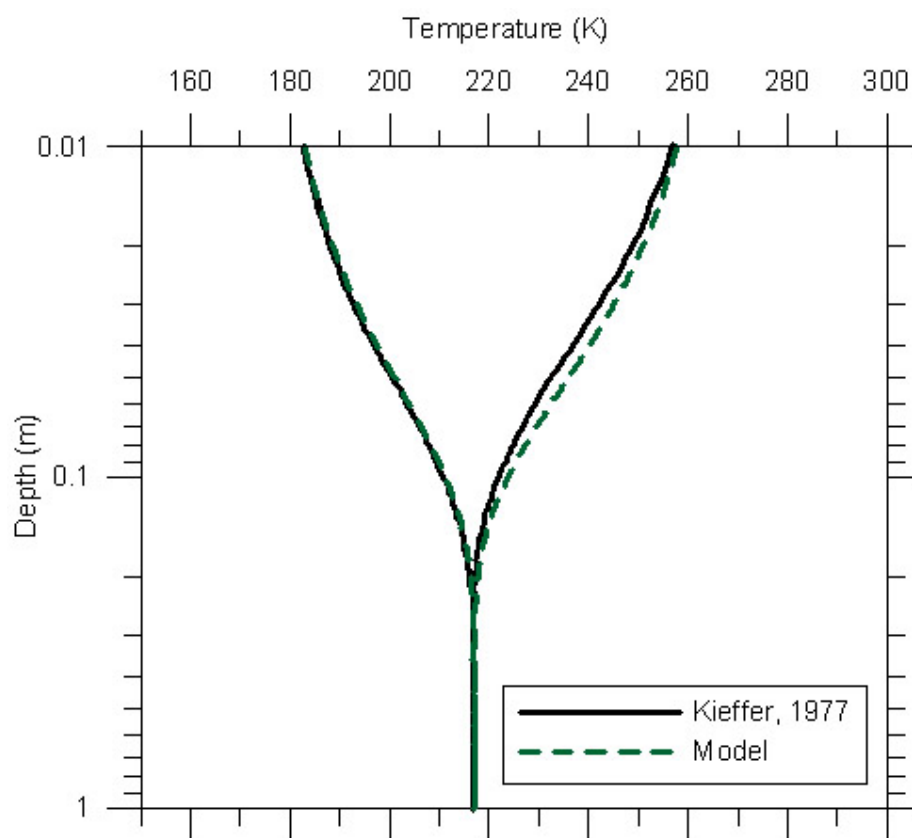


Figure 6.2. Temperature versus depth profile for a diurnal variation at the Viking 1 landing site (22°N). The black line shows Kieffer's model and the green dashed line shows the diurnal model used in this study.

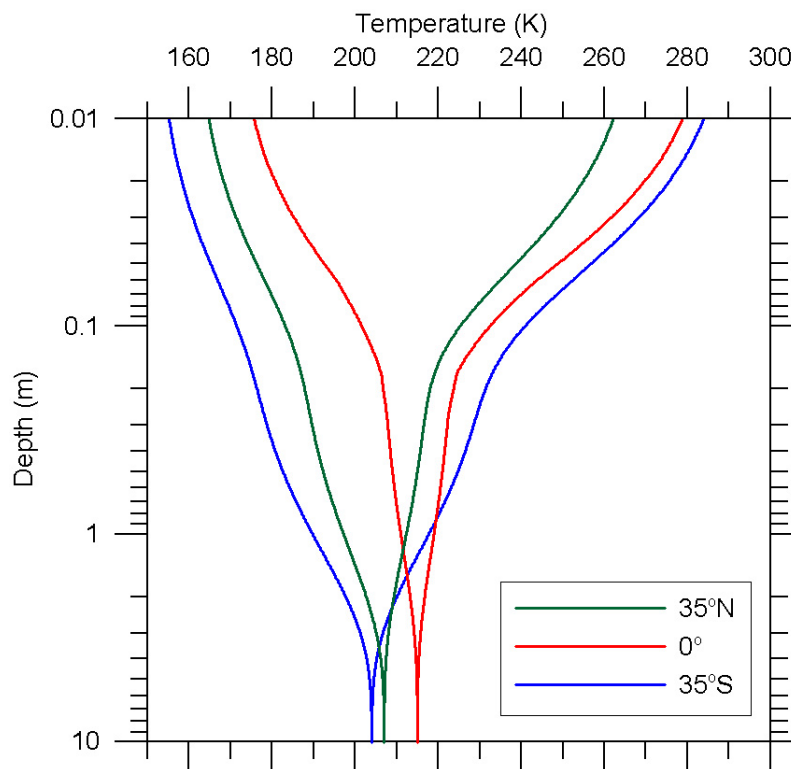


Figure 6.3. Temperature versus depth profile for seasonal and diurnal variations at three Martian latitudes.

#### 6.2.2.2 Dielectric Permittivity Modeling

At Meridiani Planum (Latitude 5°N – 6°S), the concentration of grey hematite in the lag deposits ranges from 5-15%, with the remaining composition being basaltic sediments [Christensen, 2001]. To simulate this material, the Bruggeman, Hanai, Sen (BHS) mixing equation (Equation 2.40) was used to simulate grey hematite combined with basaltic sediments. The Cole-Cole model values of the GHKwMI sample were used for grey hematite since it was a purer sample. For basaltic sediments, the Cole-Cole model values of the PuNeHIC (Pu'u Nene horizon C) sample were used. Once the mixed

complex dielectric permittivity was found, it was then converted into radar loss using Equation 6.5, which assumes a relative magnetic permeability of one.

$$A = 8.686 \frac{\omega Z}{c} \sqrt{\frac{\epsilon'_{MP}(\omega, T, \Omega)^2 + \epsilon''_{MP}(\omega, T, \Omega)^2}{2}} - \epsilon'_{MP}(\omega, T, \Omega) \quad (6.5)$$

where:

A = loss (dB)

c = speed of light in vacuum

$\epsilon'_{MP}(\omega, T, \Omega)$  = real part of the relative dielectric permittivity predicted for Meridiani Planum which is dependent on angular frequency, temperature, and grey hematite concentration

$\epsilon''_{MP}(\omega, T, \Omega)$  = imaginary part of the relative dielectric permittivity predicted for Meridiani Planum which is dependent on angular frequency, temperature, and grey hematite concentration

Figure 6.4 (annual) and Figure 6.5 (diurnal) show the difference (between hot and cold temperature envelopes) in two-way loss versus frequency of various grey hematite and Pu'u Nene horizon C concentrations at three Martian latitudes. The cusp in the loss difference curves is created because one temperature envelope (hot or cold) does not always create more loss than the other. The cusp location changes as a function of grey hematite percentage because the losses of the Pu'u Nene horizon C change the frequency at which the losses from both temperature envelopes are equal.

Figure 6.6 (annual) and Figure 6.7 (diurnal) show the real part of the relative dielectric permittivity profile at three frequencies and two latitudes at 100% and 20% grey hematite concentrations. The dielectric relaxation at the average temperature,  $T_o$ , causes the downward shift of the real part of the relative dielectric permittivity profile at increasing frequency, while increasing density causes the sharp increase in dielectric permittivity. EM properties also control the EM velocity in the ground. The EM velocity was calculated using Equation 2.21, and Figures 6.8 (annual) and 6.9 (diurnal) show the difference in two-way traveltime of a reflector that is below the subsurface zone of varying temperature.

## Annual Loss Difference

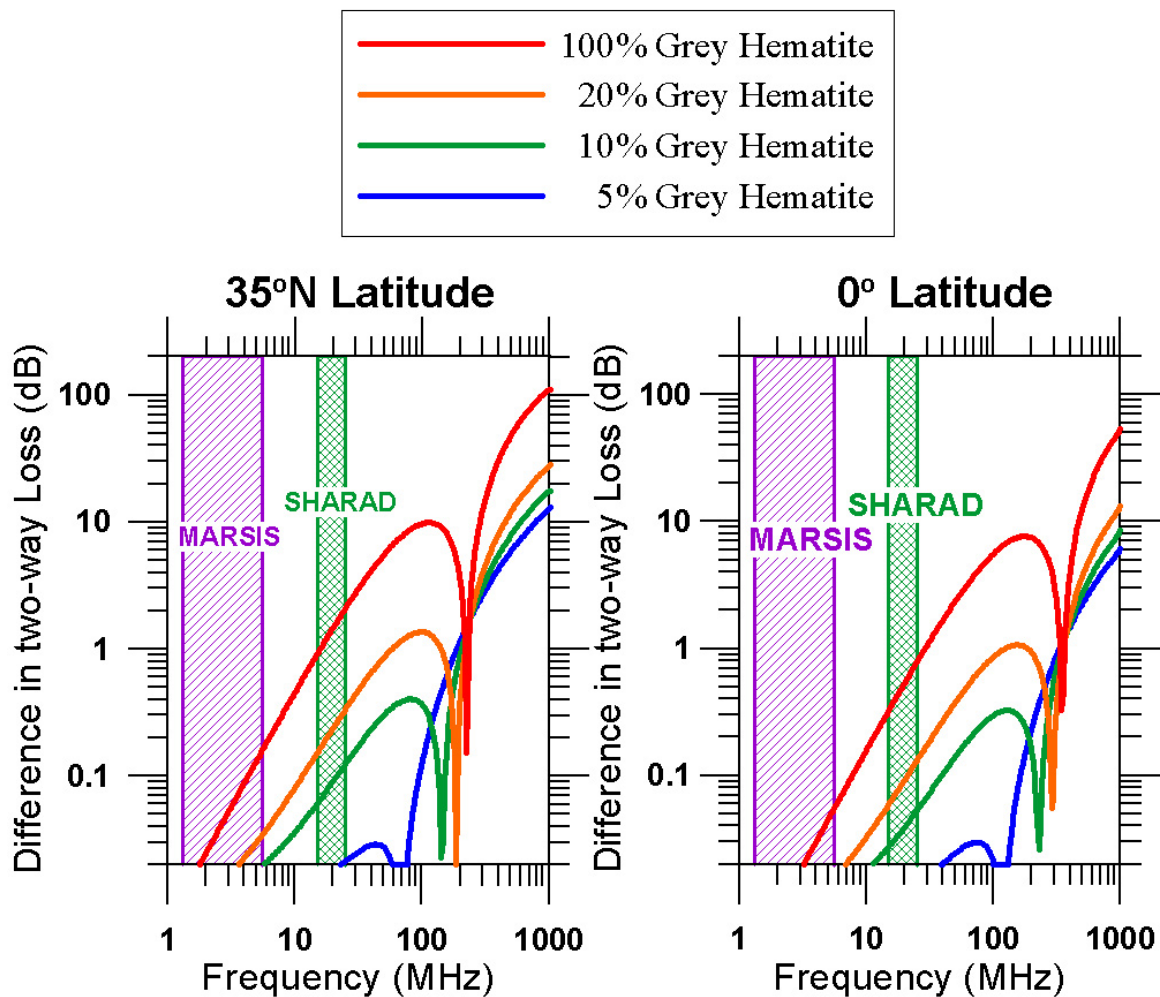


Figure 6.4. Difference in two-way loss with varying grey hematite concentrations mixed with Pu'u Nene horizon C at three different Martian latitudes with annual temperature variations.

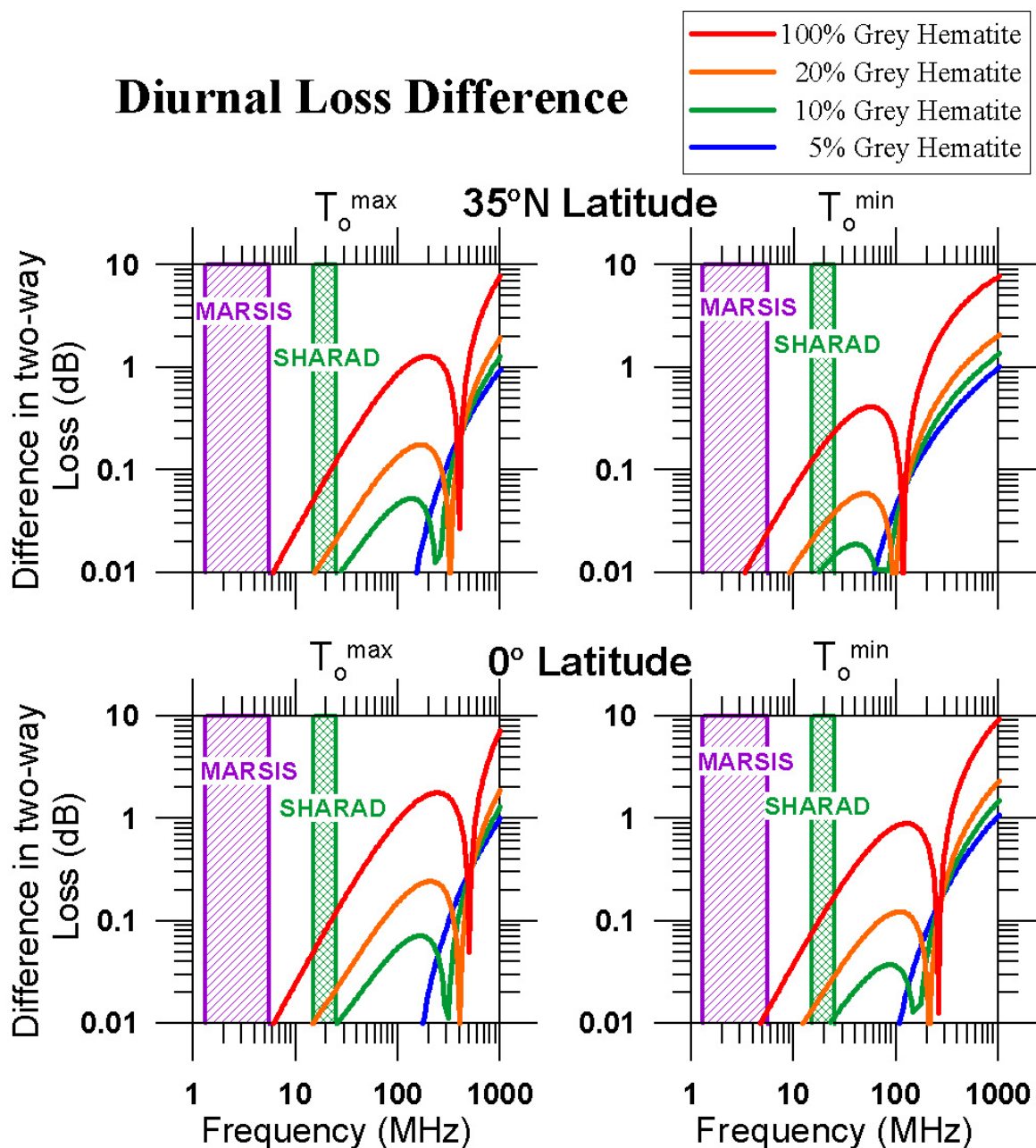


Figure 6.5. Difference in two-way loss with varying grey hematite concentrations mixed with Pu'u Nene horizon C. Each latitude has two graphs; the left graph shows the diurnal variation during summer or  $T_o^{\max}$ , while the right graph is when during winter or  $T_o^{\min}$ .

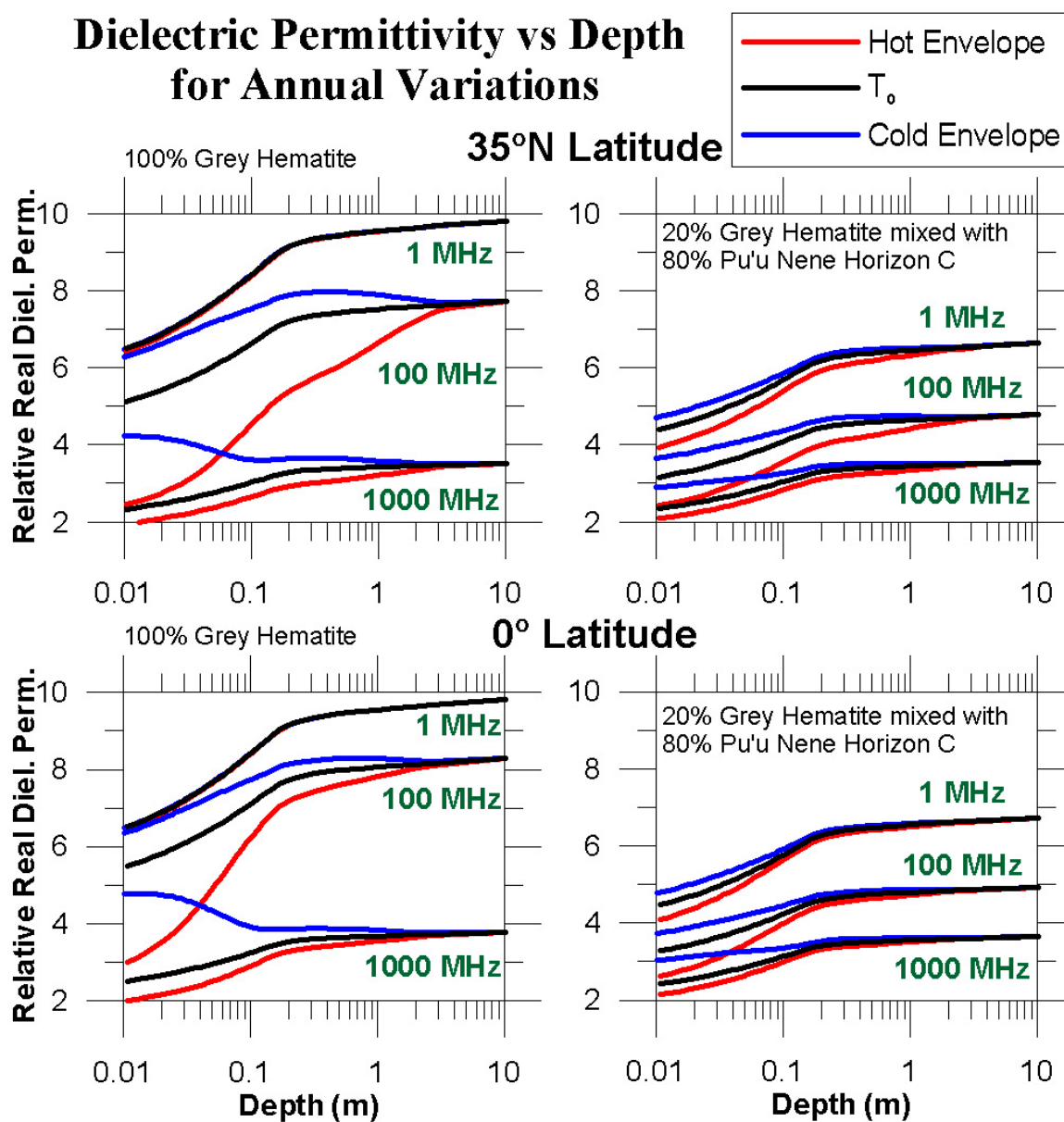


Figure 6.6. (Right) Real part of relative dielectric permittivity profile with 100% grey hematite at three frequencies and two latitudes for annual temperature variations. (Left) Real part of relative dielectric permittivity profile with 20% grey hematite and 80% Pu'u Nene horizon C at three frequencies and two latitudes for annual temperature variations.

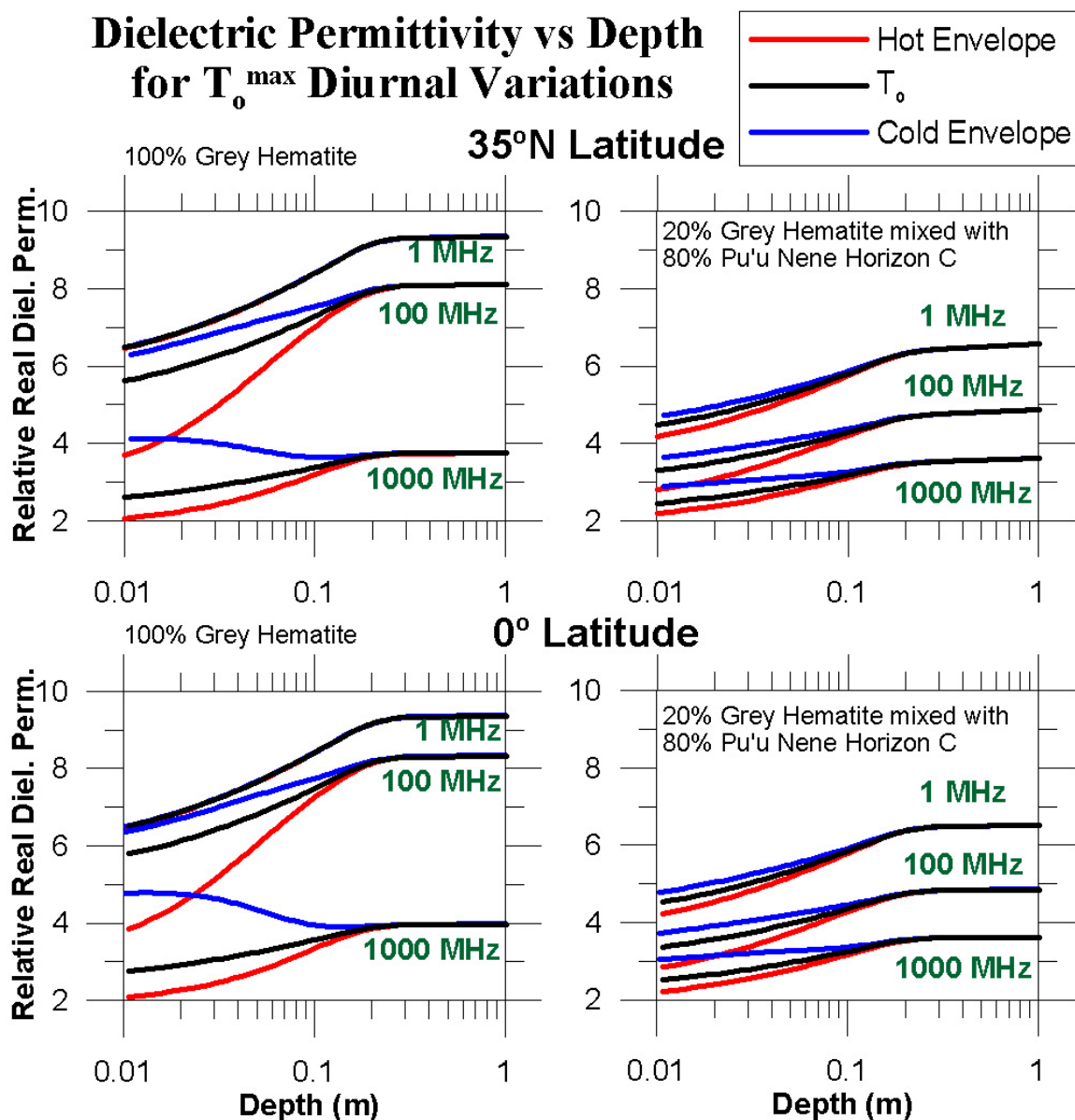


Figure 6.7. (Right) Real part of relative dielectric permittivity profile with 100% grey hematite at three frequencies and two latitudes for diurnal temperature variations during summer or  $T_o^{\max}$ . (Left) Real part of relative dielectric permittivity profile with 20% grey hematite and 80% Pu'u Nene horizon C at three frequencies and two latitudes for diurnal temperature variations during summer or  $T_o^{\max}$ .

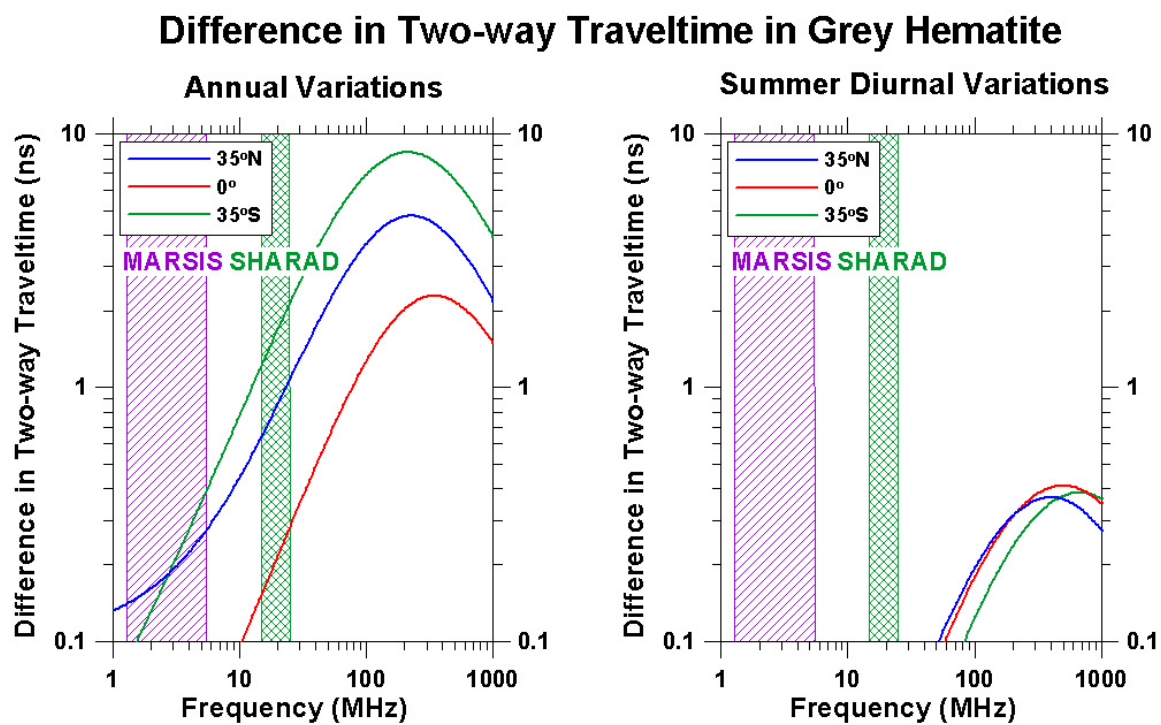


Figure 6.8. Difference in two-way traveltime in grey hematite versus latitude for annual variations (left) and diurnal variations during summer or  $T_o^{\max}$  (right).

## Difference in Two-way Traveltime in Grey Hematite mixed with Pu'u Nene Horizon C at the Martian Equator

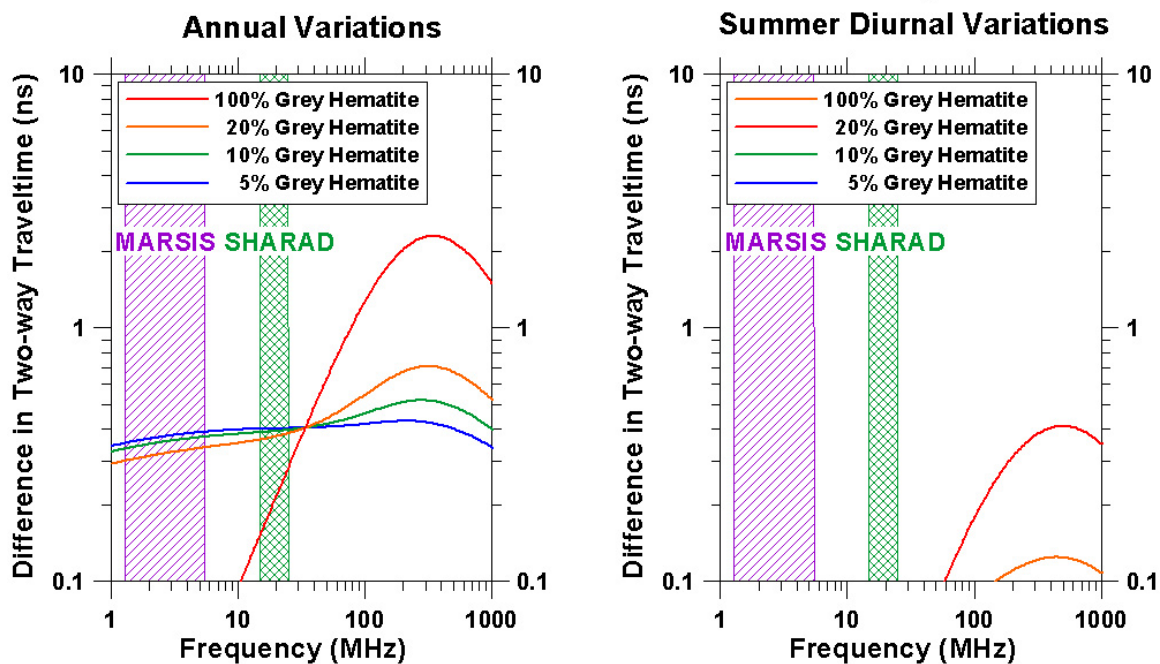


Figure 6.9. Difference in two-way traveltime in grey hematite versus concentration for annual variations (left) and diurnal variations during summer or  $T_o^{\max}$  (right).

### 6.2.2.3 Thermal Modeling Results

Unfortunately, the diurnal temperature cycle only penetrates about 20 cm into the subsurface while the annual cycle penetrates about 3 m. This means that radar measurements must be sensitive to changes in the first 20 cm of the subsurface to detect diurnal changes or 3 m to detect annual changes. Therefore, the frequencies of MARSIS and SHARAD possess wavelengths that are too large to detect any diurnal or annual subsurface temperature changes. As shown in Figures 6.4 and 6.5, the difference in loss increases as frequency increases. This means the reflection strength will change as a

function of the subsurface temperature. Figures 6.6, and 6.7 show how the dielectric permittivity of the subsurface can change as a function of the subsurface temperature. This will produce a change in near surface reflectance as the contrast between near surface layers changes as a function of the subsurface temperature. This effect will be greatest at high frequencies due to the increased resolution (lower wavelength). If the grey hematite is concentrated in concretions as it is at Meridiani Planum, then changes in EM scattering off these concretions would be temperature dependent. Increased scattering would occur at cold temperatures due to the larger dielectric contrast between the bedrock material and the concretions. However, only EM energy with a frequency greater than 3 GHz would have enough spatial resolution to resolve individual concretions.

Since dielectric permittivity changes as a function of depth, so too does the EM velocity. Consequently, the two-way traveltime of any reflection will change depending on the temperature of the subsurface. Figures 6.8 and 6.9 show that change is maximized in the frequency range from 215-345 MHz for the annual temperature cycle and 390-670 MHz for the diurnal temperature cycle. The subsurface EM property changes are small, but measurable by GPR at the correct frequency. Overall, a radar frequency of about 650 MHz would maximize the differences seen in loss, near surface reflectance, and two-way traveltime to measure diurnal temperature variations. Likewise, a lower frequency of about 340 MHz would suffice to measure annual temperature variations.

### 6.3 Magnetite

Magnetite had been debated as the mineral causing the magnetic properties of the global Martian dust layer since Viking [Hargraves, 1979; Hviid et al., 1997, 1998; Madsen et al., 1999; Hargraves et al., 2000; Morris et al., 2001]. However, it was not until the Mössbauer spectroscopy measurements were made by both Spirit (MER-A) and Opportunity (MER-B) that magnetite was accepted as the mineral causing the magnetic

properties of the Martian dust [Morris et al., 2004; Bertelsen et al., 2004; Madsen et al., 2005; Goetz et al., 2005; Yen et al., 2005]. Not only is magnetite in the dust layer, but it has also been found in basaltic rocks at Gusev crater and it is the most likely mineral causing the remnant magnetic field of Mars [Dunlop and Arkani-Hamed, 2005]. The percentage of magnetite in the global Martian dust layer is about 2% by volume [Morris et al., 2004; Bertelsen et al., 2004; Madsen et al., 2005; Goetz et al., 2005; Yen et al., 2005], while the crust has been estimated at 0.2-0.4% by volume [Dunlop and Arkani-Hamed, 2005]. The estimation of the crust only includes singledomain magnetite, therefore the total magnetite concentration may be larger.

Magnetite samples measured in this study possess a temperature independent magnetic relaxation at relatively high frequencies. The largest relaxation was observed in a magnetite rich sample from the Champion mine dump in Michigan (MagRCh). This sample has the lowest relaxation frequency at 199 (+22, -19) MHz. Magnetite from Peru (Magn) possesses a relaxation frequency of 579 ( $\pm 19$ ) MHz. Magnetite found in a stream bed near Yuma, Arizona (Yuma) possesses a relaxation frequency of 540 (+221, -345) MHz. No magnetic relaxations were measured in the grey hematite sample from the Champion mine dump (GHSChp), which also possesses about 10% magnetite and has a magnetic permeability of 1.22 ( $\pm 0.03$ ). However, any magnetic relaxations occurring with a frequency greater than 400 MHz would not have been detected due to resonance.

Magnetite also possesses a frequency independent dielectric permittivity that is above its predicted density derived electronic polarization value. This indicates that magnetite possesses a dielectric relaxation at frequencies greater than 800 MHz. The following sections will explain the cause of the temperature independent magnetic relaxation in magnetite and the implications of this loss mechanism for future GPR missions.

### 6.3.1 Temperature Independent Magnetic Relaxation Mechanism of Magnetite

The magnetic relaxations observed in magnetite samples in this study are believed to be caused by magnetic domain wall displacement. Evidence for this mechanism include the following: the relaxations were temperature independent, the relaxations possessed a relaxation frequency in the range of 177-884 MHz, and magnetite has multidomain grains. While magnetic domains can change as a function of temperature [Dunlop and Özdemir, 1997], the magnetic permeability measurements in this study were only sensitive to the way magnetic domains move in response to an external magnetic field as a function of temperature. The measurements in this study show that magnetic domain displacement is not sensitive to temperature from 180 – 300 K. However, none of the samples were measured near their Curie temperature where magnetic domain displacement may be sensitive to temperature. Above the Curie temperature, no magnetic relaxations could exist because the low frequency limit of the relative magnetic permeability would be one. Therefore, magnetic relaxations must be temperature dependent near the Curie temperature of the mineral and could be in the Martian temperature range if enough titanium was present to lower their Curie temperatures.

### 6.3.2 Implications of the Temperature Independent Magnetic Relaxation of Magnetite for MARSIS, SHARAD, and Future GPR Missions

Figure 6.10 shows the GPR maximum depth of penetration for the three magnetite samples that contained measurable magnetic losses. The figure shows that the maximum GPR depth of penetration significantly varies depending on the magnetite concentration. The Magn and the MagRCh samples are composed of almost entirely magnetite. The Magn sample may have a lower magnetic loss because it contains more titanium impurities in its crystal structure or has a different grain size. The Yuma sample is not only comprised of magnetite, but also has a sand component as well. This explains why the Yuma sample has lower magnetic losses. Lastly, the Martian magnetic global dust

layer was modeled by mixing 2% by volume of the MagRCh sample with 98% by volume of the synthetic hematite sample (FeOxd). At such a low concentration of magnetite, the maximum GPR depth of penetration is greater than 5 km at all frequencies.

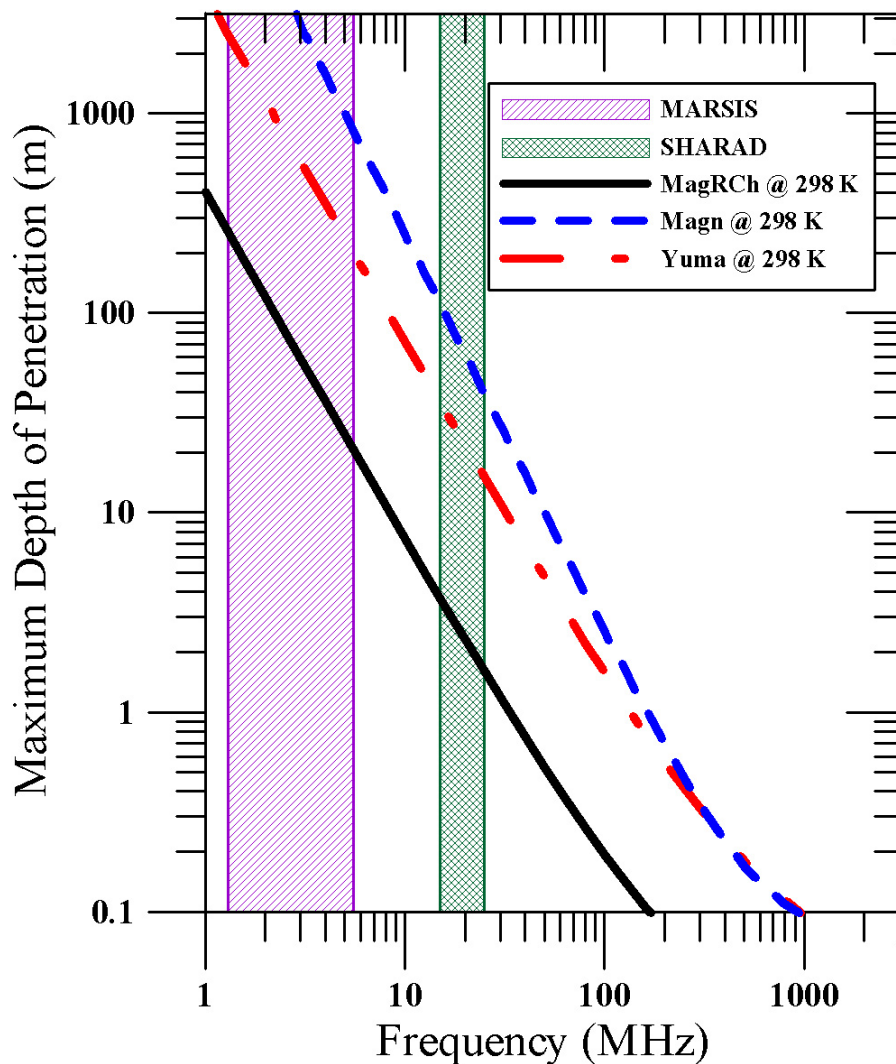


Figure 6.10. GPR maximum depth of penetration of the three magnetite samples that possessed measurable magnetic losses at their measured densities. The MARSIS and SHARAD radar systems were assumed to have a dynamic range of 50 dB. A perfect reflector at the maximum depth of penetration and no other losses other than the magnetic loss of magnetite were assumed.

#### 6.4 Implication of EM Losses of Other Martian Analog Samples for MARSIS, SHARAD, and Future GPR Missions

JSC Mars-1 and Pu'u Nene horizon C samples possess a small, broad, dielectric relaxation. This relaxation is believed to be caused by an interfacial polarization mechanism because of its large distribution in the time constant of relaxation. Both of these samples are primarily composed of plagioclase feldspar. Plagioclase feldspar is not a mineral type, but rather a combination of two minerals: albite ( $\text{NaAlSi}_3\text{O}_8$ ) and anorthite ( $\text{CaAl}_2\text{Si}_2\text{O}_8$ ). The composition of plagioclase feldspar becomes more albite rich as the magma cools [Wenk and Bulakh, 2004]. This process is known as zoning, as the concentration of albite and anorthite varies in concentric layers. The interfacial polarization mechanism can arise from the electrical differences between these concentric layers. Since this relaxation is small, it means that the contrast in electrical properties is also small, which is consistent with this explanation. The large distribution in the time constant of relaxation, which causes the broad dielectric relaxation, occurs because the concentric layers of plagioclase feldspar vary in size.

Plagioclase feldspar is also a major component of both intrusive and extrusive igneous rocks. On Earth, about 60% of the volume of the continental crust is composed of plagioclase feldspar [Chernicoff and Venkatakrisnan, 1995]. Not only is the Martian surface dominated by igneous flows, but spectral models of both surface type 1 and 2 have estimated plagioclase feldspar content to be between 30-60% by volume [Wyatt and McSween, 2002]. Therefore, this small broad dielectric relaxation loss mechanism may limit the maximum GPR depth of penetration on Mars as is shown in Figure 6.11. The plagioclase in PuNeHIC gives a maximum GPR depth of penetration at MARSIS frequencies of 70 m and 15 m at SHARAD frequencies. The plagioclase in JSC1 gives a maximum GPR depth of penetration at MARSIS frequencies of 200 m and 30 m at SHARAD frequencies. It is difficult to tell from the XRD results which sample possess more plagioclase feldspar, but the EM measurements suggest PuNeHIC possess more.

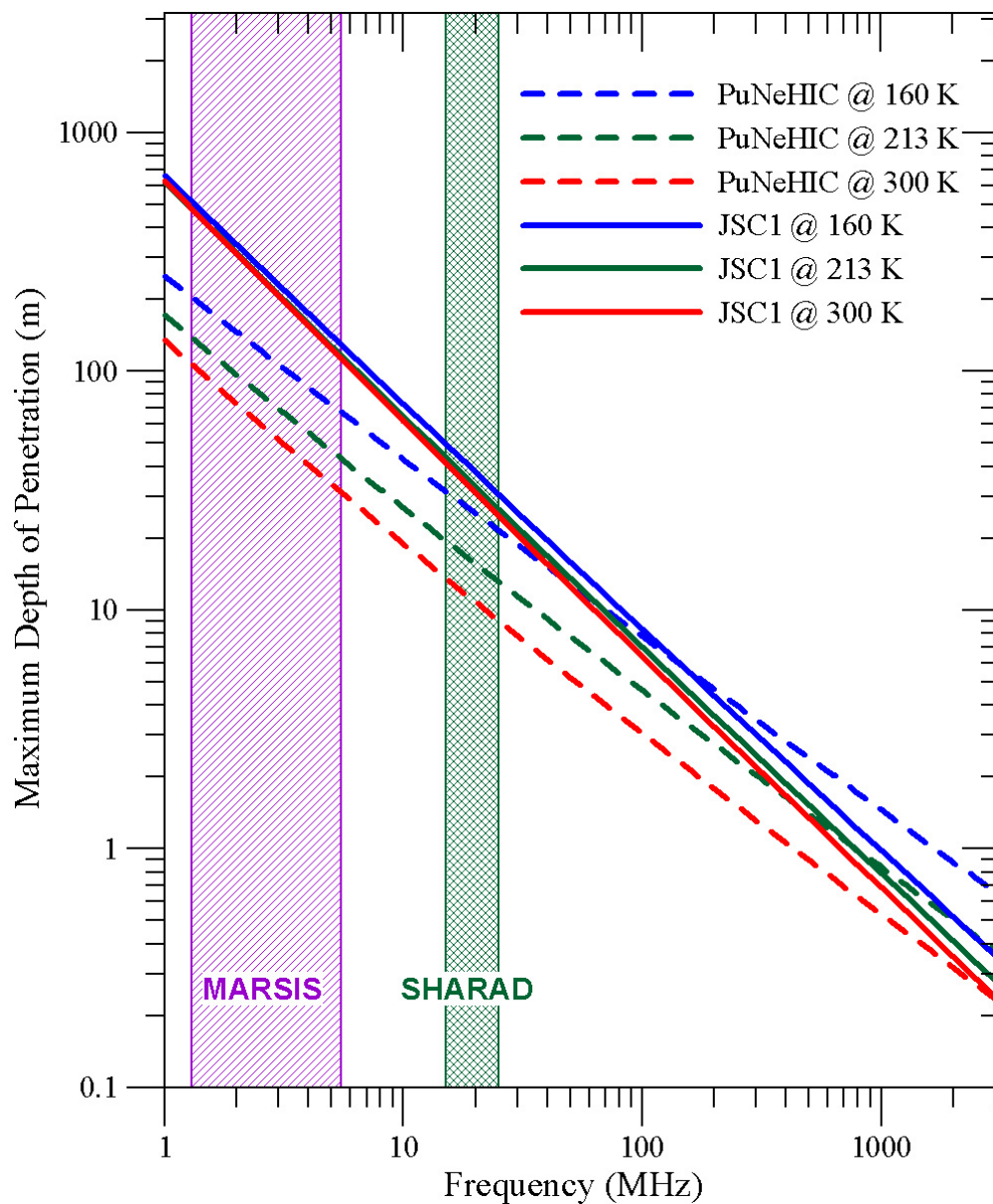


Figure 6.11. GPR maximum depth of penetration for Mars JSC-1 (JSC1) and Pu'u Nene horizon C (PuNeHIC) at their measured densities. Both of these samples are primarily composed of plagioclase feldspar, which is believed to be responsible for a interfacial polarization loss mechanism.

The maghemite (Hem) sample measured in this study possesses a frequency independent magnetic permeability of  $1.28 \pm 0.02$  at radar frequencies. However, the magnetic permeability high frequency limit must relax to a value of one at frequencies greater than 1 GHz (highest frequency measured with this sample). Other Martian analogs measured in this study including red hematite, jarosite, and olivine all possess no measurable EM losses. Thus, GPR depth of penetration will likely be limited by other factors such as scattering losses in these minerals.

### 6.5 Conclusion

Results from these measurements yielded several significant EM relaxations in Martian analog minerals that had never before been observed. This study also found that dielectric relaxations of Martian analogs do vary as a function of temperature. Therefore, lab measurements of EM properties must be made at Martian temperatures. As shown in Figure 6.1, there is a half order of magnitude difference between the maximum depth of penetration at terrestrial room temperature (298 K) and at Martian average temperature (213 K). Surprisingly, the magnetic relaxations that were measured did not vary as a function of temperature. However, ferromagnetic and ferrimagnetic materials near their Curie temperature must be temperature dependent. The GPR maximum depth of penetration for Martian analog samples with EM relaxations is shown in Figures 6.1, 6.10 and 6.11. This reveals that the maximum depth of GPR penetration may be much less than 5 km and 1 km as predicted for MARSIS and SHARAD, respectively.

The only magnetic relaxations that can significantly affect GPR are ferromagnetic and ferrimagnetic minerals. This is because they are the only type of magnetic materials that can have a magnetic permeability greater than 1.05. Magnetic relaxations were also found to possess narrow (high  $\alpha$ ) relaxations. This is important because it means that magnetic relaxations cause attenuation only over a narrow frequency range. These magnetic relaxations were found to only occur at relatively high frequencies  $>200$  MHz.

Lastly, because magnetic properties interact low concentrations of magnetite will not cause significant attenuation. Therefore, EM energy at GPR frequencies should not significantly be attenuated through the global magnetic dust layer.

Not all of Mars will be comprised of minerals that have large dielectric or magnetic relaxation losses. However, plagioclase feldspar was found to possess a small, broad, dielectric relaxation. Plagioclase feldspar is widespread on Mars due to the large number of igneous rocks. Both surface type 1 and 2 have been modeled to contain plagioclase feldspar anywhere from 30-60% by volume. Therefore, this small, broad, dielectric relaxation loss mechanism may limit the maximum GPR depth of penetration of Mars to 70– 200 m at MARSIS frequencies and 15 – 30 m at SHARAD frequencies as is shown in Figure 6.11.

Other losses that were neglected in this study could become significant for a Martian GPR mission including geometric spreading, scattering [Grimm et al., 2005], ionospheric dispersion, attenuation, Faraday rotation [Farrell, 2005], and conduction losses if clays are found in the subsurface. Furthermore, when searching for groundwater, a gradual water/ice interface or large capillary fringe could also reduce the depth at which radar could image a target [Beaty et al., 2001]. Even if a GPR signal is received from a Martian aquifer, radar alone cannot uniquely identify this signal as a reflection from a Martian aquifer. However, if other instruments also detect an aquifer signal, this greatly increases the chance of a true Martian aquifer being identified. GPR can be used to identify many other potential shallow targets including subsurface stratigraphy and rover hazards. It can give geological context to these shallow drilling targets.

## CHAPTER 7

### FUTURE WORK

#### 7.1 Introduction

The EM properties of Martian soils will dictate if an EM (GPR or induction) mission to Mars will succeed or fail. Before making the investment to send an EM instrument to Mars, laboratory EM property measurements should be completed on Earth. This study provides a good foundation for Martian analog EM property measurements that can be expanded in a number of different ways. First, the temperature range of the measurements could be increased. Second, additional hematite, magnetite, and maghemite samples should be measured along with other recently discovered Martian analogs including sulfates, clays, and salts. Third, other measurement techniques (slotted lines, resonant chambers, and impedance analyzers) should be investigated to increase the frequency range and accuracy of the EM property measurements. Lastly, EM properties versus frequency, temperature, and water/ice content should be measured so that the Martian subsurface can be better modeled. Each of these topics will be addressed in this chapter.

#### 7.2 Temperature Range Improvements

The temperature range of the current measurement apparatus is 180 – 300 K. Measurements acquired over a broader temperature range could better constrain the Cole-Cole and Boltzmann parameters. Surface temperatures near the north and south pole of Mars are much colder (154 K) and may be of greater interest due to the near surface ground ice in the poleward latitudes  $\pm 50^\circ$ . In order to decrease the temperature in the

existing measurement apparatus, the So-Low Ultra-Low freezer could be used with liquid nitrogen (77.2 K). However, accurately measuring temperature and maintaining a constant cold temperature are both problems with this technique. To measure temperatures below 193 K, platinum resistive temperature devices would have to be used. These devices are similar to thermistors, but their resistance versus temperature does not change as drastically as thermistors. Consequently, a voltmeter with a much larger dynamic range (24 bit) would be necessary to measure the platinum resistive temperature devices to the nearest 0.2 K.

As the measurement temperature decreases, thermal contraction of the cables becomes a greater problem. Thermal contraction of the cables can be addressed by either determining a way to process it out, or by changing the measurement apparatus. If the complex magnetic permeability or the complex dielectric permittivity of a sample does not change as a function of temperature, then it may be possible to calculate the change in the cable's electrical length with temperature and thus process this change out. It may also be possible to alter the measurement apparatus so that only the sample holder's temperature is changed and not the cable's temperature.

### 7.3 Additional Martian Analog EM Measurements

The iron oxide Martian analogs measured in this study were found to possess relatively large EM attenuation mechanisms that could significantly hamper GPR depth of penetration. Measurements of additional iron oxide samples are necessary to better constrain the EM properties of grey hematite, magnetite, and maghemite. Improved characterization (grain size, XRD, IR, chemistry, and Curie temperatures) of these samples would also aid in understanding what causes the changes in the EM properties of these minerals. To more effectively constrain the temperature dependent dielectric relaxation of grey hematite, it would be interesting to measure additional hematites with different crystal grain size (red and grey) and different formation mechanisms (low and

high temperature, water and volcanic). The magnetic relaxations observed in this study were not temperature dependent. Measuring additional magnetite and maghemite samples with large titanium impurities may show that magnetic relaxations are indeed temperature dependent. For this study, only one maghemite sample was measured. Additional maghemite sample measurements are needed to determine if all maghemites possess magnetic relaxations at greater than 1 MHz. Magnetic interaction measurements also need to be made so that more precise magnetic mixing formulas can be determined.

For this study, Martian analog selection was constrained to iron oxides because they were believed to contain the greatest loss of any Martian analogs. However, recent discoveries have shown that sulfates, clays, and salts (Mg, Br, and Cl) are present on Mars. These new Martian analogs could also possess large EM attenuation mechanisms. Therefore, additional Martian analogs should be measured to better understand how GPR will perform on Mars and to improve GPR interpretation.

#### 7.4 EM Property Measurement Improvements

To better constrain the potential EM losses of the samples that were found to possess no measurable losses, a slotted line and/or resonant chambers could be used to measure the EM losses to a loss tangent of about  $10^{-4}$ , which is about an order of magnitude better than the current VNA apparatus. These measurements could also be made as a function of temperature. However, they cannot maintain their high level of accuracy over a broad frequency range unless many sample holders were constructed.

The EM losses of Martian analogs could be better constrained by making measurements at frequencies larger than the first resonant frequency. This could be accomplished by using the resonant frequencies as data points. These resonant frequencies are a function of the complex dielectric permittivity and complex magnetic permeability of the sample. Therefore, it is possible to measure the complex dielectric permittivity at a resonant frequency by assuming the complex magnetic permeability or

vice versa. Baker-Jarvis [1990, 1993] has done this with high frequency VNA measurements near 20 GHz. However, this method has a much larger error than non-resonance measurements because resonant frequencies in the frequency range of the 8753D VNA are not as distinct as those seen in the Baker-Jarvis setup. (It is unknown why the resonant frequencies measured in this study had such a broad frequency range.)

As discussed in Chapter 6, alternate geophysical methods such as EM induction may be necessary to detect water on Mars [Grimm, 2002]. EM induction could be used to search for the temperature dependent dielectric relaxation that is consistent with frozen water (kHz range). It could also be used to detect a conductive layer of saline groundwater under the ice rich subsurface. Unfortunately, the dielectric relaxation of frozen water and conductive layers is not unique to water. Therefore, additional low frequency EM property measurements of Martian analogs are necessary to determine if any Martian analog minerals possess similar dielectric or magnetic relaxations in the same frequency range as water. These low frequency EM property measurements will most likely be made with impedance analyzers. In order to measure complex dielectric permittivity and complex magnetic permeability at low frequencies (<1 MHz), different sample holders have to be used. Currently, complex magnetic permeability measurements are made using smaller sample sizes than those used in complex dielectric permittivity measurements. Therefore, it is important to understand whether small sample sizes bias the measurements. In order to be sure sample size does not influence these measurements, larger sample holders may need to be created.

Some low frequency measurements were made concurrent with this study. The magnetic susceptibility of 75 magnetite and 109 hematite (both red and grey) samples from the Colorado School of Mines Geology Museum was measured at a frequency of 600 Hz. (These measurements can be found on the DVD or Stillman et al., 2006). The magnetic susceptibility of the magnetite samples is very well constrained [Stillman et al., 2006]. However, the magnetic susceptibility of the hematite samples varies over five orders of magnitude [Stillman et al., 2006]. This variation could be caused by small

magnetite impurities, grain size differences, or formation differences. It is unknown if these magnetic variations cause variation in the dielectric permittivity as well. The two grey hematite samples measured in this study both possess a dielectric relaxation loss at nearly the same frequency, but their formation and grain size were also similar.

### 7.5 EM Property Measurements Versus Water/Ice Content

While the EM properties of dry Martian analogs constrain the depth of penetration of EM exploration, these measurements depend on mixing models to determine the EM properties at the target zone of EM exploration. Mixing models are only accurate when none of their assumptions are violated. Unfortunately, water almost always violates the assumption of electromagnetic interactions. Therefore, to better understand the EM properties of the Martian subsurface, Martian analog EM properties should also be measured versus frequency, temperature, and water/ice content. It is also important to understand how salts and capillary pressures affect EM properties by lowering the freezing point of water. Hydrates have been theoretically predicted on Mars [Pellenbarg, et al., 2003; Max and Clifford et al., 2003]; therefore their EM properties need to be investigated.

## REFERENCES CITED

- Acuña M.H., J.E.P. Connerney, N.F. Ness, R.P. Lin, D. Mitchell, C.W. Carlson, J. McFadden, K.A. Anderson, H. Rème, C. Mazelle, D. Vignes, P. Wasilewski, and P. Cloutier, 1999, Global Distribution of Crustal Magnetization Discovered by the Mars Global Surveyor MAG/ER Experiment, *Science*, v. 284, p. 790-793.
- Acuña, M. H., J. E. P. Connerney, P. Wasilewski, R.P. Lin, D. Mitchell, K.A. Anderson, C.W. Carlson, J. McFadden, H. Rème, C. Mazelle, D. Vignes, S.J. Bauer, P. Cloutier, N.F. Ness, 2001, Magnetic field of Mars: Summary of results from the aerobraking and mapping orbits, *J. Geophys. Res.*, v. 106, p. 23403 – 23418.
- Adams, S.F., 1969, *Microwave Theory and Applications*: Prentice-Hall, Inc., New Jersey, 513 p.
- Adler, R.B., Chu, L.J., and Fano, R.M., 1966, *Electromagnetic energy transmission and radiation*, Wiley, NY, 621 p.
- Agilent, 2000, Agilent AN 154 S-Parameter Design, Agilent Application Note, 43 p.
- Allen, C.C., R.V. Morris, D.J. Lindstrom, M.M. Lindstrom, and J.P. Lockwood, 1997, JSC Mars-1: Martian Regolith Simulant, 28<sup>th</sup> Lunar and Planetary Science Conference, March 17-21, 1997 Houston, Texas, abstract #1797.
- Allen, C.C., R.V. Morris, K.M. Jager, D.C. Golden, D.J. Lindstrom, M.M. Lindstrom, and J.P. Lockwood, 1998, Martian Regolith Simulant JSC Mars-1, 29<sup>th</sup> Lunar and Planetary Science Conference, March 16-20, 1998, Houston, Texas, abstract #1690.
- Allen, C.C., K.M. Jager, R.V. Morris, D.J. Lindstrom, M.M. Lindstrom, and J.P. Lockwood, 1998, Martian Soil Simulant Available for Scientific Educational Study, *EOS*, v. 79, p. 405, 408-409.
- Allen, C.C. and R.V. Morris, 1999, Forum: Caution advised on Suitability of a Mars Soil Simulant: Reply, *EOS*, v. 80, p. 169.
- Arkani-Hamed, Jafar, 2005, Magnetic Crust of Mars, *J. Geophys. Res.*, v. 110, E08005.

- Arvidson, R.E., R. C. Anderson, P. Bartlett, J. F. Bell III, D. Blaney, P. R. Christensen, P. Chu, L. Crumpler, K. Davis, B.L. Ehlmann, R. Fergason, M.P. Golombek, S. Gorevan, J.A. Grant, R. Greeley, E.A. Guinness, A.F.C. Haldemann, K. Herkenhoff, J. Johnson, G. Landis, R. Li, R. Lindemann, H. McSween, D.W. Ming, T. Myrick, L. Richter, F.P. Seelos IV, S.W. Squyres, R.J. Sullivan, A. Wang, J. Wilson, 2004, Localization and physical properties experiments conducted by Spirit at Gusev crater, *Science*, v. 305, p. 821–824.
- Arvidson, R.E., S.W. Squyres, R.C. Anderson, J.F. Bell III, D. Blaney, J. Bruckner, N.A. Cabrol, W.M. Calvin, M.H. Carr, P.R. Christensen, B.C. Clark, L. Crumpler, D.J. Des Marais, P.A. de Souza Jr., C. d’Uston, T. Economou, J. Farmer, W.H. Farrand, W. Folkner, M. Golombek, S. Gorevan, J.A. Grant, R. Greeley, J. Grotzinger, E. Guinness, B.C. Hahn, L. Haskin, K.E. Herkenhoff, J.A. Hurowitz, S. Hviid, J.R. Johnson, G. Klingelhöfer, A.H. Knoll, G. Landis, C. Leff, M. Lemmon, R. Li, M.B. Madsen, M.C. Malin, S.M. McLennan, H.Y. McSween, D.W. Ming, J. Moersch, R.V. Morris, T. Parker, J.W. Rice Jr., L. Richter, R. Rieder, D.S. Rodionov, C. Schröder, M. Sims, M. Smith, P. Smith, L.A. Soderblom, R. Sullivan, S.D. Thompson, N.J. Tosca, A. Wang, H. Wanke, J. Ward, T. Wdowiak, M. Wolff, and A. Yen, 2006a, Overview of the Spirit Mars Exploration Rover Mission to Gusev Crater: Landing site to Backstay Rock in the Columbia Hills, *J. Geophys. Res.*, v. 111, E02S01, doi: 10.1029/2005JE002499.
- Arvidson, R.E., L. Barge, J. Barnes, W. Boynton, J. Friedson, M.P. Golombek, J. Guinn, D.M. Kass, R. Kirk, M. Malin, M. Mellon, T. Michaels, D. Paige, T.J. Parker, S. Rafkin, K. Seelos, M.D. Smith, P.H. Smith, L. Tamppari, and D. Tyler, 2006b, Overview of Mars Exploration Program 2007 Phoenix Mission Landing Site Selection, 37<sup>th</sup> LPSC, March 13-17, 2006, Houston, TX. abstract #1328.
- Arvidson R.E. and S. Slavney, 2006, PDS Geoscience Node, Washington University, St. Louis, Missouri, <http://pds-geosciences.wustl.edu/>, viewed on 4/5/06.
- Baker-Jarvis, J., M. Janezic, J. Grosvenor, and R. Geyer, 1993, Transmission/Reflection and Short-Circuit Line Methods for Measuring Permittivity and Permeability, NIST Technical Note 1355-R, 112 p.
- Balanis, C.A., 1989, *Advanced engineering electromagnetics*, Wiley, NY, 981 p.
- Bandfield, J.L., V.E. Hamilton, and P.R. Christensen, 2000, A Global View of Martian Surface Compositions from MGS-TES, *Science*, v. 287, p. 1626-1630.

- Bandfield, J.L., P.R. Christensen, and T.D. Glotch, 2003, Spectroscopic Identification of Carbonate Minerals in the Martian Dust, *Science*, v. 301, p. 1084-1087.
- Bandfield, J.L., V.E. Hamilton, P.R. Christensen, and H.Y. McSween, Jr., 2004, Identification of quartzofeldspathic materials on Mars, *J. Geophys. Res.*, v. 109, E10009, doi: 10.1029/2004JE002290.
- Basilevsky, A.T., M.L. Litvak, I.G. Mitrofanov, W.V. Boynton, R.S. Saunders, and J.W. Head, 2003, Search for Traces of Chemically Bound Water in the Martian Surface Layer Based on HEND Measurements onboard the 2001 Mars Odyssey Spacecraft, *Solar System Research*, v. 37, p. 387-396.
- Beatty, D.W., S. Clifford, P. Gogineni, R. Grimm, C. Leuschen, G.R. Olhoeft, K. Raney, and A. Safaenili, 2001, Report of the virtual instrument Science Definition Team on a Facility Orbital Radar Sounder Experiment for Mars Reconnaissance Orbiter 2005 (FORSE), from JPL to NASA Headquarters, April 9, 2001, 35p.
- Bertelsen P., W. Goetz, M.B. Madsen, K.M. Kinch, S.F. Hviid, J.M. Knudsen, H.P. Gunnlaugsson, P. Nornberg, S.W. Squyers, J.F. Bell III, K.E. Herkenhoff, S Gorevan, A.S Yen, T. Myrick, G. Klingelhöfer, R. Rieder, R. Gellert, 2005, Magnetic Properties Experiments on the Mars Exploration rover Spirit at Gusev Crater, *Science*, v. 305, p, 827-829.
- Bell III, J.F., H.Y. McSween Jr., J.A. Crisp, R.V. Morris, S.L. Murchie, N.T. Bridges, J.R. Johnson, D.T. Britt, M.P. Golombek, H.J. Moore, A. Ghosh, J.L. Bishop, R.C. Anderson, J. Brückner, T. Economou, J.P. Greenwood, H.P. Gunnlaugsson, R.M. Hargraves, S. Hviid, J.M. Knudsen, M.B. Madsen, R. Reid, R. Rieder, and L. Soderblom, 2000, Mineralogic and compositional properties of Martian soil and dust: Results from Mars Pathfinder, *J. Geophys. Res.*, v. 105(E1), p. 1721-1756.
- Bhattacharya, J.P., T.H.D. Payenberg, S.C. Lang, M. Bourke, 2005, Dynamic river channels suggest a long-lived Noachian crater lake on Mars, *Geophysical Research Letters*, v. 32, L10201, doi:10.1029/2005GL022747.
- Bibring, J.P., Y. Langevin, A. Gendrin, B. Gondet, F. Poulet, M. Berthe, A. Soufflot, R. Arvidson, N. Mangold, J. Mustard, P. Drossart, and the OMEGA team, 2005, Mars Surface Diversity as Revealed by the OMEGA/Mars Express Observations, *Science*, v. 307, p. 1576-1581.
- Bogard D.D., and P. Johnson, 1983, Martian gases in an Antarctic meteorite? *Science* v. 221, p. 651-654.

- Böttcher, C.J.F., 1952, *Theory of Electric Polarization*, v. 1, Elsevier Publishing Company, New York, 492 p.
- Böttcher, C.J.F. and P. Bordewijk, 1978, *Theory of Electric Polarization: Dielectrics in time-dependent fields*, v. 2, Elsevier Scientific Publishing Company, Amsterdam, 561p.
- Boynton, W.V., J.I. Trombka, W.C. Feldman, J.R. Arnold, P. Englert, A.E. Metzger, R.C. Reedy, S.W. Squyres, H. Waenke, S.H. Bailey, J. Brückner, J.L. Callas, D.M. Drake, P. Duke, L.G. Evans, E.L. Haines, F.C. McCloskey, H. Mills, C. Shinohara, and R. Starr, 1992, *Science Applications of the Mars Observer Gamma Ray Spectrometer*, *J. Geophys. Res.*, v. 97(E5), p. 7681-7698.
- Boynton, W.V., W.C. Feldman, S.W. Squyres, T.H. Prettyman, J. Brückner, L.G. Evans, R.C. Reedy, R. Starr, J.R. Arnold, D.M. Drake, P.A.J. Englert, A.E. Metzger, I. Mitrofanov, J.I. Trombka, C. d'Uston, H. Waenke, O. Gasnault, D.K. Hamara, D.M. Janes, R.L. Marcialis, S. Maurice, I. Mikheeva, G.J. Taylor, R. Tokar, and C. Shinohara, 2002, *Distribution of Hydrogen in the Near Surface of Mars: Evidence for Subsurface Ice Deposits*, *Science*, v. 297, p. 81-85.
- Boynton, W.V., G.J. Taylor, D. Hamara, K. Kerry, D. Janes, J. Keller, W. Feldman, T. Prettyman, R. Reedy, J. Brückner, H. Waenke, L. Evans, R. Starr, S. Squyres, S. Karunatillake, and O. Gasnault, 2003, *Compositional Diversity of the Martian Crust: Preliminary Data from the Mars Odyssey Gamma Ray Spectrometer*, 34<sup>th</sup> Lunar and Planetary Science Conference, March 17-21, 2003, Houston, TX, abstract #2108.
- Burton, B., 2004, *Attenuation Analysis of Ground Penetrating Radar Data Acquired over a Crude Oil Spill*, Masters thesis, Dept. of Geophysics, Colorado School of Mines, Golden, 176 p. + CD-ROM.
- Canan, B., 1999, *Dielectric properties of clay-water-organic compounds*, PhD thesis, Dept. of Geophysics, Colorado School of Mines, Golden, 332 p. + CD-ROM.
- Carr, M.H., L. Crumpler, J. Cutts, R. Greeley, J. Guest, and H. Masursky, 1977, *Martian impact craters and emplacement of ejecta by surface flow*, *J. Geophys. Res.*, v. 82, p. 4055–4065.
- Carr, M.H., 1990, *D/H on Mars: Effects of floods, volcanism, impacts, and polar processes*, *Icarus*, 87, p. 210–227.
- Carr, M.H., 1996, *Water on Mars*, Oxford Univ. Press, New York, 229 p.

- Calvin W., S. Squyres, R. Arvidson, J. Bell, P. Christensen, K. Herkenhoff, B. Jolliff, G. Klingelhöffer, J. Farmer, W. Farrand, S. Gorevan, J. Grotzinger, A. Knoll, M. Madsen, R. Morris, S. McLennan, J. Rice, R. Rieder, L. Soderblom, P. de Souza, C. Weitz, A. Fallacaro, T. Glotch, W. Watters and the Athena Science Team, 2004, "Blueberries": A Summary of the Hematite Concretions found at the Opportunity Landing Site, 2<sup>nd</sup> Conference on Early Mars, October 11-15, 2004, Jackson Hole, WY, abstract #8074.
- Chan, W., 2005, Crystal Structures, <http://home3.netcarrier.com/~chan/SOLIDSTATE/CRYSTAL/>, viewed on 12/6/05.
- Chernicoff, S., and R. Venkatakrishnan, 1995, *Geology*, Worth Publishers, Inc., New York, 593p.
- Chikazumi, S., 1964, *Physics of Magnetism*, John Wiley & Sons, Inc., New York, 554p.
- Christensen, P.R., D.L. Anderson, S.C. Chase, R.N. Clark, H.H. Kieffer, M.C. Malin, J.C. Pearl, J. Carpenter, N. Bandiera, F.G. Brown, and S. Silverman, 1992, Thermal Emission Spectrometer Experiment: Mars Observer Mission, *J. Geophys. Res.*, 97, p. 7719-7734.
- Christensen, P.R., 1998, Variations in Martian surface composition and cloud occurrence determined from thermal infrared spectroscopy: Analysis of Viking and Mariner 9 data, *J. Geophys. Res.*, v. 103(E1), p. 1733-1746, doi: 10.1029/97JE02114.
- Christensen, P.R., R.V. Morris, M.D. Lane, J.L. Bandfield, and M.C. Malin, 2001, Global mapping of Martian hematite mineral deposits: Remnants of water-driven processes on early Mars, *J. Geophys. Res.*, v. 106, p. 23,873-23,885.
- Christensen, P.R., 2003, Formation of recent Martian gullies through melting of extensive water-rich snow deposits, *Nature*, v. 422, p. 45-48, doi: 10.1038/nature01436.
- Christensen, P. R., B.M. Jakosky, H.H. Kieffer, M.C. Malin, H.Y. McSween Jr., K. Nealson, G.L. Mehall, S.H. Silverman, S. Ferry, M. Caplinger and M.A. Ravine, 2004, The Thermal Emission Imaging System (THEMIS) for the Mars 2001 Odyssey Mission, *Space Science Reviews*, v. 110, p. 85-130.
- Christensen, P.R., S.W. Ruff, R.L. Fergason, T.D. Glotch, N. Gorelick, B.M. Jakosky, M.D. Lane, A.S. McEwen, H.Y. McSween, Jr., G.L. Mehall, K. Milam, J.E. Moersch, S.M. Pelkey, A.D. Rogers, and W.B. Wyatt, 2005, Mars Exploration Rover candidate landing sites as viewed by THEMIS, *Icarus*, 187, p. 12-43.

- Christensen, P.R., H.Y. McSween, Jr., J.L. Bandfield, S.W. Ruff, A.D. Rogers, V.E. Hamilton, N. Gorelick, M.B. Wyatt, B.M. Jakosky, H.H. Kieffer, M.C. Malin, and J.E. Moersch, 2005, Evidence for igneous diversity and magmatic evolution on Mars from infrared observations, *Nature*, v. 436, p. 504-509.
- Clancy, R.T., S.W. Lee, G.R. Gladstone, W.W. McMillan, and T. Rousch, 1995, A new model for Mars atmospheric dust based upon analysis of ultraviolet through infrared observations from Mariner 9, Viking, and Phobos, *J. Geophys. Res.*, v. 100, p. 5251-5263.
- Clancy, R. T., M. J. Wolff, and P. R. Christensen, 2003, Mars aerosol studies with the MGS TES emission phase function observations: Optical depths, particle sizes, and ice cloud types versus latitude and solar longitude, *J. Geophys. Res.*, 108(E9), 5098, doi: 10.1029/2003JE002058.
- Clifford S.M. and T.J. Parker, 2001, The Evolution of the Martian Hydrosphere: Implications for the Fate of a Primordial Ocean and the Current State of the Northern Plains, *Icarus*, v. 154, 40-79.
- Cole, K.S., and Cole, R.H., 1941, Dispersion and Absorption in Dielectrics: *The Journal of Chemical Physics*, v. 9, p. 341-351.
- Connerney, J.E.P., M.H. Acuña, P.J. Wasilewski, G. Kletetschka, N.F. Ness, H. Rème, R.P. Lin, and D.L. Mitchell, 2005, The Global Magnetic Field of Mars and Implications for Crustal Evolution, *Geophysical Research Letters*, v. 28, p. 4015-4018.
- Connerney, J.E.P., M.H. Acuña, N.F. Ness, G. Kletetschka, D.L. Mitchell, R.P. Lin, and H. Rème, 2005, Tectonic implications of Mars crustal magnetism, *Proceedings of the National Academy of Sciences*, v. 102, p. 14970-14975.
- Cornell and Schwertmann, 2003, *The Iron Oxides*, Wiley-VCH, Weinheim, 664 p.
- Debye, P., 1929, *Polar Molecules*, New York: Chemical Catalog Company, 172 p.
- Dekker, A.J., 1957, *Solid State Physics*, Englewood Cliffs, N.J., Prentice-Hall, Inc., 540 p.
- Delaney, A.J., S.A. Arcone, A. O'Bannon, J. Wright, 2004, Crevasse detection with GPR across the Ross Ice Shelf, Antarctica, 10<sup>th</sup> International Conference on Ground Penetrating Radar, June 21-24, 2004, Delft, The Netherlands, p. 777-780.

- Dunlop, D.J., and O. Özdemir, 1997, *Rock Magnetism Fundamentals and Frontiers*: Cambridge University Press, Cambridge, 573 p.
- Dunlop, D.J. and J. Arkani-Hamed, 2005, Magnetic minerals in the Martian crust, *J. Geophys. Res.*, v. 110, E12S04.
- Dyar, M.D., Y. Rothstein, M.W. Schaefer, and D. Agresti, 2006, Mossbauer Spectroscopy of Outcrop at the Meridiani Planum Site, 37<sup>th</sup> Lunar and Planetary Conference, March 13-17, 2006, Houston TX, abstract #2382.
- Edgett, K.S., and M.C. Malin, 2000, Martian Dust raising and surface albedo controls: Thin, dark (and sometimes bright) streaks and dust devils in MGS MOC high resolution images, 31<sup>st</sup> Lunar and Planetary Conference, March 13-17, 2000, Houston TX, abstract #1073.
- Eugster O., Busemann H., Lorenzetti S. and Terribilini D., 2002, Ejection ages from <sup>81</sup>Kr-<sup>83</sup>Kr dating and pre-atmospheric sizes of Martian meteorites. *Meteoritics & Planet. Sci.*, v. 37, p. 1345-1360.
- Evans, L.G., R. C. Reedy, R. D. Starr, W. V. Boynton, and J. I. Trombka, 2002, Background lines in the Mars Odyssey 2001 gamma ray detector, *Proc. of SPIE*, July 29 – Aug. 1, 2002, Boston, MA, v. 4784, p. 31-44.
- Fanale, F.P., 1976, Martian volatiles: Their degassing history and geochemical fate, *Icarus*, v. 28, p. 179-202.
- Farrell, W.M., 2005, Ionospheric Transmission Losses Associated with Mars-Orbiting Radars, Workshop on Radar Investigation of Planetary and Terrestrial Environments, February 7-10, 2005, Houston, Texas, abstract #6021.
- Feldman, W.C., T.H. Prettyman, W.V. Boynton, J.R. Murphy, S. Squyres, S. Karunatillake, S. Maurice, R.L. Tokar, G.W. McKinney, D.K. Hamara, N. Kelly, and K. Kerry, 2003, CO<sub>2</sub> frost cap thickness on Mars during northern winter and spring, *J. Geophys. Res.*, 108(E9), 5103, doi:10.1029/2003JE002101.
- Feldman, W.C., T.H. Prettyman, S. Maurice, J.J. Plaut, D.L. Bish, D.T. Vaniman, M.T. Mellon, A.E. Metzger, S.W. Squyres, S. Karunatillake, W.V. Boynton, R.C. Elphic, H.O. Funsten, D.J. Lawrence, and R.L. Tokar, 2004, Global Distribution of near-surface hydrogen on Mars, *J. Geophys. Res.*, v. 109, E09006, doi: 10.1029/2003JE002160.

- Ferguson D.C., J.C. Kolecki, M.W. Siebert, D.M. Wilt, and J.R. Matijevic, 1999, Evidence for Martian electrostatic charging and abrasive wheel wear from the Wheel Abrasion Experiment on the Pathfinder Sojourner rover, *J. Geophys. Res.*, v. 104(E4), p. 8747-8789.
- Formisano, V., S. Atreya, T. Encrenaz, N. Ignatiev, and M. Giuranna, 2004, Detection of Methane in the Atmosphere of Mars, *Science*, v. 306, p. 1758-1761.
- Frey, H., S.E.H. Sakimoto and J.H. Roark, 1999, Discovery of a 450km diameter, multiring basin on Mars through analysis of MOLA topographic data, *Geophys. Res. Lett.*, v. 26, p. 1657-1660.
- Frey, H., L. Hutchison, S.E.H. Sakimoto and J.H. Roark, 2000, A large population of possible buried impact basins on Mars revealed by MOLA topographic data, LPSC XXXI, March 13-17, Houston, TX, abstract #1736.
- Frey, H., K.M. Shockey, J.H. Roark, E.L. Frey and S.E.H. Sakimoto, 2001, A very large population of likely buried impact basins in the northern lowlands of Mars revealed by MOLA data, LPSC XXXII, March 12-16, Houston, TX, abstract #1680.
- Frey, H., J.H. Roark, K.M. Shockey, E.L. Frey and S.E.H. Sakimoto, 2002, Ancient lowlands on Mars, *Geophys. Res. Lett.*, v. 29(10), doi:10.1029/2001GL013832.
- Gellert R., R. Rieder, R.C. Anderson, J. Brückner, B.C. Clark, G. Dreibus,<sup>1</sup> T. Economou, G. Klingelhöfer, G.W. Lugmair, D.W. Ming, S.W. Squyres, C. d'Uston, H. Wänke, A. Yen, J. Zipfel, 2004, Chemistry of Rocks and Soils in Gusev Crater from the Alpha Particle X-ray Spectrometer, *Science*, v. 305, p. 829 – 832.
- Grimm, R., 2002, Low-frequency electromagnetic exploration for groundwater on Mars, *J. Geophys. Res.*, v. 107(E2), 5006, doi: 10.1029/2001JE001504.
- Grimm, R., E. Heggy, S. Clifford, and C. Dinwindie, 2005, Scattering Limits to Depth of Radar Investigation: Lessons from the Bishop Tuff, Workshop on Radar Investigation of Planetary and Terrestrial Environments, February 7-10, 2005, Houston, Texas, abstract #6025.
- Goetz, W., P.W. Bertelsen, C.S. Binau, H.P. Gunnlaugsson, S.F. Hviid, K.M. Kinch, M.B. Madsen, M. Olsen, R. Gellert, G. Klingelhöfer, D. W. Ming, R.V. Morris, R. Rieder, D.S. Rodionov, P.A. de Souza Jr, C. Schröder, S.W. Squyres, T. Wdowiak, and A. Yen, 2005, Indication of drier periods on Mars from the chemistry and mineralogy of atmospheric dust, *nature*, v. 436, p. 62-64.

- Haberle, R.M., C.P. McKay, J. Schaeffer, N.A. Cabrol, E.A. Grin, A.P. Zent, and R. Quinn, 2001, On the possibility of liquid water on present-day Mars, *J. Geophys. Res.*, v. 106(E10), p. 23,317-23,326, doi:10.1029/2000JE001360.
- Hamilton, V.E., and P.R. Christensen, 2005, Evidence for extensive olivine-rich bedrock in Nili Fossae, Mars, *Geology*, v. 33, p. 433-436.
- Hargraves, R.B., D.W. Collinson, R.E. Arvidson, and P.M. Cates, 1979, Viking Magnetic Properties Experiment: Extended Mission Results, *J. Geophys. Res.*, v. 84, p. 8,379-8,384.
- Hargraves, R.B., J.M. Knudsen and M.B. Madsen, 1999, Forum: Caution advised on Suitability of a Mars Soil Simulant, *EOS*, v. 80, p. 168-169.
- Hargraves R.B., J.M. Knudsen, P. Bertelsen, W. Goetz, H.P. Gunnlaugsson, S.F. Hviid, M.B. Madsen, and M. Olsen, 2000, Magnetic enhancement on the surface of Mars?, *J. Geophys. Res.*, V. 105, p. 1819-1827.
- Head, J.W. III, W.C. Feldman, K.R. Moore, and T.H. Prettyman, 2003, Correlation of Neutron-Sensed Water Ice Margin with Topography Statistics, Sixth International Conference on Mars, July 20-25, 2003, CalTech., abstract #3181.
- Heggy, E., P. Paillou, G. Ruffie, J.M. Malezieux, F. Costard, and G. Grandjean, 2001, On Water Detection in the Martian Subsurface using Sounding Radar, *Icarus*, 154, p. 244-257.
- Heggy, E., P. Paillou, F. Costard, N. Mangold, G. Ruffie, G. Grandjean, and J.M. Malezieux, 2003, Local Geoelectric Models of the Martian Subsurface for shallow groundwater detection using Sounding Radars, *J. Geophys. Res.*, 108(E4), 8030.
- Heggy, E., and A. Pommerol, 2005, Dielectric Map of the Martian Surface, Workshop on Radar Investigations, February 7-10, Houston, TX, 6028.
- Herkenhoff, K.E., S.W. Squyres, J.F. Bell III, J.N. Maki, H.M. Arneson, P. Bertelsen, D.I. Brown, S.A. Collins, A. Dingizian, S.T. Elliott, W. Goetz, E.C. Hagerott, A.G. Hayes, M.J. Johnson, R.L. Kirk, S. McLennan, R.V. Morris, L.M. Scherr, M.A. Schwochert, L.R. Shiraishi, G.H. Smith, L.A. Soderblom, J.N. Sohl-Dickstein, and M.V. Wadsworth, 2003, Athena Microscopic Imager investigation, *J. Geophys. Res.*, v. 108(E12), 8065, doi:10.1029/2003JE002076.

- Hiesigner, H., and J.W. Head, 2002, 33<sup>th</sup> Lunar and Planetary Science Conference, March 11-15, 2002, Houston, Texas, abstract #1063.
- Hewlett-Packard, 1994, HP8752C and HP8753D Network Analyzers: Technical Specifications, Hewlett-Packard, 5962-9770E, USA, 35 p.
- Hoefen T.M., R.N. Clark, J.L. Bandfield, M.D. Smith, J.C. Pearl, and P.R. Christensen, 2003, Discovery of Olivine in the Nili Fossae Region of Mars, *Science*, v. 302, p. 627-630.
- Hunt, C.P., B.M Moskowitz, and S.K. Banerjee, 1995, Magnetic properties of rocks and minerals: in *Rock physics and phase relations*, T.J. Ahrens, ed., AGU, Washington DC, p. 189-204.
- Hviid, S.F., M.B. Madsen, H.P. Gunnlaugsson, W. Goetz, J.M. Knudsen, R.B. Hargraves, P. Smith, D. Britt, A.R. Dinesen, C.T. Pedersen, and L. Vistisen, 1997, Magnetic Properties Experiments on the Mars Pathfinder Lander: Preliminary Results, *Science*, v. 278, p. 1,768-1,770.
- Hviid, S.F., M.B. Madsen, J.M. Knudsen, H.P. Gunnlaugsson, W. Goetz, A.R. Dinesen, C.T. Mogensen, C.T. Pedersen, and R.B. Hargraves, 1998, Results of the Magnetic Properties Experiments on the Mars Pathfinder Lander, 29<sup>th</sup> Lunar and Planetary Science Conference, March 16-20, 1998 Houston, Texas, abstract #1605.
- Iben, I.E.T., W.A. Edelman, and P.B. Roemer, 1996, Dielectric Properties of Soil: Application to Radio Frequency Ground Heating, GE Global Research, Report Number 96CRD150, 33 p.
- Irwin, R.P., III, A.D. Howard, and T.A. Maxwell, 2004, Geomorphology of Ma'adim Vallis, Mars, and associated paleolake basins, *J. Geophys. Res.*, v. 109, E12009, doi: 10.1029/2004JE002287.
- Jakosky, B.M., and C.B. Farmer, 1982, The seasonal and global behavior of water vapor in the Mars atmosphere: Complete global results of the Viking Atmospheric Water Detector experiment, *J. Geophys. Res.*, 87, p. 2999-3019.
- Jakosky, B. M., 1991, Mars volatile evolution: Evidence from stable isotopes, *Icarus*, 94, p. 14-31.

- Jakosky, B.M., M.T. Mellon, E.S. Varnes, W.C. Feldman, W.V. Boynton, R.M. Haberle, 2005, Mars low-latitude neutron distribution: Possible remnant near-surface water ice and a mechanism for its recent emplacement, *Icarus*, v. 175, p. 58-67.
- Johnson, J.R., P. R. Christensen, and P. G. Lucey, 2002a, Dust coatings on basaltic rocks and implications for thermal infrared spectroscopy of Mars, *J. Geophys. Res.*, 107(E6), doi:10.1029/2000JE001405.
- Johnson, J. R., F. Hörz, P. G. Lucey, and P. R. Christensen, 2002b, Thermal infrared spectroscopy of experimentally shocked anorthosite and pyroxenite: Implications for remote sensing of Mars, *J. Geophys. Res.*, 107(E10), 5073, doi: 10.1029/2001JE001517.
- Kauzmann, W., 1942, Dielectric Relaxation as a Chemical Rate Process, *Reviews of Modern Physics*, v. 14, p. 12-44.
- Kieffer H.H., 1976, Soil and Surface Temperatures at the Viking Landing Sites, *Science*, v. 194, p. 1344-1346.
- Kieffer H.H., S.C. Chase Jr., T.Z. Martin, E.B. Miner, and F.D. Pallucuni, 1976, *Science*, v. 194, p. 1341-1343.
- Kieffer, H.H., T.Z. Martin, A.R. Peterfreund, B.M. Jakosky, E.D. Miner, F.D. Palluconi, 1977, Thermal and Albedo Mapping of Mars during the Viking primary mission. *J. Geophys. Res.*, v. 82, p 4249–4291.
- Kirkland, L., Herr, K. and Adams, P., 2003, Infrared stealthy surfaces: Why TES and THEMIS may miss some substantial mineral deposits on Mars and implications for remote sensing of planetary surfaces, *J. Geophys. Res.*, 108(E12), doi: 10.1029/2003JE002105.
- Klingelhöfer G., R.V. Morris, B. Bernhardt, D.S. Rodionov, P.A. de Souza, Jr., S.W. Squyres, J. Foh, E. Kankeleit, U. Bonnes, R. Gellert, C. Schröder, S. Linkin, E. Evlanov, B. Zubkov, and O. Prilutski, 2003, Athena MIMOS II Mössbauer spectrometer investigation, *J. Geophys. Res.*, v. 306(E12), 8067, doi: 10.1029/2003JE002138..

- Klingelhöfer G., R.V. Morris, B. Bernhardt, C. Schröder, D.S. Rodionov, P.A. de Souza, Jr., A. Yen, R. Gellert, E.N. Evlanov, B. Zubkov, J. Foh, U. Bonnes, E. Kankeleit, P. Gütlich, D.W. Ming, F. Renz, T. Wdowiak, S.W. Squyres, and R.E. Arvidson, 2004, Jarosite and Hematite at Meridiani Planum from Opportunity's Mössbauer Spectrometer, *Science*, v. 306, p. 1740-1745.
- LaVoie, S., M. McAuley, E.D. Rye, K. Boggs, E. De Jong, L. Soderblom, 2006, Images of Mars and All Available Satellites, <http://photojournal.jpl.nasa.gov/targetFamily/Mars>, viewed 1/13/06.
- Lemmon, M.T., M.J. Wolff, M.D. Smith, R.T. Clancy, D. Banfield, G.A. Landis, A. Ghosh, P.H. Smith, N. Spanovich, B. Whitney, P. Whelley, R. Greeley, S. Thompson, J.F. Bell III, S.W. Squyres, 2004. Atmospheric Imaging Results from the Mars Exploration Rovers: Spirit and Opportunity, *Science*, v. 306, p. 1753-1756, doi: 10.1126/science.1104474.
- Leshin, L.A., S. Epstein, and E.M. Stolper, 1996, Hydrogen isotope geochemistry of SNC meteorites, *Geochim. Cosmochim. Acta*, v. 60, p. 2635-2650.
- Leshin, L.A., 2000, Insights into Martian water reservoirs from analyses of Martian meteorite QUE94201, *Geophys. Res. Lett.*, 27, p. 2017–2020.
- Leuschen, C., 1999, Analysis of the Complex Permittivity and Permeability of a Martian Soil Simulant from 10 MHz to 1 GHz, *Proceedings of the 1999 IEEE Geoscience and Remote Sensing Symposium*, July, Hamburg, Germany , v. 4, p. 2264-2266.
- Levenberg, K., 1944, A Method for the Solution of Certain Problems in Least Squares, *Quart. Appl. Math.*, v. 2, p. 164-168.
- Lockhart, N.C., 1980a, Electrical properties and the surface characteristic and structure of clays: I. Swelling clays: *Journal of Colloid and Interface Science*, v. 74, p. 509-519.
- Lockhart, N.C., 1980b, Electrical properties and the surface characteristic and structure of clays: II. A nonswelling clay: *Journal of Colloid and Interface Science*, v. 74, p. 520-529.
- Luhman, J.G., R.E. Johnson, and M.H.G. Zhang (1992), Evolutionary impact of sputtering of the Martian atmosphere by O<sup>+</sup> pickup ions, *Geophys. Res. Lett.*, 19, p. 2151–2154.

- Madsen M.B., S.F. Hviid, H.P. Gunnlaugsson, J.M. Knudsen, W. Goetz, C.T. Pedersen, A.R. Dinesen, C.T. Mogensen, M. Olsen, and R.B. Hargraves , 1999, The magnetic properties experiments on Mars Pathfinder, *J. Geophys. Res.*, v. 104, p. 8,761-8,779.
- Madsen, M.B., P. Bertelsen, W. Goetz, C.S. Binau, M. Olsen, F. Folkmann, H.P. Gunnlaugsson, K.M. Kinch, J.M. Knudsen, J. Merrison, P. Nørnberg, S.W. Squyres, A.S. Yen, J.D. Rademacher, S. Gorevan, T. Myrick, and P. Bartlett, 2003, Magnetic Properties Experiments on the Mars Exploration Rover mission, *J. Geophys. Res.*, v. 108(E12), 8069, doi:10.1029/2002JE002029.
- Madsen, M.B., H.M. Arneson, P. Bertelsen, J.F. Bell III, C.S. Binau, R. Gellert, W. Goetz, H.P. Gunnlaugsson, K.E. Herkenhoff, S.F. Hviid, et al., 2005, An Update on Results from the Magnetic Properties Experiments on the Mars Exploration Rovers Spirit and Opportunity, LPSC XXXVI, Houston, TX, March 14-18, abstract #2379.
- Malin, M.C., and K.S. Edgett, 2000, Evidence for Recent Groundwater Seepage and Surface Runoff on Mars, *Science*, v. 288, p. 2330-2335.
- Malin, M.C., and K.S. Edgett, 2003, Evidence for Persistent Flow and Aqueous Sedimentation on Early Mars, *Science*, v. 302, p. 1931-1934.
- Markiewicz, W.J., R.M. Sablotny, H.U. Keller, N. Thomas, D. Titov, and P.H. Smith, 1999, Optical properties of the Martian aerosols as derived from Imager for Mars Pathfinder midday sky brightness data, v. 104(E4), p. 9009-9017.
- Martin, P.D., 2003, The ESA Mars Express Mission: Spectral and Compositional Investigations, 6<sup>th</sup> International Conference on Mars, Pasadena, CA, July 20-25, abstract #3085.
- Martin, T.Z., N.T. Bridges, and J.R. Murphy, 2003, Near-surface temperatures at proposed Mars Exploration Rover landing sites, *J. Geophys. Res.*, 108(E12), 8089, doi:10.1029/2003JE002063.
- Marquardt, D., 1963, An Algorithm for Least-Squares Estimation of Nonlinear Parameters, *SIAM J. Appl. Math.*, v. 11, p. 431-441.
- Max, M.D. and S.M. Clifford, 2003, Methane Hydrate Exploration on Mars: A test bed for Development of Strategies for Planetary Exploration, 6<sup>th</sup> International Conference on Mars, Pasadena, CA, July 20-25, abstract #3160.

- McIntosh, R.L., 1966, Dielectric Behavior of Physically Adsorbed Gases, Marcel Dekker, Inc., NY, 160 p.
- McKay D.S., E.K. Gibson, K.L. Thomas-Keprta, H. Vali, C.S. Romanek, S.J. Clemett, X.D.F. Chillier, C.R. Maechling, and R.N. Zare, 1996, Search for life on Mars: Possible relic biogenic activity in Martian meteorite ALH84001, *Science*, 273, p. 924-930.
- Mellon, M.T., and B.M. Jakosky, 1993, *J. Geophys. Res.*, v. 98, p. 3345-3364.
- Mellon, M. T., B. M. Jakosky, and S. E. Postawko, 1997, The persistence of equatorial ground ice on Mars, *J. Geophys. Res.*, 102(E8), 19,357– 19,369.
- Merrill R. T., M. W. McElhinny and P. L. McFadden, 1996, *The Magnetic Field of the Earth: Paleomagnetism, the Core, and the Deep Mantle*, Academic Press, San Diego, CA, 531 p.
- Meyer, C., 2005, Mars Meteorite Compendium (JSC #27672 Revision C), Johnson Space Center, Houston, TX, <http://www-curator.jsc.nasa.gov/antmet/mmc/index.cfm>, viewed on 5/16/06.
- Ming, D.W., R.V. Morris, R. Gellert, A. Yen, J.F. Bell, III, D. Blaney, P.R. Christensen, L. Crumpler, P. Chu, W.H. Farrand, S. Gorevan, K.E. Herkenhoff, G. Klingelhöfer, R. Rieder, D.S. Rodionov, S.W. Ruff, C. Schröder, S.W. Squyres, and the Athena Science Team, 2005, Geochemical and Mineralogical Indicators for Aqueous Process on the West Spur of the Columbia Hills in Gusev Crater, 36<sup>th</sup> Lunar and Planetary Science Conference, March 14-18, 2005, Houston, TX, abstract #2125.
- Mitchell, J.K., W.N. Houston, R.F. Scott, W.D. Carrier and L.G. Bromwell, 1972, Mechanical properties of lunar soil: density, porosity, cohesion and angle of internal friction, *Geochim. Cosmochim. Acta, Suppl.* 3, 3235-3253.
- Mitrofanov, I, D. Anfimov, A. Kozyrev, M. Litvak, A. Sanin, V. Tret'yakov, A. Krylov, V. Shvetsov, W. Boynton, C. Shinohara, D. Hamara, and R. S. Saunders, 2002, Maps of Subsurface Hydrogen from the High Energy Neutron Detector, Mars Odyssey, *Science*, v. 297, p. 78-81.
- Mitrofanov, I.G., M.L. Litvak, A.S. Kozyrev, A.B. Sanin, V.I. Tret'yakov, V.Y. Grin'kov, W.V. Boynton, C. Shinohara, D. Hamara, and R.S. Saunders, 2004, Soil Water Content on Mars as Estimated from Neutron Measurements by the HEND Instrument Onboard the 2001 Mars Odyssey Spacecraft, v. 38, p. 253-265.

- Moore, J. M., A. D. Howard, W. E. Dietrich, and P. M. Schenk, 2003, Martian layered fluvial deposits: Implications for Noachian climate scenarios, *Geophys. Res. Lett.*, v. 30(24), 2292, doi:10.1029/2003GL019002.
- Morris, R.V., D.C. Golden, and J.F. Bell III, 1997, Low-temperature reflectivity spectra of red hematite and the color of Mars, *J. Geophys. Res.*, v. 102, p. 9,125-9,133.
- Morris, R.V., D.C. Golden, J.F. Bell III, T.D. Shelfer, A.C. Scheinost, N.W. Hinman, G. Furniss, S.A. Mertzman, J.L. Bishop, D.W. Ming, C.C. Allen, and D.T. Britt, 2000, Mineralogical, composition, and alteration of Mars Pathfinder rocks and soils: Evidence from multispectral, elemental and magnetic data on terrestrial analogue, SNC meteorite, and Pathfinder samples, *J. Geophys. Res.*, v. 105, p. 1757-1817.
- Morris, R.V., D.C. Golden, D.W. Ming, T.D. Shelfer, L.C. Jorgensen, J.F. Bell III, T.G. Graff, and S.A. Mertzman, 2001, Phyllosilicate-poor palagonitic dust from Mauna Kea Volcano (Hawaii): A mineralogical analogue for magnetic Martian dust?, *J. Geophys. Res.*, v. 106, p. 5,057-5,083.
- Morris, R.V., G. Klingelhöfer, B. Bernhardt, C. Schröder, D.S. Rodionov, P.A. de Souza, Jr., A. Yen, R. Gellert, E.N. Evlanov, B. Zubkov, J. Foh, E. Kankeleit, P. Gütlich, D. W. Ming, F. Renz, T. Wdowiak S.W. Squyers, and R.E. Arvidson, 2004, Mineralogy at Gusev Crater from the Mössbauer Spectrometer on the Spirit Rover, *Science*, v. 305, p. 833-836.
- Morrish, A.H., 1966, *The Physical Principles of Magnetism*, John Wiley & Sons, Inc., New York, 680 p.
- Mouginis-Mark, 1979, Martian fluidized crater morphology – Variations with crater size, latitude, altitude, and target material, *J. Geophys. Res.*, v. 84, p. 8,011-8,022.
- Nicolson, A.M. and Ross, G.F., 1970, Measurements of the intrinsic properties of materials by time domain techniques, *IEEE Trans. Instrum. Meas.*, vol. IM-19, p. 377-382.
- Olhoeft, G.R., D.W. Strangway, 1974, Electrical Properties of the Surface Layers of Mars, *Geophysical Research Letters*, Vol. 1, No. 3, p. 141-143.
- Olhoeft, G.R., and D.W. Strangway, 1975, Electrical properties of the first 100 meters of the moon, *Earth and Planetary Science Letters*, v. 24, p. 394-404.

- Olhoeft, G.R., 1976, Electrical properties of rocks, in the *Physics and Chemistry of Rocks and Minerals*, Strens, R. J. G., ed.: Wiley, London, p. 261-278 (proceedings of a NATO Short Course).
- Olhoeft, G.R., 1985, *Electrical Properties of Rocks and Minerals: Short Course Notes*, Golden, CO, November 19-21, 218 p.
- Olhoeft, G.R., 1989, Electrical properties of rocks, in *Physical Properties of Rocks and Minerals*, in Touloukian, Y. S., Judd, W. R., and Roy, R. F., eds.: New York, McGraw-Hill, p. 257-297.
- Olhoeft, G. R., and Capron, D. E., 1993, Laboratory measurements of the radio frequency electrical and magnetic properties of soils from Yuma, Arizona: U.S.G.S. Open-File Report 93-701, 214 p.
- Olhoeft, G.R. and D.E. Capron, 1994, Petrophysical causes of electromagnetic dispersion: in *Proc. of the Fifth Int'l. Conf. on Ground Penetrating Radar*, Kitchener, Ontario, 12-16 June 1994, p. 145-152.
- Olhoeft, G. R., 1998, Electrical, magnetic and geometric properties that determine ground penetrating radar performance: in *Proc. of GPR'98, Seventh Int'l. Conf. on Ground Penetrating Radar*, May 27-30, 1998, The University of Kansas, Lawrence, KS, USA, p. 177-182.
- Olhoeft, G.R., D.B. Sinex, K.A. Sander, M.M. Lagmanson, D.E. Stillman, S. Lewis, B.T. Clark, E.L. Wallin, J.P. Kauahikaua, 2000, Hot and cold Lava Tube Characterization with Ground Penetrating Radar, 8<sup>th</sup> International Conference on GPR, Gold coast, Australia, 22-25, May 2000, p. 482-487.
- Olhoeft, G.R., 2003, Subsurface Exploration for Water on Mars, 6th International Conference on Mars, July 20-25, 2003, CalTech, abstract #3213.
- Papanastassiou, D.A. and G.J. Wasserburg, 1974, Evidence for the Late Formation and Young Metamorphism in the Achondrite Nakhla, *Geophys. Res. Let.*, v. 1, p. 23-26.
- Pellenbarg, R.E., M.D. Max, and S.M. Clifford, 2003, Methane and carbon dioxide hydrates on Mars: Potential origins, distribution, detection, and implications for future in situ resource utilization, *J. Geophys. Res.*, 108(E4), 8042, doi:10.1029/2002JE001901.

- Pettinelli, E., G. Vannaroni, A. Cereti, A. R. Pisani, F. Paolucci, D. Del Vento, D. Dolfi, S. Riccioli, and F. Bella, 2005, Laboratory investigations into the electromagnetic properties of magnetite/silica mixtures as Martian soil simulants, *J. Geophys. Res.*, v. 110, E04013, doi:10.1029/2004JE002375.
- Picardi, G., J.J. Plaut, D. Biccari, O. Bombaci, D. Calabrese, M. Cartacci, A. Cicchetti, S.M. Clifford, P. Edenhofer, W.M. Farrell, C. Federico, A. Frigeri, D.A. Gurnett, T. Hagfors, E. Heggy, A. Herique, R.L. Huff, A.B. Ivanov, W.T. K. Johnson, R.L. Jordan, D.L. Kirchner, W. Kofman, C.J. Leuschen, E. Nielsen, R. Orosei, E. Pettinelli, R.J. Phillips, D. Plettemeier, A. Safaeinili, R. Seu, E.R. Stofan, G. Vannaroni, T.R. Watters, E. Zampolini, Radar Soundings of the Subsurface of Mars, *Scienceexpress*, November 30, 2005, 10.1126/science.1122165.
- Pollack, J.B. and J.N. Cuzzi, 1980, *Journal of Atmospheric Science*, v. 37, p. 868-881
- Pollack, J.B., M.E. Ockert-Bell, M.K. Shepard, 1995, Viking Lander image analysis of Martian atmospheric dust, *J. Geophys. Res.*, v. 100, p. 5235-5250.
- Powers, M.H., 1995, Dispersive Ground Penetrating Radar Modeling in 2D: Colorado School of Mines, Geophysics Department, PhD, Thesis, CO, USA, 198 p.
- Prettyman, T. H., W.C. Feldman, M.T. Mellon, G.W. McKinney, W.V. Boynton, S. Karunatillake, D.J. Lawrence, S. Maurice, A.E. Metzger, J.R. Murphy, S.W. Squyres, R.D. Starr, and R.L. Tokar<sup>1</sup>, 2004, Composition and structure of the Martian surface at high southern latitudes from neutron spectroscopy, *J. Geophys. Res.*, v. 109, doi:10.1029/2003JE002139, E05001.
- Ramsey, M. S., and P. R. Christensen, 1998, Mineral abundance determination: Quantitative deconvolution of thermal emission spectra, *J. Geophys. Res.*, v. 103, p. 577–596.
- Rieder R., R. Gellert, R.C. Anderson, J. Brückner, B.C. Clark, G. Dreibus, T. Economou, G. Klingelhöfer, G.W. Lugmair, D.W. Ming, S.W. Squyres, C. d'Uston, H. Wänke, A. Yen, and J. Zipfel, 2004, Chemistry of Rocks and Soils at Meridiani Planum from the Alpha Particle X-ray Spectrometer, *Science*, v. 306, p. 1746 – 1749.
- Ruff, S.W., P.R. Christensen, R.N. Clark, H.H. Kieffer, M.C. Malin, J.L. Bandfield, B.M. Jakosky, M.D. Lane, M.T. Mellon, and M.A. Presley, 2001, Mars' "White Rock" feature lacks evidence of an aqueous origin: Results from Mars Global Surveyor, *J. Geophys. Res.*, v. 106, 23921–23928.

- Safaenili, A., D. Biccari, O. Bombaci, D. Gurnett, W.T.K. Johnson, R.L. Jordan, R. Orosei, G. Picardi, J. Plaut, R. Seu, E. Zampolini, and C. Zelli, 2001, Radar Sounding of Mars: A Focus on MARSIS, Conference on the Geophysical Detection of Subsurface Water on Mars, abstract #7032.
- Schenk, C.J., Gautier, D.L., Olhoeft, G.R., and Lucius, J.E., 1993, Internal structure of an eolian dune using ground penetrating radar, in Lancaster, N., and Rye, K., eds., *Ancient and Modern Eolian Sediments: Spec. Publ. Int. Ass. Sediment*, v. 16, p. 61-69 p.
- Schubert, G. and T. Spohn, 1990, Thermal history of Mars and the sulfur content of its core, *J. Geophys. Res.*, v. 95, p. 14,095-14,104.
- Seu, R., D. Biccari, L.V. Lorenzoni, R.J. Phillips, L. Marinangeli, G. Picardi, A. Masdea, and E. Zampolini, 2004, SHARAD: The MRO 2005 shallow radar, *Planetary and Space Science*, v. 52, p. 157-166.
- Sen, P.N., C. Scala, and M.H. Cohen, 1981, A self-similar model for sedimentary rocks with application to the dielectric constant of fused glass beads, *Geophysics*, v. 46, p. 781-795.
- Sheriff, R.E., 1999, *Encyclopedic Dictionary of Exploration Geophysics*, Society of Exploration Geophysicists, Tulsa, OK, 384 p.
- Smith D.E., M.T. Zuber, S.C. Solomon, R.J. Phillips, J.W. Head, J.B. Garvin, W.B. Banerdt, D.O. Muhleman, G.H. Pettengill, G.A. Neumann, F.G. Lemoine, J.B. Abshire, O. Aharonson, C.D. Brown, S.A. Hauck, A.B. Ivanov, P.J. McGovern, H.J. Zwally, and T.C. Duxbury, 1999, The global topography of Mars and implication for surface evolution, *Science*, 284, p. 1495-1503.
- Spanovich, N., M.D. Smith, P.H. Smith, M.J. Wolff, P.R. Christensen, S.W. Squyres, 2006, Surface and near-surface atmospheric temperatures for the Mars Exploration Rover landing sites, *Icarus*, v. 180, p 314-320.
- Spohn, T., 1991, Mantle differentiation and thermal evolution of Mars, Mercury, and Venus, *Icarus*, v. 90, p. 222-236.
- Stevenson, D.J., T. Spohn, and G. Schubert, 1983, Magnetism and thermal evolution of the terrestrial planets, *Icarus*, v. 54, p. 466-489.

- Stillman, D.E., and G.R. Olhoeft, 2005, EM Properties of Magnetic Minerals at radar Frequencies, Workshop on Radar Investigations of Planetary and Terrestrial Environments, February 7-10, 2005, Houston, Texas. abstract #6029.
- Stillman, D.E., G.R. Olhoeft, B. Douthit, M. Kass, P. Schwering, G. Scherer, M. Hergert, B. Winters, F. Li, R. Wagle, J. Modroo, J. Rittgers, 2006, CSM Geology Museum Measurements, <http://mars.mines.edu/magsus/gmuseum.htm> , viewed on 3/13/06.
- Sihvola, A.H., 1999, Electromagnetic mixing formulas and applications: IEEE electromagnetic waves series 47: Institution of Electrical Engineers, London, 284 p.
- Strangway D.W., 1967, Magnetic Characteristics of Rocks, in Mining Geophysics, Hansen, D.A., Heinrichs, W.E., Holmer, R.C., MacDougall, R.E., Rogers, G.R., Sumner, J.S., and Ward, S.H., ed, Society of Exploration Geophysicists, v. 2, Tulsa, Oklahoma, p. 454-473.
- Squyres, S.W., and A.H. Knoll, 2005, Sedimentary rock at Meridiani Planum: Origin, diagenesis, and implications for life on Mars, Earth and Planetary Science Letters, v. 240, p. 1-10.
- Taylor, G.J., L.M.V. Martel, and W.V. Boynton, Mapping Mars Geochemical, 37<sup>th</sup> LPSC, March 13-17, 2006, Houston, TX. abstract #1981.
- Thomas-Keptra, K.L., S.J. Clemett, D.A. Bazylinski, J.L. Kirschvink, D.S. McKay, S.J. Wentworth, H. Vali, E.K. Gibson Jr, and C.S. Romanek, 2002, Magnetofossils from Ancient Mars: a Robust Biosignature in the Martian Meteorite ALH84001, Applied and Environmental Microbiology, v. 68, No. 8, doi: 10.1128/AEM.68.8.3663-3672.2002, p. 3663-3672.
- Titus, T.N., H.H. Kieffer, P.R. Christensen, 2003, Exposed Water Ice Discovered near the South Pole of Mars, Science, v. 299, p. 1048-1051.
- Toksöz, M.N., A.T. Hsui, and D.H. Johnson, 1978, Thermal evolution of the terrestrial planets, Earth Moon Planets, v. 18, p. 281-320.
- Tomasko M.G., L.R. Doose, M. Lemmon, P.H. Smith, and E. Wegryn, 1999, Properties of dust in the Martian atmosphere from the Imager on Mars Pathfinder, J. Geophys. Res., v. 108(E4), p. 8987-9007.
- Tomonaga, S., and T. Oka (Translator), 1998, The Story of Spin, University of Chicago Press, Chicago, 265 p.

- Ulaby, F.T., Moore, R.K., and Fung, A.K., 1982. *Microwave Remote Sensing, Active and Passive Volume II: Radar Remote Sensing and Surface Scattering and Emission Theory*. Addison-Wesley Publishing Company: London, 1064 p.
- Ward, S. H., and G.W. Hohmann, 1988, *Electromagnetic Theory for Geophysical Applications*, in *Electromagnetic Methods in Applied Geophysics*, M.N. Nabighian, ed., Society of Exploration Geophysicists, v. 1, Tulsa, Oklahoma, p. 131-311.
- Wdowiak, T.J., G. Klingelhofer, M.L. Wade, and J.I. Nuñez, 2003, Extracting science from Mössbauer spectroscopy on Mars, *J. Geophys. Res.*, v. 108(E12), 8097, doi: 10.1029/2033JR002071.
- Wenk, H., and A. Bulakh, 2004, *Minerals: Their Constitution and Origin*, Cambridge University Press, New York, 646p.
- Williams, S. H. and J. R. Zimbelman, 1994, "White Rock": An eroded Martian lacustrine deposit(?), *Geology*, v. 22, p. 107–110.
- Williams, K.K. and R. Greeley, 2004, Measurements of dielectric loss factors due to a Martian dust analog, *J. Geophys. Res.*, v. 109, E10006.
- Weir, W.B., 1974, Automatic measurement of complex dielectric constant and permeability at microwave frequencies, *Proc. IEEE*, vol. 62, p 33-36.
- Wyatt, M.B., and H.Y. McSween Jr., 2002, Spectral evidence for weathered basalt as an alternative to andesite in the northern lowlands of Mars, v. 417, p. 263-266.
- Yen, A.S., R. Gellert, C. Schröder, R.V. Morris, J.F. Bell III, A.T. Knudsen, B.C. Clark, D.W. Ming, J.A. Crisp, R.E. Arvidson, D. Blaney, J. Brucknew, P.R. Christensen, D.J. DesMarais, P.A. de Souza Jr, T.E. Economou, A. Ghosh, B.C. Hahn, K.E. Herkenhoff, L.A. Haskin, J.A. Hurtowitz, B.L. Joliff, J.R. Johnson, G. Klingelhöfer, M.B. Madsen, S.M McLennan, H.Y. McSween, L. Richer, R. Rieder, D.S. Rodionov, L. Soderblom, S.W. Squyres, N.J. Tosca, A. Wang, M. Wyatt, and J. Zipfel, 2005, An integrated view of the chemistry and mineralogy of Martian soils, v. 436, p. 49-53.
- YSI, 2006, Specifications – YSI 44000 & 44100 Series Epoxy-Encapsulated Thermistors, <http://www.yei.com/extranet/TEMPKL.nsf/447554deba0f52f2852569f500696b21/e436f9a1454a5396852569f80071ea37!OpenDocument> , viewed on 3/23/06.

Yung, Y.L., J.S. Wen, J.P. Pinto, M. Allen, K.K. Pierce, and S. Paulson, 1988, HDO in the Martian atmosphere: Implications for the abundance of crustal water, *Icarus*, 76, p. 146–159.

## APPENDIX

The appendix is included on a DVD in a pocket inside the back cover of this thesis. An outline of the directory structure is included below and appears in the root directory on the DVD in the README.doc, README.pdf, and README.txt file.

The appendix has been separated into six sections: CHAPTERS, DATA, FIGURES, TABLE, THERMISTOR, and XRD. A brief discussion of each section is provided below. Specific details can be found in the README documents that accompany some sections. In order for the Grapher 3.0 and Surfer 7.0 files to work, the entire CD must be copied to the C drive. A table of the sample abbreviations can be found in the THESIS directory under SMPL\_LST.xls (Microsoft Excel 2002 format).

CHAPTERS section contains all the chapters of the thesis. It is split into 2 subsections: DOC and PDF. The DOC subsection contains each chapter (CHAPTERX.doc) in Microsoft Word 2002. The PDF subsection contains the full thesis (Thesis.pdf) and each chapter (CHAPTERX.pdf) in Adobe Acrobat 7.0.

DATA section contains two folders.

- SOFTWARE contains three folders
  - VISC++ contains the software that was used to acquire the data. For more details on these files, see the README file:  
C:\THESIS\DATA\SOFTWARE\DOS\README.doc
  - MATLAB contains the MatLab codes that were used to process the data. For more details on these files, see the README file:  
C:\THESIS\DATA\SOFTWARE\MATLAB\README.doc
  - DOS contains programs to read in and model the data acquired with the old computer (HP-9000). For more details on these files, see the README file: C:\THESIS\DATA\SOFTWARE\VISC++\README.doc
- VNA contains all of the vector network analyzer data taken in the thesis along with the logbook for each experiment including temperature data. The data results for each sample can be found in the folder named after the sample abbreviation (ID name). Within each sample folder, other folders exist to further organize the data. For more details on these files, see the README file in data abbreviation folder (i.e. C:/THESIS/DATA/GHKwMI/README.doc).

FIGURES contains all the figures given in the thesis. Each figure has its own folder labeled (FigX\_Y), where X is the chapter and Y is the number of figure in the chapter. The figures are organized into CHAPTER folders (CHAPTERX). The figures are in all sorts of formats including jpg's (\*.jpg), tiff's (\*.tif), gif's (\*.gif), Photoshop 7 (\*.psd), Grapher 3.0 (\*.grf), and Surfer 7.0 (\*.srf).

TABLE contains all the table given in the thesis. Each table has its own folder labeled (TableX\_Y), where X is the chapter and Y is the number of table in the chapter. The tables are organized into TABLE folders (CHAPTERX). The tables are in different formats: Microsoft Excel 2002 (\*.xls), jpg's (\*.jpg), and Adobe Acrobat 7.0 (\*.pdf).

THERMISTOR contains all the (Microsoft Excel 2002 format) spreadsheets used to calculate the temperature of the thermistors used in the thesis. ThermR.xls can be used to interpolate thermistor resistance values into temperatures. DecadeR.xls shows a table of typical decade resistance values and total input voltage used to measure the temperature.

XRD contains all the X-Ray Diffraction results. The XRD results can then be found in 2 different formats. This is because they were done by 2 different labs (The mineral lab ran 4 samples, while Steve Sutley at the USGS-Federal center ran 11 samples). The mineral lab samples have been reduced into the nearest percentage for each mineral found. While the USGS results just give major, minor, and trace mineralogical components.

- MinLab folder contains the 4 samples (MagRCh, YUMA, GHSChp, RM5CO) run by the Mineral Lab. This folder contains two folders. The TXT folder contains the \*.uxd files which display the counts versus angle. The PDF folder contains the \*.pdf files display the results of the Mineral Labs analysis of the data.
- USGS folder contains the 11 samples (GHKwMI, GHSMMX, Goeth, Hem, HemOr, HI4, HI9, Jaro, JSC1, Magn, PuNeHID) run by Steve Sutley at the USGS. This folder contains 6 folders.
  - The BMP and TIF folders show the number of counts versus angle in a \*.bmp and \*.tif format, respectively.
  - GRF folder contains the Grapher 3.0 files used to make the tif's.
  - RESULTS gives a table of the findings in \*.xls Microsoft Excel 2002 format and \*.pdf Adobe Acrobat 7.0 format.
  - TXT shows the raw data collected by the XRD instrument.
  - XLS contains spreadsheets for each of the samples that display the counts versus angle.